Multi-model coupling for fluid structure interaction

Alexandre Fernier

université PARIS-SACLAY

NNT: 2019SACLY001

Thèse de doctorat

Couplage multi-échelle pour l'interaction fluide-structure en dynamique rapide

Thèse de doctorat de l'Université Paris-Saclay
préparée à l'École Nationale Supérieure de Techniques Avancées (ENSTA)

École doctorale n° 579 - Sciences mécaniques et énergétiques, matériaux et géosciences (SMEMaG)
Spécialité de doctorat: Mécanique des Solides

Thèse présentée et soutenue au CEA Saclay, le 25 Janvier 2019, par

Alexandre Fernier

Composition du jury:

Florian De Vuyst – Professeur LMAC, Sorbonne Universités, Université de Technologie Compiègne	Président du jury
Dominique Eyheramendy – Professeur LMA, CNRS, Aix-Marseille Université, Centrale-Marseille	Rapporteur
Anthony Gravouil – Professeur LaMCoS, CNRS, Université de Lyon, INSA Lyon	Rapporteur
Régis Cottereau – Chargé de recherche CNRS HDR, LMA, CNRS, Aix-Marseille Université, Centrale Marseille	Examinateur
Christian Tenaud – Directeur de recherche CNRS LIMSI, CNRS	Examinateur
Eric Deletombe – Maître de recherche HDR, ONERA	Examinateur
Olivier Jamond – Ingénieur-chercheur CEA	Encadrant
Vincent Faucher – Expert Senior HDR, CEA	Directeur de thèse

Are you a map ?
Gilles Fournerie

Remerciements

Ce manuscrit de thèse marque la fin de trois années de travail qui n'auraient eu lieu ni pu s'accomplir sans de nombreuses personnes que je tiens à remercier ici.

En premier lieu, je tiens à remercier Vincent, mon directeur de thèse, qui m'a fait confiance pour effectuer ce travail ainsi que pour son soutien permanent. J'ai beaucoup apprécié la qualité de nos échanges qui ont toujours été productifs et intéressants. Je tiens évidemment à remcercier chaleureusement Olivier pour ces trois années passées ensemble. Les mots me manquent pour décrire la chance que j'ai eu de t'avoir comme encadrant: un grand merci pour tous les moments passés ensemble qui ont ont largement dépassé le cadre du travail comme en témoignent les nombreuses anecdotes qui me sont restées. Un grand merci également aux membres du Laboratoire DYN qui m'a très bien accueilli (et nourri). Ce fut un vrai plaisir de passer ces trois années dans une aussi bonne ambiance et je leur témoigne ici toute mon amitié. J'ai naturellement une pensée pour mes partenaires de coinche pour tous nos fou-rire, mais également à Thierry dont la sagesse n'a d'égal que son grand âge. Une mention spécial à Robert, alias Bob, qui m'a non seulement beaucoup aidé dans mon travail (bien que ce ne soit pas dans ses prérogatives) mais également pour m'avoir appris les paroles de l'*Internationale* et ce que c'est que d'être un vrai résistant. Enfin, je tiens à féliciter Marwa et Gianluca qui ont réussi à me supporter au quotidien dans notre bureau.

Je souhaite témoigner ma profonde gratitude aux membres de mon jury pour l'intérêt porté à mon travail. Je tiens à remercier en particulier Dominique Eyheramendy et Anthony Gravouil pour avoir accepté d'être rapporteurs de mon travail et pour leur remarques judicieuses. Je tiens également à remercier Florian De Vuyst qui a accepté d'être président de mon jury.

Tout travail nécessite une forme d'équilibre/d'hygiène de vie afin d'être effectué sainement. Je tiens donc à profiter de cette page de remerciements pour exprimer ma profonde gratitude à tous ceux qui m'ont entouré pendant ces trois dernières années, mais également plus généralement toutes les personnes qui m'ont permis de devenir la personne que je suis. Ma première pensée va naturellement à Jenna, qui égaie mon quotidien depuis quelques années déjà et qui m'a beaucoup aidé dans le processus de rédaction de mon travail. Je pense naturellement aussi à ma famille et mes cousins (trop nombreux pour être cités) avec qui j'ai grandi. Je pense aussi à mes amis, que ce soit les copains des scouts; les copains des soirées festives (la secte, les copains de l'ENSTA), les copains de randonnées (Tanzanie, Tadjikistan ou lors de weekends plus ou moins improvisés); les copains du foot du lundi, du mercredi, du dimanche voir du mardi, jeudi ou samedi occasionnel; ou les copains de toujours avec qui l'on se retrouve moins régulièrement, par simple plaisir de se voir (Camille, Gael, Adrien, Maylis, Célie, etc). Vous avez tous, d'une certaine façon, contribué à ce travail et je vous en remercie.

Contents

List of Figures

List of Tables

Introduction

In the nuclear industry, the study of the various operational states is decisive when designing nuclear plants [1] [2]. These operational states can be divided into three categories [2]. A first category, called normal operation occurrences, includes operations within specified operational limits and conditions. Another one, called Anticipated Operational Occurrences (AOO) refers to occurrences that are deviating from normal operations but that, with appropriate design, can not cause any significant damage nor lead to accident conditions. They are expected to occur at least once during the lifetime of the facility and do not prevent the structure from operating. The last category corresponds to accidents, which are defined as deviations from normal operations that can put in jeopardy the operating of the facility.

The study of accident scenarios is essential to demonstrate that the facility design meets the acceptance criteria[1] defined by national agencies[2]. Accidents scenarios that are critical in showing that the design is appropriate are called Design Basis Accidents (DBA). For DBA, the most fundamental criterion is that there should be no, or at most very limited, radiological consequences to the public [2]. Examples of DBAs are the Loss Of Cooling Accidents (LOCA) [6] [7] [8] and Reactivity Initiated Accidents (RIA) [5] [9] [10] for Pressurized Water Reactors (PWRs) and Core Disruptive Accidents (CDA) [11] [12] [13] for Fast-Breeder Reactors (FBR).

In order to evaluate if designs meet acceptance criteria, numerical simulations of DBAs have become essential. At the Dynamics Laboratory[3] (DYN) of the Commissariat á l'Énergie Atomique et aux Energies Alternatives (CEA), Europlexus[4] software, hereafter abbreviated EPX, is used to simulate DBAs such as LOCA and CDA at the reactor scale. Yet, simulating accidents still faces difficulties such as taking into account localized geometric details which need to be modelled through other means [14]. Another difficulty is due to mesh generation which can be very costly, especially for such large systems. Hence, modifying the mesh to optimize the position or shape of a specific component can be prohibitive. Instead, numerical zooms are a possible way to consider such local details. In the nuclear industry, such numerical zooms are very useful as they allow to (1) test if the modelling of local geometries/phenomenons is accurate, (2) locally change the modelling for specific applications or (3) optimize the shape and position of specific components. Additionally, numerical zooms would

[1] These criteria aim to minimize the possible consequences of operating nuclear plants [3] [4] [5] and thus have direct consequences on the design.

[2] For example l'Agence de Sûreté Nucléaire (ASN) for France and the United States Nuclear Regulatory Commission (US NRC) for the United States of America.

[3] CEA/DEN/DANS/DM2S/SEMT/DYN.

[4] EPX is a fast transient dynamics program jointly owned by the French Commissariat à l'Energie Atomique et aux Energies Alternatives and the Joint Research Center of the European Commission (http://www-epx.cea.fr).

allow to do all these deeds at reduced human cost and computer resources.

In the following section, we briefly present LOCA and CDA and illustrate how numerical zooms can improve the modelling in EPX simulations. Based on these examples, we establish the specifications of the numerical tool to be implemented in EPX. Next, we review existing methods and point out why they do not, in their current state, fulfill all the specifications previously established. Finally, we describe the scientific approach adopted in this work.

Underlining the use of numerical zooms in Design Basis Accidents

In this section, we present representative LOCA and CDA scenarios and explain why the current modelling in EPX fails to represent certain aspects. For each example, we then show how numerical zooms can improve the modelling in EPX simulations and thus lead to more accurate evaluations of acceptance criteria in the design of nuclear plants.

Presentation of Loss Of Coolant Accidents

The Loss Of Coolant Accident (LOCA) in Pressurized Water Reactor (PWR) refers to any scenario[5] that results in the brutal opening[6] of one of the main coolant pipes and of its consequences. In accordance with the ASN, the French nuclear authority, the quadratic addition of LOCA and earthquake effects is considered as the reference accident to design the vessel internals. In the following, we present, without loss of generality, a particular scenario corresponding to a large break as it leads to the most significant mechanical consequences[7].

We assume for example that, initially, a guillotine break occurs between the reactor coolant pump and the reactor vessel (see Figure 1). The break provokes a steep drop in the pressure, from 155 bar to 90 bar. At the same time, the core is emptied out and rapidly shuts down due to the drop of control rods and the resulting negative reactivity. The injected coolant still leaks through the break so that the stored energy causes the temperature inside the vessel to rise from 300°C to about 800°C. This is called the blowdown period (0 to 30 s).

Then, once the pressure has sufficiently decreased, low-pressure injection systems activate and water is efficiently injected into the system. While the lower plenum fills with water, the core is still not cooled down and continues to heat up. During that period, called the refill period (30 to 40 s), some fuel rods can burst or break, limiting the pathway through which the rising water will be able to go through.

Once the plenum is filled, the core water injected begins to cool down the core. This is called the reflood period (40 to 200 s). The quenching front moves upward, cooling

[5]The different scenarios are usually categorized into large break LOCA (flow areas larger than 0.1 m^2 in diameter) and small break LOCA (flow area typically between 2.5 cm^2 and 950 cm^2 in diameter).

[6]sometimes referred to as a *guillotine break*.

[7] Intermediary breaks are currently being studied when it comes to studying the consequences on the fuel.

the bottom part of the core and thus decreasing the heating velocity. Eventually, the peak cladding temperature is reached at around 1080°C. Then, the cooling overcomes the heating and the core is efficiently cooled down.

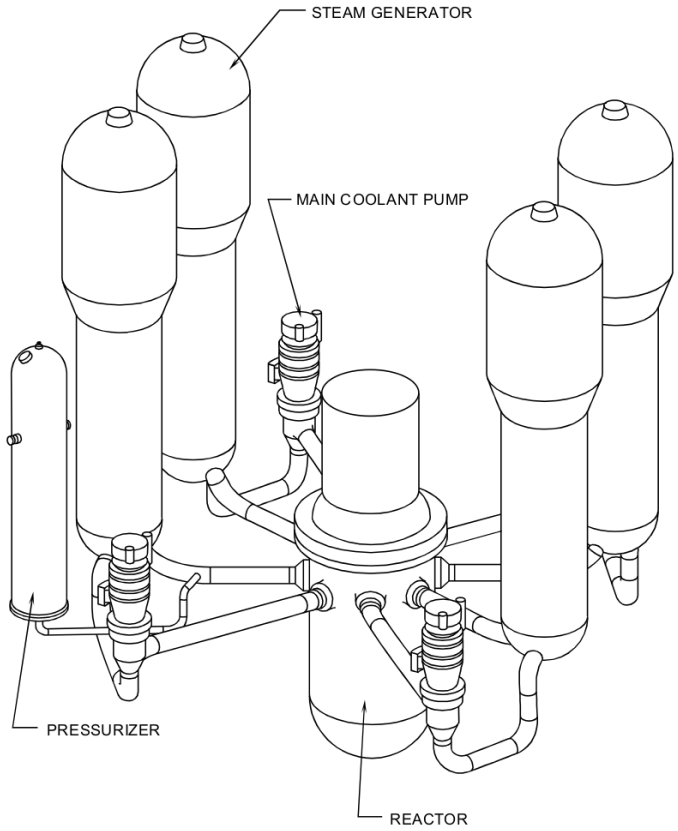

Figure 1: PWR primary system arrangement [15].

During a LOCA, the main mechanical loadings on the reactor and the vessel internals occur rapidly due to the rarefaction wave initiated by the break. These loadings are particularly high when the rarefaction wave impacts the core barrel and in its subsequent propagation through the core. In the latter case, when the wave spreads between the Lower Core Plate and the Upper Core Plate, it can either go through the core center, containing the fuel assemblies, or go through the by-pass behind the baffle plates (see Figure 2). The travel time differs in both paths yielding pressure forces on the baffle. These forces need to be evaluated in order to ensure that LOCA has no consequence on the integrity of the core during the accident. In particular, the influence of the perforated reinforcement plates attached to the baffle on time delays needs to be evaluated in order to precisely quantify the resulting pressure forces (see Figure 2).

At DYN, EPX software is used for LOCA simulations [16] [17]. In these simulations, the 3D effects of the perforated plates are approximated by impedance relations applied at the nodes of the domain[8]. These relations are calibrated on experimental

[8]The impedance actually approximates all the localized geometric details that have a significant influence on the fluid flow, such as cavities, orifice plates, sudden enlargements/narrowings in the pipes or perforated plates.

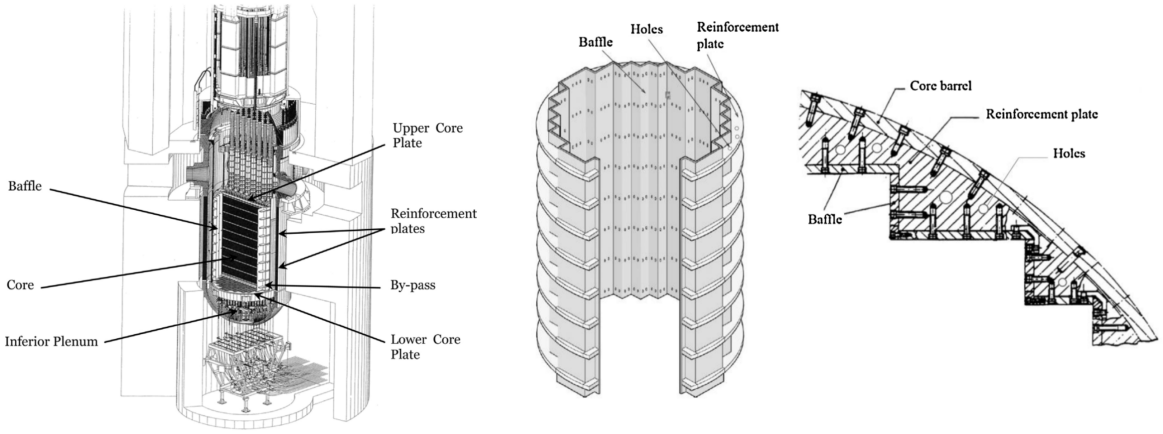

Figure 2: PWR vessel and internal components (RIGHT), baffle (CENTER) and perforated plates (LEFT) [16].

results and representative, locally scaled, simulations [17]. However, the influence of the reinforcement plates needs to be assessed at the reactor scale. As impedance relations are being used, these plates are not meshed in EPX simulations and it would require both human and computational resources to adequately modify the existing mesh. This is why a numerical tool that allows for the superimposition of independently meshed reinforcement plates is necessary. Moreover, for additional flexibility, that numerical tool should allow for the main mesh and the one representing the plates to be non conforming (see Figure 3).

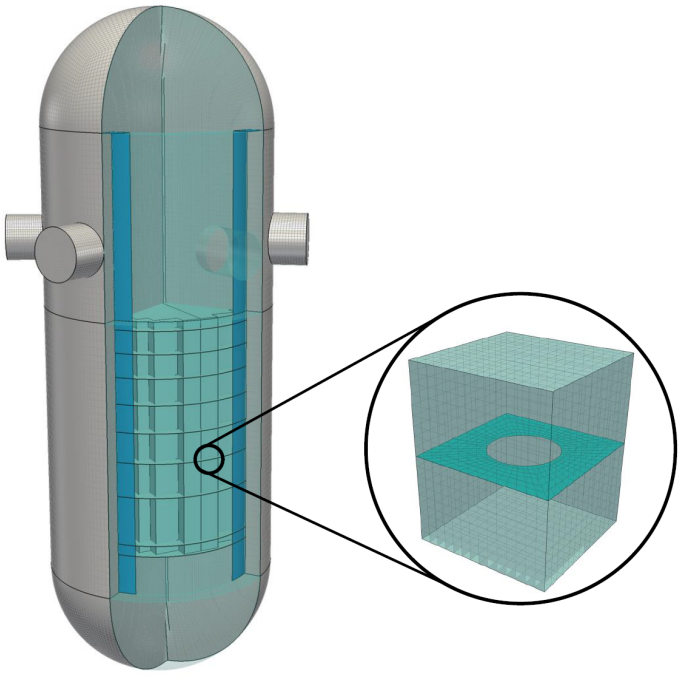

Figure 3: The reinforcement plates (circled in black) are independently meshed. We propose to superimpose that mesh in the domain representing the reactor (mesh on the left) in order to evaluate the accuracy of the impedance relations.

Presentation of Core Disruptive Accidents

The Core Disruptive Accident refers to scenarios resulting in the melt down of the core of a Fast Breeder Reactor (FBR). In accordance with the Western European Nuclear Regulators Association (WENRA), the study of CDAs is necessary in order to reduce potential radioactive releases in the environment [18]. Although there are no known scenario that can realistically lead to a core melt and that there is a very low probability of such an event happening in FBRs, the analysis of CDAs is still used for the design of FBRs as part of the so-called defense-in-depth. That is why CDAs are sometimes referred to as Beyond Design Basis Events [13]. In the following, we present a possible chain of events during a CDA.

Initially, a large amount of energy is released in the vicinity of the core due to a primary nuclear power excursion caused by, for example, an Unprotected Loss of Flow (ULOF) [19]. This energy release causes the vaporization of the fuel and coolant which then form, along with gas resulting from chemical reactions into a core bubble. The bubble then expands, generating pressure waves in every directions, causing plastic deformations on the surrounding structures. Because of the presence of cover gas space above the sodium free level, there are less resistance for the sodium to move upwards. Hence, a net force develops in the downward direction so that the main vessel is pulled-down (0 to 50 ms).

The sodium accelerated upwards eventually reaches the top shield (around $t = 100$ ms). During this "sodium slug impact", the kinetic energy of the moving sodium creates an upward force. Consequently, the pressure in the cover gas as well as in the sodium increases steeply, resulting in an impact force on the top shield in the upward direction and causing further overall plastic deformation on the main vessel (100 to 150 ms).

Then, the fuel may melt due to the stored energy which can ignite local nuclear reactions and/or cause secondary power excursions. If the energy released is significant enough, melted fuel is scattered in the sodium so that $UO_2 - Na$ interactions occur. The latter are very similar to steam explosions so that it has the same effects as the core bubble, only with greater intensity. Eventually, the core cools down and there are no more power excursions (150 to 900 ms).

During the slug impact (both after the primary and secondary excursion), the bolts of top shield components elongate and the seals may fail. As a result, sodium may penetrate the top shield and leak to the Reactor Containment Building (RCB). The leaked sodium catches fire so that the temperature and the pressure rise in the RCB. It is very important to quantify the quantity of sodium leaked as it is one of the parameters taken into account when designing the RCB.

In CDA simulations by EPX, the seals are considered impervious so that it is necessary to change the modelling. Thus, a numerical tool able to locally superimpose a model containing a gap between, for example, the intermediate heat exchangers and the top shield (see Figure 5) would save both human and computer resources.

Main objectives of the proposed research

Through these two examples, we asserted the need for a numerical tool able to locally change the modelling when simulating fluid structure interaction phenomenons in fast

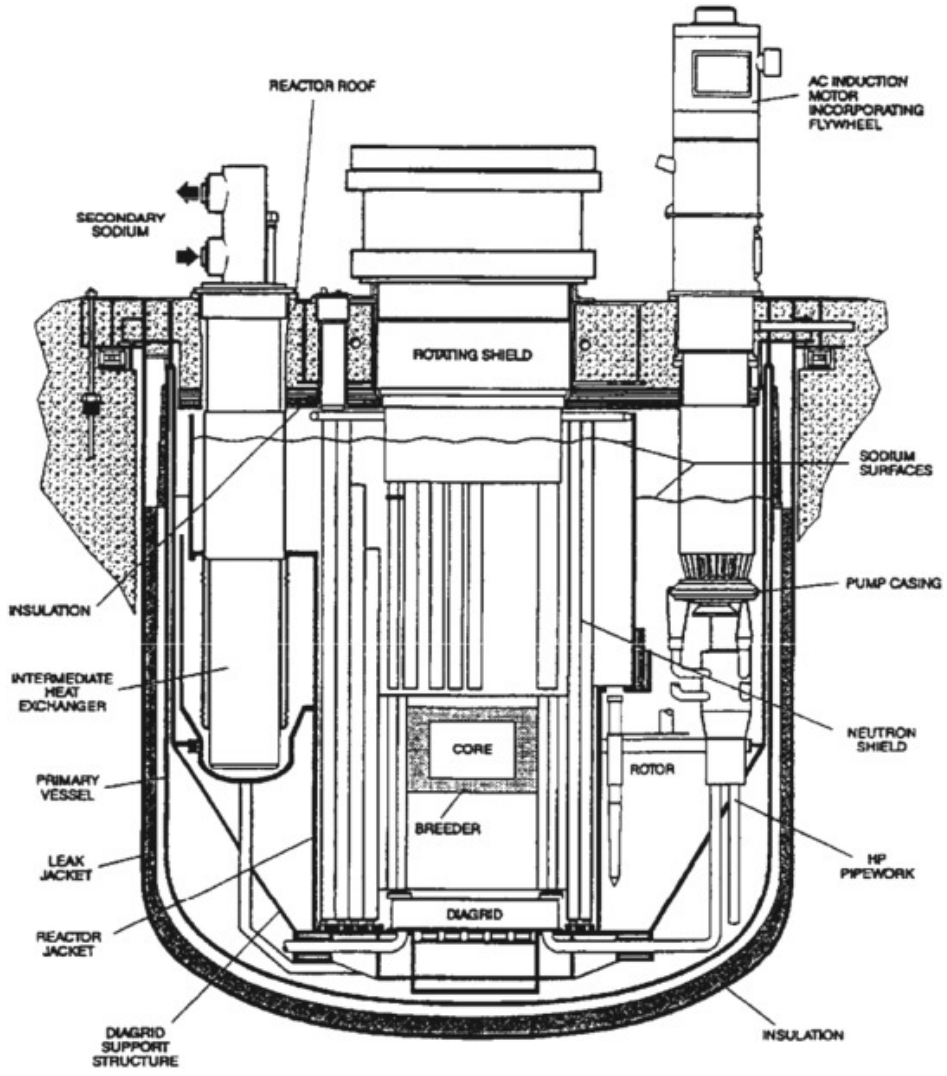

Figure 4: Example of a FBR internal components [20].

transient dynamics. We hereafter recall the specificities the numerical tool we want to implement in EPX needs to have.

1. It needs to be able to simulate fluid structure interaction (FSI) phenomenons. Indeed, in the examples observed, strong shocks propagate and the response of the surrounding structures is critical when simulating the different accidents.

2. It should not alter the initial, global mesh[9] and allow for the superimposed domains to have non conforming meshes.

3. It needs to be compatible with explicit time integration. Indeed, the software EPX uses such time-integrators in order to simulate these accidents which are conditionally stable. Thus, the numerical tool implemented needs to remain stable when they are used.

[9]This requirements implies that re-meshing techniques [21] [22] [23] [24] are not considered.

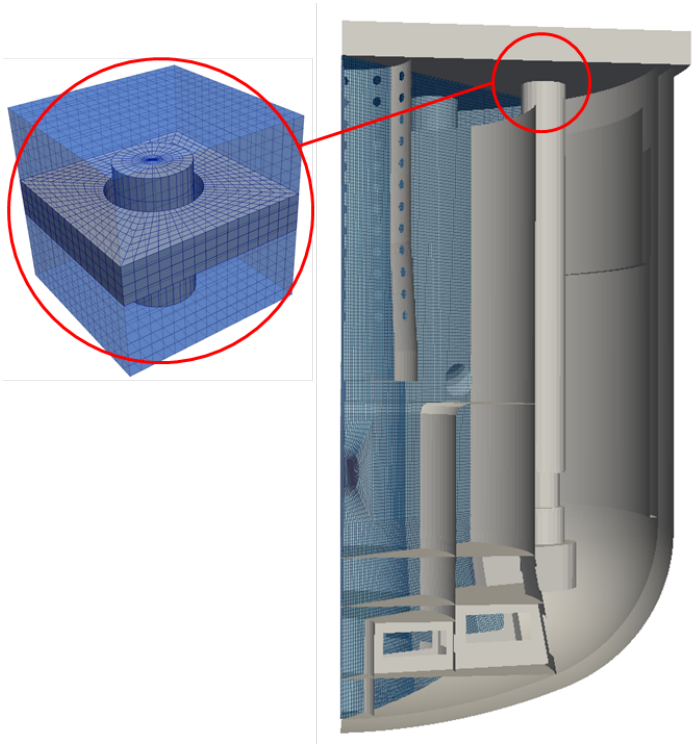

Figure 5: A gap between the top shield and equipment going through the shield is modelled (circled in red) and superimposed in the main global domain (mesh on the right) for reactor prototype ASTRID.

Now that the characteristics of the numerical tool are specified, we present existing methods that aim to tackle similar issues. In order to give a comprehensive review, we chose to present a review of multi-modelling methods and underline if and how they are suitable to the applications considered here.

Bibliography

The field of multi-modelling has been a topic of significant interest since the 1960s and the work of Volkov who introduced overset grids, or patches, in order to obtain better solutions in corner points of a domain for the Laplace equation [25] [26]. Since then, the expansion of multi-model coupling techniques has been closely related to research made in multi-scale modelling. Thus, it is not surprising that many multi-modelling techniques have multi-scale applications and vice-versa. We can distinguish three different fields of research: the determination of solutions on multiple grids, enriched finite element methods and superimposition methods. Note that these three fields of research are not an exhaustive overview of the research in multi-modelling. However, it does give a general idea of the main research fields being explored. In particular, we focused on methods which bring refinement in the modelling and/or permits local numerical zooms.

Computation on multiple grids

The first family of approaches propose to solve the equations of the problem on different grids. For these approaches, two scales are usually considered. The first one, macroscopic, represents the global behaviour of the domain while the second one, microscopic, includes specific characteristics of the model. These approaches take into account each scale by representing them on different, independent grids and by coupling them through dedicated operators. These operators allow for the transfer of information from one grid to another, that is, from on scale to another. Generally, these operators are built using principles very similar to those of homogenisation [27] [28] [29].

Multi-grid methods [30] [31] are a very efficient[10] iterative computation strategy, initially proposed for elliptic problems [30]. These methods rely on the fact that iterative relaxation methods [33] quickly compute the high frequency components of the solution but fail to obtain the lower ones in less than a few iterations. The idea is then to compute the solution on a series of coarser grids in order to obtain, through relaxation methods, all the frequency components of the discrete solutions. The computation iterations usually follow V- or W-shaped cycles, alternating between fine and coarse meshes. The transfer of the solution from one grid to the other is done through operators that either interpolate or project the solution. It allowed, for example, Fish and Belsky to study the behaviour of periodical composite structure [34] [35].

While the standard theory of multi-grid methods generally assumes ellipticity [31], it was extended to hyperbolic systems by Ni [36]. The idea is to accelerate the wave propagation on multiple grids by using larger time steps on coarse grids without violating the CFL condition. Thus, low frequency components are rapidly expelled through the outer boundary while higher ones are locally damped by the smoother [37] [38]. The method has proved particularly efficient for the simulation of the Euler equations [39] [40] [41] and was extended to convection problems [42] and hyperbolic conservations laws [38]. The multigrid methods can thus be used, locally, to introduce a specific modelling. However, they are mainly used in order to obtain steady state solution and their use for the simulation of evolution problems such as shocks is thus limited. Moreover, they require specific features to handle local changes in the geometry of the domain.

Hierarchical Dirichlet Projection Methods (HDPM) also tackle the issue of multi-modelling through computation on multiple grids [43] [44]. First, a hierarchy of the physics of the problem is set up, ranging from the coarsest description to the most detailed one. This approach then proposes to compute a first solution u_0 on the coarsest scale. Then, error estimates identify the cells where the solution is not precise enough [44]. The value of the solution is then corrected by localized computations at finer grid levels. Indeed, on each critical region, a new solution u_1 is computed and uses the solution u_0 as its boundary condition. Finally, it projects the fine scale solution on the coarse scale grid. If a posteriori estimates of the projected solution are still too high, the process is repeated for larger cells so that in the worst case scenario, the fine scale is used for the entire domain, ensuring the convergence of the method [43].

[10] The computational work is proportional to the number of unknowns [32].

This method allowed Oden *et al.* to model the behaviour of heterogeneous composite structures [45].

A variety of techniques were developed that use the same methodology: a coarse solution is computed on a coarse grid and finer grid are used, locally, to take into account local changes in behaviour. This is the case, for instance, of the EF^2 method [46]. It proposes, in identified integration points, to introduce a fine finite element grid that best describes the physics of the problem. Computation on this local grid yields the value of the integrated physical quantity at that integration point. This method allowed Feyel *et al.* to describe the elastoviscoplastic behaviour of composite materials [46] [47] and Ramiere *et al.* to simulate the behaviour of heterogeneous nuclear fuel [48]. Another multi-scale method was designed by Loehnert and Belytschko in order to simulate crack growth [49] [50]. Projection methods were also developed in fluid mechanics. For instance, a Cartesian grid projection method was developed in order to solve the incompressible Euler equations in complex geometries [51]. For example, the solution is first computed on a coarse grid for one time step. Then, the solution is computed on smaller grid with multiple, smaller, time steps until the two solutions can be synchronized [52]. Finally, the method allows for local change in modelling and, in particular, for changes in geometries [53].

These projection methods allow for changes in geometry and local refinement. However, as noted in [54], these techniques have yet to tackle dynamic problems such as wave propagation and multi-physics coupled field problems such as fluid-structure interaction. Moreover, they are not well suited for explicit dynamics and unsteady problems.

Computation on multiple grids are an effective way to take into account local behaviours, in particular for steady states. However, it is not well suited neither for evolution problems such as the propagation of waves nor for the adding of new elements outside the main domain.

Enriched finite elements

In the standard finite element method, it is rather difficult to capture quick oscillations or strong gradients without refined meshes. In explicit dynamics, tiny elements imply smaller time step due to the Courant-Friedrichs-Levy condition and thus a higher computational cost. Hence, the second family of approaches propose to enrich the already existing vector space with special functions that reproduce these high frequency phenomenons. This way, the global solution is obtained by the sum of the standard finite element method and a corrective term yielded by the special functions.

A few difficulties arise from this formulation. First, if the corrective term is computed on each element independently, then the global solution can be discontinuous and special treatment is needed to remedy to that issue. Secondly, as the corrective term reproduces, by construction, high frequency phenomenons, special care in the integration process is needed. Finally, there is no guarantee that the standard solution vector space and the enriched vector space are linearly independent so that the stiffness and mass matrices need extra work to be well conditioned.

The multiscale variational method introduced by Hughes is based on this reasoning [55] [56]. In this method, the corrective term is computed using analytical formulas. For example, when applied to the Poisson equation with homogeneous Dirichlet boundary conditions and a bounded domain, the analytical corrective term is equal to $-\int_\Omega\ g(x,y)r(u)(y)\ dy$ where x is the position, g is the Green function for the Laplace operator and r the residual of the finite element solution. In order to implement this formula, the green function is approximated by small finite element grids[11]. Moreover, in order to ensure the continuity of the function and the fact that the vector spaces need to be linearly independent, Hughes proposes to nullify the corrective term on each element's border. The corrective term then appears as local bubble-shaped contributions.

The multiscale variational method has had many applications in acoustics, electromagnetic [56] but especially in computational fluid dynamics [57]. Indeed, the method has been found to be useful in the simulation of laminar and turbulent incompressible flows [58] [59] [60]. They are particularly used in Large Eddy Simulations (LES) [61] [62]. However, the multiscale method is not well suited for the simulation of shocks. Moreover, as seen for the Poisson problem, it is also not well suited for modelling alterations across elements.

Another set of enriched methods were developed thanks to the general framework of the Partition of Unity Method (PUM) proposed by Babuska and Melenk [63] [64]. In the PUM, the corrective term is computed using special functions $(f_j)_{1\leq j\leq M}$ adapted to the enrichment considered. In order to guarantee the continuity of the solution across the entire domain, the solution are weighted by finite element shape function $(\phi_i)_{1\leq i\leq N}$ so that the corrective term equals $\sum_i \sum_j b_{ij} f_j \phi_i$. By construction, the shape functions form a partition of unity, that is $\sum_i \phi_i = 1$, which gave the name to the method. The choice of the special functions is critical and gave rise, amongst others, to two methods [65]: the Generalized Finite Element Method (GFEM) [66] and the eXtended Finite Element Method (XFEM) [67] [68].

The GFEM improves the physical description of the domain by choosing special functions that are either asymptotic developments, specific modes, polynomial functions or solution of locally obtained, finite element methods solution [69] [70]. The XFEM addresses mechanical problems under the assumption of small perturbations and uses Heaviside functions as their special functions. These Heaviside functions are usually used to represent cracks. They are determined thanks to signed-distances functions defined through level-sets techniques [71] [72]. Both these methods are widely used for a wide range of applications, among which, propagation of cracks [73] [74], the introduction of holes in a global domain [75] and fracture problems [69] [70]. Although the methods are mostly used in statics or quasi-statics, it was extended to crack dynamics with explicit time integration [76] [77] [78] [79].

These methods, although very efficient, has not yet been extended to the simulation of fluid mechanics and particularly to the propagation of shocks. Moreover, the XFEM can be computationally costly for complex geometries as it introduces additional degrees of freedom for every element the method is applied to. Nonetheless, a few ingredients, such as the weighting by functions that form a partition of unity,

[11] This method also belongs to the family of approaches that compute the solution on multiple grids.

were used in other methods for the simulation of structural and fluid mechanics (see hereafter).

Superimposition techniques

The last set of approaches concerns superimposition techniques and can be identified as part of the more general field of decomposition domains. In the following, we focus on the two superimposition techniques that offer the most general framework for the applications considered. But first, we briefly mention other techniques not considered in the following.

In particular, we do not present surface coupling methods such as the mortar method [80] [81] [82] as they do not allow for overlapping domains but instead require the boundaries of the two models to be compatible (but not necessarily conforming). Yet, many of these techniques rely on Lagrange multipliers to impose link conditions [83] which can give strategy hints for the coupling of overlapping domains. Other methods not presented here but worth mentioning are the superimposition techniques developed to couple atomistic/molecular models with continuum ones. They constitute a wide field of research and have led to the development of many methods, amongst which the quasi-continuum method [84] [85], the handshake method [86] [87], the bridging domain method [88] [89] [90] and the bridging scale method [91] [92].

The first superimposition technique presented here is called the Arlequin method and was first introduced by Ben Dhia in the late 1990s [93] [94] [95] [96] [97] [98]. He conceived an approach for the resolution of superimposed models with non conforming meshes and/or different modelling for static and quasi-static cases [94], [93]. The author uses a partition of unity approach for the superimposition of models and introduces weight parameters in order to split the energy between each model. In [97], he studies the computational specificities of the application of the Arlequin framework to the finite element methods. In particular, he describes a method for the computation of the coupling matrices as well as the integration of the weight parameters. He was then able to study the behaviour of beams [94] and the propagation of cracks [97] but also to simulate contact problems [99].

Rateau, working with Ben Dhia, extended the Arlequin framework to the fitting of 3D modelling with plates and hulls [100] [96]. In particular, Rateau studied the influence of both Arlequin parameters and refinement differences across models on the solution. For instance, he showed that for basic tests, it was suitable to project the mediator space on the coarser meshed model. Indeed, it prevents locking phenomenons from appearing and lets both models contribute with their own specificity. Moreover, he showed that on the coupling zone, if the arlequin weights are chosen to be constant, giving more weight to the model whose modelling best describes the problem[12] yields a more precise solution.

Prudhomme, Bauman *et al.* extended the Arlequin method to problems that involved both an atomistic model and a continuum model [101] [102] [103] [104]. In [103], they mathematically prove that problems are well-posed for certain coupling norms only. For example, the L^2 norm coupling is shown not to meet the Babuska-Brezzi condition [105]. Moreover, they studied the influence of the solution of the size of the

[12] for example the model with the finer mesh or whose modelling include more physical phenomenons.

coupling zone (negligible variations) as well as the influence of the distance between the coupling zone and the alteration. The influence of the latter on the solution was observed to be exponentially decreasing with the distance [101] [102]. It allowed them to study the equilibrium of cracks and square lattices [101] [102] as well as large-scale hybrid molecular-continuum statics problems for the manufacturing of semiconductors [103] [104].

Chamoin *et al.* also analysed the influence of the Arlequin framework for the coupling of an atomistic model and a continuum model [106] [107]. They identified four possible sources of instability when coupling continuum models with atomistic ones [107] that are not restricted to atomistic/continuum problems. The first one is the appearance of oscillating solutions, or free modes, when discontinuous arlequin weights are used for models with significantly different discretization size. Secondly, instabilities may appear at both ends of the coupling zone because of ghost forces. Finally, a local loss of the coercive property may appear if the arlequin weight assigned to the particles gets to zero too quickly[13].

Chuzel-Marmot *et al.* and later Caleyron *et al.* applied the Arlequin framework to the coupling of a SPH model and a finite element one in structural dynamics [108] [109] [110] [111] [112] [113]. Chuzel-Marmot observed small perturbations can appear in the solution due to reflections on the coupling zone. However, he did not justify the fact that the method remains stable in the Arlequin framework, nor did he mention if the simulations were obtained for optimal time steps [109] [112]. Caleyron *et al.* noticed that the type of arlequin weights (piecewise constant, linear or cubic) did not impact the solution. In particular, they observed that contrary to other works [114] [112], no reflections on the coupling zone appeared. They used the Arlequin method to simulate fluid structure interaction applications [113] and evaluate the constraint caused by impacts on large structures [109].

Ghanem extended the Arlequin framework to the explicit-implicit time integration of structural dynamics [115] [116]. He analysed the influence of the coupling on the solution. in particular, he proved that by using a linear interpolation of the Lagrange multipliers obtained on the implicitly integrated domain, no energy was added to the system. This way, he was able to extend the Arlequin framework to heterogeneous time integrators with multi time steps while ensuring total energy conservation. It allowed him to simulate rotating machinery phenomenons while superimposing 1D models on 3D ones [116].

Although the influence of the coupling operator on the solution was studied in many works [97] [103] [116], Guidault and Belytshko [114] accomplished an extensive study of the H^1 and L^2 coupling operators. Although problems have been theoretically proven to be well posed for a H^1 coupling operator but not the L^2 one. Yet, they advise that the latter should still be considered as it yields more accurate solutions. In particular, they show that use of the L^2 coupling operator merely implied more restrictions on the components of the Arlequin method, such as the need for continuous weight functions. Ben Dhia *et al.* and Guidault *et al.* also showed that for both H^1 and L^2 coupling operators, the Lagrange multipliers should be projected on the coarser mesh. Indeed, locking phenomenons can appear otherwise and the authors even advise to use a mesh coarser than the ones of both models.

[13] As is the case for cubic arlequin weights.

The second main approach considered in this work, called the Chimera method, was first introduced by Steiger *et al* in 1983 in order to couple two models with overlapping domains for the simulation of aerodynamics [117] [118] [119]. In the Chimera method, the information is transmitted from one grid to another through interpolation techniques. Thus, the user needs to determine the degrees of freedom (for instance, nodal values or values at elementary integrations points) of each domain where the solution is interpolated. Let us consider, as an example, a domain B fully embedded inside another domain A. The so-called interpolated degrees of freedom of domain B are the ones on its boundary. In this case, domain A is called the giving grid while domain B is called the receiving grid. Indeed, the value of the quantities on grid B are assigned through the interpolation of these quantities on grid A. The degrees of freedom of grid A that are used to interpolate the value on grid B form the stencil of the interpolation. Similarly, degrees of freedom need to be defined on grid A so that information can be transmitted from grid B to grid A.

The Chimera method offers many advantages. First, it can be used for simplified mesh generation as it allows for each region of the domain to be independently meshed [119] [120]. Secondly, it allows for local refinements [121] [122] as local areas can be refined, which offers an alternative to codes that do not handle adaptivity. It is also an efficient way to simulate moving components [123] [124] [125] as the independent mesh can move freely with respect to each other, preventing mesh distortions. Finally, the Chimera method is very efficient in configuration optimization [126] as the independent mesh can be moved freely around the domain. The Chimera method and more generally the use of overlapping grids have had many applications in CFD. For instance, it was used to simulate the airflow around aircraft [127] [128] [129] and space shuttles [130] [131]. Moreover, it was used to solve the Euler equations [132] [39] [133] as well as the Navier-Stokes equations [123] [134].

Berger gave a definition for the concept of global conservation for multi-grid systems in order to propose conservative interpolation techniques for multi-grid systems [135]. The definition states that a multi-grid system is globally conservative if, for a constant flow[14] on the outside boundary of the global domain, the numerical approximation of $\int_\Omega u(x,t)d\Omega$ (u is the exact solution) is also independent of time. Benoit [136] analysed conservative interpolation schemes and concluded that none of them were stable. He advised that a compromise between stability and convergence should be made and that, more specifically, discontinuities should not propagate over superimposed regions. Wu also showed that a conservative treatment of the boundary leads to marginally stable solutions [137]. Other approaches proposed to change the discretization in the overlapping zone in order to ensure global conservation while maintaining stability. For instance, Wang *et al.* [138] [139] and Brenner [140] chose to create a new mesh formed by the intersection of the overlapping meshes while Kao *et al.* [121] and Berglind [141] opted for a re-meshing of the entire overlapping zone. However, both methods are particularly costly, especially of the grid represent objects in relative motions. Moreover, the intersection of the meshes can lead to irregular elements and/or small elements unfit for explicit time integration.

Starius was the first to study the stability of hyperbolic differential equations for computations on multiple grid [142] [143]. He proved that the composite mesh difference methods (CMDM) for one dimensional problems was stable. Later, Wu *et al.*

[14] with respect to time.

studied the conservation and convergence of composite grid methods in computational dynamics and used the GKS-theory [144] to study their stability [145] [146]. In particular, Wu concludes that ensuring stability is more desirable than using a conservative treatment of the boundaries. Indeed, they point out that a non conservative treatment of the boundary does not exclude conservative solutions, as observed in other works [147]. Moreover, he showed that using sufficiently dissipative schemes (such as TVD, ENO) and the normal interpolation interface condition ensured conservative solutions in a stable way. Lions, Pironneau *et al.* proved the convergence of the Chimera method for different cases [148] [149].

Peron, in [150], underlines a few practical hints when using the Chimera method. First, she showed that it is more desirable to have meshes of the same size in the overlapping region, and more specifically in the stencil region of a domain and in the corresponding interpolated region of the other domain. Moreover, the interpolation order should be greater or equal to the order of the numerical scheme. Indeed, if both conditions are not met, then the numerical error will be imposed by the interpolation error and not by the numerical scheme. Peron, based on work by Jameson *et al.* [132], also noted that in explicit dynamics, the overlapping area needs to have a minimal size. Indeed, in explicit dynamics, all the quantities at time step t^{n+1} are determined from quantities at time step t^n. Thus if the stencil is larger than the overlapping zone, then a degree of freedom of grid A that needs to be interpolated from grid B can also be in the stencil used for the interpolation of a degree of freedom of grid B. This is clearly not feasible so that the user needs to ensure that the overlapping zone is larger than the stencil.

Remark. *These different sets of approaches are not mutually exclusive and can be combined together. For example and to name just a few, Ben Dhia and Jamond combined the eXtended finite element method with the Arlequin method in order to simulate crack propagation [74] [151]; the multiscale variational method can also be considered as a multiple grid approach [57].*

Partial Conclusion

Numerous methods allow for a change in the modelling without altering the initial mesh. Among those methods, superimposing techniques provide the most flexibility for the development of the numerical tool previously described. In particular, the Chimera and Arlequin methods have proven to accurately simulate wave propagations in structural and fluid dynamics. Moreover, they allow for the local modification to be independently meshed which simplifies mesh generation and makes it easier to test different configurations. However, to the best of my knowledge, these methods were neither extended to the explicit time integration for structural dynamics nor to the simulation of fluid structure interaction multi-modelling for which both the structure and the fluid are locally changed. Finally, the influence of the Arlequin framework on the stability in explicit dynamics still needs to be studied.

These shortcomings of the Chimera and Arlequin methods justify the work presented in this work. It consists in developing a numerical tool able to superimpose two different models when simulating fast transient, fluid structure interaction phenomena with explicit time integration.

Presentation of the scientific approach of this work

The first step is to develop a multi-model formulation of the structural component of the domain. Starting with the structural component rather than the fluid one is justified by the fact that the momentum equation of the Euler equations is very similar to the equation of structural dynamics[15]. Thus, the conclusions of the study of structural dynamics can give practical hints for the modelling of the fluid component. In order to model the structural component, we chose to extend the Arlequin framework to structural explicit dynamics for reasons explained earlier. First, we establish the continuous and discrete formulations of structural elastodynamics in the Arlequin framework. Then, we study the stability of the multi-model formulation in order to ensure that its simulation is computationally feasible. Next, the approach is implemented to simulate wave propagations in elastic structures. Finally, we study the accuracy of the approach in order to ensure the relevance of the proposed method (Chapter 1). Part of the work presented in this was chapter was published [152].

The next step is to develop a multi-model approach for the fluid component of the domain for FSI oriented applications. It is accomplished over the next three chapters.

The fluid component is modelled by the Euler equations and different discretization are used for each equation[16]. Indeed, the momentum equation is treated in its non conservative form using the Finite Element Method (FEM) while the other two conservations equations are treated by a Finite Volume scheme. Thus, the first goal is to determine the possible multi-model approaches that can be used to model the conservation of mass and energy equations. In order to do so, we propose different multi-model approaches for the simulation of transport phenomenons. First, we establish their continuous and discrete formulation. Then, we study the stability of these approaches so as to determine which approaches are stable and computationally feasible. Then, we study the accuracy of each stable approach by measuring the difference between the solution yielded by these approaches with a reference one (Chapter 2). The stable and most accurate approaches can then be used to model the Euler equations when simulating multi-model fluid dynamics.

The next step is then to use the former approaches in order to formulate different multi-model approaches for the Euler equations. Once formulated, we studied the stability of each approach in order to determine whether or not they are computationally feasible. Yet, the stability of the Euler equations is associated to the acoustic waves. Thus, for each approach, we establish the continuous and discrete formulations of the corresponding, multi-model, wave equation problem. The wave equation problem is considered in its mixed form in order to be representative of the Euler equations formulation[17]. Next, the stability of each corresponding wave problem is studied so as to determine the influence of the multi model frameworks on the critical time step. Finally, we infer, from the latter study, stability results for the Euler equations (Chapter 3).

The last step in developing a multi-model approach for fluid dynamics was to study the convergence of the multi-model approaches for the Euler equations. To do so, we

[15]For the applications proposed, the momentum equation is discretized using the FEM, see Appendix A.

[16]See Appendix A.

[17]This is equivalent to linearizing about the motionless state, see [153] and [154].

established the continuous and discrete formulations for each multi-model approach taking into account the practical hints from the studies of the previous chapters. Next, we design test cases with various geometries and initial conditions and defined reference solutions. Convergence studies of the multi-model approaches were completed for different gas laws and for each test case (Chapter 4). The work presented in the last two chapters was synthesized in an article to be submitted.

A final step would have been to develop a multi-model approach for the simulation of fluid structure interaction phenomenons. However, this work was not completed because of a lack of time.

N.B. In this work, every vector is expressed through the column matrix of its components in a fixed orthonormal basis of the 3D Euclidian space $\{\vec{e}_i\}_{i\in\{1,2,3\}}$. Such a column matrix is denoted with a single underline. The second order tensors are expressed through the matrix of their components in the basis $\{\vec{e}_i \otimes \vec{e}_j\}_{(i,j)\in\{1,2,3\}^2}$. Such a matrix is denoted with a double underline. The matrices and column vectors related to discrete systems are also denoted with double and single underline, respectively.

Chapter 1

Multi-model Arlequin method for transient structural dynamics with explicit time integration

Contents

The objective of this work is to develop a multi-model approach able to account for local effects in transient FSI[1] simulations. The first step towards achieving this goal is to develop a multi-model approach for transient structural dynamics with explicit time integration. There are a few reasons for doing so. Firstly, transient FSI simulations have both a fluid and structural component so that the multi-model approach to be developed has to be practical for overlapping structures. Secondly, in our applications[2], the behaviour of the structural component is modelled by a single equation while the fluid is modelled by three coupled equations. Moreover, both the equilibrium equation describing structural dynamics and the momentum equation in the fluid description are treated using the finite element method while the other two equations describing the fluid[3] are discretized differently. Thus, developing a multi-model formulation for structural dynamics may give practical hints for the momentum equation.

As explained in the introduction, among the different methods developed in the field of multi-modelling, the Arlequin method provides a suitable framework for structural dynamics. We thus start by extending the Arlequin method to the simulation of transient

[1]Fluid Structure Interaction.

[2]See Appendix [REF] for the description of the modelling of transient FSI phenomenons in Europlexus (Epx).

[3]the conservation of mass equation and the conservation of total energy equation.

structural dynamics. To do so, we introduce the continuous and discrete mono-model and multi-model Arlequin problem formulations of an elastodynamics problem using the FEM. In particular, we propose a mass matrix lumping technique in the Arlequin framework and recall the energy balance formulas (section 1.1). Then, we study the influence of the Arlequin framework on the stability of the time-integrator in order to ensure that the formulations are computationally feasible. Thus, the theoretical impact on the stability of both the Lagrange multipliers (section 1.2) and the weight functions (section 1.3) are examined. As the weight functions are found to possibly jeopardize the stability, we propose two approaches to mitigate their influence, which are then validated on a consistency test case (section 1.3). Next, we compare the solutions obtained by the multi-model approaches with a reference one in order to evaluate their accuracy (section 1.4). The work presented in this chapter was published as is in [152]. Later, we came upon works from other fields that faced similar issues to those dealt with in this chapter. We briefly present these works and compare their methodologies with the one adopted in this work (section 1.5).

1.1 Governing equations

In order to present a comprehensive study of the Arlequin problem, we consider the following representative elastodynamics problem.

1.1.1 Continuous mono-model problem formulation

We consider an isotropic elastic body occupying a bounded, regular domain $\Omega_1 \in \mathbb{R}^d$. Let $\underline{u}$, $\underline{\dot{u}}$ and $\underline{\ddot{u}}$ denote the displacement, velocity, and acceleration fields while $\underline{u}^0$ and $\underline{\dot{u}}^0$ are the initial displacement and velocity. The boundary $\partial\Omega_1$ of Ω_1 is partitioned into two parts, Γ_u and Γ_h, such that $\Gamma_u \cap \Gamma_h = \emptyset$. The body is submitted to volume forces $\underline{g} \in L^2(\Omega_1)$, prescribed displacements $\underline{u}_p$ on $\Gamma_u \neq \emptyset$ and prescribed boundary forces $\underline{h}$ on Γ_h. Let ρ be the material density, $\underline{\underline{\sigma}}$ the Cauchy stress tensor, and $\underline{\underline{\varepsilon}}$ the infinitesimal strain tensor. The strain tensor is given by $\underline{\underline{\varepsilon}} = \underline{\underline{\nabla^S u}} = \frac{1}{2}(\underline{\underline{\nabla u}} + \underline{\underline{\nabla^T u}})$ while the stress tensor is given by Hooke's law : $\underline{\underline{\sigma}} = \underline{\underline{\underline{D}}} : \underline{\underline{\varepsilon}}$ where $\underline{\underline{\underline{D}}}$ is the elastic tensor.

The weak mono-model formulation of this problem reads as follows:

Given $\underline{g}$, $\underline{h}$, $\underline{u}_p$, $\underline{u}^0$ and $\underline{\dot{u}}^0$, find $\underline{u}(t) \in \mathcal{V}, t \in [0,T]$ such that

$$\forall \underline{v} \in \mathcal{V}_0,\ m(\underline{u}(t), \underline{v}) + k(\underline{u}(t), \underline{v}) = f(\underline{v}) \tag{1.1}$$

with

$$\left\{ \begin{array}{lcl} m(\underline{u}(t), \underline{v}) & = & \displaystyle\int_{\Omega_1} \rho \frac{d^2\underline{u}}{dt^2}(t) \cdot \underline{v}\ d\Omega_1 \\ k(\underline{u}(t), \underline{v}) & = & \displaystyle\int_{\Omega_1} \underline{\underline{\sigma}}(\underline{u}(t)) : \underline{\underline{\varepsilon}}(\underline{v})\ d\Omega_1 \\ f(\underline{v}) & = & \displaystyle\int_{\Omega_1} \underline{g}(t) \cdot \underline{v}\ d\Omega_1 + \int_{\Gamma_h} \underline{h}(t) \cdot \underline{v}\ d\Gamma_h \end{array} \right. \tag{1.2}$$

where $\mathcal{V} = \{\underline{u}(t) \in H^1(\Omega_1)^d \mid \underline{u} = \underline{u}_p \text{ on } \Gamma_u\}$ is the trial function space and $\mathcal{V}_0 = \{\underline{w} \in H^1(\Omega_1)^d \mid \underline{w} = \underline{0} \text{ on } \Gamma_u\}$ is the test function space.

Remark 1.1.1. *This work focuses on the influence of the Arlequin framework on the stability of the central difference time-integrator. To address the most detrimental case for stability and unless specified, no damping is considered.*

Now that a reference, mono-model, problem formulation was established, we introduce the equivalent multi-model problem in the Arlequin framework.

1.1.2 Continuous Arlequin problem formulation

The Arlequin method is a flexible modelling framework which consists of two or more defined sub-domains with overlapping zones. Each sub-domain can have its own physical model, numerical model, and scale. Although this method allows as many sub-domains as needed, for the sake of clarity, we will restrict ourselves to two sub-domains, Ω_1 and Ω_2, without any loss of generality.

In this study a local model, Ω_2, is superimposed to the global model, Ω_1, in the neighbourhood of an area of interest. We assume that Ω_2 is strictly embedded in Ω_1. Sub-domain Ω_2 is partitioned into two regular, non-overlapping domains: the coupling zone Ω_c and the free zone Ω_f (see Figure 1.1). In the first partition the models are coupled so that they have to be quite similar, while in the second the models are superimposed, but free from each other so that they can have very different characteristics.

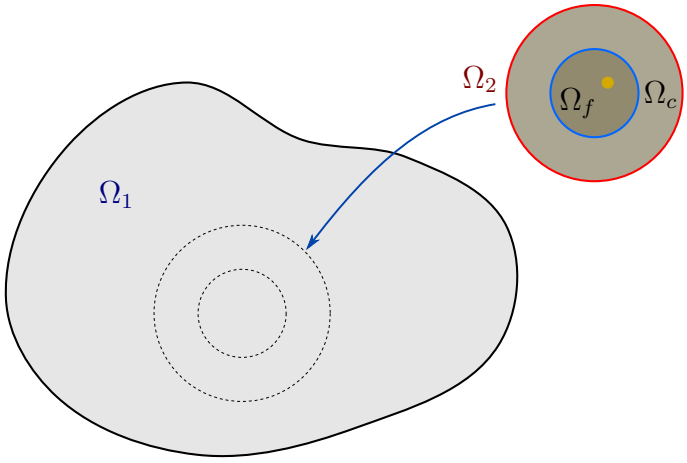

Figure 1.1: Model zones – The global model, Ω_1, is represented in light grey, and the second model domain Ω_2 is represented in dark gray (upper right). The second model domain, Ω_2, is divided into two zones: the coupling zone Ω_c and the free zone Ω_f, which contains a local alteration represented in yellow. Examples of possible local alterations include a hole or source of energy.

The two models are combined together using a partition of energy through weight functions α_i $(i = 1, 2)$ and a coupling operator c, leading to a continuous Arlequin formulation of the problem. For simplicity, the quantities corresponding to each sub-domain have the subscript $i = 1, 2$.

The weak formulation of the Arlequin problem reads:

Given $\underline{g}$, $\underline{h}$, $\underline{u}_p$, $\underline{u}_0$ *and* $\dot{\underline{u}}_0$, *find* $(\underline{u}_1(t), \underline{u}_2(t), \underline{\lambda}(t)) \in \mathcal{V}^1 \times \mathcal{V}^2 \times \mathcal{M}, t \in [0,T]$ *such that*

$$\left\{ \begin{array}{ll} \forall\ \underline{v}_1 \in \mathcal{V}_0^1, & m_1(\underline{u}_1(t), \underline{v}_1) + k_1(\underline{u}_1(t), \underline{v}_1) + c(\underline{v}_1, \underline{\lambda}(t)) = f_1(\underline{v}_1) \\ \forall\ \underline{v}_2 \in \mathcal{V}_0^2, & m_2(\underline{u}_2(t), \underline{v}_2) + k_2(\underline{u}_2(t), \underline{v}_2) - c(\underline{v}_2, \underline{\lambda}(t)) = f_2(\underline{v}_2) \\ \forall\ \underline{\mu} \in \mathcal{M}, & c(\underline{\mu}, \underline{\ddot{u}}_1(t) - \underline{\ddot{u}}_2(t)) = 0 \end{array} \right. \tag{1.3}$$

with (i=1,2)

$$\left\{ \begin{array}{lcl} m_i(\underline{u}(t), v) & = & \displaystyle\int_{\Omega_i} \alpha_i \rho\ \frac{d^2\underline{u}}{dt^2}(t) \cdot \underline{v}\ d\Omega_i \\ k_i(\underline{u}(t), \underline{v}) & = & \displaystyle\int_{\Omega_i} \alpha_i\ \underline{\underline{\sigma}}(\underline{u}(t)) : \underline{\underline{\varepsilon}}(\underline{v})\ d\Omega_i \\ f_i(\underline{v}) & = & \displaystyle\int_{\Omega_i} \alpha_i\ \underline{g}(t) \cdot \underline{v}\ d\Omega_i + \int_{\Gamma_{f_i}} \alpha_i\ \underline{h}(t) \cdot \underline{v}\ d\Gamma_{f_i} \\ c(\underline{\mu}, \underline{w}(t)) & = & \displaystyle\int_{\Omega_c} \underline{\mu} \cdot \underline{w}(t) + \mathcal{L}^2\ \underline{\underline{\varepsilon}}(\underline{\mu}) : \underline{\underline{\varepsilon}}(\underline{w}(t))\ d\Omega_c \end{array} \right. \tag{1.4}$$

where $\mathcal{V}^i = \{\underline{w}(t) \in H^1(\Omega_i)^d \mid \underline{w} = \underline{u}_p \text{ on } \Gamma_{d_i}\}$ and $\mathcal{V}_0^i = \{\underline{w} \in H^1(\Omega_i)^d \mid \underline{w} = \underline{0} \text{ on } \Gamma_i\}$. $\mathcal{M} = \{\underline{\lambda} \in H^1(\Omega_c)^d\}$ is called the mediator space, $\mathcal{L}$ is a strictly positive parameter homogeneous to a length (typically the thickness of the coupling zone), and $\underline{w} \in \mathcal{V} = H^1(\Omega_c)^d$ is an acceleration gap field.

Remark 1.1.2. *The scope of this work is to apply the Arlequin framework to the central difference time-integrator. We chose to impose the coupling through the acceleration variable as it is the natural choice in explicit dynamics. Note that by time integration, if the initial conditions (1.5)*

$$\forall \underline{\mu} \in \mathcal{M}, \left\{ \begin{array}{lcl} c(\underline{\mu}, \underline{u}_1(0) - \underline{u}_2(0)) & = & 0 \\ c(\underline{\mu}, \underline{\dot{u}}_1(0) - \underline{\dot{u}}_2(0)) & = & 0 \end{array} \right. \tag{1.5}$$

are true, then the third equation of system (1.3) implies

$$\forall t \in [0,T], \forall \underline{\mu} \in \mathcal{M}, \left\{ \begin{array}{lcl} c(\underline{\mu}, \underline{u}_1(t) - \underline{u}_2(t)) & = & 0 \\ c(\underline{\mu}, \underline{\dot{u}}_1(t) - \underline{\dot{u}}_2(t)) & = & 0 \end{array} \right. \tag{1.6}$$

Remark 1.1.3. *Note that although* Ω_2 *is strictly embedded in* Ω_1*, new boundaries and, thus, prescribed boundary forces and displacements, may appear inside the free zone* Ω_f*. For example, one can think of a hole on whose boundary some tractions are applied (see section 1.4.2 for example).*

The internal energy weight parameter functions α_i, $i = 1, 2$, are defined in the whole domain Ω_1. They are assumed to be independent of time and satisfy (see Figure 1.2):

$$\left\{ \begin{array}{ll} \alpha_i \in [0,1] & \text{in } \Omega_1 \\ \alpha_1 + \alpha_2 = 1 & \text{in } \Omega_1 \\ \alpha_1 = 1 & \text{in } \Omega_1 \backslash \Omega_2 \\ \exists\ \alpha_0 > 0,\ \alpha_i \geq \alpha_0 & \text{in } \Omega_f \end{array} \right. \tag{1.7}$$

Remark 1.1.4. *The constant* α_0 *has to be arbitrarily small for the Arlequin method to be relevant [98].*

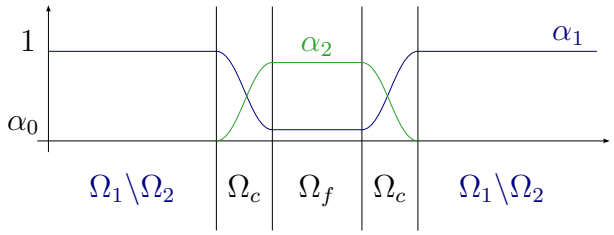

Figure 1.2: Weight functions – An example of the internal energy weight parameter functions where cubic continuous functions were chosen in the coupling zone.

This subsection outlined two mathematical results concerning the Arlequin method for static elastic problems. We assume that these two results still hold true for the dynamics problem (1.3)-(1.7). Note that from now on, for clarity purposes, the global domain, Ω_1, will be referred to as the substrate and Ω_2 as the patch.

- The mixed Arlequin problem defined in [95] was analysed mathematically and proved to be well-posed in [98] and [95], but under more stringent conditions on the weight function, which did not allow them to be regular.
- Even though the physical properties or the geometry in the substrate restricted to the free zone $\Omega_1|_{\Omega_f}$ do not match those of the patch $\Omega_2|_{\Omega_f}$, [98] shows that when the weight function of the patch tends towards one in the free zone ($\alpha_2|_{\Omega_f} \to 1$), the solution of the Arlequin problem tends towards the patch. Thus, a change can be introduced in the patch only. This result, proved and assessed by previously published numerical tests [98], is used in the following for a flexible construction of the discrete Arlequin problems.

1.1.3 Discretized problem

In this section we consider the discrete formulation of the continuous problems previously introduced. The mono-model and both models of the Arlequin problem are integrated in time by the central difference time-integrator described in the next subsection.

1.1.3.1 Discrete time-integrator

The time interval $[0, T]$ is subdivided into N steps $\Delta t = \frac{T}{N}$. Let $\underline{U}_i^n$, $\underline{\dot{U}}_i^n$ and $\underline{\ddot{U}}_i^n$ denote, respectively, the discrete displacement, velocity and acceleration of model i at time instant $t^n = n\Delta t,\ n \in [\![0, N]\!]$. In this study we consider the explicit central difference time-integrator defined by:

Given $\underline{U}^0$ *and* $\underline{\dot{U}}^0$,

$$\left\{ \begin{array}{l} \underline{U}^{n+1} = \underline{U}^n + \Delta t \underline{\dot{U}}^n + \frac{1}{2}\Delta t^2\ \underline{\ddot{U}}^n \\ \underline{\dot{U}}^{n+1} = \underline{\dot{U}}^n + \frac{1}{2}\Delta t(\underline{\ddot{U}}^{n+1} + \underline{\ddot{U}}^n) \end{array} \right. \tag{1.8}$$

1.1.3.2 Discrete mono-model problem formulation

The equations of motion for linear structural dynamics for the mono-model problem (1.2) are discretized using the finite element method. It reads:

Given initial conditions $\underline{U}_1^0$ *and* $\underline{\dot{U}}_1^0$, $\forall\ n \in [\![0, N]\!]$

$$\underline{\underline{M}}\,\underline{\ddot{U}}^n + \underline{\underline{K}}\,\underline{U}^n = \underline{F}^n \tag{1.9}$$

where $\underline{\underline{M}}$ and $\underline{\underline{K}}$ are, respectively, the mass and stiffness matrices on Ω_1 while $\underline{F}$ is the load vector applied on domain Ω_1.

1.1.3.3 Discrete Arlequin problem formulation

The discrete equations of motion for linear structural dynamics problem (1.3)-(1.7) then read:

Given initial conditions $\underline{U}_i^0$ *and* $\underline{\dot{U}}_i^0$ *for* $i = 1, 2$ *and* $\forall n \in [\![0, N]\!]$

$$\left\{ \begin{array}{l} \underline{\underline{M}}_1\underline{\ddot{U}}_1^n + \underline{\underline{K}}_1\underline{U}_1^n + \underline{\underline{C}}_1^T\underline{\lambda}^n = \underline{F}_1^n \\ \underline{\underline{M}}_2\underline{\ddot{U}}_2^n + \underline{\underline{K}}_2\underline{U}_2^n - \underline{\underline{C}}_2^T\underline{\lambda}^n = \underline{F}_2^n \\ \underline{\underline{C}}_1\underline{\ddot{U}}_1^n + \underline{\underline{C}}_2\underline{\ddot{U}}_2^n = \underline{0} \end{array} \right. \tag{1.10}$$

where $\underline{\underline{M}}_i$, $\underline{\underline{K}}_i$ are, respectively, the mass and stiffness matrices on sub-domain Ω_i. $\underline{F}_i$ is the load vector applied on sub-domain Ω_i, while $\underline{\underline{C}}_i^T$ and $\underline{\lambda}$ are, respectively, the coupling matrix and the Lagrange multiplier vector in the coupling zone Ω_c.

Remark 1.1.5. *Note that in system* (1.10)*, the coupling equations are applied to the time-discretized accelerations, with no right-hand side. It is shown in [155] that velocities or displacements could be chosen in the general case to express the coupling at next time step. Doing so produces a right-hand side in the coupling equations due to the link, through the time-integration scheme, between the actually coupled variables (for instance velocities or displacements) and the variables used for the system solution (which are always accelerations). This choice is known to possibly affect the solution of the system when the constraints are only weakly satisfied (for instance in the case of time subcycling) or if some numerical perturbations occur in the system (see* ***Remark*** *1.2.1 for some details on this particular topic). However, it is demonstrated in section 1.2 that under reasonable initial conditions always valid in this work, the coupling equations are strongly verified and simultaneously valid for all discrete kinematic variables. Thus, the potential right-hand side is always null whatever the chosen coupled variable.*

This system of equations can be rewritten as a differential algebraic system (DAS):

$$\left(\begin{array}{cc} \underline{\underline{M}} & \underline{\underline{C}}^T \\ \underline{\underline{C}} & \underline{\underline{O}} \end{array} \right) \left[\begin{array}{c} \underline{\ddot{U}}^n \\ \underline{\nu}^n \end{array} \right] + \left(\begin{array}{cc} \underline{\underline{K}} & \underline{\underline{0}} \\ \underline{\underline{0}} & \underline{\underline{0}} \end{array} \right) \left[\begin{array}{c} \underline{U}^n \\ \underline{\nu}^n \end{array} \right] = \left(\begin{array}{c} \underline{F}^n \\ 0 \end{array} \right) \tag{1.11}$$

where

$$\underline{\underline{M}} = \left(\begin{array}{cc} \underline{\underline{M}}_1 & \underline{\underline{0}} \\ \underline{\underline{0}} & \underline{\underline{M}}_2 \end{array} \right),\ \underline{\underline{K}} = \left(\begin{array}{cc} \underline{\underline{K}}_1 & \underline{\underline{0}} \\ \underline{\underline{0}} & \underline{\underline{K}}_2 \end{array} \right),\ \underline{\underline{C}} = [\underline{\underline{C}}_1, -\underline{\underline{C}}_2] \tag{1.12}$$

and

$$\underline{U}^n = [\underline{U}_1^n, \underline{U}_2^n]^T,\ \underline{F}^n = [\underline{F}_1^n, \underline{F}_2^n]^T,\ \underline{\ddot{\nu}}^n = \underline{\lambda}^n \tag{1.13}$$

Remark 1.1.6. *Note that in (1.10), the Lagrange multipliers* $\underline{\lambda}^n$ *can be eliminated such that we have, using definitions (1.12):*

$$\underline{\underline{M}}\,\underline{\ddot{U}}^n + \underline{\underline{K}}^*\underline{U}^n = \underline{F}^{n*} \tag{1.14}$$

where $\underline{\underline{K}}^* = \underline{\underline{S}}\,\underline{\underline{K}}$, $\underline{F}^{n*} = \underline{\underline{S}}\,\underline{F}^n$, $\underline{\underline{S}} = \underline{\underline{I}} - (\underline{\underline{C}}\,\underline{\underline{M}}^{-1}\underline{\underline{C}}^T)^{-1}\underline{\underline{C}}\,\underline{\underline{M}}^{-1}$ *and* $\underline{\underline{I}}$ *the identity matrix.*

1.1.4 Mass lumping

As is usual in explicit time integration, the mass matrix of every model should be lumped[4]. In the Arlequin framework one has to deal with weighed densities, which can be non-uniform on an element. Although the density ρ is uniform, if the Arlequin weight α is not uniform on the element then the weighted density $\alpha\rho$ will also not be uniform. Thus, the Arlequin weights have to be taken into account in the lumping technique of the mass matrix in order to conserve the overall mass.

By definition, the consistent mass matrix in the Arlequin framework is given by:

$$\underline{\underline{M}}_{i,j} = \int_\Omega \alpha\rho N^T_{\eta(i)} N_{\eta(j)}\ d\Omega \tag{1.15}$$

where N_k is the shape function for node k, η is the numbering mapping function that connects degree of freedom i to its node number $\eta(i)$, ρ is the density, α is the Arlequin weight, and Ω is the global domain. For the lumped matrix, we propose the following definition:

$$\underline{\underline{M}}^L_{i,j} = \begin{cases} 0 & \text{if } \ i \neq j \\ m_i = \displaystyle\int_\Omega \alpha\rho N_{\eta(i)}\ d\Omega & \text{otherwise} \end{cases} \tag{1.16}$$

with the same notations as before. This formula takes into account the heterogeneity of the density within the element and preserves the global mass.

In this paper all presented computations make use of lumped matrices. For mono-model computations, the lumping technique defined in (1.16) is used with $\alpha = 1$ on the entire domain.

1.1.5 Energy balance

The conservation of energy for the continuous formulation of both the mono-model and Arlequin problem was demonstrated in previous work [155], [115]. For specific time-integrators, the energy term associated with the constraints is zero.

The discrete conservation of energy was also studied in both cases. For the mono-model problem (1.2) with a central difference time-integrator, the discrete energy balance reads:

$$[T^n + V^n] = E_{ext} \tag{1.17}$$

where

$$\begin{cases} [\underline{X}^n] = \underline{X}^{n+1} - \underline{X}^n, \\ V^n = \frac{1}{2}(\underline{\dot{U}}^n)^T \underline{\underline{K}}\,\underline{\dot{U}}^n \\ T^n = \frac{1}{2}(\underline{\ddot{U}}^n)^T \underline{\underline{A}}\,\underline{\ddot{U}}^n \ \text{ with } \ \underline{\underline{A}} = \underline{\underline{M}} - \frac{1}{4}\Delta t^2 \underline{\underline{K}} \\ E_{ext} = \frac{1}{\Delta t}[\underline{\dot{U}}^n]^T [\underline{F}^n] \end{cases} \tag{1.18}$$

[4]The use of consistent matrices does not always improve precision and always requires more computation time [156].

For the multi-model problem with a central difference time-integrator, the discrete energy balance reads:

$$[T^n + V^n] = E_{ext} + E_{coupling} \tag{1.19}$$

where we used the same notations as in (1.18) and definitions (1.12) and (1.13). A new term $E_{coupling}$ is introduced and represents the contribution of the Lagrange multipliers:

$$E_{coupling} = \frac{1}{\Delta t}[\underline{\lambda}^n]^T \underline{\underline{C}}[\underline{\dot{U}}^n] \tag{1.20}$$

We observe that if the time-integrator and the problem properties are such that $\underline{\underline{C}}[\underline{\dot{U}}^n] = \underline{0}$, then $E_{coupling} = 0$ and the energy is conserved. For the central difference time-integrator (1.22), we have:

$$[\underline{\dot{U}}^n] = \frac{1}{2}\Delta t(\underline{\ddot{U}}^{n+1} + \underline{\ddot{U}}^n) \tag{1.21}$$

Furthermore, in the Arlequin problem (1.11) the constraint is imposed on acceleration such that $C\underline{\ddot{U}}^n = 0$ is verified at every time step. Thus, for the Arlequin problem (1.11) and the central difference time-integrator, $E_{coupling} = 0$ and the energy is conserved.

Remark 1.1.7. *It can be shown that* $T^n + V^n = E_p^n + E_c^n + E_z^n$ *, where* $E_p^n = \frac{1}{2}\underline{U}^n \underline{\underline{K}}\underline{U}^n$ *and* $E_c^n = \frac{1}{2}\underline{\dot{U}}^n \underline{\underline{M}}\underline{\dot{U}}^n$ *are the potential and kinetic energy, respectively, while* $E_z^n = -\frac{1}{8}\Delta t^2 \underline{\ddot{U}}^n \underline{\underline{M}}\underline{\ddot{U}}^n$ *is an extra term, whose variation is usually negligible.*

In this study we focus on the stability of the multi-model problem (1.3)-(1.7), and on the two components of the Arlequin method likely to affect it: the Lagrange multipliers, used for coupling the two sub-domains, and the weight functions. The next two sections focus on the impact of these two components on the stability of the Arlequin method.

1.2 Stability of differential algebraic system

There are two main approaches to study the stability of a model written $\underline{\underline{M}}\underline{\ddot{U}} + \underline{\underline{K}}\underline{U} = \underline{F}$. The first one, called spectral analysis, evaluates the spectral radius of the the amplification matrix $\underline{\underline{\mathcal{A}}}$ of the chosen time-integrator in order to ascertain under which condition it becomes greater than one [157], [158]. The second one, an energy-based analysis, uses the mathematical properties of the mass and stiffness matrices in order to show whether or not the kinematic quantities are bounded [159].

If the spectral radius is strictly inferior to one (spectral analysis) or if the kinematic quantities always stay confined (energy-based analysis), the time-integrator is said to be *unconditionally stable*. If the spectral radius is greater or equal to one (spectral analysis) or if at least one of the kinematic quantities is not bounded (energy-based analysis), the time-integrator is said to be *conditionally stable*, except in the case where a specific constraint on the time step is verified. In any other cases, the time-integrator is said to be *unstable*.

For the central difference time-integrator, the two approaches show that it is conditionally stable under the condition:

$$\Delta t < \Delta t_c = \sqrt{\frac{2}{\omega_{max}^2}} \tag{1.22}$$

where Δt_c is the critical time step and ω_{max} is the maximum eigenfrequency of the generalized eigenvalue problem of $\underline{\underline{K}}$ and $\underline{\underline{M}}$. However, this result is only valid for a differential system with the right properties ($\underline{\underline{K}}$ is not singular and $\underline{\underline{A}}$ is positive definite). For the differential algebraic system (1.11), further analysis must be done.

In the following subsections, we examine the influence of the coupling on both approaches.

1.2.1 Energy-based stability analysis

In this section, we demonstrate that for the central difference time-integrator, the kinematic quantities are bounded. In the previous section we proved that for the Arlequin problem (1.11), the energy is conserved. As is usual in stability analyses, we will not consider external forces as they do not affect it [155].

From [159], we have the following lemma:

Lemma 1.2.1. *For the central difference time-integrator, if $\underline{\underline{A}}$ is positive definite and $\underline{\underline{K}}$ is not singular and if the energy is conserved, then $\underline{\dot{U}}^n$ and $\underline{\ddot{U}}^n$ are uniformly bounded.* □

We can thus prove the following result:

Proposition 1.2.2. *For the central difference time-integrator, if*

- *The coupling matrix $\underline{\underline{C}}$ is of maximal rank.*
- *$\underline{\underline{A}}$ is positive definite*
- *The energy is conserved*
- *$\underline{\underline{K}}$ is not singular*
- *$\underline{\underline{C}}\underline{\dot{U}}^0 = \underline{0}$ and $\underline{\underline{C}}\underline{U}^0 = \underline{0}$.*

then $\underline{\lambda}^n$ and $\underline{U}^n$ are also bounded.

Proof. By hypothesis, $\underline{\underline{K}}$ is not singular so that we can multiply the equation of structural dynamics (1.10) by $\underline{\underline{C}}\underline{\underline{K}}^{-1}$ which yields:

$$\underline{\underline{C}}\underline{\underline{K}}^{-1}\underline{\underline{M}}\underline{\ddot{U}}^n + \underline{\underline{C}}\underline{U}^n = \underline{\underline{C}}\underline{\underline{K}}^{-1}\underline{\underline{C}}^T\underline{\lambda}^n \tag{1.23}$$

By induction, it can be shown that, for the central difference time-integrator, if $\underline{\underline{C}}\underline{\dot{U}}^0 = \underline{0}$ and $\underline{\underline{C}}\underline{U}^0 = \underline{0}$ then $\underline{\underline{C}}\underline{U}^n = \underline{0}$ at every time step. Thus, equation (1.23) becomes:

$$\|\underline{\underline{C}}\underline{\underline{K}}^{-1}\underline{\underline{C}}^T\underline{\lambda}^n\| \leq \|\underline{\underline{C}}\underline{\underline{K}}^{-1}\underline{\underline{M}}\|\|\underline{\ddot{U}}^n\| \tag{1.24}$$

By hypothesis, we can use Lemma 1.2.1 so that $\underline{\ddot{U}}^n$ is bounded. Thus, $\underline{\underline{C}}^T$ has maximal rank, and the Lagrange multipliers are bounded. Finally, the equation of structural dynamics yields

$$\|\underline{U}^n\| \leq \|\underline{\underline{K}}^{-1}\|(\|\underline{\underline{M}}\|\|\underline{\ddot{U}}^n\| + \|\underline{\underline{C}}^T\underline{\lambda}^n\|) \tag{1.25}$$

which completes the proof. □

In this study, $\underline{\underline{K}}$ is not singular and the rank of $\underline{\underline{C}}^T$ is maximal by hypothesis, while $\underline{\underline{A}}$ is positive definite if (1.22) is verified. Thus, both **Lemma** 1.2.1 and **Proposition** 1.2.2 can be applied, and all kinematic quantities are, therefore, bounded. The central difference scheme is, thus, conditionally stable for the differential algebraic system (1.11).

In conclusion, the energy-based stability analysis shows that coupling models does not have an adverse impact on the stability. In other words, the critical time step for the Arlequin problem is greater or equal to that of the uncoupled problem $\underline{\underline{M}}\ddot{\underline{U}} + \underline{\underline{K}}\underline{U} = \underline{F}$ as defined in equations (1.12)–(1.13).

1.2.2 Spectral analysis

In this section we analyse the stability of coupled problem through the spectral approach. We use the results and method detailed in [158] to reach the same conclusion as that of the previous section.

In this analysis the time step Δt is set and $\underline{\underline{\mathcal{A}}}(\omega^2\Delta t^2)$ is the amplification matrix of the chosen time-integration algorithm applied to a single degree of freedom oscillator and defined for the complete state vector $[q, \Delta t\dot{q}, \Delta t^2\ddot{q}]$:

$$\ddot{q} + w^2 q = 0 \tag{1.26}$$

From [158], we have the following result:

Proposition 1.2.3. *The stability of a time-integrator applied to the DAS equations (1.11) is governed by the spectral radius of* $\underline{\underline{\mathcal{A}}}_0 = \underline{\underline{\mathcal{A}}}(0)$ *for null frequencies.*

For the central difference time-integrator, we have:

$$\underline{\underline{\mathcal{A}}}_0 = \frac{1}{2}\begin{pmatrix} 2 & 2 & 1 \\ 0 & 2 & 1 \\ 0 & 0 & 0 \end{pmatrix} \tag{1.27}$$

which has three eigenvalues: $\mu_1 = 0$ and $\mu_2 = \mu_3 = 1$. The latter is defective and therefore $\underline{\underline{\mathcal{A}}}_0$ is not diagonalizable. By induction, or using the Jordan Form, it can be shown that the nth power of $\underline{\underline{\mathcal{A}}}_0$ is equal to:

$$\underline{\underline{\mathcal{A}}}_0^n = \frac{1}{2}\begin{pmatrix} 2 & 2n & n \\ 0 & 2 & 1 \\ 0 & 0 & 0 \end{pmatrix} \tag{1.28}$$

The above expression of $\underline{\underline{\mathcal{A}}}_0^n$ implies that the zero frequencies:

- do not contribute to the second time-derivative field.
- have a constant contribution to the first time-derivative field.
- introduce a weak instability in the zero time-derivative field (linear growth).

As explained in [158], this result is not surprising because the constraint is applied on the second derivative. Therefore, one would expect to observe such a rigid body motion. However, for a differential algebraic system, this rigid body motion does not correspond to global structural rigid body modes. Thus, in order to assess the conditional stability of the differential algebraic system, these zero frequencies should be filtered out. In [158], the following result is proved:

Proposition 1.2.4. *If the differential algebraic system and the time-integrator algorithm is such that*

$$\underline{\underline{C}}\,\underline{\ddot{U}}^n = \underline{0} \implies \underline{\underline{C}}\,\underline{U}^n = \underline{0} \tag{1.29}$$

then the algebraic constraints (1.29) filter out the zero frequencies from the displacement solution.

For the central difference time-integrator, it can be shown by induction that condition (1.30) implies (1.29), so that we can state the following result:

Proposition 1.2.5. *The central difference time-integrator is conditionally stable for the differential algebraic system (1.11) if*

$$\underline{\underline{C}}\,\underline{\dot{U}}^0 = \underline{0} \text{ and } \underline{\underline{C}}\,\underline{U}^0 = \underline{0} \tag{1.30}$$

The critical time step is then greater or equal to the critical time step of the uncoupled problem.

In summary, the spectral stability for the central difference time-integrator is the same for both the Arlequin problem and the classical unconstrained dynamic equations of motion. Indeed, they are both conditionally stable under condition (1.30).

Remark 1.2.1. *Note that if condition (1.30) is true and* $\forall n$, $\underline{\underline{C}}\,\underline{\ddot{U}}^n = \underline{0}$ *is imposed, then* $\forall n$, $\underline{\underline{C}}\,\underline{U}^n = \underline{0}$ *and* $\underline{\underline{C}}\,\underline{\dot{U}}^n = \underline{0}$. *But if, for any reason, numerical perturbations appear such that at a given time step* n_0, $\underline{\underline{C}}\,\underline{\dot{U}}^{n_0} \neq \underline{0}$, *these perturbations will be integrated in time and lead to a linear drift of the displacements of both models. Yet, it is still possible to tackle this issue by using a more sophisticated discrete coupling condition (even with variable time step due to nonlinear materials*[5]*) to filter out these perturbations. :*

$$\forall n > 0,\ \underline{\underline{C}}\,\underline{\ddot{U}}^n = -\frac{2}{\Delta t^2}\left(\underline{\underline{C}}\,\underline{U}^n + \Delta t\,\underline{\underline{C}}\,\underline{\dot{U}}^{n-1} + \frac{\Delta t^2}{2} C\,\underline{\ddot{U}}^{n-1}\right) \tag{1.31}$$

Conclusion In the last two sections, we saw that both the energy and spectral approach lead to the same conclusion: if (1.30) is verified, then the Lagrange multipliers do not prejudice the stability. Moreover, condition (1.30) means that the speed and displacement of both models must be set equal in the overlapping zone. This is the case in practice, as it is advised to use the same physical properties and behaviour in the overlapping zone to achieve better results. The critical time step is then at least equal to that of the uncoupled system (1.22). In other words, the coupling matrices do not affect the stability.

[5] If such a case, (1.31) becomes $\forall n > 0, \underline{\underline{C}}\,\underline{\ddot{U}}^n = \frac{-2}{\Delta t_n(\Delta t_n+\Delta t_{n-1})}(\underline{\underline{C}}\,\underline{U}^n + \Delta t_n \underline{\underline{C}}\,\underline{\dot{U}}^{n-1} + \frac{\Delta t_n \Delta t_{n_1}}{2} C\,\underline{\ddot{U}}^{n-1})$.

1.3 Impact of the Arlequin weights on the critical time step

The other component of the Arlequin framework that can affect the stability is the Arlequin weighting. In most industrial codes, instead of computing the maximum eigenfrequency of the global problem to define the critical time step, as in (1.22), the maximal eigenfrequency on each element is computed. Indeed, [155] states that:

Proposition 1.3.1. *Let ω_G be the highest frequency of the generalised eigenvalue problem of the global matrices of $\underline{\underline{K}}$ and $\underline{\underline{M}}$ as defined in equation (1.12). Let ω_E be the highest frequency of the generalised eigenvalue problem of $\underline{\underline{K}}_E$ and $\underline{\underline{M}}_E$, the stiffness and mass matrix of element E. We have then*

$$\omega_G^2 \leq \max_E \omega_E^2 \tag{1.32}$$

Thus, if $\max \omega_E^2$ is substituted to ω_G^2 in the computation of the critical time step (1.22), then the time-integrator remains stable. Such a computed critical time step is noted $\Delta_E t_c$ and we thus have $\Delta_E t_c \leq \Delta t_c$. In this analysis, in order to study the impact of the weighting on ω_E^2, we will consider a single element.

1.3.1 Impact on a single element

It is not always possible to ensure that the Arlequin weights are constant on an element, such as when linear or cubic weight functions are used in the overlapping zone, or when the meshes of different models do not match. In this section, we will consider a one dimensional element in which the Arelquin weight is piecewise constant, as shown in Figure 1.3.

The goal of this simplified case is to identify the parameters that influence the critical time step and use any relevant conclusions for higher dimension computations. In this scope, the parameter δ represents the location of the weight function discontinuity within the element. It is important to note that when dealing with 2D or 3D meshes that do not match, the position of the discontinuities can not be controlled and, therefore, δ is arbitrary and can take any value in its range.

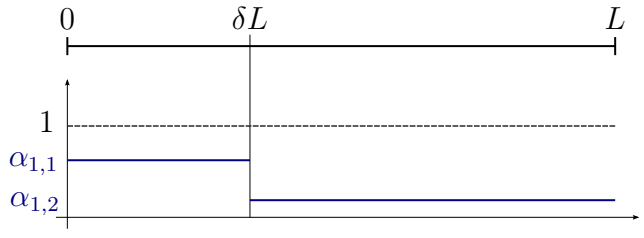

Figure 1.3: Model of a one dimensional elastic beam with Young modulus E and density ρ following Hooke's law. The weight function is piecewise constant and linear shape functions are used.

The beam of length L is assumed to be elastic with density ρ and Young modulus E so that $\sigma = E\varepsilon$. The weight function is piecewise constant equal to α_1 on $[0, \delta L]$ and equal to α_2 on $[\delta L, L]$ where $\delta \in [0, 1]$ is the previously introduced geometric parameter.

The critical time step was determined using a formal algebra software and is given by (1.33):

$$\Delta t_c = \gamma(q_\alpha, \delta)\ \widetilde{\Delta t_c} \tag{1.33}$$

with

$$\begin{cases} \gamma(q_\alpha, \delta) = \dfrac{\sqrt{q_\alpha^2 + 2q_\alpha(1-q_\alpha)\delta + (1-q_\alpha)^2(2\delta^3 - \delta^4)}}{q_\alpha + (1-q_\alpha)\delta} \\ q_\alpha = \dfrac{\alpha_{1,2}}{\alpha_{1,1}} \\ \widetilde{\Delta t_c} = \sqrt{\dfrac{\rho}{E}} \end{cases}$$

where $\widetilde{\Delta t_c}$ is the critical time step of the unweighed problem.

It is interesting to note that the critical time step depends on only two variables: parameter δ and the ratio of the two weights q_α. As the function has symmetry[6], we can consider that $0 < q_\alpha < 1$. Function γ is plotted in Figure 1.4.

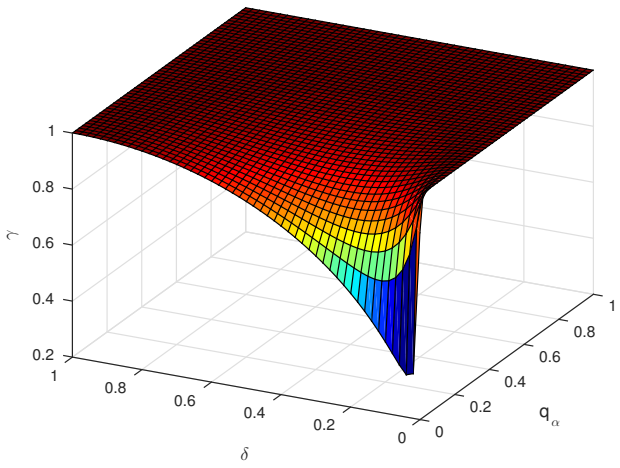

Figure 1.4: Evolution of γ, the normalized critical time step, as a function of δ and q_α.

First of all, we observe that function γ, and, thus, the critical time step can drop significantly. Assuming that δ is arbitrary and can take any value, the critical time step drastically drops when q_α is small. Secondly, we note that if $\delta = 0$, $\delta = 1$, or $q_\alpha = 1$, that is, if the weight is constant on the element, the critical time step is not altered. We thus propose two approaches to circumvent situations in which the critical time step significantly drops. They are detailed in the next two subsections.

1.3.2 q_α-control approach

1.3.2.1 Limiting q_α

We observed that the critical time step drops when parameter q_α, which can be partially controlled by the user, is very small. From Figure 1.4, we can expect that

[6]It can be shown that $\gamma(\frac{1}{q_\alpha}, 1-\delta) = \gamma(q_\alpha, \delta)$.

if q_α is high enough, the drop in the critical time step is small regardless of the value of δ. The value of $\beta = \min_\delta \gamma(\delta, q_\alpha)$ for a set q_α was numerically determined and is shown in Figure 1.5. We can see that the highest possible value of β corresponds to

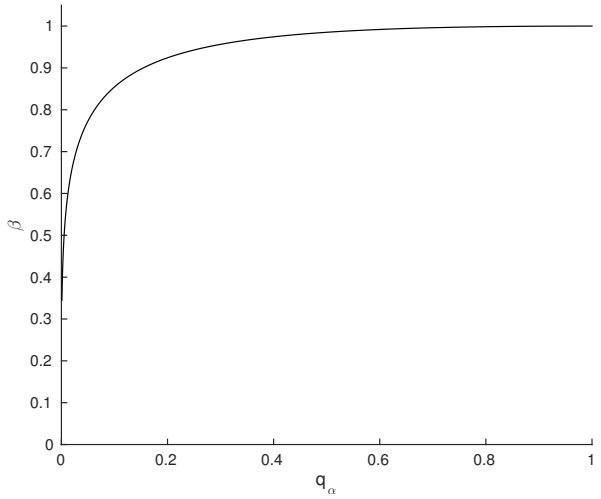

Figure 1.5: Evolution of $\beta = \min_\delta \gamma(\delta, q_\alpha)$ for a set q_α.

a constant weight on the element. Also, we see that $q_\alpha = 0.5$ implies $\beta > 0.985$. In other words, if the user ensures that no element's weight varies by more than half, then the critical time step will drop by less than 2%, which is acceptable. Similarly, if the maximum value of the weight on an element is ten times that of its minimum, then the critical time step drops by 15% (if $q_\alpha \sim 0.1$, then $\beta \sim 0.85$), which allows feasible computations.

1.3.2.2 Choice of the coupling zone

In the Arlequin framework, due to the partition of unity, the value of q_α can not be set on both models at the same time. In this section we describe an approach that ensures that the q_α of any element of any model is always above a minimum value, q_{min}, which is high enough for the critical time step not to drop significantly.

First of all, by using piecewise constant weight functions, the only elements in which the weights will vary are the ones crossed by the coupling zone's borders. By setting the weights of both models to $\frac{1}{2}$ in Ω_c, we ensure that $q_\alpha \geq \frac{1}{2}$ on elements split between the coupling zone and the zone where the model is prevailing (that is, α equal or close to 1).

However, when elements of the substrate are split between the coupling zone and the free zone, where it is not prevailing, q_α can drop quite low. In order for the Arlequin method to be relevant, α_0 needs to be as small as possible, and, therefore, q_α is also low. In order to bypass this problem, we propose to align the external border of the coupling zone, $\partial\Omega_c \setminus \partial\Omega_f$, with the mesh of the patch and the internal one, $\partial\Omega_f$, with the mesh of the substrate (see Figure 1.6). This way there is no element in both the free and the coupling zones. Thus, on every element we have $q_\alpha \geq \frac{1}{2}$. The preceding study then establishes that the critical time step drops by at most 2.5%.

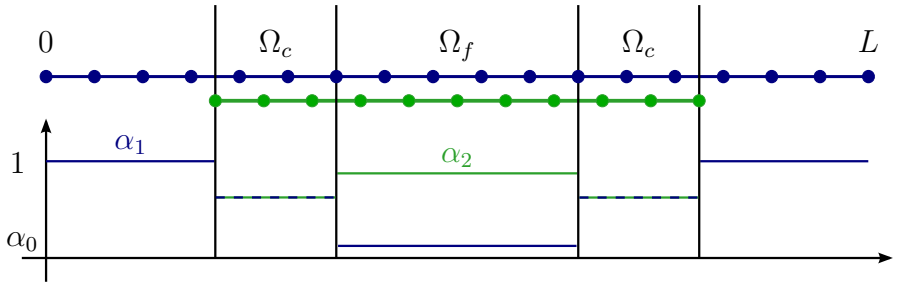

Figure 1.6: q_α-control approach – The outermost border cuts through an element of the substrate (in blue) so that $q_\alpha = 0.5$ on that element. The internal one cuts an element of the brown domain so that $q_\alpha \geq 0.5$ on it. The critical time thus only drops by 2.5%.

In this section, we showed that the drop in the critical time step can be limited by controlling the parameter q_α. As in the Arlequin framework, there is only partial control over that parameter, we optimized the position of the coupling zone's borders in order to ensure a feasible time step. In the next section, an averaged weight approach is introduced.

1.3.3 Averaged weight approach

In section 1.3.1, we observed that if the Arlequin weight is constant on an element, then the critical time step is not altered. One can easily check if, given any element (2D, 3D, any shape functions), the Arelquin weight is constant and $\Delta_E t_c$ remains unaltered. The critical time step is determined by the frequencies of the eigenvalue problem $\det(\underline{\underline{K}}_E - \omega_E^2 \underline{\underline{M}}_E) = 0$. As the weight is constant on the element, we have:

$$\det(\underline{\underline{K}}_E - \omega_E^2 \underline{\underline{M}}_E) = \alpha_E^{dof_E} \det(\underline{\underline{\widetilde{K}}}_E - \omega_E^2 \underline{\underline{\widetilde{M}}}_E) \tag{1.34}$$

where α_E is the weight, dof_E is the number of degrees of freedom of the element and $\widetilde{\bullet}$ denotes unweighed quantities. Therefore, if the Arlequin weights are constant on every element then the critical time step is not altered. Thus, we propose another approach in which an averaged weight is defined on every element.

The way the average weight is computed should not modify the physical properties of the problem. Thus, we recommend using an average weight that conserves the mass of the element, which leads to the following definition of the averaged weight $\bar{\alpha}_E$:

$$\bar{\alpha}_E = \frac{\int_{\Omega_E} \alpha\rho \; d\Omega_E}{\int_{\Omega_E} \rho \; d\Omega_E} \tag{1.35}$$

Moreover, note that the definition is consistent, such that when α is constant, $\bar{\alpha}_E = \alpha$.

Remark 1.3.1. *Note that the density ρ is usually considered constant inside an element so that definition (1.35) is equivalent to*

$$\bar{\alpha}_E = \frac{1}{|\Omega_E|} \int_{\Omega_E} \alpha \; d\Omega_E \tag{1.36}$$

where $|\Omega_E|$ is the volume of element E.

This approach maintains an optimal critical time step, is very easy to implement, and ensures that no geometric parameter affects the stability. However, the partition of unity in equations (1.7) is no longer verified on elements in which the weight would normally vary (see Figure 1.8). Thus, one can expect a loss in accuracy.

1.3.4 Validation

In order to validate the two methods previously presented, we consider a consistent test case in which the patch does not bring any new features. If the patch does not bring any modification to the substrate, then the solution should not be altered. After describing the consistent test case, an error measurement is introduced to compare the solution of the two approaches with the mono-model solution. The last paragraph discusses the results.

1.3.4.1 Consistency test case presentation

Let Ω_1, the substrate's domain, be composed of a hundred elements of unit length, of constant density ρ, and constant Young's modulus E. The patch's sub-domain, Ω_2, is made of twenty elements of unit length, and has the same physical properties as the substrate. The patch is centered on the substrate and then slightly translated from the center of the substrate by a distance, δ, in order to introduce a mesh incompatibility between the patch and the substrate. The substrate is clamped on its far left end and a constant external force, $\underline{F}$, is applied on its far right end during a set time, Δt_F. The initial kinematic conditions are null.

The weight functions for the q_α-control approach and the averaged weight approach are shown in Figure 1.7 and Figure 1.8. As prescribed, the Arlequin weight functions are piecewise constant and equal to 0.5 in the coupling zone.

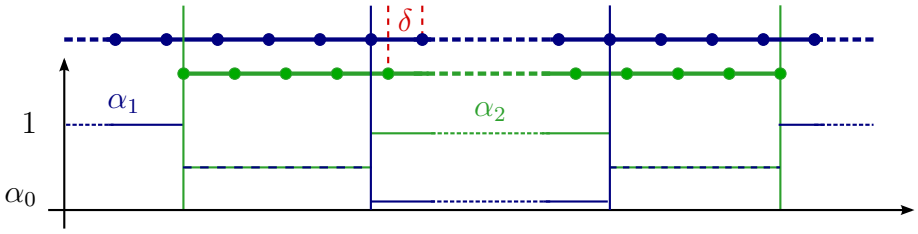

Figure 1.7: Zoom on the overlapping zone for the q_α-control approach.

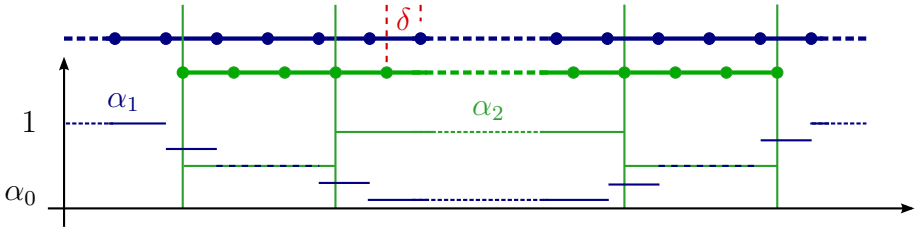

Figure 1.8: Zoom on the overlapping zone for the averaged weight approach.

The reference solution is the substrate by itself, as described in the previous paragraph.

For numerical applications, the physical properties are set to that of steel ($E = 200\ GPa$ and $\rho = 8000\ kg.m^{-1}$), the parameter δ to 0.1, the time step to $1.0\ 10^{-4}\ s$ and the Arlequin parameter α_0 to $1.\ 10^{-3}$. The load $||\underline{F}|| = 4\ 10^8 N$ is applied during a time $\Delta t_F = 5.0\ 10^{-3}\ s$. The solution is computed for a total time of $0.4\ s$, equal to 10 round trips of the wave.

1.3.4.2 Error measurement

In order to evaluate how precise the two approaches are, we compare them to the mono-model solution. To make the comparison, we introduce the following error measurement:

$$E_u(t) = \frac{||\underline{u}^r(t) - \underline{u}^a(t)||_{L^2(\Omega_1)}}{\max\limits_{\tau} ||\underline{u}^r(\tau)||_{L^2(\Omega_1)}} \tag{1.37}$$

where $\underline{u}$ is the displacement. The subscript $'r'$ denotes the reference, mono-model solution while $'a'$ denotes the Arlequin solution ($\underline{u}^a = \alpha_1 \underline{u}_1 + \alpha_2 \underline{u}_2$).

The error is normed by $\max\limits_{\tau} ||\underline{u}^r(\tau)||_{L^2(\Omega_1)}$ and not $||\underline{u}^r(t)||_{L^2(\Omega_1)}$ because $\underline{u}^r$ equals zero each time the wave reaches the free end.

1.3.4.3 Results

The elementary critical time step, $\Delta_E t_c$, and the global critical time step, Δt_c, were calculated for each approach. The global critical time step was calculated using definition (1.22) and the generalised eigenvalue problem of $\underline{\underline{K}}^*$ and $\underline{\underline{M}}$, as defined in (1.12)–(1.14). The results are given in Table 1.1. As expected, both the mono-model

	Monomodel	q_α-control	Averaged weights	Patch-aligned Ω_c
Δt_c	2.000	1.999	2.000	1.031
$\Delta_E t_c$	2.000	1.993	2.000	0.941

Table 1.1: Critical time step in $10^{-4}\ s$ for different approaches.

and the averaged weight approaches yield the same critical time step while, the critical time step yielded by the q_α-control approach is slightly inferior. It is interesting to note that if both the inner and outer border of the coupling zones are aligned with the patch, which is a more natural choice, and no weight is averaged, then the critical time step drops more significantly (48.5% drop for Δt_c and 52.9% for $\Delta_E t_c$). This last approach is named patch-aligned Ω_c in Table 1.1. These results demonstrate the effectiveness of the the q_α-control approach.

Remark 1.3.2. *Note that the value of α_0 greatly impacts the drop in the critical time steps Δt_c and $\Delta_E t_c$ for the patch-aligned Ω_c approach. In agreement with our study, any value lower than $1.0\ 10^{-3}$ makes that drop more significant.*

The averaged weight and the q_α-control approaches were implemented and compared to the mono-model solution. Three depictions of the displacement of the beam are represented for all three computations in Figure 1.9. We observe that the wave fronts of all three computations are in very good agreement, even after ten round-trips.

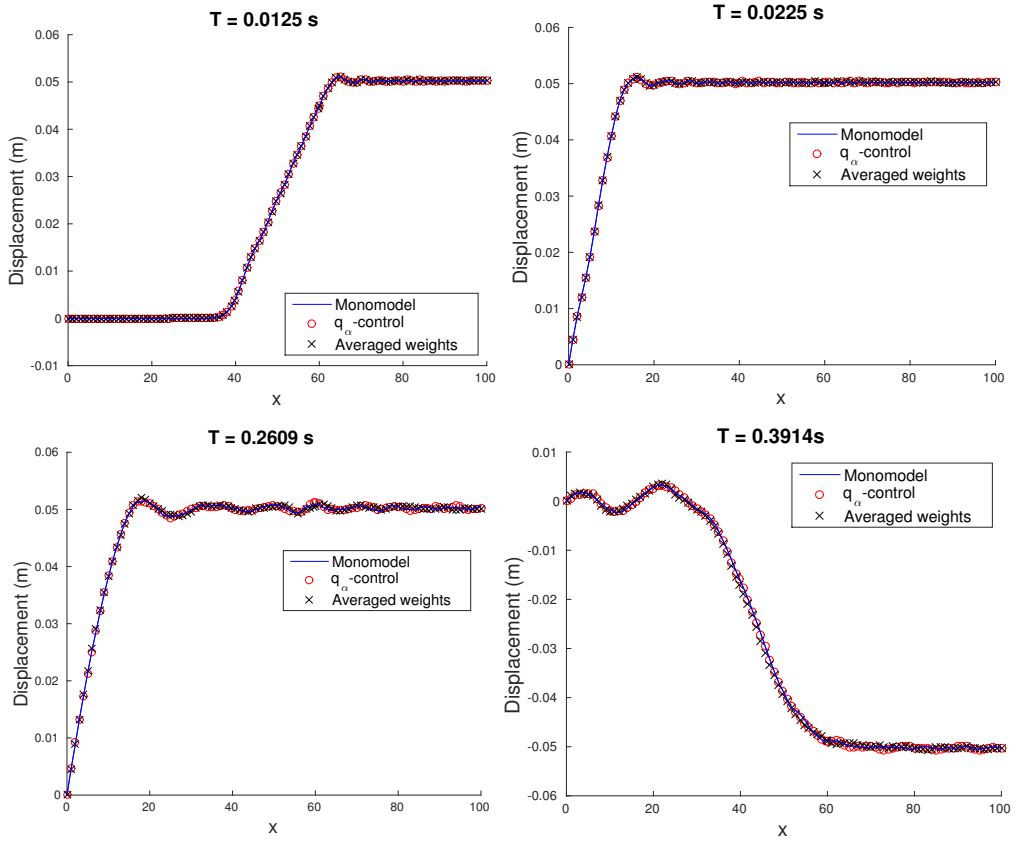

Figure 1.9: Snapshots of the displacement of the beam at different times – Top left: the wave is on its way forward (moving left) on its first round-trip. – Top right: the wave is reflecting on the left clamped edge for the first time. – Bottom left, the wave is reflecting on the left clamped edge after 5 round-trips – Bottom right: the wave is on its way back (moving right) during the tenth round-trip.

The error measurement is shown in Figure 1.10. The results show that both ap-

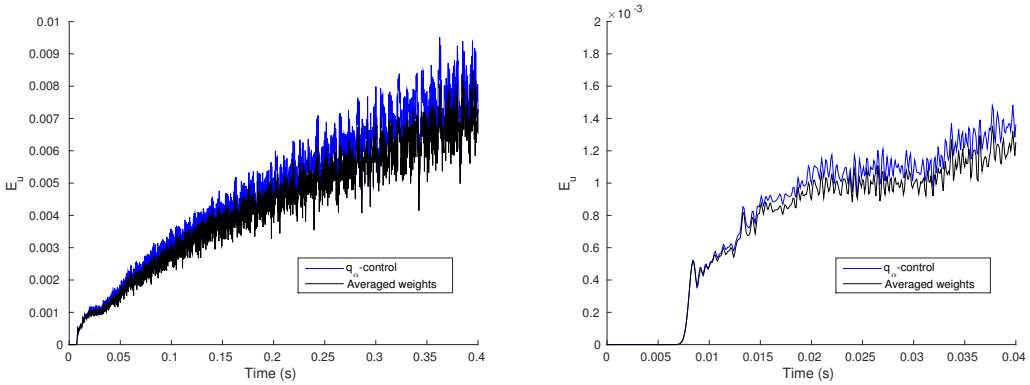

Figure 1.10: Error E_u as defined by equation (1.37) over time for both approaches. The q_α-control approach is in blue while the averaged weight approach is in black. The stopping time corresponds to 10 round trips of the wave (left) and one round trip (right).

proaches lead to precise solutions, with the q_α-control approach yielding a slightly

better solution. After the wave completes 10 round trips, the error is still negligible (less than 0.15%). Both methods are, thus, validated.

The error measure is shown in Figure 1.10. The results show that both approaches lead to precise solutions, with the averaged weight approach yielding a slightly better solution. After the wave completes 10 round trips, the error is still negligible (less than 0.6%). Both methods are, thus, validated. We also observe three different behaviours of the error over time. At first, the error can be considered zero. Since the wave has not reached the patch, it is not surprising that the solutions are identical. Then, at time $t^1 = 8.0 \times 10^{-3}$ s, the wave enters the patch and there is a relatively quick rise in the error (while remaining small). This increase was proven to be independent of the force's value or its duration. Then, no matter how many times the wave is reflected and goes through the patch, the error increases regularly, but slowly, over time.

Remark 1.3.3. *When the two meshes match ($\delta = 0$ or 1), the order of magnitude of the error (1.37) between the mono-model solution and the Arlequin one is 10^{-12}. Therefore, the error in Figure 1.10 is attributable to the fact that the meshes do not match, rather than the Arlequin framework.*

Remark 1.3.4. *In additional computations, various parameters were independently modified (including the size of the coupling zones, different values of $\delta \in]0,1[$, and α_0), and found that the order of magnitude of the error remained the same.*

1.3.5 Partial conclusion

Sections 1.2 and 1.3 analyzed of the influence of the Arlequin framework on the stability for linear structural dynamics, and revealed that the weight functions affect the stability. Further analysis showed that the effects were due to varying weights on an element. We proposed two approaches to circumvent these practical issues, and validated them on a consistency test case.

Both of these methods require the use of piecewise constant weight functions. This is not a significant constraint as, to the best of our knowledge, the type of weight function used does not affect the precision of the solution for finite element problems.

In the upcoming section we check whether the method extends to higher dimension and present a relevant example.

1.4 Numerical examples

In this section we first test the averaged weight and q_α-control approaches on a 2D consistent case. We then consider a 2D example in which the patch adds a feature to the substrate.

1.4.1 A 2D consistency test

1.4.1.1 Presentation

In this section we consider a quarter of a thick-walled tube, as represented in Figure 1.11. We assume the tube to be made of steel ($E = 200\ GPa$, $\nu = 0,3$ and $\rho =$

8000 $kg.m^{-3}$) and use plane strain. The horizontal (bottom) and vertical (left) sides

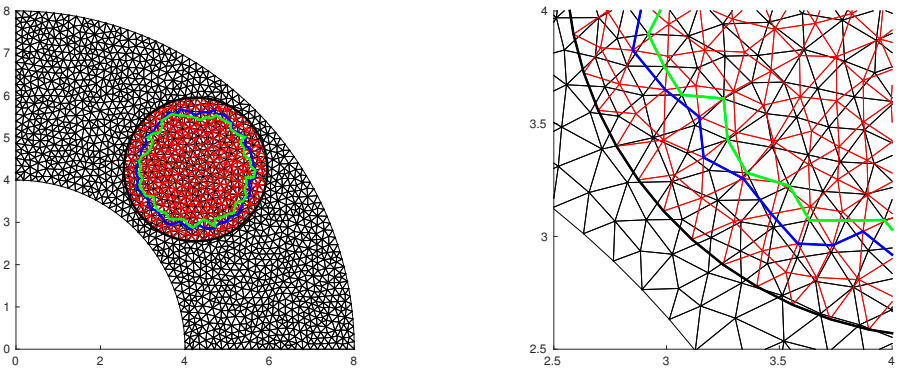

Figure 1.11: Figure of the meshes and the boundaries of the coupling zone (left), and a zoom on the frontiers (right). The substrate (and mono-model) mesh is in black, and the patch mesh is in red. The blue line represents the inner boundary of the coupling zone for the averaged weights approach, and the green line represents that of the q_α-control approach. The outer boundary of the coupling zone is in black, and is common to both approaches.

of the tube are clamped in their normal direction, but free to move in their tangential direction. A constant, uniform force, $||\underline{F}|| = 4\ 10^8 N$, is applied on the inner side of the tube in the normal direction during a time $\Delta t_F = 3.0\ 10^{-4}\ s$. The time step is set to $1.0\ 10^{-5}\ s$ and the simulation lasts for $0.014\ s$, which is about ten round trips of the wave. A small, linear damping equal to $5.0\ 10^{-3}$ is also implemented in order to observe neater solutions.

For the Arlequin models, parameter α_0 is set to $1.0\ 10^{-3}$, while $\alpha_1 = \alpha_2 = 0.5$ in the coupling zone (before averaging for the Averaged weights approach).

The mono-model mesh is unstructured, as represented in black in Figure 1.11. Let the substrate, Ω_1, be the exact same mesh as that of the mono-model and let the patch, Ω_2, be a circular, unstructured mesh with elements similar in size to those of the substrate. The patch is superimposed in the middle of the substrate. The latter two meshes are shown in Figure 1.11.

1.4.1.2 Results

As in section 1.3.4.3, we first study the critical time steps Δt_c and $\Delta_E t_c$. In line with Remark 1.3.2, we see that for the patch-aligned Ω_c approach, the critical time step should strongly decrease with α_0 while the two approaches proposed should maintain a high value of $\Delta_E t_c$ and thus of Δt_c. The evolution of both critical time steps as a function of α_0 for the current meshes is depicted in Figure 1.12.

In Figure 1.12, we can see that both the Averaged weight approach and the q_α-control approach are independent of α_0. However, for the patch-aligned approach, both critical time steps drop drastically (the graph needs to be read from right to left) with α_0. The evolution of $\Delta_E t_c$ is particularly interesting for that approach (figure on the right). At

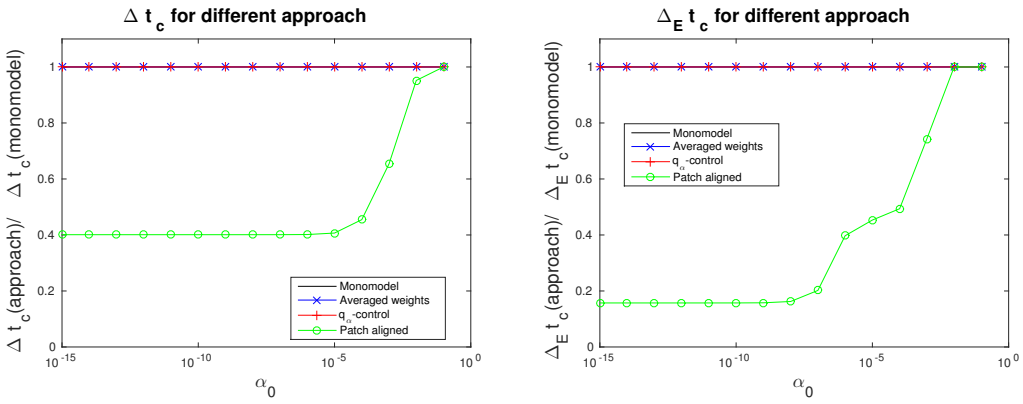

Figure 1.12: Evolution of the global critical time step Δt_c and the elementary critical time step $\Delta_E t - c$ as a function of α_0, the value of the Arlequin weight in the free zone. Their value for the mono-model problem, the Averaged weights approach, the q_α-control approach and the patch-align Ω_c approaches are represented in black, blue, red and green respectively. We have $\Delta t_c = 1.813$s and $\Delta_E t_c = 1.102$s for the mono-model problem.

first, for high values[7] of α_0, the element that yields the lowest time step is the smallest of the two meshes and is located in the substrate, outside the coupling zone. This is consistent with our study as for high values of α_0, q_α is close to one and only the size of the element matters. As α_0 decreases, we observe a first drop around $\alpha_0 \approx 10^{-3}$. For these values of α_0, the lowest time step is obtained for an element in the coupling zone which is also consistent with our study. Indeed, this element is partly in the coupling zone and in the free zone so that its q_α is low and its geometry is equivalent[8] to a low δ. The second drop that appears for values of α_0 below 10^{-6} corresponds to a third element with the same q_α but with a smaller volume and a lower δ.

The evolution of Δt_c does not present these jumps. Yet, we can see that, consistent with formula (1.32), computing the global critical time step yields higher value than computing the elementary one.

As in previous sections, both the averaged weight and the q_α-control approaches were implemented and compared to the mono-model solution. Depictions of the displacement are represented in Figure 1.13. After ten round trips, the displacements are all very similar. The only noticeable difference is that the wave fronts of the Arlequin solutions are not as smooth, especially in the patch, as compared to the mono-model solution.

The error computation using the error measurement (1.37) confirms good agreement between the Arlequin solutions and the mono-model solution. Figure 1.14 shows that both Arlequin approaches yield a very small error that steadies around 0.5%, validating them.

[7] right part of the graph.
[8] the relative area of the element in the coupling zone is close to 0.

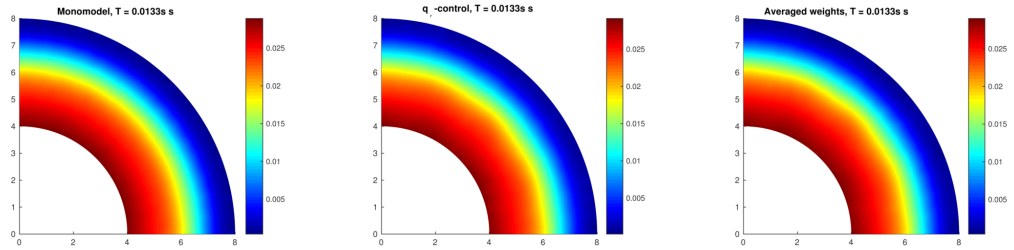

Figure 1.13: Snapshots of the displacement (in meters) in the tube for all three approaches: mono-model on the left, q_α-control in the middle, and the averaged weight on the right. The wave is expanding outward after completing ten round trips.

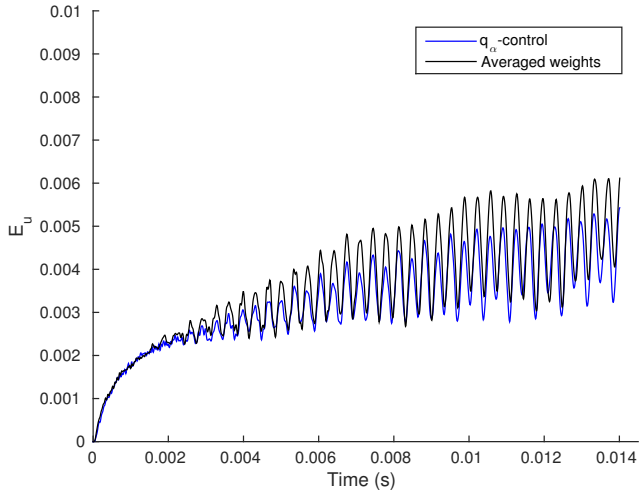

Figure 1.14: Error, E_u, as defined by equation (1.37), plotted over time for both approaches. The q_α-control approach is in blue, and the averaged weight approach is in black.

1.4.2 Geometric discrepancy: a holed plate

1.4.2.1 Presentation

In this section we consider a square plate containing a hole. The plate is of constant density, constant Young's modulus, is assumed to be made of steel ($E = 200\ GPa$, $\nu = 0,3$ and $\rho = 8000\ kg.m^{-3}$), and plane stress is used.

First, we consider the Arlequin models. Let the substrate, Ω_1, be a square plate of side length $100m$, composed of 50×50 square elements of side $2m$. Let the patch, Ω_2, be a web shaped mesh with a hole in it. The outer radius is 20 m, and the inner one is 4 m. The patch is superimposed in the center of the substrate. The reference mono-model is constructed such that it is identical to the substrate in its outer part and is fairly close to the patch in its center. The meshes of the Arlequin models and the mono-model are shown in Figure 1.15 and Figure 1.16. In Figure 1.16, we see that the holes from both the mono-model and the Arlequin formulation are fairly similar, reducing the risk of discrepancies due to mesh differences.

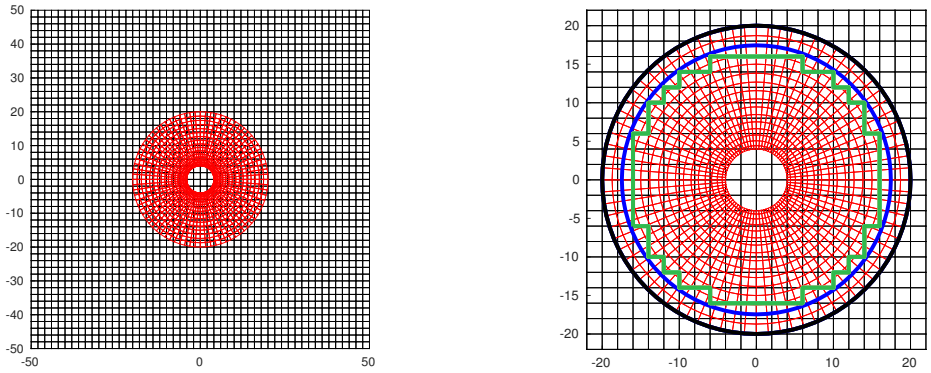

Figure 1.15: Representation of the meshes of the substrate (black) and the patch (red). The right figure is a zoom on the patch region, and shows the coupling zone's borders. The outer and inner borders of the coupling zone for the averaged weight approach are in black and blue, and the outer and inner borders of the q_α-control approach are in black and green.

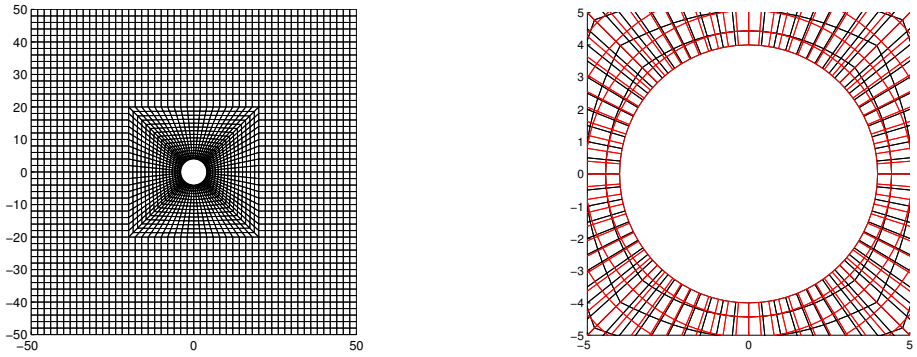

Figure 1.16: The mono-model mesh (left) and a comparison of the holes as meshed in both formulations (right): the mono-model mesh is in black and the Arlequin model mesh is in red.

The left side of the square plate is clamped on the x (horizontal) axis and free to move on the y (vertical) axis. A constant, uniform force, $||\underline{F}|| = 4\ 10^8 N$, is applied on the right side of the plate in the x direction during a time $\Delta t_F = 5.0\ 10^{-3}\ s$. The time step is set to $1.0\ 10^{-5}\ s$ and the simulation lasts for $0.08\ s$, which equals two round trips of the wave. A small linear damping equal to $5.0\ 10^{-3}$ was also implemented.

For the Arlequin models, parameter α_0 is set to $1.0\ 10^{-3}$, while $\alpha_1 = \alpha_2 = 0.5$ in the coupling zone (before averaging for the Averaged weights approach).

1.4.2.2 Error measurement

In order to compare the two solutions, the difference in the shape of the hole was evaluated using a similar error measurement as in previous sections, but is instead

measured on the hole boundary:

$$E_u(t) = \frac{||\underline{u}^r(t) - \underline{u}^a(t)||_{L^2(\partial\Omega_H)}}{\max_\tau ||\underline{u}^r(\tau)||_{L^2(\partial\Omega_H)}} \tag{1.38}$$

with the same notations as before and where $\partial\Omega_H$ is the hole's boundary.

1.4.2.3 Results

The solutions of the mono-model, the averaged weights, and the q_α-control approaches were implemented to calculate displacement across time (see Figure 1.17). The left column of figures show the wave before it enters the patch, and the middle

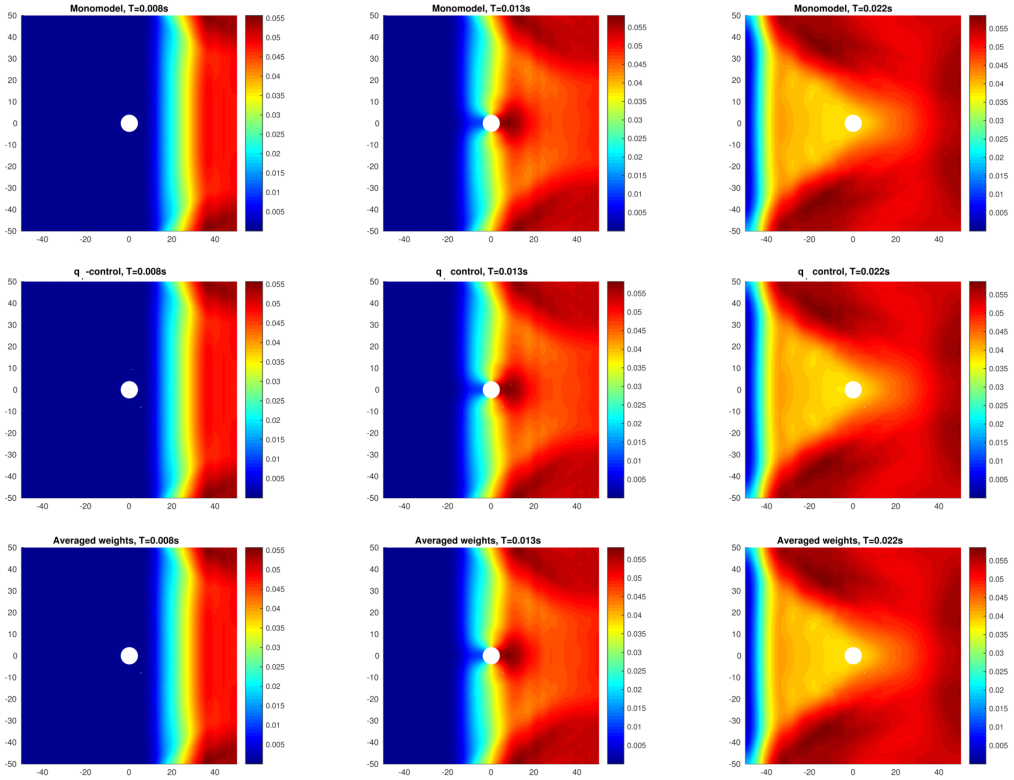

Figure 1.17: Snapshots of the displacement (in meters) of the plate for three approaches: mono-model in the top row, q_α-control in the middle row, and the averaged weights in the bottom row. The displacement is represented at three different time steps. The left column of figures shows the wave just before it enters the patch. In the center column, the wave has entered the patch and hit the hole. In the right column, the wave bounced off the left boundary and is moving back towards the hole.

column shows the displacement when the wave has hit the the hole. The right column shows the displacement right after the wave has bounced. For each time step, all computations are in good agreement.

Figure 1.18 confirms that the solutions of the Arlequin models agree. Both approaches yield low error measures. The error seems to steady around 0.5%, and does not exceed 0.8%, once more validating both approaches.

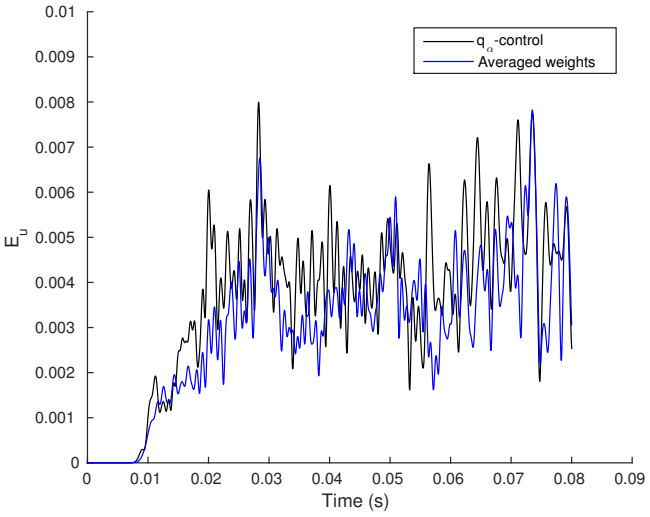

Figure 1.18: Error E_u as defined by equation (1.38) over time for both the q_α-control approach (blue) and the averaged weight one (black).

For this test case, we do not consider the influence of parameter α_0 on the critical time step for geometrical reasons. Indeed, the critical time step is always determined by the elements around the hole, which are a lot smaller than those in the coupling zones. Computations show that both Δt_c and $\Delta_E t_c$ are optimal for all three multi-model approaches, independently of the value of α_0.

1.5 Similar stability issues in other works

After this analysis was completed, we found out that similar issues were faced when using the eXtended Finite Element Method (XFEM) with explicit time integration. The issues faced are not quite the same but the solutions implemented are worth being mentioned.

1.5.1 Presentation of stability issues in explicit dynamics with XFEM

The XFEM uses a local partition of unity to incorporate discontinuities so that the mesh does not have to be conformed with the geometrical support of the discontinuities [67] [68] [160] [74]. The XFEM is widely used for the simulation of crack propagations in two and three dimensions [161] [162] [163] as well as for applications such as creating holes and inclusions [75] [164] [165]. The discontinuities are usually introduced by enriched functions such as the Heavyside function or the generalized Heavyside function. An example of the Heavyside function H on a one dimensional element of size L is as follows.

$$H(x) = \begin{cases} 1 & \text{if } x < \delta L \\ 0 & \text{if } x > \delta L \end{cases} \tag{1.39}$$

where $\delta \in [0, 1]$. An analogue of this enriched function in the Arlequin framework is an element with piecewise constant weight functions equal to 0 if $x < \delta L$ and 1 if $x > \delta L$.

A major difference however is that in XFEM, enriched functions correspond to new, or added, degrees of freedom while in the Arlequin framework the weight functions are introduced for existing ones.

When studying XFEM, it was soon noticed that the use of these enrichment functions in explicit dynamics could cause a null critical time step, especially when the discontinuity is close to a node [166]. This issue is very similar to the one analysed in section 1.3.1 for which $q_\alpha = 0$ and δ is close to 0.

In the XFEM community, the first solutions proposed were to use implicit time integrators [167] [168] or to impose that the crack does not get too close to a node [169] [170]. Then, Menouillard *et al.* proposed mass lumping schemes to ensure non zero critical time steps, independently of the geometry [76] [77]. Their work was generalized from Heavyside functions to arbitrary ones by Gravouil *et al.* in order to simulate three dimensional crack propagation [79] [78].

In both [76] and [79], the critical time step is shown not to drop below a non zero bounded value. In [77], they use a block diagonal lumping technique in order to obtain optimal stability (the enriched functions do not alter the critical time step) for the Heavyside enrichment function only while in [78], optimal stability for arbitrary enrichment functions is obtained thanks to an improved explicit time integrator introduced in [171].

1.5.2 Comparison of the methodology

It is interesting to note that all these works share a similar methodology. First, the problem is restricted to an analysis at the element level, thanks to the argument presented in Proposition 1.32. Thus, for each type of element, a specific study needs to be done. Next, all enriched nodes of the element are assumed to have equal enriched mass, denoted m. Finally, the value of m is scaled.

In this work, we also restricted our study to an analysis at the element level (see Proposition 1.32). The methodology followed for the Averaged weights approach differs from the q_α-control one.

On the one hand, in the Averaged weights approach (section 1.3.3), the implementation proposed implies that all nodes have the same weight so that its influence on the nodal mass contribution is the same for all nodes. This is similar to the proposed XFEM solution in which the same enriched mass contribution is assigned to all enriched nodes of an element. In the Averaged weights approach, the constant weight is defined so that the mass of the element remains constant after averaging. In XFEM works however, the enriched mass is defined so that the discrete kinetic energy for rigid body motions remains constant after the lumping is applied [76] [78].

The $q_\alpha-$control approach (section 1.3.2) on the other hand, does not impose for all nodes to have equal masses. Instead, we impose that the boundaries of the coupling zone are compatible with the appropriate mesh. Such a solution was not found in the XFEM literature. This is because it would be equivalent to imposing that the path of the crack is compatible with the mesh, which defeats the purpose of using enriched functions in the first place.

Although in this work we limited our study of the impact of Arlequin weights to a one dimensional element, Menouillard *et al.* did the calculations for 2D and 3D elements[9]. They too, showed that for 1D elements the critical time step drops to zero with $\delta = \frac{\Delta L}{L}$ (see section 1.3.1). They showed that for 2D elements and 3D elements, similar results were obtained with $\delta = \frac{\Delta S}{S}$ and $\delta = \frac{\Delta V}{V}$ respectively, in agreement with our reasoning.

1.6 Conclusion

In this chapter, we developed and implemented a multi-model approach for the simulation of transient structural dynamics with explicit time integration. In order to do so, we established the multi-model problem formulation for explicit structural dynamics in the Arlequin framework. As the time-integrator is explicit and thus the formulation conditionally stable, our main focus was to study the influence of the Arlequin framework on the stability.

We first studied the influence of the coupling matrices and showed that for the central difference scheme, the explicit scheme has a weak instability. Yet, the algorithm remains stable as long as the initial kinematic conditions of both models agree on the overlapping zone. Then, we studied the influence of the Arlequin weights on the critical time step. We introduced a simplified case to assess the adverse effect of the Arlequin weights on the critical time step. From this test case, we derived a reasoning whereas to why the Arlequin weights deteriorates the stability and deduced two approaches to circumvent this issue. The approaches were validated on a consistent test case and then applied to two 2D applications. For the later, the approaches showed good agreement with reference results.

Now that a stable and accurate multi-model approach has been developed for the structural component, the same must be done for the fluid component. It is achieved in the next chapters.

[9]In our study, the study of 2D and 3D elements was not necessary and the 1D study merely served the purpose of identifying the main factors.

Chapter 2

Multi-model approaches for the transient convective transport equation with explicit time integration

Contents

The objective of this thesis is to develop a multi-model approach able to account for local effects in transient FSI[1] simulations. In the first chapter, we developed a multi-model approach for overlapping structures. Over the next three chapters, we develop a multi-model approach for the fluid component, described by the Euler equations. A possible way to numerically model fluid structure interaction (FSI) is to use a Finite Element discretization for the structure and a hybrid Finite Element/Finite volume discretization for the fluid [172] [173]. To do so offers the advantage that both the fluid and structural kinematic variables are located at the nodes of their respective grid. Thus, a simple framework is provided to impose link conditions between the two entities. This is the modelling adopted in this work.

Such a modelling implies that the momentum equation is treated by the Finite Element Method (FEM) in its non-conservative form. Its treatment is then very similar to that of the equilibrium equation of structural dynamics studied in Chapter 1. The Arlequin framework is thus a natural choice for the treatment of this equation. The other two equations, namely the equation of conservation of mass and total energy, are discretized by the Finite Volume Method. Although multi-model approaches, such as the

[1]Fluid Structure Interaction.

Chimera method [117] [150], have already been proposed for Finite Volume Methods, other methods are worth being explored. This is why, in this chapter, we focus on the study of suitable multi-model frameworks for the treatment of such equations.

In order to do so, we first introduce a reference problem for the convective transport of a scalar quantity q which is representative of both the conservation of mass equation and the conservation of energy equation (section 2.1). Then, we propose different multi-model approaches (section 2.2) and study their respective stability (section 2.3) and accuracy (section 2.4). Finally, we conclude by determining which approaches are admissible to model the convective transport equations of the fluid component.

2.1 Mono-model formulation for the convective transport equation

In order to present a comprehensive study of the multi-model approaches for the convective transport equation, we consider the following representative problem. The latter describes the convective transport of a scalar quantity q for a single model. If $q = \rho$, where ρ is the density, then we obtain the conservation of mass equation. Similarly, if $q = \rho E$, where E is the specific total energy, then the conservation of energy equation is obtained. The solution of the multi-model approaches later proposed will aim to converge towards the solution obtained by this reference problem formulation.

2.1.1 Continuous formulation of the transport equation

We consider a body occupying a bounded, regular domain $\Omega_1 \in \mathbb{R}^d$. Let q and v denote the transported quantity and the velocity fields while $q^0 = q(t = 0)$ denotes the initial value of q. The velocity v is imposed and assumed to be independent of time. Let $\Gamma_{inflow} \subset \partial\Omega_1$ be the part of the boundary of the domain for which inflow boundary conditions are necessary. The continuous formulation of the transport equation reads (see [154])

Given q^0, $\underline{v}$ and inflow boundary conditions on Γ_{inflow}, find $q(t)$, $t \in [0, T]$, such that:

$$\forall\ \Omega \subset \Omega_1, \int_\Omega \frac{\partial q}{\partial t}\ d\Omega + \int_\Omega \mathrm{div}(\phi_q \underline{v})\ d\Omega = 0 \tag{2.1}$$

where $f = \phi_q \underline{v}$ is called the flow.

Remark 2.1.1. *If $q = \rho$, then $\phi_q = \rho$ and problem (2.1) is representative of the conservation of mass equation. If $q = \rho E$, then $\phi_q = \rho E + p$ with p the pressure and problem (2.1) is representative of the conservation of energy equation.*

Remark 2.1.2. *In this work and unless specified, we consider domains Ω_1 in $\mathbb{R}^2$. Thus, two adjacent elements of the discretized domain are separated by an edge. Yet, all results still hold for domains in $\mathbb{R}$ and $\mathbb{R}^3$, in which case elements are separated by nodes and faces respectively.*

2.1.2 Discretized formulations

In this section we give the discrete formulation of the continuous problem previously introduced. First, we describe the time-integrator considered for the integration of the transport equation. Then, we introduce the discrete mono-model formulation.

2.1.2.1 Discrete time-integrator

The time interval $[0,T]$ is subdivided into N steps Δt^i. Let q^n and $\dot{q}^n$ denote the discrete quantity q and its derivative at time $t^n = \sum_{i=1}^{n} \Delta t^i,\ n \in [\![0,N]\!]$. As the velocity is assumed to be independent of time, we denote by $\underline{v}$ its value throughout the integration. In this study, we consider the Forward Euler explicit time-integrator.

Given q^0,

$$q^{n+1} = q^n + \Delta t^n \dot{q}^n \tag{2.2}$$

2.1.3 Discrete mono-model problem formulation

2.1.3.1 Finite Volume discretization

A Finite Volume scheme with a first order upwind scheme is used for the discretization of the transport equation (see [154]). Let us denote by $\mathcal{T}_1$ the mesh representing Ω_1 and by $\mathcal{S}_E$ the set of elements of $\mathcal{T}_1$. We can write, on every element $E \in \mathcal{S}_E$ occupying Ω_E and at every time step n

$$\int_{\Omega_E} \left(\frac{\partial q}{\partial t}\right)^n \, d\Omega_E + \int_{\Omega_E} \mathrm{div}(\phi_q^n \underline{v}) \, d\Omega_E = 0 \tag{2.3}$$

In the Finite Volume scheme considered[2], the quantity q is averaged on every element such that the left hand side of (2.3) can be rewritten:

$$\begin{aligned} \int_{\Omega_E} \left(\frac{\partial q}{\partial t}\right)^n \, d\Omega_E &= \frac{d}{dt} \int_{\Omega_E} q^n \, d\Omega_E \\ &= \dot{q}_E^n |\Omega_E| \end{aligned} \tag{2.4}$$

where $q_E^n = \int_{\Omega_E} q^n d\Omega_E$ is the averaged value of q^n on element E and $|\Omega_E|$ is the volume of element E. The second term of the left hand side of (2.3) is not, in practice, computed as is. Instead, we use the Green-Ostrogradski formula and the following approximation:

$$\begin{aligned} \forall E \in \mathcal{S}_E,\ \int_{\Omega_E} \mathrm{div}(\phi_q^n \underline{v}) \, d\partial\Omega_E &= -\int_{\partial\Omega_E} \phi_q^n \underline{v} \cdot \underline{n} \, d\Omega_E \\ &\approx -\sum_{e \in \mathcal{S}_e^E} \phi_{q,e}^n \int_e \underline{v} \cdot \underline{n} \, de \end{aligned} \tag{2.5}$$

where $\mathcal{S}_e^E$ is the set of edges of E, $\phi_{q,e}^n$ is the upwind value of ϕ_q^n at edge e and n the outward normal to edge e of element E. Let e be one of these edges so that it is

[2] See for instance [154].

between E and another element E^*. The first order upwind scheme implemented [154] reads:

$$\phi^n_{q,e} = \begin{cases} \phi^n_q(E) & \text{if } \int_e \underline{v}\cdot\underline{n}\ de > 0 \\ \phi^n_q(E^*) & \text{if } \int_e \underline{v}\cdot\underline{n}\ de < 0 \\ 0 & \text{otherwise} \end{cases} \tag{2.6}$$

The discrete mono-model formulation then reads

Given $\{q^0_E\}_{E\in\mathcal{S}_E}$, *v and inflow boundary conditions on* Γ_{inflow}, *find* $\forall n \in [\![0,N]\!]$, $\{q^n_E\}_{E\in\mathcal{S}_E}$ *such that*

$$\forall E \in \mathcal{S}_E,\ q^{n+1}_E = q^n_E - \frac{\Delta t}{|\Omega_E|}\sum_{e\in E}\phi^n_{q,e}\int_e \underline{v}\cdot\underline{n}\ de \tag{2.7}$$

2.1.3.2 FEM-like description

The problem (2.7) can be written using shape-like functions, which will prove useful hereafter. The idea is that considering that q^n is averaged on every element is the equivalent to considering that q^n can be written

$$q^n(\underline{x}) = \sum_{E\in\mathcal{S}_E} q^n_E \bar{N}_E(\underline{x}) \ \text{ with } \begin{cases} \bar{N}_E(\underline{x}) = 1 & \text{if } \underline{x}\in\Omega_E \\ \bar{N}_E(\underline{x}) = 0 & \text{otherwise} \end{cases} \tag{2.8}$$

Let us denote by $\mathcal{V}\subset L^2(\Omega)$ the space of functions that can be written this way. The FEM-like discrete formulation of (2.7) is then:

Given q^0, *v and inflow boundary conditions on* Γ_{inflow}, *find* $\forall n \in [\![0,N]\!]$, q^n *such that*

$$\forall w\in\mathcal{V}, \int_{\Omega_1}\dot{q}^n w\ d\Omega_1 + \int_{\Omega_1}\mathrm{div}(\phi^n_q\underline{v})w\ d\Omega_1 = 0 \tag{2.9}$$

Remark 2.1.3. *Note that both (2.7) and (2.9) can be written in matrix form:*

$$\underline{\underline{M}}\dot{\underline{Q}}^n + \underline{F}^n = 0 \tag{2.10}$$

with $\underline{Q}^n = [q^n_1,...,q^n_{\mathcal{N}_E}]^T$, $\underline{\underline{M}} = \mathrm{diag}(|\Omega_{E_1}|,...,|\Omega_{E_{\mathcal{N}_E}}|)$ *where* $\mathcal{N}_E$ *is the number of elements in* $\mathcal{S}_E$ *and* $\underline{F}^n$ *is the vector representing the divergence terms. Moreover, if* ϕ_q *is a linear combination of* q^n *then we have*[3] $\underline{F}^n = \underline{\underline{K}}\underline{Q}^n$.

Now that we have defined a discretized formulation for the reference problem, the next section is dedicated to establishing multi-model approaches for the treatment of convective transport.

2.2 Multi-model approaches for convective transport

We use the same notations than in section 1.1.2 which are recalled hereafter. We thus consider a first body, referred to as the substrate, occupying a bounded, regular

[3]This is the case for the conservation of mass equation for which $\phi_\rho = \rho$.

domain $\Omega_1 \in \mathbb{R}^2$. We also consider a second body, referred to as the patch, occupying a bounded, regular domain $\Omega_2 \in \mathbb{R}^2$ and assumed to be strictly embedded in Ω_1, as shown in Figure 1.1. Quantities relative to the substrate are denoted by a subscript equal to 1 while those relative to the patch are denote by a subscript equal to 2.

The different multi-model approaches proposed in this chapter all have in common that they transmit the information from one body, or domain, to the other in an area called the coupling zone, denoted by Ω_c and delimited by two boundaries, represented in blue and red in Figure 1.1. The free zone, denoted Ω_f, is the inner area of Ω_2, where the solution is given by the patch. The multi-model approaches proposed here only differ by the way the information is transmitted between domains. They are introduced hereafter.

Remark 2.2.1. *We recall that, in this work, the boundaries of the coupling zone can either be compatible with the mesh of the substrate or with that of the patch. As the patch is assumed to be strictly embedded in the substrate, the outer boundary (in, red in Figure 1.1) is always assumed to be compatible with the mesh of the patch. We will see that for one of the multi-model approaches proposed here the inner boundary can be aligned with either mesh (see section 2.2.2) while for the other two proposed approaches it is assumed[4] to be aligned with the mesh of the substrate (see sections 2.2.1 and 2.2.3).*

2.2.1 A Chimera formulation of the transport equation

For the treatment of the transport equation, the Chimera method is the most natural choice. Indeed, the method has proven to be precise and efficient in multi-model fluid dynamics and has been widely studied [139] [134]. Thus, we propose a first multi-model approach that uses the Chimera method for the discrete transport equation (2.7).

In the Chimera method, the information is transmitted between domains through interpolation techniques. In order to do so, two boundaries across which the information is transmitted need to be defined. A first boundary, $\Gamma_{1\to2}$ (in red in Figure 1.1), determines where the information is transmitted from Ω_1 to Ω_2. The other boundary, $\Gamma_{2\to1}$ (in blue in Figure 1.1), determines where the information is transmitted from Ω_2 to Ω_1.

For both models, the convective transport equation is discretized by the finite volume method with an upwind scheme (see section 2.1.3) except at the boundaries $\Gamma_{1\to2}$ and $\Gamma_{2\to1}$. In the following, $\Gamma_{1\to2}$ is assumed to be conformed with the mesh of the patch while $\Gamma_{2\to1}$ is assumed to be conformed with the mesh of the substrate. At each edge e of model j aligned with boundary $\Gamma_{i\to j}$, a value of the flow $\phi^n_{q,e}\underline{v}$ needs to be computed.

Let us first consider an edge e of an element E of the patch and aligned with boundary $\Gamma_{1\to2}$. If the velocity on that edge is such that $\int_e v \cdot n \; de > 0$, then the upwind value of $\phi^n_{q,e}$ is computed on the element E, as is done is the mono-model formulation. However if $\int_e v \cdot n \; de < 0$, $\phi^n_{q,e}$ must be defined upstream where there are no elements of the patch. A so-called ghost element is thus created upstream and its overlapping volumes with elements of the substrate are computed. The upstream value of $\phi^n_{q,e}$ is then defined as the volume average of ϕ^n_q of each overlapped elements.

[4] by construction.

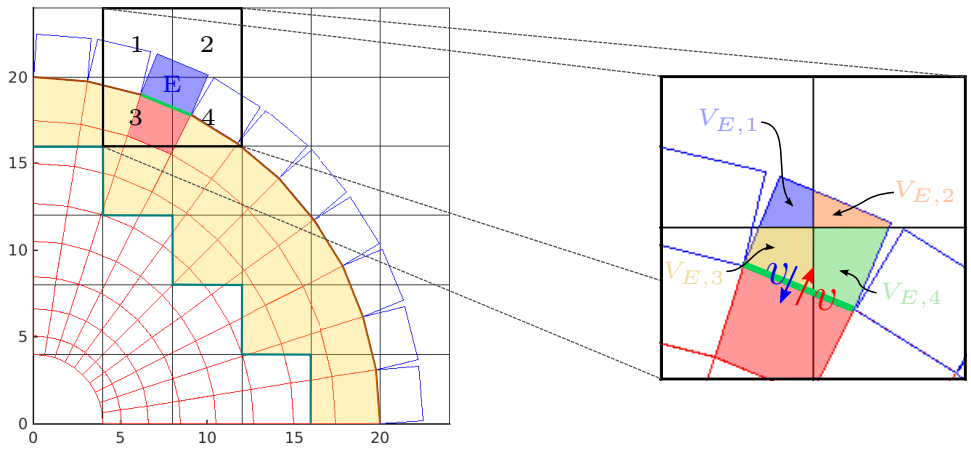

Figure 2.1: LEFT – The meshes of the substrate (in black), of the patch (in red) and of the ghost elements of the patch (in blue) are represented. The coupling zone Ω_c is represented in light yellow (and includes the element filled in red) while its boundaries, $\Gamma_{1\to2}$ and $\Gamma_{2\to1}$ are represented in brown and dark green respectively. We consider the edge (in bright green) of the element of the patch filled in red. RIGHT – If $\underline{v}\cdot\underline{n}$ is positive (arrow in red), then upwind corresponds to a region in Ω_c where both models are equally relevant. We arbitrary choose the patch in order to save computing resources. Indeed, choosing the substrate would require creating more ghost elements and compute more mesh intersections. The value of $\phi_{q,e}$ is then equal to $\phi_q^n(red)$. However, if $\underline{v}\cdot\underline{n}$ is negative (arrow in blue), then upstream corresponds to a region where the substrate is the only model relevant. Thus, a ghost element is generated (element E) and the overlap volume with elements of substrate are computed ($(V_{E,k})_{k\in[|1,4|]}$ on the figure). The quantity $\phi_{q,e}^n$ is then defined as its volume average on these elements, that is, $\phi_{q,e}^n = \frac{1}{V_E}(\phi_q^n(1)V_{E,1} + \phi_q^n(2)V_{E,2} + \phi_q^n(3)V_{E,3} + \phi_q^n(4)V_{E,4})$.

Symmetric computations are accomplished for edges of the substrate aligned with $\Gamma_{2\to2}$. This entire process is illustrated in Figure 2.1.

Remark 2.2.2. *The distance between the two boundaries needs to be larger than the stencil defined to interpolate ϕ_q^n [150]. In our case, our equivalent of the stencil is, at most, the size of one element. Thus, we ensure that an element of either domain can not be cut by both boundaries.*

Remark 2.2.3. *In practice, the size of the ghost element introduces new parameters. In this work, ghost elements are exclusively rectangles of which one side is an edge of the element. The width of that element is defined as half the shortest length of all the elements of the problem*[5]*.*

Remark 2.2.4. *On Ω_f, the patch is the only model relevant so that the solution is not computed for the substrate in that area. Instead, the degrees of freedom of the substrate are either deleted or are artificially maintained constant over time.*

[5]for clarity purposes, it is not the case in Figure 2.1.

2.2.2 An Arlequin formulation of the transport equation

In order to establish an Arlequin formulation[6], we first have to determine where the weight functions fit in the FEM-like formulation (2.9). Then, we choose an appropriate coupling operator and finally, we choose the type of weight function.

2.2.2.1 Weight functions for the convection term

The first step towards formulating an Arlequin formulation for the transport equation is to determine where the weight functions fit in the convection term, that is, $\int_\Omega \mathrm{div}(\phi_q \underline{v}) w \; d\Omega$. In order to do so, we consider the continuous equations and aim to write the mono-model convective transport equation (2.1) in a form to which the Arlequin framework can be applied. We have

$$\begin{aligned} \int_\Omega \mathrm{div}(\phi_q \underline{v}) w \; d\Omega &= \int_\Omega \mathrm{div}(\phi_q w \underline{v}) - (\phi_q \underline{v}) \cdot (\underline{\nabla} w) \; d\Omega \\ &= \int_{\partial\Omega} \phi_q w \underline{v} \cdot \underline{n} \; d\partial\Omega - \int_\Omega (\phi_q \underline{v}) \cdot (\underline{\nabla} w) \; d\Omega \end{aligned} \tag{2.11}$$

so that the equation of convective transport (2.1) can be rewritten as follows:

$$\int_\Omega \frac{\partial q}{\partial t} w \; d\Omega - \int_\Omega (\phi_q \underline{v}) \cdot (\underline{\nabla w}) \; d\Omega = \int_\Omega \phi_q w \underline{v} \cdot \underline{n} \; d\Omega \tag{2.12}$$

which is of the form

$$\int_\Omega \frac{\partial q}{\partial t} w \; d\Omega + \int_\Omega \underline{\underline{\sigma}}(q) : \underline{\underline{(\nabla w)}} \; d\Omega = \int_{\partial\Omega} f \; d\partial\Omega \tag{2.13}$$

We can thus apply the Arlequin framework to equation (2.12) which yields the following problem formulation[7].

Given q_1^0, q_2^0, $\underline{v}$ and inflow boundary conditions on Γ_{inflow}, find $(q_1(t), q_2(t)) \in \mathcal{V} \times \mathcal{V}$ such that, $\forall (w_1, w_2, \underline{\mu}) \in \mathcal{V} \times \mathcal{V} \times \mathcal{M}^q$,

$$\begin{cases} \displaystyle\int_{\Omega_1} \widehat{\alpha}_1^q \frac{\partial q_1}{\partial t} \; w_1 \; d\Omega_1 - \int_{\Omega_1} \alpha_1^q \phi_{q_1} \underline{v} \cdot (\underline{\nabla w_1}) \; d\Omega_1 + c_t(w_1, \lambda) = \int_{\partial\Omega_1} \tilde{\alpha}_1^q \phi_{q_1} w_1 \underline{v} \cdot \underline{n} \; d\partial\Omega_1 \\ \displaystyle\int_{\Omega_2} \widehat{\alpha}_2^q \frac{\partial q_2}{\partial t} \; w_2 \; d\Omega_2 - \int_{\Omega_2} \alpha_2^q \phi_{q_2} \underline{v} \cdot (\underline{\nabla w_2}) \; d\Omega_2 - c_t(w_2, \lambda) = \int_{\partial\Omega_2} \tilde{\alpha}_2^q \phi_{q_2} w_2 \underline{v} \cdot \underline{n} \; d\partial\Omega_2 \\ c_t(\dot{q_1} - \dot{q_2}, \mu) = 0 \end{cases} \tag{2.14}$$

where c_t is a coupling operator to be defined, $\mathcal{M}^q$ is the mediator space and $(\hat{\alpha}_1^q, \hat{\alpha}_2^q)$, (α_1^q, α_2^q) and $(\tilde{\alpha}_1^q, \tilde{\alpha}_2^q)$ are sets of weight functions as defined in section 1.1.2.

The transport equations are not treated as such as it would be computationally costly. Instead, we impose $(\tilde{\alpha}_1^q, \tilde{\alpha}_2^q) = (\alpha_1^q, \alpha_2^q)$ so that we can do the reverse calculations done in (2.11) and obtain the following problem formulation.

[6] see Appendix B.
[7] see Appendix B.

$$\begin{cases} \displaystyle\int_{\Omega_1} \widehat{\alpha}_1^q \frac{\partial q_1}{\partial t}\ w_1\ d\Omega_1 + \int_{\Omega_1} \mathrm{div}(\alpha_1^q \phi_{q_1} \underline{v}) w_1\ d\Omega_1 + c_t(w_1, \lambda) = 0 \\ \displaystyle\int_{\Omega_2} \widehat{\alpha}_2^q \frac{\partial q_2}{\partial t}\ w_2\ d\Omega_2 + \int_{\Omega_2} \mathrm{div}(\alpha_2^q \phi_{q_2} \underline{v}) w_2\ d\Omega_2 - c_t(w_2, \lambda) = 0 \\ c_t(\dot{q_1} - \dot{q_2}, \mu) = 0 \end{cases} \tag{2.15}$$

Note that the global solution for quantity q is then obtained by $q = \hat{\alpha}_1^q q_1 + \hat{\alpha}_2^q q_2$.

In this formulation, we can see that the weight function for the convection term appears in the divergence term which was not, *a priori*, obvious.

Remark 2.2.5. *In [110], Caleyron uses the work of Guidault et al. [114] to establish strong formulations for equations including divergence terms. Through an energy analysis, they then reach the same conclusion, that is, that the weight functions fit inside the divergence term.*

Note that the discretized system (2.15) can be written in matrix form as

$$\begin{pmatrix} \underline{\underline{D}}_1 & \underline{\underline{0}} & \underline{\underline{C}}_1^T \\ \underline{\underline{0}} & \underline{\underline{D}}_2 & \underline{\underline{C}}_2^T \\ \underline{\underline{C}}_1 & \underline{\underline{C}}_1 & \underline{\underline{0}} \end{pmatrix} \begin{pmatrix} \dot{\underline{Q}}_1^n \\ \dot{\underline{Q}}_2^n \\ \underline{\lambda} \end{pmatrix} = \begin{pmatrix} \underline{F}_1^n \\ \underline{F}_2^n \\ \underline{0} \end{pmatrix} \tag{2.16}$$

where $\underline{\underline{C}}_1$ and $\underline{\underline{C}}_2$ are the coupling the matrices (see section 2.2.2.2). We have, $\forall i \in \{1; 2\}$,

$$\begin{cases} (\underline{\underline{D}}_i)_{jk} &= \displaystyle\int_{\Omega_i} \hat{\alpha}_i^q \bar{N}_j^i \bar{N}_k^i\ d\Omega_i &= \left(\int_{\Omega_j} \hat{\alpha}^q d\Omega_j\right) \delta_{jk} \\ (\underline{F}_i^n)_j &= -\displaystyle\int_{\Omega_j} \bar{N}_j^i\ \mathrm{div}(\alpha_i^q \phi_{q_i}^n \underline{v}_i)\ d\Omega_j &= -\displaystyle\sum_{e \in \mathcal{S}_e^j} \phi_{q_i,e}^n \int_e \alpha_i^q \underline{v}_i \cdot \underline{n}\ de \\ (\underline{\underline{C}}_i)_{jk} &= \displaystyle\int_{\Omega_k} \bar{N}_j^i \bar{N}_k^\lambda\ d\Omega_k \end{cases} \tag{2.17}$$

where $\bar{N}_k^\lambda$ are the shape functions associated to the mediator space.

Moreover, if $\phi_{q_i,e}^n$ is a linear function of $\underline{Q}_i^n$, then we can write $\underline{F}_i^n = \underline{\underline{K}}_i \underline{Q}_i^n$ so that we have

$$\underline{\underline{D}} \dot{\underline{Q}}^n + \underline{\underline{K}}^* \underline{Q}^n = 0 \tag{2.18}$$

with $\underline{\underline{D}} = \mathrm{diag}(\underline{\underline{D}}_1, \underline{\underline{D}}_2)$ is the mass-like matrix, $\underline{\underline{C}} = [\underline{\underline{C}}_1, \underline{\underline{C}}_2]^T$, $\underline{\underline{K}}^* = (\underline{\underline{I}} - (\underline{\underline{C}}\underline{\underline{D}}^{-1}\underline{\underline{C}}^T)^{-1}\underline{\underline{C}}\underline{\underline{D}}^{-1})$ $\mathrm{diag}(\underline{\underline{K}}_1, \underline{\underline{K}}_2)$ and $\underline{Q}^n = [\underline{Q}_1^n, \underline{Q}_2^n]^T$.

2.2.2.2 Choice of the coupling operator

In this work, we use a first order upwind scheme and a Finite Volume discretization for the transport equations. Hence, there is no immediate definition of ∇q so that using a L^2 coupling operator is the most natural choice. Therefore, the continuous coupling operator c_t is defined as

$$\forall (q, \mu) \in \mathcal{V} \times \mathcal{M}^q,\ c_t(q, \mu) = \int_{\Omega_c} q\mu\ d\Omega_c \tag{2.19}$$

In [103], the authors failed to prove that an L^2-coupling operator always leads to well posed problem and thus advice not to use it. In [114], the authors argue that an L^2-coupling operator can be implemented if specific conditions are met such as the use of continuous weight functions. Moreover, in both works, they observed that using a L^2-coupling operator leads to more accurate solutions than a H^1-coupling one.

2.2.2.3 Choice of the weight parameter

However, just like for the Chimera approach, a value for an inward upwind flow needs to be defined for an edge e of the patch compatible with $\partial\Omega_2$ (see Figure 2.1). In the Arlequin approach, the flow is equal to $\int_e \alpha\phi_{q,e} v \cdot n \, de$ (see section 2.2.2.1). Thus, if the weight function $\alpha \equiv 0$ on the entire edge, then, no matter what the value of $\phi_{q,e}$ is, the flow is null. Hence, the actual value of $\phi_{q,e}$ does not need to be computed and there are no need to generate ghost elements.

In the rest of this work, we impose that the weight function α_2^q is globally continuous, linear on Ω_c and equal to 0 on $\partial\Omega_2$. By symmetry, we impose that α_1^q is globally continuous, linear on Ω_c and equal to α_0 on $\partial\Omega_f$ (see examples in section 2.4). The choice of linear weight functions for the divergence term is also compatible with the choice of a L^2 coupling operator, as previously explained.

In 1D, linear weight parameters can be simply defined. In higher dimensions however, it can be more difficult[8]. In this work, the weight parameter α^q in Ω_c is defined as follows. For every point in Ω_c, the distance to both the outer and the inner boundaries of Ω_c, L_{out} and L_{in} respectively, is computed. The value of α^q is then:

$$\begin{cases} \alpha_1^q(\underline{x}) = 1 - \dfrac{1-\alpha_0}{L_{in}(\underline{x}) + L_{out}(\underline{x})} L_{out}(\underline{x}) \\ \alpha_2^q(\underline{x}) = (1-\alpha_0) - \dfrac{1-\alpha_0}{L_{in}(\underline{x}) + L_{out}(\underline{x})} L_{in}(\underline{x}) \end{cases} \tag{2.20}$$

Remark 2.2.6. *The Chimera method implemented here requires the generation of ghost elements which can be computationally costly. Although the choice of weight functions in the Arlequin formulation circumvents this issue, the coupling matrices induce the resolution of a linear problem which can also be computationally costly.*

In the following, we propose a third alternative for the treatment of convective transport.

2.2.3 A hybrid formulation of the transport equation

The main idea behind this third alternative is to combine both the Chimera and Arlequin frameworks. In this third approach, hereafter referred to as the Chimix approach, information is transferred between domains throughout the coupling zone Ω_c. We consider here the Finite Volume description of the transport equation as defined in (2.7).

Let us consider an edge inside the coupling zone that separates two elements E_1 and E_2 of the substrate. The flow f between the two elements is approximated by $f \approx \phi_{q,e}^n \int_e v \cdot n \, de$. Let us now assume that the flow is such that E_1 is the upwind

[8] see for instance the test case presented in section 2.4.1.

element. In the Chimix approach, the term $\phi^n_{q,e}$ has two contributions. The first contribution is equal to $\phi^n_q(E_1)\int_e \alpha^q_1\, de$. The second contribution is obtained using a Chimera-like approach (see section 2.2.1).

The intersections of E_1 with overlapping elements of the patch are computed and the volume average of ϕ^n_q, denoted ϕ^p_q is calculated (see Figure 2.1). The second contribution is then equal to $\phi^p_q\left(1-\int_e \alpha^p_q\, de\right)$. Such an approach is illustrated in Figure 2.2 for a 1D problem.

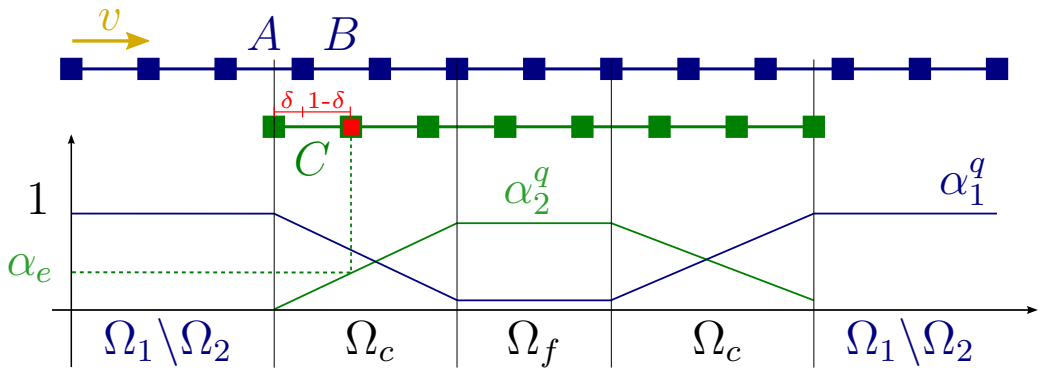

Figure 2.2: We consider the 1D multi-model problem. The substrate is represented in blue while the patch is represented in green. We assume that the velocity is uniformly equal to $v = +1\text{m.s}^{-1}$ and consider the edge e (edges are nodes in 1D) of the patch in red in the figure. The quantity $\phi^n_{q,e}$ is the sum of two terms. The first term represents the contribution of the patch and is equal to $\alpha_e q^n_2(C)$ while the second, representing the contribution of the substrate, is equal to $(1-\alpha_e)(q^n_1(A)\delta + q^n_1(B)(1-\delta))$. This process is repeated for all edges inside the coupling zone.

Using this approach presents two advantages. First, weight functions are used so that, similarly to the Arlequin approach, no ghost elements need to be generated on the outer boundary of the patch. The second advantage is that no coupling matrices are required so that the integration in time can be completed element by element[9] and no linear system needs to be solved. One drawback of the Chimix approach is that the intersection between elements in the coupling zone of each model needs to be calculated. However, when dealing with the Euler equations, the equation of momentum will be treated using the Arlequin framework so that these intersections are computed anyway (see Chapter 3).

Remark 2.2.7. *Let us consider the strong form of the mono-model problem* (2.1)*:*

$$\frac{\partial}{\partial t} q + \text{div}(\phi_q \underline{v}) = 0 \tag{2.21}$$

When introducing the weight parameters for the Chimix formulation, we can either

[9]For higher computational performances, the treatment of such equations is usually completed edge by edge. In the current Chimix approach, the absence of coupling matrices ensures that that treatment holds.

include them in the divergence term or outside. If the former case, we thus have

$$\begin{cases} \dfrac{\partial}{\partial t}(\alpha_1^q q_1) + \operatorname{div}(\alpha_1^q \phi_{q_1} \underline{v}) = 0 \\ \dfrac{\partial}{\partial t}(\alpha_2^q q_2) + \operatorname{div}(\alpha_2^q \phi_{q_2} \underline{v}) = 0 \end{cases} \tag{2.22}$$

whose sum yields

$$\frac{\partial}{\partial t}(\alpha_1^q q_1 + \alpha_2^q q_2) + \operatorname{div}((\alpha_1^q \phi_{q_1} + \alpha_2^q \phi_{q_2})\underline{v}) = 0 \tag{2.23}$$

which is of the form of (2.21) *with* $q = \alpha_1^q q_1 + \alpha_2^q q_2$ *and* $\phi_q = \alpha_1^q \phi_{q_1} + \alpha_2^q \phi_{q_2}$.

If the weight parameter is introduced outside the divergence term, we have

$$\begin{cases} \dfrac{\partial}{\partial t}(\alpha_1^q q_1) + \alpha_1^q \operatorname{div}(\phi_{q_1} \underline{v}) = 0 \\ \dfrac{\partial}{\partial t}(\alpha_2^q q_2) + \alpha_2^q \operatorname{div}(\phi_{q_2} \underline{v}) = 0 \end{cases} \tag{2.24}$$

whose sum, after calculations, yields:

$$\frac{\partial}{\partial t}(\alpha_1^q q_1 + \alpha_2^q q_2) + (\alpha_1^q \phi_{q_1} + \alpha_2^q \phi_{q_2}) \operatorname{div}(\underline{v}) + (\alpha_1^q \underline{\nabla} \phi_{q_1} + \alpha_2^q \underline{\nabla} \phi_{q_2}) \cdot \underline{v} = 0 \tag{2.25}$$

which is not of the form of (2.21)*. Thus, in line with previous results, the weight parameter should indeed be inside the divergence term.*

2.3 Study of the stability of the multi-model approaches

2.3.1 Strategy for the stability study of the multi-model approaches

The use of the explicit time integrators defined in section 2.2 implies that the problem formulation is conditionally stable [174]. In fact, for the mono-model formulation (2.9), it was shown that the time step Δt^n needs to verify the following condition:

$$\Delta t < \Delta t_c = \frac{1}{\max \omega} \tag{2.26}$$

where the ω are the eigenvalues of the generalized eigenvalue problem of M and K (defined in section 2.1.3) and Δt_c is called the critical time step.

As the stability is conditional, the influence of multi-model components on the stability need to be studied in order to ensure that the critical time step is not adversely altered and thus that the approaches proposed are computationally feasible. These components are (1) the Chimera-like treatment of the flow at the boundaries of the coupling zone, (2) the coupling matrices of the Arlequin framework and (3) the weight functions. They are considered in the next sections.

Example 2.3.1. *Let us consider an Arlequin approach for the multi-model convective transport as introduced in section 2.2.2. Let us assume that the flow is a linear function of the convected quantity q so we can write the problem as in (2.18). By definition, the critical time step of the Arlequin multi-model problem is defined by*

$$\Delta t_c^{Arlequin} = \frac{1}{\max \omega} \tag{2.27}$$

where ω are the eigenvalues of the generalized eigenvalue problem of $\underline{\underline{K}}^*$ and $\underline{\underline{D}}$. In order for the problem to be computationally feasible, the critical time step $\Delta t_c^{Arlequin}$ can not be too small. We recall that $\underline{\underline{K}}^* = (\underline{\underline{I}} - (\underline{\underline{C}}\underline{\underline{D}}^{-1}\underline{\underline{C}}^T)^{-1}\underline{\underline{C}}\underline{\underline{D}}^{-1})\underline{\underline{K}}$ and that both $\underline{\underline{D}}$ and $\underline{\underline{K}}$ are functions of the weight functions α^q. We can thus observe that both the coupling matrices $\underline{\underline{C}}$ and the weight functions can influence the critical time step.

Remark 2.3.1. *In practice, the elementary time step is computed as follows:*

$$\Delta t = \text{csta} \times \min_{E \in \mathcal{S}_E} \frac{L_E}{|v_E|} \tag{2.28}$$

where L_E is a characteristic length of the element E, $|v_E|$ a norm of the velocity in that element and csta *a positive coefficient lower or equal to 1. In this work we refer to* csta *as the security coefficient.*

2.3.2 Influence of the coupling matrices on the critical time step

We showed, in section 1.2, that for the case of elastodynamics, the dual management of additional kinematic constraints through Lagrange Multipliers does not adversely affect the stability of the explicit time integration scheme. The same results would hold for convective transport equation for which the convective term exhibits a linear dependency from the convective quantity, as is the case in (2.18). An example of such linear dependency is the conservation of mass equation taken alone.

The extension of this result to the general case can be obtained by considering the physical interpretation of the practical stability condition given in (2.3.2), commonly known as the Courant-Friedrich-Levy (CFL) condition for the explicit time integration of propagative systems. In fact, the CFL condition associates the integration stability to the way the scheme propagates information. Indeed, it states that there are no unstable accumulation of truncation error as long as the convected information does not cross more than one element within one single time step.

We can apply the same physical interpretation logic to the management of kinematic constraints and conclude that they do not adversely affect the stability in the general case. Indeed, introducing additional unknowns computed at each time step with no prediction through the time integration scheme do not produce extra accumulation of truncation error. Therefore, the dual management of such constraints through Lagrange multipliers is always safe regarding the integration stability and can be excluded from the dedicated analyses led in this work.

Remark 2.3.2. *The dual management of kinematic constraints can also be seen as an implicit way to evaluate the reaction forces associated to the constraints, which leads*

to the unconditional stability conclusions expressed above for this particular feature. This treatment of the kinematic constraints can be directly opposed to the primary management of constraints, through penalty coefficients for instance, where the reaction forces conserve their explicit nature and are known to have a significant influence on the global integration stability [175].

2.3.3 Influence of Chimera-like boundary conditions

The treatment of Chimera-like boundaries has been of considerable interest, especially for finite differences discretizations [144] [176]. Hereafter, we recall the following guidelines found in literature in order to ensure stability [150].

- The size of the overlapping zone should be greater than the stencil,
- In the overlapping zone, the size of elements of both domains should be similar,
- The interpolation order for the transfer of information between domains should be greater or equal to the order of the numerical scheme.

In this work, we assume that as long as these guidelines are respected, the stability of the Chimera approach is guaranteed.

2.3.4 Influence of the weight functions on the stability

The weight functions have shown to affect the critical time step[10] and their influence on the stability needs to be studied. As seen previously (see section 1.3), the eigenvalues of the generalized eigenvalue problem are, in practice, not computed. Instead, eigenvalues for the generalized eigenvalue problem of every element are computed and their maximum is generally used in definition (2.26). From **Proposition** 1.32, we can deduce that substituting $\max_{E\in\mathcal{S}_E}\omega_E$ for ω_G in (2.26) is conservative. Such a critical time step is hereafter referred to as the elementary critical time step. Hence, if we can ensure that the weight functions do not cause the elementary critical time step to significantly drop, then the formulation is bound to be stable.

2.3.4.1 Study of the influence of the weight functions on a single element

Let E be an element and q_0 an eigenvector of the elementary generalized eigenvalue problem, that is, we assume that $\exists\ \omega$ such that (see (2.17)):

$$\left(\sum_{e\in E}\int_e \alpha^q\phi_q^n\underline{v}\cdot\underline{n}\ de\right)q_0 = \omega\left(\int_{\Omega_E}\hat{\alpha}^q\ d\Omega_E\right)q_0 \tag{2.29}$$

which immediately yields[11]

$$\omega = \frac{\displaystyle\sum_{e\in E}\int_e \alpha^q\phi_q^n\ \underline{v}\cdot\underline{n}\ de}{\displaystyle\int_{\Omega_E}\hat{\alpha}^q\ d\Omega_E} \tag{2.30}$$

[10] See section 1.3 or [152].

[11] $q_0 \neq 0$ as it is an eigenvector.

Note that the eigenvalue for a mono-model formulation element is obtained by imposing $\hat{\alpha}^q = \alpha^q = 1$ in (2.30), that is:

$$\omega_{mono} = \frac{1}{|\Omega_E|} \sum_{e \in E} \int_e \phi_q^n \ \underline{v} \cdot \underline{n} \ de \tag{2.31}$$

One way to ensure that the critical time step does not drop is to guarantee that $\omega = \omega_{mono}$. As only the value of α^q has already been set in expression (2.30), conditions can be imposed on $\hat{\alpha}^q$. Thus, we first propose to impose $\hat{\alpha}^q$ to be set to:

$$\frac{\sum_{e \in E} \int_e \alpha^q \phi_q^n \ \underline{v} \cdot \underline{n} \ de}{\sum_{e \in E} \int_e \phi_q^n \ \underline{v} \cdot \underline{n} \ de} \tag{2.32}$$

This definition (2.32) of $\hat{\alpha}^q$ ensures that the critical time step is optimal. However, it is dependent of time as it is a function of the flow $\phi_q^n \underline{v}$ and thus needs to be computed at every time step, which is computationally costly. Moreover, as the term $\phi_q^n \underline{v} \cdot \underline{n}$ can be negative, this definition does not ensure positivity for $\hat{\alpha}_q$ nor does it ensure a partition of unity for the set $(\hat{\alpha}_1^q, \hat{\alpha}_2^q)$ and is thus not satisfactory (see section 1.7). Instead, we choose to impose a uniform $\hat{\alpha}^q$ on the element, whose value is set to:

$$\tilde{\alpha}^q = \frac{1}{|\partial\Omega_E|} \sum_{e \in E} \int_e \alpha^q \ de \tag{2.33}$$

where $|\partial\Omega_E|$ is the size of the boundary of element E. Imposing $\hat{\alpha}^q = \tilde{\alpha}^q$ ensures both the positivity and the partition of unity of the weight functions (see section 1.1.2), in the sense that if an element of the substrate, denoted E_s, perfectly overlaps one of the patch, denoted E_p, then we clearly have $\hat{\alpha}^q(E_s) + \hat{\alpha}^q(E_p) = 1$.

It is interesting to note that with this definition, the value of $\hat{\alpha}_q$ is determined by the value of α^q on the border of the element only. In the next section, we compare that definition with a more natural one, that is, a volume integration of α^q.

2.3.4.2 Analysis of $\hat{\alpha}^q$ for specific elements

In this section we compare $\tilde{\alpha}^q$ proposed in (2.33) with $\bar{\alpha}^q$, the value resulting from the numerical integration of α^q on the entire element:

$$\bar{\alpha}^q = \frac{1}{|\Omega_E|} \int_{\Omega_E} \alpha^q \ d\Omega_E \tag{2.34}$$

The goal is to underline why using $\tilde{\alpha}^q$ to define $\hat{\alpha}^q$ is preferable. We recall that the critical time step is proportional to the value of the weight function associated to $\dot{q}$ (either $\tilde{\alpha}^q$ or $\bar{\alpha}^q$) so that the higher its value is, the more stable the approach is.

1D element

Let us consider a one dimensional element of size L connecting two nodes 1 and 2 and a piecewise linear weight function α^q such that $\alpha^q(1) = \alpha_{1,1}$ and $\alpha^q(2) = \alpha_{1,2}$ and $\alpha_{1,1} > \alpha_{1,2}$. We then consider three possible cases for the evolution of the weight function α^q inside an element[12]. They are introduced hereafter and represented in Figure 2.3.

Case A: The weight function is linear all throughout the element.

Case B: The weight function is constant on $[0, \delta L]$ and then linear on $[\delta L, L]$.

Case C: The weight function is linear on $[0, \delta L]$ and then constant on $[\delta L, L]$.

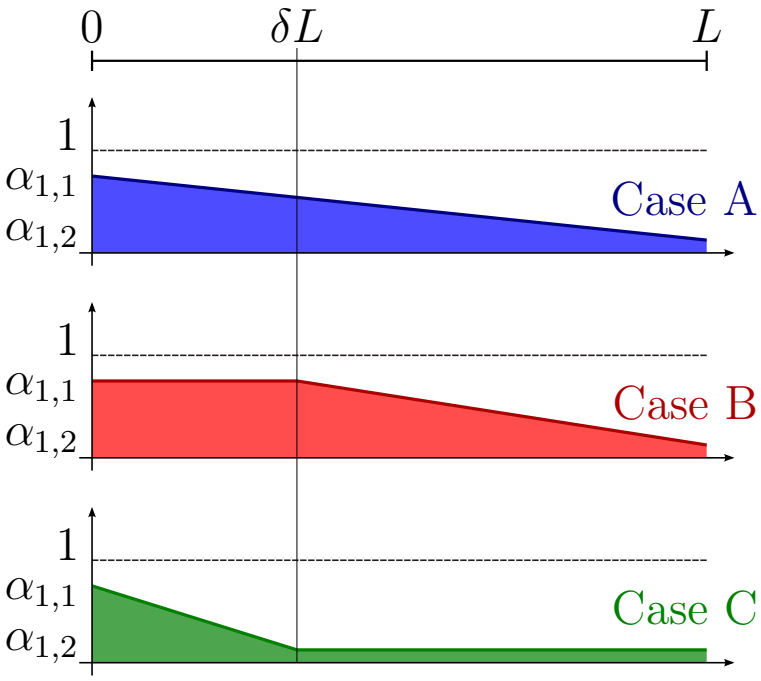

Figure 2.3: The three different 1D cases for elements whose weight function changes. The value of $\bar{\alpha}^q$ depends on the behaviour of the weight function inside the element and is equal to the area below the weight function. The value of $\tilde{\alpha}^q$ is independent of the behaviour of the weight function inside the element and is equal to the area in blue for all three cases.

For all three cases, the value of $\tilde{\alpha}^q$ is the same and equal to $\frac{1}{2}(\alpha_{1,1} + \alpha_{1,2})$. The value of $\bar{\alpha}^q$, on the other hand, differs. We have:

$$\begin{cases} \text{Case A:} & \bar{\alpha}^q_A = \frac{1}{2}(\alpha_{1,1} + \alpha_{1,2}) & \text{so that } \bar{\alpha}^q_A = \tilde{\alpha}^q \\ \text{Case B:} & \bar{\alpha}^q_B = \frac{1}{2}(\alpha_{1,1}(1+\delta)L + \alpha_{1,2}(1-\delta)L) & \text{so that } \bar{\alpha}^q_B > \tilde{\alpha}^q \\ \text{Case C:} & \bar{\alpha}^q_C = \frac{1}{2}(\alpha_{1,1}(1-\delta)L + \alpha_{1,2}(1+\delta)L) & \text{so that } \bar{\alpha}^q_B < \tilde{\alpha}^q \end{cases} \tag{2.35}$$

We can see that definition (2.34) is very dependent on the geometrical configuration and although it sometimes leads to a higher critical time step than definition (2.33)

[12]Elements on which α^q is uniform yields trivial results.

(Case B), it can also lead to a critical time step almost equal to 0 (Case C with a small value of δ). Thus, using $\tilde{\alpha}^q$ is more more preferable than using $\bar{\alpha}^q$. This can easily be explained by the fact that using $\tilde{\alpha}^q$ is equivalent to imposing a linear weight α^q on the entire element. Note that, as a consequence, when using $\tilde{\alpha}^q$, the partition of unity is, in a way, locally breached, as can be seen in Figure 2.4.

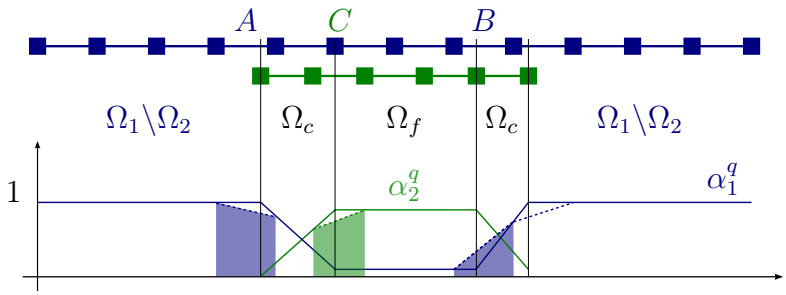

Figure 2.4: Weight functions (α_1^q, α_2^q) for two overlapping 1D models (in solid line). Using $\tilde{\alpha}^q$ is equivalent to using the dashed lines for the weight functions, which clearly breaches the local partition of unity (see elements A, B and C). If $\bar{\alpha}^q$ is used, the elementary critical time step is proportional to the area below the weight function. Thus if the boundaries of the coupling zone are adequate (left coupling zone), then $\bar{\alpha}^q > \tilde{\alpha}^q$ (the area corresponding to $\tilde{\alpha}^q$ is represented in solid for elements A, B and C). If the boundaries of the coupling zone are not adequate (right coupling zone), then $\bar{\alpha}^q < \tilde{\alpha}^q$ as can be observed for element B.

Yet, if we can ensure that there are no elements in which the behaviour of α^q corresponds to Case C, then using $\bar{\alpha}^q$ is preferable. In the following, we show how that can be achieved.

First of all, notice that for elements whose weight function is entirely uniform or linear (Case A), $\tilde{\alpha}^q = \bar{\alpha}^q$ so that neither expression is more advantageous. Thus, it is only on elements whose weight function α^q is partly uniform and partly linear that the two expressions are worth being compared. These elements are the ones cut by the boundaries of the coupling zone. For clarity, we assume that an element can not be cut by the two boundaries simultaneously, and are thus restricted to the three cases previously introduced. Hereafter, we denote by Γ_{out} the outer boundary ($\Gamma_{1\to2}$ in the Chimera framework) and by Γ_{in} the inner one ($\Gamma_{2\to1}$ in the Chimera framework).

On the one hand, Γ_{out} is naturally aligned with $\partial\Omega_2$, that is, with the mesh of the patch. Thus, for elements of the patch whose edge is aligned with Γ_{out}, α^q is linear. These elements correspond to the "Case A" configuration previously mentioned. As the meshes of the substrate and the patch are not conforming, Γ_{out} is bound to cut elements of the substrate. Hence, the part of the element in the coupling zone is linear while the one in $\Omega_1 \setminus \Omega_c$ is equal to 1 so that these elements are representative of "Case B" configurations. For these elements, using $\bar{\alpha}^q$ instead of $\tilde{\alpha}^q$ yields a higher critical time step.

On the other one hand, there are no natural choice for which mesh Γ_{in} should be aligned with, if any. First, we assume that Γ_{in} is aligned with the mesh of the patch. Elements of the patch on either side of the boundary have either a uniform weight or a

linear one so that for these elements $\tilde{\alpha}^q = \bar{\alpha}^q$ and neither choice is detrimental. As in the previous paragraph, elements of the substrate are bound to be cut by Γ_{in}, except that this time part of the element in the coupling zone is linear while the one in Ω_f is equal to α_0. These elements are thus in the "Case C" configuration which is detrimental to the stability. Thus, Γ_{in} should not be aligned with the mesh of the patch if $\bar{\alpha}^q$ is to be used.

Let us now assume that Γ_{in} is aligned with the mesh of the substrate. Elements of the substrate on either side of the boundary have either a uniform weight or a linear one so that for these elements $\tilde{\alpha}^q = \bar{\alpha}^q$ and neither choice is detrimental. This time however, it is elements of the patch that are bound to be cut by Γ_{in}. For these elements, part of the element in the coupling zone is linear while the one in Ω_f is equal to $1-\alpha_0$. These elements are thus in the "Case B" configuration which is advantageous with regards to stability. Thus, Γ_{in} should be aligned with the mesh of the substrate if $\bar{\alpha}^q$ is to be used.

Note that if the user decides to align Γ_{out} with the mesh of the substrate, similar stability issues as when Γ_{in} is aligned with the mesh of the patch will arise.

In conclusion, for the 1D element considered, using $\bar{\alpha}^q$ rather than $\tilde{\alpha}^q$ yields a higher critical time step as long as the boundaries of the coupling zone are aligned with the appropriate mesh.

Remark 2.3.3. *The above analysis reaches similar conclusions as those obtained for structural dynamics (see section 1.3). Indeed, using $\tilde{\alpha}^q$ is an analogue of the Averaged weights approach as an optimal critical time step is obtained no matter where the boundaries of the coupling zone are but at the cost of a local breach of the partition of unity. Similarly, using $\bar{\alpha}^q$ is an analogue of the q_α-control approach as it respects the partition of unity but only maintains an optimal critical time step if Γ_{out} is aligned with the mesh of the patch and Γ_{in} with that of the substrate.*

2D and 3D elements

The aim of this section is to show that what was true for 1D elements, that is, that there is a way for the user to use $\bar{\alpha}^q$ rather than $\tilde{\alpha}^q$ to define $\hat{\alpha}^q$, does not hold for 2D/3D elements. The previous statement is hereafter illustrated on a triangular element.

We thus consider a triangular element cut by the boundary of the coupling zone so that the element is in one of the three cases A, B or C represented in Figure 2.5. We make the assumption that the weight parameter α^q is piecewise planar. Although unrealistic, this assumption will prove useful as it simplifies calculations.

Under the previous assumption and for the elements of Figure 2.5, we have $\bar{\alpha}^q = \tilde{\alpha}^q$ in all three cases. It then seems that using $\bar{\alpha}^q$ rather than $\tilde{\alpha}^q$ is not detrimental. However, this is due to the fact that we only considered cases for which the element is cut by a straight line. Let us consider the elements presented in Figure 2.6 and 2.7. Moreover, we assume that α^q is piecewise planar and that α^q is the same along the edges for Cases B.A, B.B and B.C and Cases C.A, C.B and C.C. We thus have $\tilde{\alpha}^q_{B.A} = \tilde{\alpha}^q_{B.B} = \tilde{\alpha}^q_{B.C} = \tilde{\alpha}^q_B$ and $\tilde{\alpha}^q_{C.A} = \tilde{\alpha}^q_{C.B} = \tilde{\alpha}^q_{C.C} = \tilde{\alpha}^q_C$ respectively.

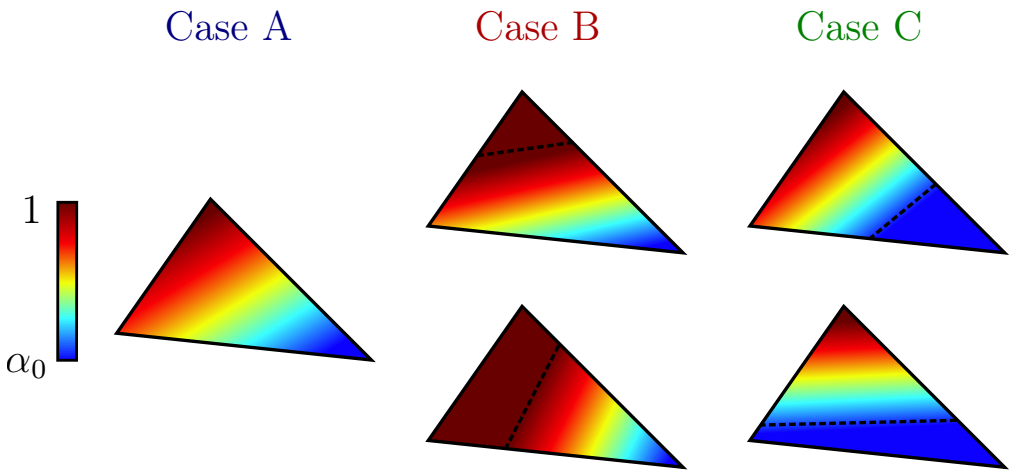

Figure 2.5: Example of weight functions α^q for a 2D triangular element. For cases B and C, the area where the weight function is uniform and the one where it is planar are separated by a dashed line.

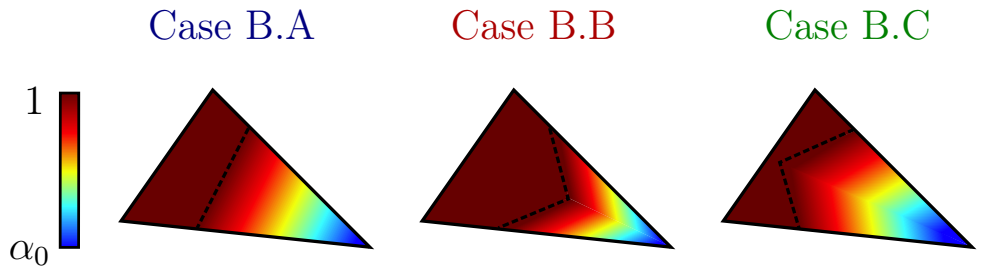

Figure 2.6: Examples of a weight function α^q for 2D triangular elements in the configuration of the bottom case B of Figure 2.5. The value of α^q is allegedly the same along the edge for all three cases.

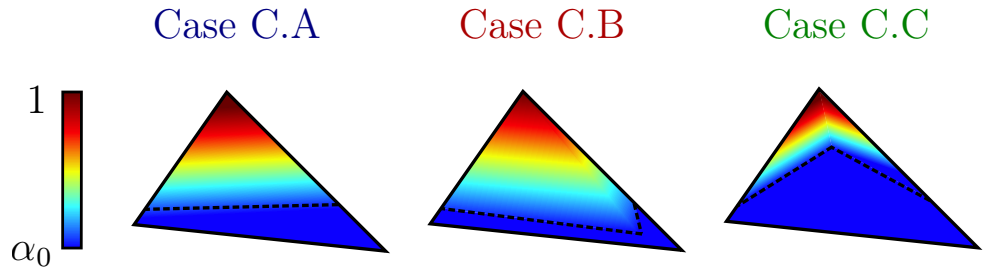

Figure 2.7: Examples of a weight function α^q for 2D triangular elements in the configuration of the bottom case C of Figure 2.5. The value of α^q is allegedly the same along the edge for all three cases.

We then have:

$$\left\{\begin{array}{ll} \text{Case B.A:} & \bar{\alpha}^q_{B.A} = \tilde{\alpha}^q_B \\ \text{Case B.B:} & \bar{\alpha}^q_{B.B} > \tilde{\alpha}^q_B \\ \text{Case B.C:} & \bar{\alpha}^q_{B.C} < \tilde{\alpha}^q_B \end{array}\right. \text{and} \left\{\begin{array}{ll} \text{Case C.A:} & \bar{\alpha}^q_{C.A} = \tilde{\alpha}^q_C \\ \text{Case C.B:} & \bar{\alpha}^q_{C.B} > \tilde{\alpha}^q_C \\ \text{Case C.C:} & \bar{\alpha}^q_{C.C} < \tilde{\alpha}^q_C \end{array}\right. \tag{2.36}$$

First, let us recall that in both Case B and Case configurations, the value of of $\tilde{\alpha}^q$

is independent of the inner evolution of α^q and, a priori, does not approach zero. Let us now analyse whether definition $\bar{\alpha}^q$ can be more feasible than $\tilde{\alpha}^q$.

The analysis of Case C configurations shows that $\bar{\alpha}^q$ can not be ensured to be higher than $\tilde{\alpha}^q$. In fact, the Case C.C configuration shows that $\bar{\alpha}^q$ can tend to 0. The reasoning done for 1D elements would suggest that aligning the inner boundary Γ_{in} with the mesh of the substrate would prevent Case C configurations from happening and ensure a feasible time step when using $\bar{\alpha}^q$. However, doing so is not sufficient. Indeed, Case B configurations can still occur and, in particular, any element in a Case B.C configuration would lead to a lower value of $\bar{\alpha}^q$ when compared to $\tilde{\alpha}^q$. Nevertheless, it is important to note that although we have $\bar{\alpha}^q_{B.C} < \tilde{\alpha}^q_{B.C}$ for such elements, $\bar{\alpha}^q_{B.C}$ can not drop to a near null value for these elements. In fact, we can easily show that $\bar{\alpha}^q_{B.C} > \tilde{\alpha}^q_A$.

Note that this is also true for $\tilde{\alpha}^q$. Indeed, we clearly have $\tilde{\alpha}^q_B > \tilde{\alpha}^q_A > \tilde{\alpha}^q_C$ so that aligning Γ_{in} with the mesh of the substrate would ensure that any element for which the weight is not uniform has a weight parameter $\hat{\alpha}^q$ greater or equal to $\tilde{\alpha}_A$.

Thus, although these calculations assume that the weight functions are piecewise planar, we recommend systematically aligning Γ_{in} with the mesh of the substrate. The previous observations are illustrated in the following representative example.

Example 2.3.2. *We consider the overlapping two unstructured meshes represented in Figure 2.8. The outer boundary (in red) of the coupling zone is aligned with the mesh of the patch (in red) while the inner one (in blue) is aligned with the mesh of the substrate (in black). The geometry and meshes are such that elements of the patch are randomly cut by the inner boundary of the coupling zone. In Figure 2.8, the weight function is represented for two such elements.*

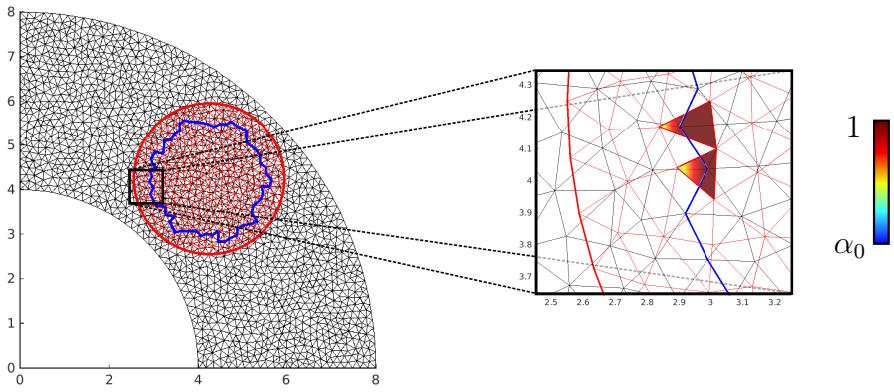

Figure 2.8: Two unstructured meshes are overlapped. In order to ensure stability, the boundaries of the coupling zone are such that Γ_{out} (in red) is aligned with the mesh of the patch (in red) while Γ_{in} (in blue) is aligned with the mesh of the substrate (in black). The inner boundary Γ_{in} thus randomly cuts elements of the patch. The weight function for two elements is also represented.

The top element considered is cut in a "Case B.B" configuration (see Figure 2.6) so that using $\bar{\alpha}^q$ rather than $\tilde{\alpha}^q$ leads to a higher critical time step. The lower element however, is cut in a "Case B.C" configuration (see Figure 2.6) so that using $\bar{\alpha}^q$ rather than $\tilde{\alpha}^q$ leads to a lower critical time step which can drop to a near null value. On the

other hand, using $\tilde{\alpha}^q$ ensures that the time step is not dependent of the behaviour inside the element. Thus, regardless of how the boundaries of the coupling zone are placed, the user should always use formula (2.33) to define the weight function associated to the time derivative of q.

Partial conclusion

We compared the proposed definition (2.33) for $\hat{\alpha}^q$ with a volume integration. We observed that for one dimensional elements, a volume integration can lead to a more stable problem as long as the boundaries of the coupling zone are adequately defined. However, for 2 and 3 dimensional elements, expression (2.33) should always be used as, although it does not guarantee an optimal time step[13], it is the only one to guarantee a computationally feasible time step critical time step, in the sense that it can not drop to zero.

2.4 Study of the accuracy of multi-model approaches

In this section, we consider the transport of a quantity q such that $\phi_q = q$, that is,

$$\forall \bar{w} \in \mathcal{V},\ \int_\Omega \frac{\partial q}{\partial t}\bar{w}\ d\Omega + \int_\Omega \mathrm{div}(q\underline{v})\bar{w}\ d\Omega = 0 \tag{2.37}$$

An example of physical phenomenon described by equation (2.37) is the conservation of mass, for which $q = \rho$.

2.4.1 Local introduction of a fixed cylinder

2.4.1.1 Presentation

We consider a closed square domain with a rigid, fixed, cylinder as shown in Figure 2.9. The domain is 100m long while the cylinder has a 4m wide diameter. The velocity is assumed to be independent of time and was chosen such that it is divergence free (see Figure 2.9). As can be seen in the figure, quantity q has a slip condition on the center cylinder as well as on the top and bottom side. On the left side, an inward boundary condition $q_L v$ is imposed while quantity q flows outward on the right side.

In one region (in blue in Figure 2.9), the initial value of quantity q is $q_R = 1$. In the second region, left of the cylinder (in brown in Figure 2.9), the value of quantity q is $q_L = 10$.

The reference solution is computed on a mono-model mesh and is represented in Figure 2.11. Away from the cylinder, the mesh is made of 2m $\times$ 2m square quadrangles. The quadrangles progressively diminish in size towards the cylinder so that the cylinder is discretized by 40 edges. The multi-model meshes are represented in Figure 2.10. The main domain, referred to as the substrate and in black in the figure, is uniformly composed of the same 2m $\times$ 2m square quadrangles. The local domain, referred to as the patch and in red in the figure, models the cylinder. Its mesh is in the shape of

[13]Expression (2.33) is an approximation of the optimal value given by (2.32).

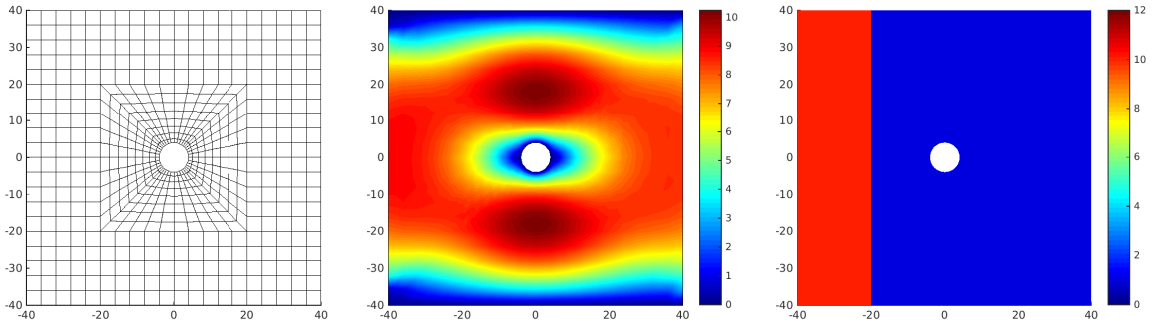

Figure 2.9: Mono-model mesh (left), the initial norm of the velocity in m.s^{-1}(center) and initial condition q^0 (right).

a web, which is adapted to circles, and is designed so that the cylinder has a similar discretization as in the mono-model mesh (see Figure 2.10). On the farthest ring of the mesh, the elements are about the same size as those of the substrate. The weight functions are also represented in Figure 2.10.

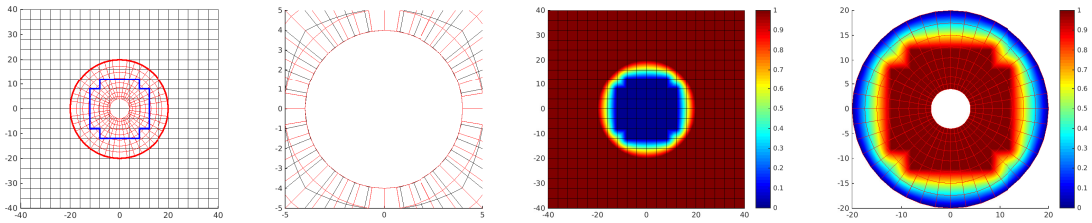

Figure 2.10: From left to right: the multi-model meshes as well as the boundaries of the coupling zone (in red and blue) are represented. – The meshes of the mono-model and the patch are compared near the hole. – The value of α^q is represented for the substrate and the patch.

For all these computations, we imposed csta $= 0.9$ and, when relevant, $\hat{\alpha}^q = \tilde{\alpha}^q$ and $\alpha^q = 1.0 \times 10^{-6}$ in the free zone. For the Arlequin computations and unless specified differently, the Mediator space is discretized as the patch.

2.4.1.2 Solution

The solution for q are represented in Figures 2.13, 2.12 and 2.14 for the Arlequin approach[14], the Chimera one and the Chimix approach respectively. As the vector field for the velocity is divergence free and given the initial conditions, the solution should evolve towards a stationary state with $q = 10$ everywhere. Such a behaviour can be observed on the reference solution represented in Figure 2.11.

Two observations can be made for the multi-model approaches. First, the Chimera and the Arlequin approaches yield accurate solution while instabilities can be observed for the the Chimix approach. In fact, the value of q reaches 30 in parts of the domain

[14]For the solution presented hereafter, the mediator space was discretized as the patch.

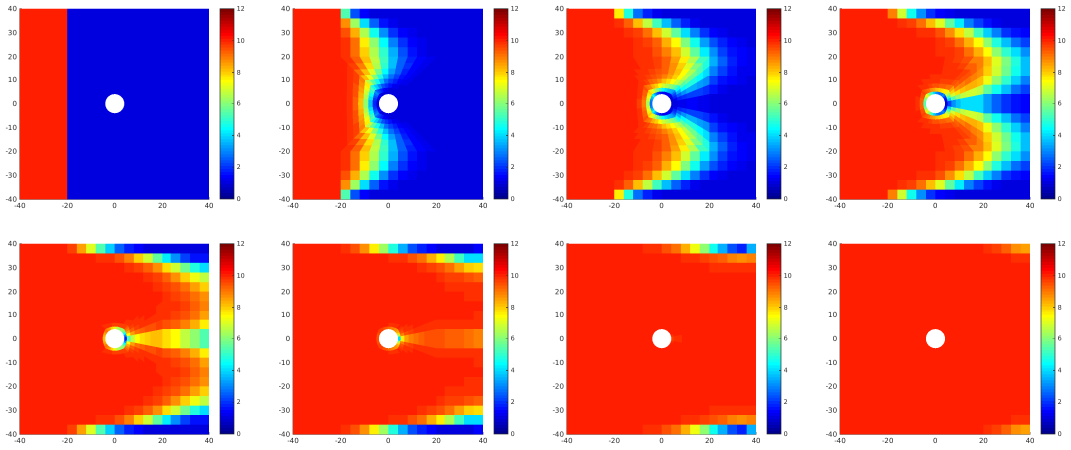

Figure 2.11: Mono-model solution for quantity q at, from left to right and top to bottom, instant $t_0 = 0$s, $t_1 = 2$s, $t_2 = 4$s, $t_3 = 6$s, $t_4 = 8$s, $t_5 = 10$s, $t_6 = 12.5$s and $t_7 = 25$s.

while it should, theoretically, never be greater than 10. Secondly, we observe that in all multi-model approaches, the quantity q slowly accumulates around the hole. This can not be blamed on the different multi-modelling framework has they appear in the free zone Ω_f. In fact, this accumulation of q is due to the fact that the velocity is not perfectly divergence free in that area[15].

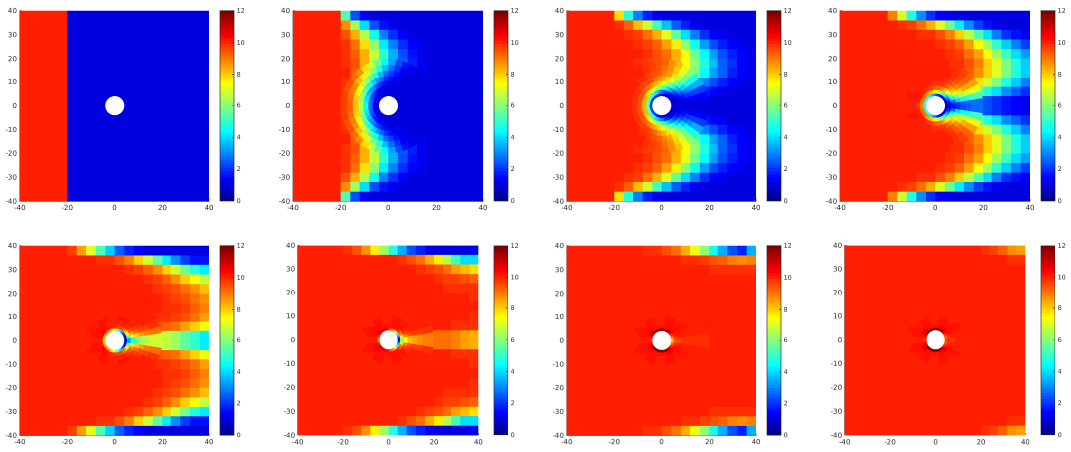

Figure 2.12: Chimera solution for quantity q at, from left to right and top to bottom, instant $t_0 = 0$s, $t_1 = 2$s, $t_2 = 4$s, $t_3 = 6$s, $t_4 = 9$s, $t_5 = 12.5$s, $t_6 = 25$s and $t_7 = 50$s.

2.4.1.3 Error measures of the solution

In order to quantify the gap between the multi-model approaches and the reference solution, we choose to compare the solution downstream so as to measure the influence of the multi-model approaches on the accuracy. We thus consider the following error

[15]the divergence free velocity field is obtained numerically on the mono-model mesh.

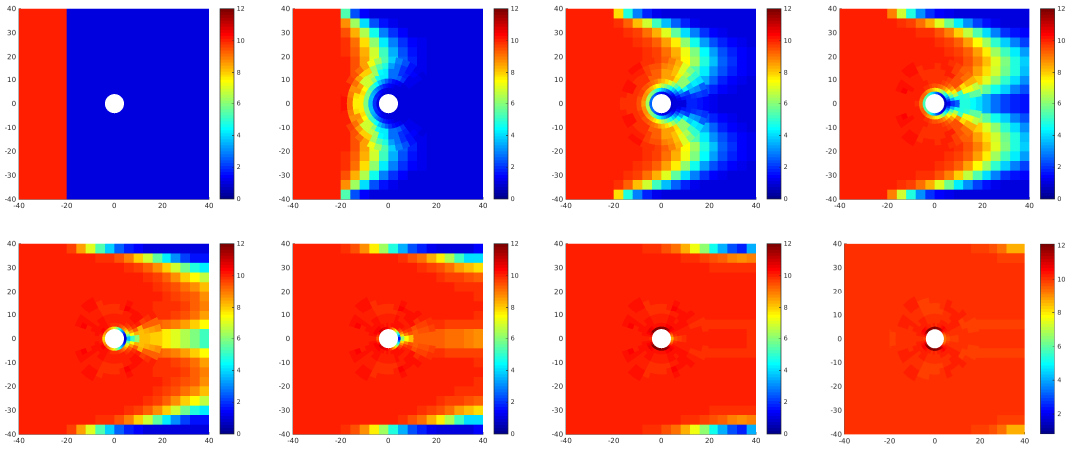

Figure 2.13: Arlequin solution for quantity q at, from left to right and top to bottom, instant $t_0 = 0$s, $t_1 = 2$s, $t_2 = 4$s, $t_3 = 6$s, $t_4 = 9$s, $t_5 = 12.5$s, $t_6 = 25$s and $t_7 = 50$s. The Mediator space is discretized on the patch.

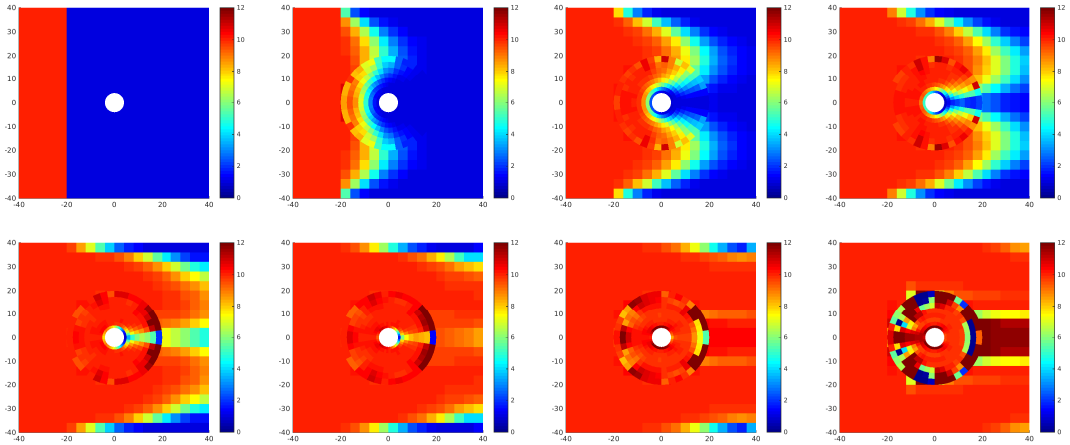

Figure 2.14: Chimix solution for quantity q at, from left to right and top to bottom, instant $t_0 = 0$s, $t_1 = 2$s, $t_2 = 4$s, $t_3 = 6$s, $t_4 = 9$s, $t_5 = 12.5$s, $t_6 = 25$s and $t_7 = 50$s.

measure on elements such that $x = 34$m (second to last column of elements).

$$Err(x,t) = \frac{q_m(x,t) - q_r(x,t)}{\max_\tau q_r(\tau,x)} \tag{2.38}$$

where q_m refers to the solution of a multi-model approach while q_r refers to the reference solution. The error measure over time is represented in Figure 2.15.

We can see that, as observed previously, the Chimix approach diverges behind the hole[16]. The Arlequin and the Chimera approaches, however, are stable and converge towards the steady solution. Yet, the Arlequin approach seems to yield a better solution on two points:

- the maximum error over time is smaller than that of the Chimera approach;

[16]Note that simulations were run with lower csta values (down to 0.05) and they all diverged.

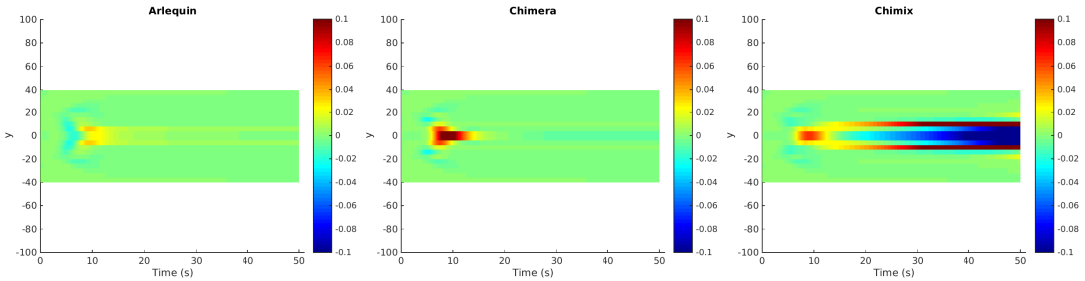

Figure 2.15: Error measure Err for the Arlequin approach (left), the Chimera approach (center) and the Chimix approach (right).

- the steady solution seems to be closer to the reference solution.

In order to quantify those observations, we introduce the following error measure:

$$E(t) = \int_{x=34\text{m}} |Err(x,t)| \, dx \tag{2.39}$$

where Err is defined in expression (2.38). The results are represented in Figure 2.16.

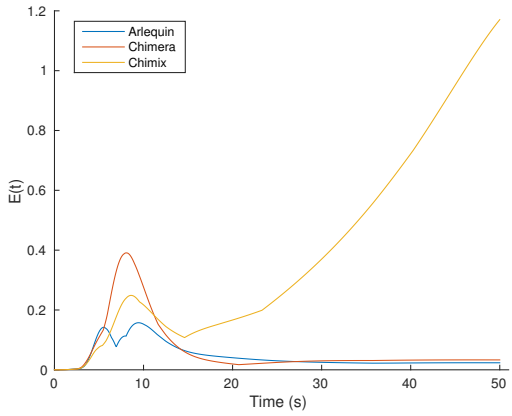

Figure 2.16: Error measure E for the Arlequin approach (in blue), the Chimera approach (in red) as well as the Chimix one (in yellow).

We can see that the observations made are confirmed.

2.4.1.4 Influence of the mediator space on accuracy

When considering the Arlequin formulation, there are two natural choices for the discretization of the mediator: the discrete space of the substrate (restricted to the coupling zone) or the discrete space of the patch (restricted to the coupling zone). If the former is chosen, we will say that the mediator space is discretized as the substrate and if the latter is chosen that it is discretized as the patch.

In Figure 2.13, the mediator space is discretized as the patch. The solution for a mediator space discretized as the substrate is represented in Figure 2.17.

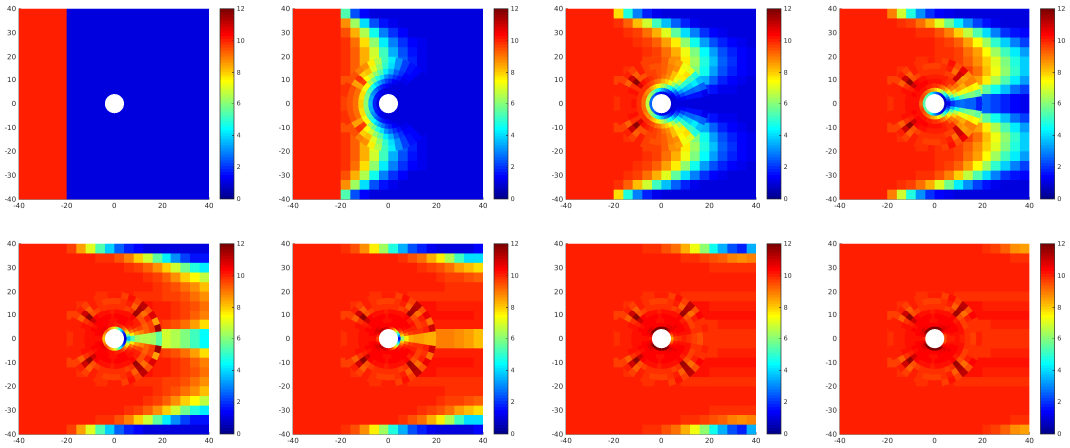

Figure 2.17: Arlequin solution for quantity q at, from left to right and top to bottom, instant $t_0 = 0$s, $t_1 = 2$s, $t_2 = 4$s, $t_3 = 6$s, $t_4 = 9$s, $t_5 = 12.5$s, $t_6 = 25$s and $t_7 = 50$s. The mediator space is discretized on the substrate.

We can observe that, if the mediator space is discretized as the substrate, variations appear in the coupling zone. These variations are due to both the discretization of q, considered uniform on an element, and the difference in size of the elements in the coupling zone (the mesh of the substrate is slightly coarser than that of the patch). Let us consider two elements of the patch in the coupling zone, namely E_1^p and E_2^p, that overlap a single element of the substrate E^s (also in the coupling zone). If the mediator space is discretized on the patch then the element of the coupling imposes that all three elements should have the same q. Indeed, we have, at each instant $n > 0$,

$$\left\{ \begin{array}{rcl} q^n(E_1^p) & = & q^n(E^s) \\ q^n(E_2^p) & = & q^n(E^s) \end{array} \right. \Leftrightarrow q^n(E_1^p) = q^n(E_2^p) = q^n(E^s). \tag{2.40}$$

If the mediator space is discretized on the substrate, then the coupling imposes that the average of the value of q on the elements of the patch has to be equal to the value of q from the substrate, that is,

$$q^n(E^s) = q^n(E_1^p) + q^n(E_2^p) \tag{2.41}$$

which is less constrained than (2.40) and can lead to variations. In general, choosing the coarser discretization for the mediator space leads to perturbations. Nonetheless, choosing the finer mesh can also lead to significant perturbations (see for instance [98]).

In order to quantify if those variations have an influence on the solution somewhere other than the coupling zone, we consider the two error measures (2.38) and (2.39). They are represented in Figure 2.18.

We can see that discretizing the mediator space as the substrate leads to a higher error measure than when it is discretized as the patch. Moreover, discretizing the mediator space as the substrate leads to a steady solution downstream with a higher error than any other approach.

In the current test case, discretizing the mediator space on the finer mesh leads to a more precise solution.

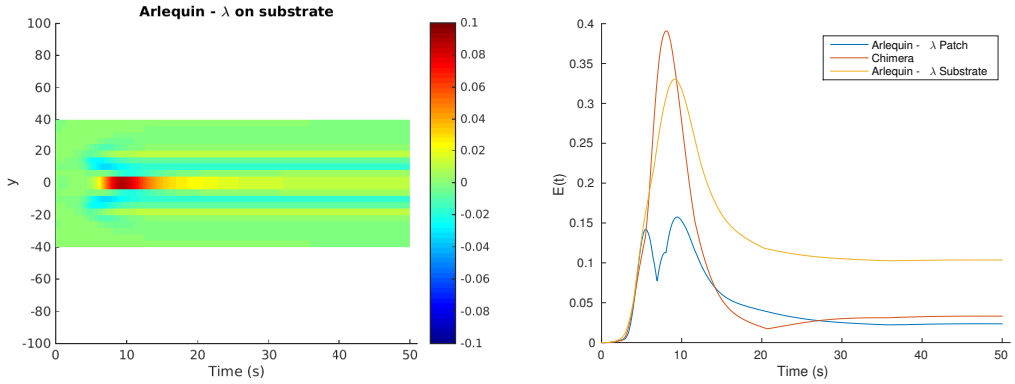

Figure 2.18: Error measure Err for the Arlequin approach with a mediator space discretized as the substrate (left) as well as E for different approaches.

2.4.2 Local change of the advection velocity

In this next example, we locally change the convective velocity in the patch and study the convergence of each multi-model approach.

2.4.2.1 Presentation

We consider the one dimensional domain $32m$ long represented in Figure 2.19. The initial conditions for q as well as the convective velocity are also represented in Figure 2.19. The velocity is uniform in two different zones and presents a slowdown zone and a speed up zone of equal size (2m). Quantity q is free to flow outward on the right boundary and the boundary condition $q = 0$ is imposed on the left boundary. The simulation lasts for 50s, the time necessary for all of quantity q to flow out of the domain.

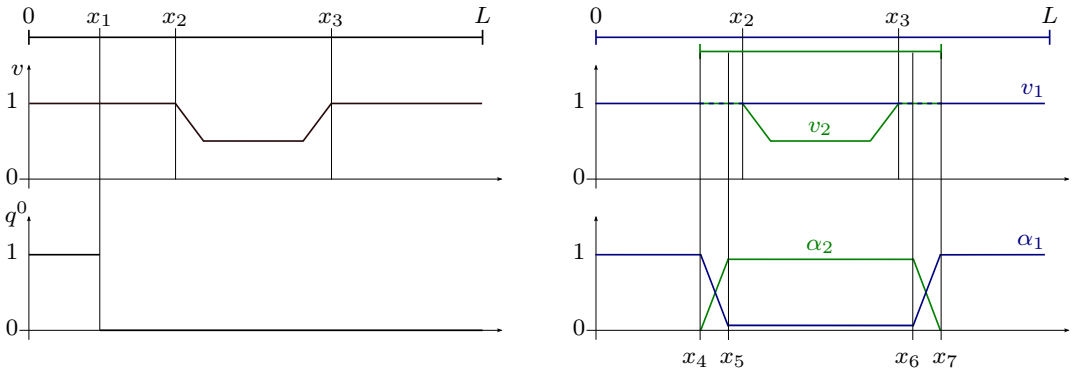

Figure 2.19: Mono-model problem (left) and multi-model problem (right). The velocity v, v_1 and v_2 are represented and we can see that the change in velocity is introduced by the patch. The initial condition q^0 is also represented. Note that we have $x_1 = 5$m, $x_2 = 10.33$m, $x_3 = 21.33$ and $L = 32$m while the slowdown and the speed-up zones are both 2m long. Moreover, $x_4 = 7.33$m and $x_7 = 24.33m$ while $x_5 \in]x_4, x_2[$ and $x_6 \in]x_3, x_7[$ determine the inner boundary of the coupling zone.

The reference solution is shown in Figure 2.20 at different instants. At first, the quantity q moves at constant speed towards the left side of the domain (top left in the figure). Then, the front reaches the slowdown zone and thus starts to accumulate (top right in the figure) and eventually forms a new rectangle, twice as high and half as wide, moving at reduced speed (middle left in the figure). Next, the front reaches the speed-up zone and spreads (middle right in the figure) until it forms its original shape (bottom left in the figure). Finally, it flows out of the domain until nothing is left (bottom right in the figure).

The reference solution was numerically obtained on a mono-model problem made up of $12,288$ elements of same size. The time step was computed with csta $= 1$.

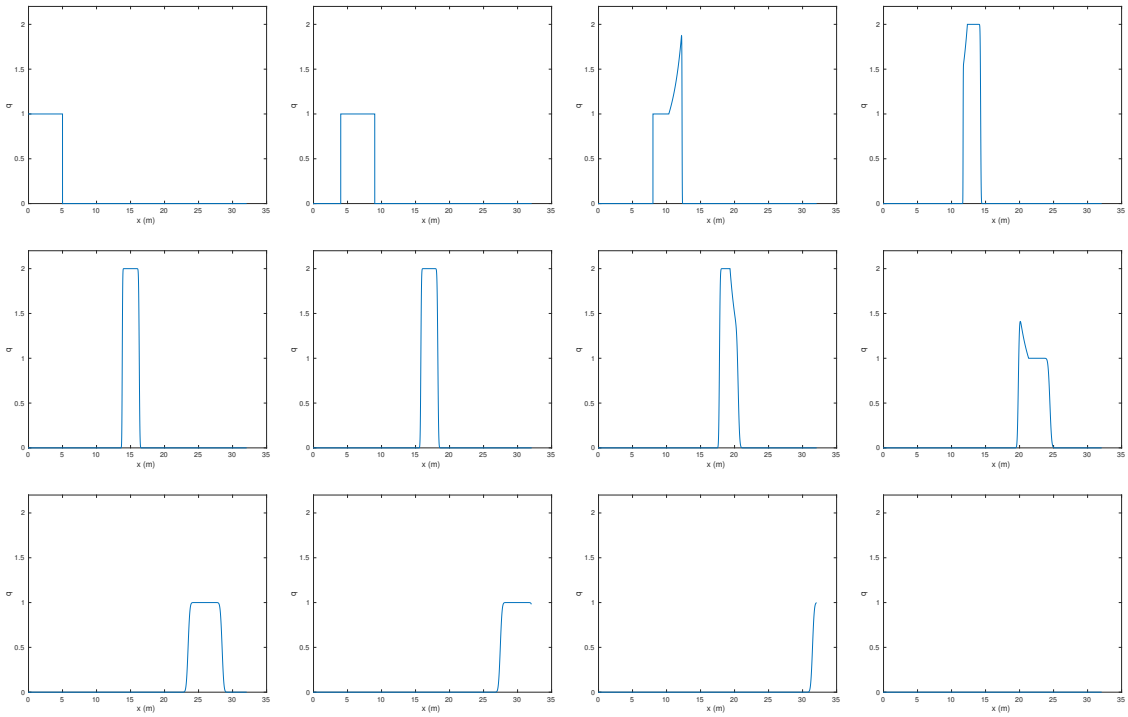

Figure 2.20: Reference solution for quantity q every four seconds (from left to right, top to bottom).

2.4.2.2 Convergence study

Two different convergence studies are led in this section. In all of them, the meshes of both models are refined so that elements of both models have the same size. The substrate occupies the entire domain and its velocity $\underline{v}_1$ is uniformly equal to 1m.s^{-1}. The patch occupies the domain $[x_4, x_7] = [7.33\text{m}, 24.33\text{m}]$ is superimposed on the substrate and accurately models the velocity of the reference problem. They are represented in Figure 2.19 (right side) along with the weight functions and their respective velocity. Just like in the previous case, the time step was computed with a security coefficient set to csta $= 1$. For the Arlequin computations, we imposed $\hat{\alpha}^q = \tilde{\alpha}^q$ and $\alpha^q = 1.0 \times 10^{-6}$ in the free zone. The outer boundary of the coupling zone Γ_{out} is aligned with the mesh of the patch and, symmetrically, the inner one, Γ_{in} is aligned with the mesh of the substrate. As elements of the two models have the same size and the two models

have symmetric roles, the choice of the mediator to space does not matter. It was arbitrarily chosen to be discretized as the substrate.

In the first study led, the number of elements (2.5 elements) in the coupling zone remains constant while in the second one, it is the size of the coupling zone that remains constant ($(x_5, x_6) = (9\text{m}, 22\text{m})$). A total of eight different meshes are considered with, respectively, 32, 64, 128, 256, 512, 1024, 2048 and 4096 degrees of freedom (for the substrate).

The Arlequin and Chimera solutions are represented in Figures 2.21 and 2.22 respectively for the finest test case (4096 degrees of freedom) and a coupling zone including 2.5 elements. We can see that both approaches accurately reproduce the solution.

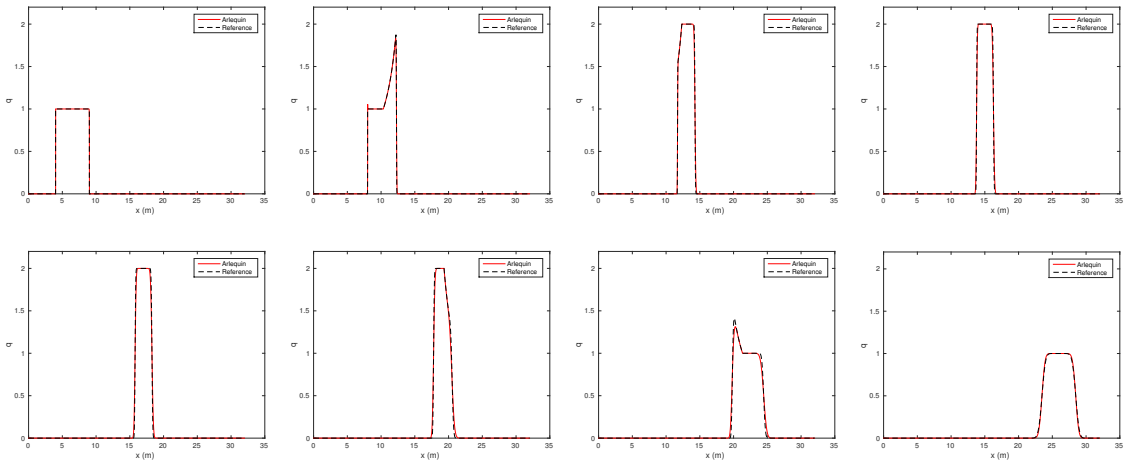

Figure 2.21: Arlequin solution (in red) for the slow down case every four seconds from $t = 4$s (top left) to $t = 32$s (bottom right). The reference solution is also represented in dashed black.

In the Arlequin approach however, we observe an overshoot when the front penetrates the coupling zone at $t = 8$s. Yet, when the entire quantity has left the patch ($t = 32$s), the solution for the Arlequin approach has travelled at the same speed as the reference solution while the Chimera one went slightly faster as can be seen in Figure 2.23,

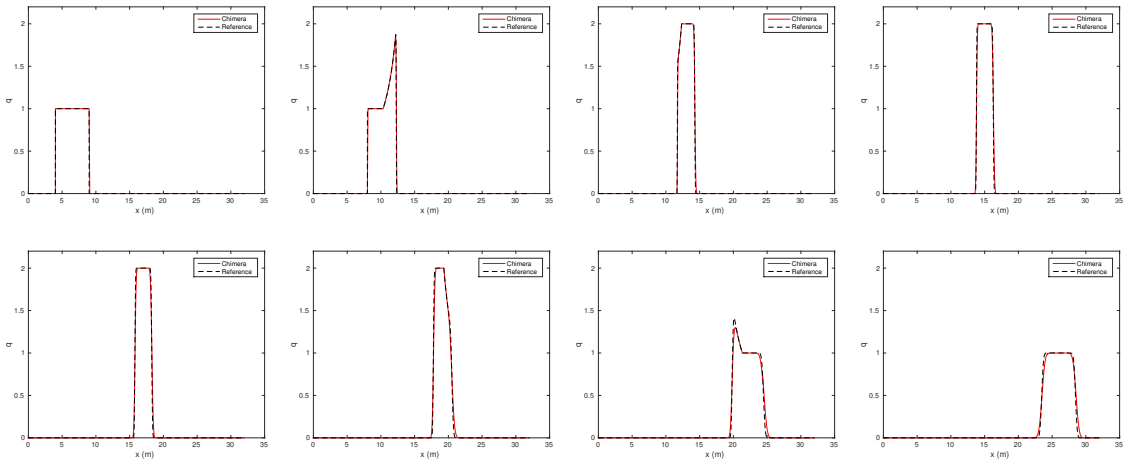

Figure 2.22: Chimera solution (in red) for the slow down case every four seconds from $t = 4$s (top left) to $t = 32$s (bottom right). The reference solution is also represented in dashed black.

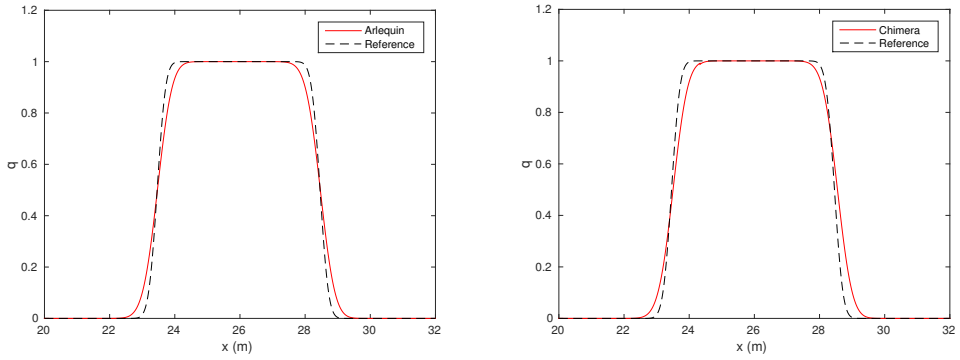

Figure 2.23: Zoom on the Arlequin (left) and Chimera (right) solutions at $t = 32$s. The reference solution is also represented in dashed black. We can observed that the reference and Arlequin approach are centered on the same axis while the Chimera solution is slightly ahead the reference one.

In order to evaluate how precise the multi-model approaches are, we compare them with the reference solution through the following error measurement.

$$Error = \frac{1}{\mathcal{N}_T} \sum_{n=1}^{\mathcal{N}_T} \left(\frac{\frac{1}{L} \int_0^L |q_m^n - q_r^n| \, dx}{\max_{n_0} |q_r^{n_0}|} \right) \tag{2.42}$$

where $\mathcal{N}_T$ is the number of instants at which the solutions are compared, q_r^n is the reference solution at instant t^n, q_m^n the multi-model approach solution at instant t^n and L the size of the domain.

The error measurement was computed for each solution and is represented in Figure 2.24. We can observe that both the Arlequin and the Chimera approaches yield the same convergence rate which is about the same as the Mono-model convergence right

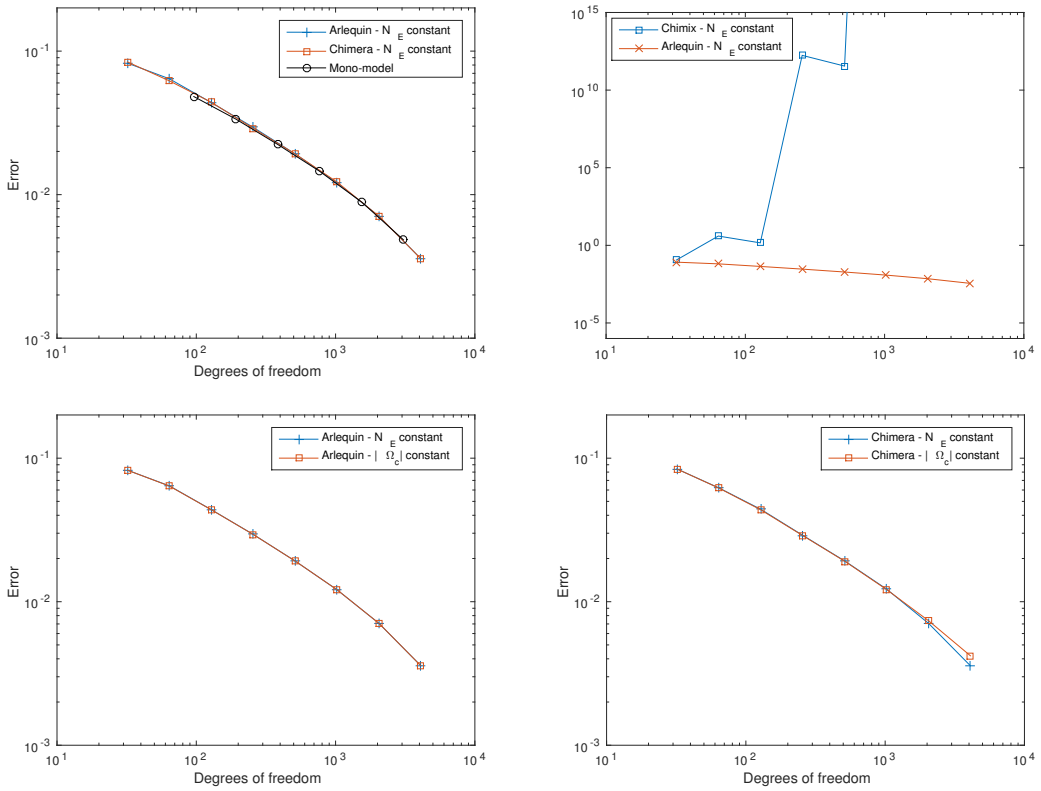

Figure 2.24: Error measure for all three multi-model approaches with a number of elements $\mathcal{N}_E$ constant in the coupling zone (top figures). Comparison of the error measure with a coupling zone whose size $|\Omega_c|$ remains constant for the Arlequin approach (bottom left) and the Chimera approach (bottom right).

(top left figure). While the solution yielded by the Arlequin approach seems to be independent of the size of the coupling zone (bottom figures), it seems that for the Chimera approach, the coupling zone should be as small as is permitted by stability. The Chimix approach on the other hand significantly diverges (top right).

2.5 Conclusion

In this chapter, we considered three different multi-model approaches for the treatment of convective transport type equations. Because explicit time integrators are used, the impact of the different multi-model frameworks on the stability was studied. In particular, it was shown that for the Arlequin approach to be stable, the weight associated to the time derivative should not be integrated on the volume of the element but instead on its edges.

Then, the different approaches proposed were implemented and tested on two test cases. While the Chimix method was observed to diverge, both the Chimera and Arlequin approaches were shown to yield accurate solutions. Yet, none proved to have significantly better convergence properties. Thus, both approaches are considered for the treatment of the convective transport equations of the Euler equations. This is accomplished in the next two chapters.

Chapter 3

Stability study of multi-model approaches for the explicit integration of the Euler equations

Contents

The objective of this thesis is to develop a multi-model approach able to account for local effects in transient FSI[1] simulations. In the first chapter, we developed a multi-model approach for overlapping structures. It also served the purpose of giving practical hints for the treatment of the momentum equation of the Euler equation discretized with the finite element method. In the second chapter, we proposed multi-model approaches for the treatment of convective transport equations using a Finite Volume discretization. Thus, we have all the ingredients to develop multi-model approaches for the Euler equations.

In order to do so, and as usual, we first introduce a reference problem for the Euler equations (section 3.1). Then, we propose different multi-model approaches taking into account the results of the previous chapters (section 3.2). Next, we study the stability of these approaches. As the stability of the Euler equations is linked to the acoustic waves, we focus our study on the equivalent acoustic problems (section 3.3). Finally, we conclude by discussing the advantages of using either approaches (section 3.4).

Note that this chapter uses results and reasonings from the previous chapter.

[1]Fluid Structure Interaction.

3.1 Mono-model formulation for the Euler equations

In order to present a comprehensive study of the multi-model approaches for the Euler equations, we consider the following representative, mono-model problem. This mono-model formulation yields the reference solution towards which the multi-model approaches should converge.

3.1.1 Continuous formulation for the mono-model problem

We consider a fluid occupying a bounded, regular domain $\Omega_1 \in \mathbb{R}^d$. Let v and $a = \dot{v}$ denote the velocity and acceleration fields. Let ρ, p, e and E denote respectively the density, the pressure, the internal energy and the total energy of the fluid. The fluid is submitted to prescribed velocities on $\Gamma_v \subsetneq \partial\Omega_1$. Finally, the superscript ^{0} on quantities denotes their initial value. The weak continuous mono-model problem formulation for the Euler equations then reads:

Given ρ^0, p^0, $\underline{v}^0$, *find* $\underline{u}(t) = (\underline{v}(t), \rho(t), E(t)) \in \mathcal{H}^1 \times \mathcal{V} \times \mathcal{V}, t \in [0,T]$ *such that* $\forall\ \underline{w} \in \mathcal{H}_0^1, \forall\ \Omega \subset \Omega_1$,

$$\left\{ \begin{array}{lcll} \displaystyle\int_{\Omega_1} \rho \frac{\partial \underline{v}}{\partial t} \cdot \underline{w}\ d\Omega_1 & + & \displaystyle\int_{\Omega_1} \underline{\underline{(v \cdot \nabla)\underline{v}}} \cdot \underline{w}\ d\Omega_1 & = \displaystyle\int_{\Omega} p\underline{\underline{I}} : \underline{\underline{\nabla w}}\ d\Omega_1 \\ \displaystyle\int_{\Omega_1} \frac{\partial \rho}{\partial t}\ d\Omega_1 & + & \displaystyle\int_{\Omega} \mathrm{div}(\rho \underline{v})\ d\Omega_1 & = 0 \\ \displaystyle\int_{\Omega_1} \frac{\partial (\rho E)}{\partial t}\ d\Omega_1 & + & \displaystyle\int_{\Omega_1} \mathrm{div}([\rho E + p]\underline{v})\ d\Omega_1 & = 0 \end{array} \right. \tag{3.1}$$

These equations are completed with an equation of state $p = f(\rho, e)$.

Remark 3.1.1. *Note that this formulation, as explained earlier, approximates the momentum equation (top equation of* (3.1)*) in a non-conservative finite element form. The conservative form would be as follows.*

$$\frac{\partial \underline{u}}{\partial t} + \underline{\nabla} \cdot \underline{F} = 0 \tag{3.2}$$

with $\underline{u} = [\rho \underline{v}, \rho, \rho E]^T$ *and* $\underline{F} = [\rho \underline{v} \otimes \underline{v} + p\underline{\underline{I}}, \rho \underline{v}, (\rho E + p)\underline{v}]^T$.

3.1.2 Discretized problem

In this section we give the discrete formulations of the continuous problem previously introduced. We first describe the time-integrators considered for the Euler equations and then we introduce the discrete mono-model formulation.

3.1.2.1 Discrete time-integrators

The time interval $[0,T]$ is subdivided into N steps Δt^i. Let $v^{n+\frac{1}{2}}$ and $\dot{v}^n$ denote the discrete velocity and acceleration at times $t^{n+\frac{1}{2}} = \sum_{i=1}^{n} \Delta t^i + \frac{1}{2}\Delta t^{n+1}$, $n \in [\![0, N]\!]$ and $t^n = \sum_{i=1}^{n} \Delta t^i$. In this study, we consider the following time integrator for the velocity:

Given v^0,

$$\underline{v}^{n+\frac{1}{2}} = \underline{v}^{n-\frac{1}{2}} + \Delta t^n \underline{\dot{v}}^n \tag{3.3}$$

Let ρ^n, $(\rho E)^n$, $\dot{\rho}^n$ and $(\dot{\rho E})^n$ denote, respectively, the discrete density, the discrete energy density and their respective time derivative at time $t^n = \sum_{i=1}^{n} \Delta t^i,\ n \in [\![0, N]\!]$. In this study, we consider the forward Euler scheme for their time integration, that is:

Given q^0,

$$q^{n+1} = q^n + \Delta t^n \dot{q}^n \tag{3.4}$$

where $\forall n \in [\![0, N]\!],\ q^n = \rho^n$ or $\forall n \in [\![0, N]\!],\ q^n = (\rho E)^n$.

3.1.2.2 Discrete mono-model problem formulation

We use a finite element discretization for the momentum equation and a Finite Volume scheme with a first order upwind scheme for the other two equations[2]. Let us denote by $\mathcal{S}_E$ and $\mathcal{S}_N$ the sets of elements and nodes respectively. Thus, the three variables $\underline{v}$, ρ and ρE are approximated spatially within an element so that we can write

$$\left\{ \begin{array}{lcl} \underline{v}(\underline{x}) & = & \displaystyle\sum_{i \in \mathcal{S}_N} v_i \underline{N}_i(\underline{x}) \\ \rho(\underline{x}) & = & \displaystyle\sum_{e \in \mathcal{S}_E} \rho_e \bar{N}_e(\underline{x}) \\ \rho E(\underline{x}) & = & \displaystyle\sum_{e \in \mathcal{S}_E} (\rho E)_e \bar{N}_e(\underline{x}) \end{array} \right. \tag{3.5}$$

where $(\underline{N}_i)_{i \in \mathcal{S}_N}$ are finite element shape functions while $(\bar{N}_e)_{e \in \mathcal{S}_E}$ are the shape functions defined in section 2.1.3.2. We introduce $\underline{\rho} = [\rho_1, ..., \rho_{\mathcal{N}_E}]^T$ and $(\underline{\rho E}) = [(\rho E)_1, ..., (\rho E)_{\mathcal{N}_E}]^T$. For the discrete velocity, we introduce the discrete vector[3] $\underline{v} = [v_{1,1}, v_{1,2}, ..., v_{\mathcal{N}_N, d}]$.

At time step n, we then have,

$$\left\{ \begin{array}{lcl} \underline{\underline{M}}_v^n \underline{\dot{v}}^n + \underline{F}_v^n & = & 0 \\ \underline{\underline{D}}_\rho^n \underline{\dot{\rho}}^n + \underline{F}_\rho^n & = & 0 \\ \underline{\underline{D}}_{\rho E}^n (\underline{\dot{\rho E}})^n + \underline{F}_{\rho E}^n & = & 0 \end{array} \right. \tag{3.6}$$

where,

$$\left\{ \begin{array}{lcl} \forall\ j,k \in \mathcal{S}_N, \quad (\underline{\underline{M}}_v^n)_{jk} & = & \left(\displaystyle\int_{\Omega_1} \rho \hat{N}_j \ d\Omega_1 \right) \delta_{jk} \\ \forall\ j,k \in \mathcal{S}_E, \quad (\underline{\underline{D}}_\rho^n)_{jk} & = & \displaystyle\int_{\Omega_1} \bar{N}_j \bar{N}_k \ d\Omega_1 \\ \forall\ j,k \in \mathcal{S}_E, \quad (\underline{\underline{D}}_{\rho E}^n)_{jk} & = & \displaystyle\int_{\Omega_1} \bar{N}_j \bar{N}_k \ d\Omega_1 \end{array} \right. \tag{3.7}$$

$\underline{\underline{M}}_v^n$ is the lumped mass matrix while $\underline{\underline{D}}_\rho^n$ and $\underline{\underline{D}}_{\rho E}^n$ are diagonal 'mass' matrices. In practice, we have $\underline{\underline{D}}_\rho^n = \underline{\underline{D}}_{\rho E}^n = \text{diag}(|\Omega_{E_i}|)$ where $|\Omega_{E_i}|$ is the volume of element E_i. In this work, because we use an Eulerian description of the flow fluid, $\underline{\underline{D}}_t = \underline{\underline{D}}_\rho^n = \underline{\underline{D}}_{\rho E}^n$

[2]See section 2.1.3 for a description of the upwind scheme implemented in this work as well as how to put it in matrix form.

[3]The distinction between the continuous and discrete velocity will be given by context.

are independent of time. Note that $\underline{F}_v^n = \underline{F}_c^n + \underline{F}_p^n$ where $\underline{F}_c^n$ represents convection forces and $\underline{F}_p^n$ the pressure forces while $\underline{F}_\rho^n$ and $\underline{F}_{\rho E}^n$ represent the flow. Note that we can write $\underline{F}_c^n = \underline{\underline{B}}^n \underline{v}^{n-\frac{1}{2}}$. The convection and pressure terms are then given by (see [177]):

$$\left\{\begin{array}{lllll} \underline{\underline{B}}^n = \mathcal{A}^E(\underline{\underline{B}}_{jk}^n)^E & \text{with} & \forall\, j,k \in \mathcal{S}_N, & (\underline{\underline{B}}_{jk}^n)^E & = \displaystyle\int_{\Omega_E} N_j(\underline{v}^{n-\frac{1}{2}} \cdot \underline{\nabla}) N_k \; d\Omega_E \\ \underline{F}_p^n = \mathcal{A}^E(\underline{F}_p^n)_j^E & \text{with} & \forall\, j \in \mathcal{S}_E, & (\underline{F}_p^n)_j^E & = \displaystyle\int_{\Omega_E} p(\underline{\nabla N_j}) \cdot \underline{x}_{d(j)} \; d\Omega_E \end{array}\right. \tag{3.8}$$

where $\mathcal{A}^E$ is denotes the assembly operator (see for instance [177]) and $\underline{x}_{d(j)}$ is the unit vector associated to the direction of the corresponding degree of freedom v_j. The flow terms are given by:

$$\left\{\begin{array}{lll} \forall\, j \in \mathcal{S}_E, \quad (\underline{F}_\rho^n)_j & = & \displaystyle\sum_{e \in \mathcal{S}_e^j} \phi_{\rho,e}^n \int_e \underline{v}^{n-\frac{1}{2}} \cdot \underline{n} \; de \\ \forall\, j \in \mathcal{S}_E, \quad (\underline{F}_{\rho E}^n)_j & = & \displaystyle\sum_{e \in \mathcal{S}_e^j} \phi_{\rho E,e}^n \int_e \underline{v}^{n-\frac{1}{2}} \cdot \underline{n} \; de \end{array}\right. \tag{3.9}$$

The discretized equation of state becomes, $\forall j \in \mathcal{S}_E$, $p_j^n = f(\rho_j^n, e_j^n)$.

3.2 Multi-model formulations for the Euler equations

As was done in sections 1.1.2 and 2.2, we consider a fluid occupying a bounded, regular domain $\Omega_1 \in \mathbb{R}^d$. A local model Ω_2, called the patch, is superimposed to the global model Ω_1, called the substrate, in the neighbourhood of a zone of interest. We assume for clarity that Ω_2 is strictly embedded in Ω_1, as shown in Figure 1.1. Quantities relative to the substrate are denoted by a subscript equal to 1 while those relative to the patch are denoted by a subscript equal to 2.

We recall that in the multi-model approaches proposed in this work, the momentum equation is treated in a non conservative finite element form in order to efficiently impose link conditions when dealing with FSI applications[4]. The Arlequin method offers a general framework to simultaneously solve multiple model problems while imposing link conditions between the different models. Moreover, as seen in Chapter 1, the Arlequin framework was successfully used to develop stable multi-model approaches for elastodynamics. Because of the equilibrium equation of elastodynamics and the momentum equation in its non conservative form bear similarities, the Arlequin method is the most natural choice for the treatment of the momentum equation.

In chapter 2, we implemented two multi-model approaches for the treatment of the convective transport equations that were both stable and accurate. Thus, two multi-model approaches are studied in this chapter[5]. The first one, referred to as the Full Arlequin approach, uses the Arlequin framework for the treatment of all three

[4] See Appendix A.

[5] In the next chapter, the solution yielded by the approaches proposed here are compared with other approaches that do not necessarily use the Arlequin framework.

equations. The second one, referred to as the Archimera approach[6], uses the Arlequin framework for the treatment of the momentum equation and a Chimera-like approach for the treatment of convective transport equations.

As seen in **Remark** 2.2.1, we assume that the outer boundary of the coupling zone is, for all multi-model approaches, always aligned with the mesh of the patch. For the inner one, it can, when possible be aligned with the mesh of either model. For each equation of the Euler equations, a choice of an inner boundary of the coupling zone needs to be made[7]. In this work, we only consider cases for which the three equations have the same inner boundary.

As both multi-model approaches proposed here use the Arlequin framework for the treatment of the momentum equation, we first focus on that equation.

3.2.1 Extension of the Arlequin method to the momentum equation

In order to establish the Arlequin formulation[8], we have to determine where the weight parameters fit in the formulation and choose a relevant coupling operator.

3.2.1.1 Weight functions for the momentum equation

In the previous chapter[9], we saw that the weight parameters should appear inside the divergence term. Yet, the momentum is not treated in its conservative form[10] so that special care is needed when introducing the weight functions.

Let us thus consider the strong, continuous Euler equations in their conservative form. We assume that the same weight functions are used for all terms of every equation. It reads, $\forall i \in \{1,2\}$:

$$\left\{\begin{array}{lcll} \dfrac{\partial}{\partial t}(\alpha_i\rho_i\underline{v}_i) & + & \mathrm{div}(\alpha_i(\rho_i\underline{v}_i\otimes\underline{v}_i + p_i\underline{\underline{I}})) & = 0 \\ \dfrac{\partial}{\partial t}(\alpha_i\rho_i) & + & \mathrm{div}(\alpha_i\rho_i\underline{v}_i) & = 0 \\ \dfrac{\partial}{\partial t}(\alpha_i\rho_i E_i) & + & \mathrm{div}(\alpha_i(\rho_i E_i + p_i)\underline{v}_i) & = 0 \end{array}\right. \tag{3.10}$$

Given the following

$$\begin{array}{rcl} \mathrm{div}(\alpha_i\rho_i\underline{v}_i\otimes\underline{v}_i) & = & \underline{v}_i(\underline{v}_i\cdot\underline{\nabla(\alpha_i\rho_i)}) + \alpha_i\rho_i\underline{\underline{(v_i\cdot\nabla)\underline{v}_i}} + \alpha_i\rho_i\underline{v}_i(\underline{\nabla}\cdot\underline{v}_i) \\ & = & \underline{v}_i(\underline{v}_i\cdot\underline{\nabla(\alpha_i\rho_i)} + \alpha_i\rho_i(\underline{\nabla}\cdot\underline{v}_i)) + \alpha_i\rho_i\underline{\underline{(v_i\cdot\nabla)\underline{v}_i}} \\ & = & \underline{v}_i(\mathrm{div}(\alpha_i\rho_i\underline{v}_i)) + \alpha_i\rho_i\underline{\underline{(v_i\cdot\nabla)\underline{v}_i}} \end{array} \tag{3.11}$$

and the fact that $\frac{\partial}{\partial t}(\alpha_i\rho_i\underline{v}_i) = \alpha_i\rho_i\frac{\partial}{\partial t}\underline{v}_i + \underline{v}_i\frac{\partial}{\partial t}(\alpha_i\rho_i)$, the first equation of (3.10) can be rewritten:

$$\alpha_i\rho_i\frac{\partial}{\partial t}\underline{v}_i + \alpha_i\rho_i\underline{\underline{(v_i\cdot\nabla)\underline{v}_i}} + \mathrm{div}(\alpha_i p_i\underline{\underline{I}})) + \underline{v}_i\left(\frac{\partial}{\partial t}(\alpha_i\rho_i) + \mathrm{div}(\alpha_i\rho_i\underline{v}_i)\right) = 0 \tag{3.12}$$

[6] for mixed ARlequin/CHIMERA approach.
[7] when possible.
[8] See Appendix B.
[9] See section 2.2.2.1 and **Remark** 2.2.7.
[10] See Appendix A or problem (3.1).

where we recognize the left hand side of the second equation in (3.10). We thus have:

$$\alpha_i\rho_i\frac{\partial}{\partial t}\underline{v}_i + \alpha_i\rho_i\underline{\underline{(v_i\cdot\nabla)\underline{v}_i}} + \mathrm{div}(\alpha_i p_i\underline{\underline{I}}) = 0 \tag{3.13}$$

The previous reasoning served the purpose of understanding where the weight functions fit in the non conservative treatment of the momentum equation. When designing the multi-model approaches, we no longer assume that the weight function should be the same for every term of every equations. Instead, for flexibility, we assume that a different set of weight function can be introduce for each term of each equations.

The weak continuous Arlequin method applied to the discretized momentum equation then reads:

$$\forall(\underline{w}_1,\underline{w}_2,\underline{\mu})\in\mathcal{H}_0^1\times\mathcal{H}_0^2\times\mathcal{M},$$

$$\left\{\begin{array}{l}\displaystyle\int_{\Omega_1}\widehat{\alpha}_1^v\rho_1^n\dot{\underline{v}}_1^n\cdot\underline{w}_1\;d\Omega_1+\int_{\Omega_1}\widetilde{\alpha}_1^v\rho_1^n(\underline{v}_1^{n-\frac{1}{2}}\cdot\underline{\nabla})\underline{v}_1^{n-\frac{1}{2}}\cdot\underline{w}_1\;d\Omega_1-\int_{\Omega_1}\overline{\alpha}_1^v p_1^n\underline{\underline{I}}:\underline{\underline{\nabla w_1}}\;d\Omega_1+c_m(\underline{w}_1,\underline{\lambda}_v^n)=0\\ \displaystyle\int_{\Omega_2}\widehat{\alpha}_2^v\rho_2^n\dot{\underline{v}}_2^n\cdot\underline{w}_2\;d\Omega_2+\int_{\Omega_2}\widetilde{\alpha}_2^v\rho_2^n(\underline{v}_2^{n-\frac{1}{2}}\cdot\underline{\nabla})\underline{v}_2^{n-\frac{1}{2}}\cdot\underline{w}_2\;d\Omega_2-\int_{\Omega_2}\overline{\alpha}_2^v p_2^n\underline{\underline{I}}:\underline{\underline{\nabla w_2}}\;d\Omega_2-c_m(\underline{w}_2,\underline{\lambda}_v^n)=0\\ c_m(\dot{\underline{v}}_1^n-\dot{\underline{v}}_2^n,\underline{\mu})=0\end{array}\right. \tag{3.14}$$

where $\mathcal{M}$ is the mediator space for the momentum equation, c_m is a coupling operator to be defined, λ_v^n the Lagrange multiplier and $(\widehat{\alpha}_1^v,\widehat{\alpha}_2^v)$, $(\widetilde{\alpha}_1^v,\widetilde{\alpha}_2^v)$ and $(\overline{\alpha}_1^v,\overline{\alpha}_2^v)$ are three sets of weight functions (see section 1.1.2). In this chapter, all sets of weight functions are assumed to be independent of time. For now, we do not specify what type of weight functions are used and, for generality, allow for the weight functions to be different for each term of equation (3.14). Note that we used the Green-Ostrogradski formula to obtain the pressure term.

3.2.1.2 Coupling operator

Many norms have been used to define the coupling operator c_m [103] [114] [98]. For the momentum equation, we use a H^1 coupling operator for two reasons. First, it was theoretically proven in structural mechanics that a H^1 coupling allowed for a well posed problem [103] [114] [98]. Secondly, the H^1 coupling operator was shown to yield precise solutions in structural elastodynamics, whose treatment is very similar to that of the momentum equation [152]. The continuous coupling operator c_m is thus defined as

$$\forall(\underline{v},\underline{\mu})\in\mathcal{H}^1\times\mathcal{M},\;\; c_m(\underline{v},\underline{\mu})=\int_{\Omega_c}\underline{v}\cdot\underline{\mu}+\mathcal{L}^2\underline{\underline{\nabla^s\underline{v}}}:\underline{\underline{\nabla^s\mu}}\;d\Omega_c \tag{3.15}$$

where $\mathcal{L}$ is a strictly positive parameter homogeneous to a length (typically the thickness of the coupling zone).

3.2.1.3 Extension to the Euler equations

Now that the Arlequin method has been applied to the momentum equation, we focus on the multi-model framework used for conservation of mass and energy equations. We

recall that these equations are treated as the convective transport equation studied in chapter 2 and thus led to two multi-model approaches.

3.2.2 A Full Arlequin approach for the Euler equations

We first consider the Arlequin framework for the treatment of both the conservation of mass and the conservation of total energy equations.

3.2.2.1 Discrete formulation

We use the discretization and notations of chapter 2 so that the the discretized convective transport equations can be written as follows.

$\forall (w_1, w_2, \mu) \in \mathcal{V} \times \mathcal{V} \times \mathcal{M}^q$,

$$\left\{ \begin{array}{l} \displaystyle\int_{\Omega_1} \widehat{\alpha}_1^q \dot{q}_1^n \; w_1 \; d\Omega_1 + \int_{\Omega_1} \mathrm{div}(\alpha_1^q \phi_{q_1}^n \underline{v}_1^{n-\frac{1}{2}}) w_1 \; d\Omega_1 + c_t(w_1, \lambda_q^n) = 0 \\ \displaystyle\int_{\Omega_2} \widehat{\alpha}_2^q \dot{q}_2^n \; w_2 \; d\Omega_2 + \int_{\Omega_2} \mathrm{div}(\alpha_2^q \phi_{q_2}^n \underline{v}_2^{n-\frac{1}{2}}) w_2 \; d\Omega_2 - c_t(w_2, \lambda_q^n) = 0 \\ c_t(\dot{q}_1^n - \dot{q}_2^n, \mu) = 0 \end{array} \right. \tag{3.16}$$

where c_t is the L^2 coupling operator defined in 2.2.2.2. The conservation of mass equation is thus obtained with $q_i = \rho_i$ and $\phi_{q_i} = \rho_i$ while the conservation of total energy equation is obtained with $q_i = \rho_i E_i$ and $\phi_{q_i} = \rho_i E_i + p_i$ (i represents the model the quantities belong to). We recall that for both equations, (α_1^q, α_2^q) are continuous piecewise linear set functions, so that, with obvious notations, $(\alpha_1^{\rho E}, \alpha_2^{\rho E}) = (\alpha_1^\rho, \alpha_2^\rho)$. The other weight functions however, namely $\hat{\alpha}_i^q$, do not have to be equal and are determined later.

Remark 3.2.1. *The complete discrete formulation for the Full Arlequin approach is given in Appendix F.*

3.2.3 An Archimera approach for the Euler equation

The second multi-model approach that we consider treats the conservation of mass and energy equations with the Chimera-like approach introduce in section 2.2.1. This approach, in which the momentum equation is treated by the Arlequin method and the other two by the Chimera method will be referred to as the *Archimera* approach for hybrid Arlequin/Chimera approach.

Two multi-model approaches have now been introduced. In the next section, we study their stability in order to ensure that they are computationally feasible.

3.3 Stability study of multi-model approaches

The use of the explicit time integrators defined in section 3.1.2 implies that the problem formulation is conditionally stable [174]. This implies that the time step between two instants at which the solution is computed is bounded by a value called

the critical time step. This critical time step depends on the different variables of the problem and it is thus necessary to study the stability of each multi-model approach in order to ensure that the critical time step does not drop and therefore that the approaches are computationally feasible.

The stability of the Euler equations is associated to acoustic waves. Thus, one way to study their stability is to study the equivalent wave equation problem formulation. Thus, for each approach, we study the stability of the equivalent wave equation problem formulation. In order for our study to be representative of the Euler equations, we consider the wave equation in its mixed form, as was done in previous works [153].

3.3.1 Mono-model wave equation problem formulation

We consider a fluid occupying a bounded, regular domain $\Omega_1 \in \mathbb{R}^d$. Let $\tilde{\underline{v}} = \underline{v}_0 + \underline{v}(t)$, $\tilde{\underline{a}} = \dot{\tilde{\underline{v}}}$, $\tilde{\rho} = \rho_0 + \rho(t)$ and $\tilde{p} = p_0 + p(t)$ denote the velocity, the acceleration, the density and the pressure. We assume that the equation of state reads $p(t) = c^2\rho(t)$, where c is the velocity of acoustic waves. Moreover, we assume that $\underline{v}_0 = \underline{0}$, $\|\underline{v}(t)\| << c$, $\|p(t)\| << \|p_0\|$ and $\|\rho(t)\| << \|\rho_0\|$. Finally, the fluid is submitted to prescribed velocities on $\Gamma_v \subsetneq \partial\Omega$.

The weak discrete mono-model problem formulation for the wave equation in its mixed form can be written:

Given ρ^0, p^0 and $\underline{v}^0$, find $\underline{u}(t) = (\underline{v}(t), p(t)) \in \mathcal{H}^1 \times L^2, t \in [0,T]$ such that $\forall\ \underline{w} \in \mathcal{H}_0^1$ and $\forall\ \Omega \subset \Omega_1$

$$\left\{ \begin{array}{lcll} \displaystyle\int_{\Omega_1} \rho_0 \frac{\partial \underline{v}}{\partial t} \cdot \underline{w}\ d\Omega_1 & - & \displaystyle\int_{\Omega_1} p\underline{\underline{I}} : \underline{\underline{\nabla w}}\ d\Omega_1 & = 0 \\ \displaystyle\int_{\Omega_1} \frac{\partial p}{\partial t}\ d\Omega_1 & + & \displaystyle\int_{\Omega_1} \rho_0 c^2\, \mathrm{div}(\underline{v})\ d\Omega_1 & = 0 \end{array} \right. \tag{3.17}$$

Remark 3.3.1. *The problem* (3.17) *can also be obtained by linearizing problem* (3.1) *around the motionless state (see [154]).*

Using the same discretization as in section 3.1.2.2, we obtain the following linear system:

$$\underline{\underline{M}}\dot{\underline{U}}^n + \underline{\underline{K}}\underline{U}^n = 0 \tag{3.18}$$

where $\underline{U}^n = [\underline{v}^n, \underline{p}^n]^T$, $\underline{\underline{M}} = \mathrm{diag}(\underline{\underline{M}}_v, \underline{\underline{\mathcal{D}}}_p)$ with $\underline{\underline{M}}_v$ the lumped mass matrix, $\underline{\underline{\mathcal{D}}}_p$ a diagonal matrix while K is defined as follows:

$$\underline{\underline{K}} = \begin{pmatrix} \underline{\underline{0}}_{\mathcal{N}_N,\mathcal{N}_N} & \underline{\underline{K}}_p \\ \underline{\underline{K}}_v & \underline{\underline{0}}_{\mathcal{N}_E,\mathcal{N}_E} \end{pmatrix} \tag{3.19}$$

where $\underline{\underline{K}}_v$ the assembled pressure matrix such that $\underline{\underline{K}}_v\underline{p}^n$ yields the pressure forces at time t^n, $\underline{\underline{K}}_p$ the assembled transport matrix such that $\underline{\underline{K}}_p\underline{v}^n$ yields the flow at time t^n and $\underline{\underline{0}}_{n_1,n_2}$ is the matrix of size $n_1 \times n_2$ with zeros everywheres. We recall that $\mathcal{N}_E$ is the number of elements of the mesh and $\mathcal{N}_N$ the number of degrees of freedom associated to the velocity. We have:

$$\begin{cases} \forall\ j,k \in \mathcal{S}_N, \quad (\underline{\underline{M}}_v)_{jk} = \left(\rho_0 \int_\Omega \hat{N}_j \ d\Omega\right) \delta_{jk} \\ \forall\ j,k \in \mathcal{S}_E, \quad (\underline{\underline{D}}_p)_{jk} = |\Omega_j| \delta_{jk} \\ \forall\ j,k \in \mathcal{S}_E \times \mathcal{S}_N, \quad (\underline{\underline{K}}_v)_{jk} = \displaystyle\int_{\Omega_j} \frac{\partial N_k}{\partial x_{d(k)}} \ d\Omega_j \\ \forall\ j,k \in \mathcal{S}_N \times \mathcal{S}_E, \quad (\underline{\underline{K}}_p)_{jk} = \displaystyle\int_{\partial\Omega_k} \rho_0 c^2 N_j \underline{n} \cdot \underline{x}_{d(j)} \ d\partial\Omega_k \end{cases} \tag{3.20}$$

where N the shape functions, $\hat{N}$ are the lumped shape functions of N and where $\underline{x}_{d(j)}$ was earlier introduce as the unit vector associated to the direction of degree of freedom v_j.

Time is discretized as usual (see section 3.1.2.1). We assume that both velocity $\underline{v}^n$ and pressure p are time integrated using the following time integrator.

$$\underline{U}^{n+1} = \underline{U}^n + \Delta t \underline{\dot{U}} \tag{3.21}$$

Note that the time step Δt stays constant over time as both matrices $\underline{\underline{M}}$ and $\underline{\underline{K}}$ are independent of time (see (3.22)).

Remark 3.3.2. *Note that in order to be representative of the way the Euler equations are treated, the velocity should be integrated in time at mid time step $\forall n \in n + \frac{1}{2}$. In this section, we use the above time integrator as it makes calculations easier. However, the main results hold (see* ***Remark*** *3.3.5 and Appendix D).*

The use of this explicit time integrator (3.21) for both the velocity and the pressure implies that the different problems are conditionally stable. In fact, for the mono-model problem (3.18), it was shown that the time step Δt needs to verify the following condition [174] [177]

$$\Delta t < \Delta t_c = \frac{2}{\max \omega} \tag{3.22}$$

where ω are the eigenvalues of the generalized eigenvalue problem of M and K and Δt_c is called the critical time step.

The lower the critical time step, the more iterations are necessary to reach the final T and thus the more computationally expensive the simulation is. This is why it is necessary to ensure that both the Arlequin and the Chimera framework do not adversely affect the critical time step.

Remark 3.3.3. *In practice, the elementary time step is computed as follows:*

$$\Delta t = \text{csta} \times \min_{E \in \mathcal{S}_E} \frac{L_E}{|v_E| + c} \tag{3.23}$$

where L_E is a characteristic length of the element E, $|v_E|$ a norm of the velocity in that element, c the velocity of the acoustic waves and csta *a positive coefficient lower or equal to 1.*

3.3.2 Study of the influence of the multi-model frameworks on the stability

As the stability is conditional, the influence of multi-model components on the stability need to be studied in order to ensure that the critical time step is not adversely altered and thus that the approaches proposed are computationally feasible. Such components are (1) the Chimera-like treatment of the flow at the boundaries of the coupling zone, (2) the coupling matrices of the Arlequin framework and (3) the weight functions.

Example 3.3.1. *Let us consider, for instance, the Full Arlequin approach. The Arlequin framework applied to the wave equation problem in its mixed form can be written as*

$$\underline{\underline{M}}\dot{\underline{U}}^n + \underline{\underline{K}}^*\underline{U}^n = 0 \tag{3.24}$$

where $\underline{\underline{M}} = \text{diag}(\underline{\underline{M}}_{v,1}, \underline{\underline{M}}_{v,2}, \underline{\underline{D}}_{p,1}, \underline{\underline{D}}_{p,2})$, $\underline{\underline{K}}^* = (\underline{\underline{I}} - \underline{\underline{C}}^T(\underline{\underline{C}}\underline{\underline{M}}^{-1}\underline{\underline{C}}^T)^{-1}\underline{\underline{C}}\underline{\underline{M}}^{-1})\underline{\underline{K}}$ *with* $\underline{\underline{C}} = \text{diag}(\underline{\underline{C}}_m, \underline{\underline{C}}_t)$ *and*

$$\underline{\underline{K}} = \left(\begin{array}{cc:cc} \underline{\underline{0}}_{\mathcal{N}_N^1,\mathcal{N}_N^1} & \underline{\underline{K}}_{p,1} & & \\ \underline{\underline{K}}_{v,1} & \underline{\underline{0}}_{\mathcal{N}_E^1,\mathcal{N}_E^1} & \multicolumn{2}{c}{\underline{\underline{0}}_{\mathcal{N}^1,\mathcal{N}^2}} \\ \hdashline & & \underline{\underline{0}}_{\mathcal{N}_N^2,\mathcal{N}_N^2} & \underline{\underline{K}}_{p,2} \\ \multicolumn{2}{c:}{\underline{\underline{0}}_{\mathcal{N}^2,\mathcal{N}^1}} & \underline{\underline{K}}_{v,2} & \underline{\underline{0}}_{\mathcal{N}_E^2,\mathcal{N}_E^2} \end{array}\right) \tag{3.25}$$

with $\mathcal{N}^i = \mathcal{N}_N^i + \mathcal{N}_E^i$ *the total number of degrees of freedom of model* i*. We also have,* $\forall i \in \{1,2\}$*:*

$$\left\{\begin{array}{l} \forall\ j,k \in \mathcal{S}_N^i, \quad (\underline{\underline{M}}_{v,i})_{jk} = \left(\rho_0 \hat{\alpha}_i^v \displaystyle\int_\Omega \hat{N}_j^i \ d\Omega\right)\delta_{jk} \\ \forall\ j,k \in \mathcal{S}_E^i, \quad (\underline{\underline{D}}_{p,i})_{jk} = \hat{\alpha}_i^p |\Omega_j^i| \delta_{jk} \\ \forall\ j,k \in \mathcal{S}_E^i \times \mathcal{S}_N^i, \quad (\underline{\underline{K}}_{v,i})_{jk} = \hat{\alpha}_i^v \displaystyle\int_{\Omega_j} \frac{\partial N_k^i}{\partial x_{d(k)}} \ d\Omega_j \\ \forall\ j,k \in \mathcal{S}_N^i \times \mathcal{S}_E^i, \quad (\underline{\underline{K}}_{p,i})_{jk} = \displaystyle\int_{\partial\Omega_k} \alpha_i^p \rho_0 c^2 N_j^i \underline{n} \cdot \underline{x}_{d(j)} \ d\partial\Omega_k \end{array}\right. \tag{3.26}$$

Expression (3.24) *is in the form of expression* (3.18) *so that the time step* Δt^a *for the Full Arlequin formulation needs to verify* (3.22) *where* ω *are the eigenvalues of the generalized eigenvalue problem of* $\underline{\underline{M}}$ *and* $\underline{\underline{K}}^*$ *as defined earlier. We can clearly see that the critical time step is,* a priori*, dependent on the coupling matrix* C *and the weight functions (through* $\underline{\underline{M}}$ *and* $\underline{\underline{K}}^*$*). Their influence thus needs to be analysed.*

With regards to the influence of both Chimera-like boundary conditions and the coupling matrices, the analysis done in the previous chapter[11] so that neither adversely affects the stability.

[11] see sections 2.3.3 and 2.3.2.

3.3.2.1 Study of the influence of the weight functions

With regards to the influence of the weight parameters on the stability, we use the same arguments as in the previous two chapters[12] and focus on their influence on the stability of an arbitrary element. Indeed, according to **Proposition** 1.3.1, if we can ensure that the weight functions do not cause the critical time step computed for any element to drop significantly, then the formulation is bound to be stable.

Let us then consider an element E and let $\underline{U}_E = [v_1, ..., v_{\mathcal{N}_N}, p_E]^T$ an eigenvector of the generalized eigenvalue problem, that is, $\exists\ \omega$ such that $\underline{\underline{K}}_E \underline{U}_E = \omega \underline{\underline{M}}_E \underline{U}_E$. The element thus has $\mathcal{N}_N$ degrees of freedom associated to the velocity and only one associated to the pressure, in line with the discretization proposed in this work. The components of $\underline{U}_E$ thus verify:

$$\left\{ \begin{array}{rcl} \omega\rho_0 \left(\displaystyle\int_{\Omega_E} \hat{\alpha}^v \hat{N}_i \ d\Omega_E \right) v_i &=& \left(\displaystyle\int_{\Omega_E} \bar{\alpha}^v \frac{\partial N_i}{\partial x_{d(i)}} \ d\Omega_E \right) p_E, \qquad \forall i \in [|1, \mathcal{N}_N|] \\ \omega \left(\displaystyle\int_{\Omega_E} \hat{\alpha}^p \ d\Omega_E \right) p_E &=& \displaystyle\sum_{i=1}^{\mathcal{N}_N} \left(\int_{\partial\Omega_E} \alpha^p \rho_0 c^2 N_i \ \underline{n} \cdot \underline{x}_{d(i)} \ d\partial\Omega_E \right) v_i \end{array} \right. \tag{3.27}$$

where $\hat{N}_i$ is the shape function associated[13] to the lumped mass of degree of freedom i, N_i are the shape functions associated to the velocity, $x_{d(i)}$ the unit vector associated to the direction of degree of freedom v_i and n the outward normal to element E. Note that the system has been set for the Full Arlequin Approach as $\hat{\alpha}^p$ and α^p appear. However, all the computations done in this work are valid for Archimera and obtained by imposing $\hat{\alpha}^p = \alpha^p = 1$.

The first N equations give an expression of v_i as a function of p_E only. Thus, we can substitute the value of v_i in the last equation. We can simplify the expression[14] which, after rearranging, yields

$$\omega^2 = \frac{1}{\left(\displaystyle\int_{\Omega_E} \hat{\alpha}^p \ d\Omega_E \right)} \sum_{i=1}^{\mathcal{N}_N} \left(\frac{\displaystyle\int_{\Omega_E} \bar{\alpha}^v \frac{\partial N_i}{\partial x_{d(i)}} \ d\Omega_E}{\displaystyle\int_{\Omega_E} \hat{\alpha}^v \rho_0 \hat{N}_i \hat{N}_i \ d\Omega_E} \right) \left(\int_{\partial\Omega_E} \alpha^p \rho_0 c^2 N_i \ \underline{n} \ \cdot \underline{x}_{d(i)} \ d\partial\Omega_E \right) \tag{3.28}$$

In expression (3.28), only the value of α^p is already set (see section 3.2.2.1) so that conditions can be imposed on the other three set of weight functions in order to ensure that the eigenvalues are the same as those of the mono-model formulation[15]. In this work we propose to ensure stability as follows.

First, and in line with stability results from other works [76] [77] [79], [152], we impose $\hat{\alpha}^v$ and $\bar{\alpha}^v$ to be uniform over each element and that $\hat{\alpha}^v = \bar{\alpha}^v = \alpha^v$. The way α^v is chosen is arbitrary but has to be compatible with conditions (1.32). Formula

[12] see section 1.3 and 2.3.4.

[13] In [156], it is shown that you can associate a shape function to every lumping technique.

[14] if $p_E = 0$ then $U_E = \vec{0}$ and U_E can not be an eigenvector.

[15] the mono-model eigenvalues are obtained by replacing all the weight functions by 1 in (3.28) (see equation (3.31)).

(3.28) then becomes:

$$\omega^2 = \frac{1}{\left(\int_{\Omega_E} \hat{\alpha}^p \, d\Omega_E\right)} \sum_{i=1}^{\mathcal{N}} \left(\frac{\int_{\Omega_E} \frac{\partial N_i}{\partial x_{d(i)}} \, d\Omega_E}{\int_{\Omega_E} \rho_0 \hat{N}_i \, d\Omega_E} \right) \left(\int_{\partial\Omega_E} \alpha^p \rho_0 c^2 N_i \, \underline{n} \, d\partial\Omega_E \right) \cdot \underline{x}_{d(i)} \tag{3.29}$$

Note that for the Archimera approach, the study stops here as since $\hat{\alpha}^p = \alpha^p = 1$. Hence, for the Archimera approach, imposing $\hat{\alpha}^v = \bar{\alpha}^v = \alpha^v$ to be uniform on the element is sufficient to guarantee stability.

In order to ensure stability, we thus impose $\hat{\alpha}^p$ uniform on the element and set to:

$$\widetilde{\alpha}^p = \frac{\sum_{i=1}^{\mathcal{N}_N} \left(\frac{\int_{\Omega_E} \frac{\partial N_i}{\partial x_{d(i)}} \, d\Omega_E}{\int_{\Omega_E} \rho_0 \hat{N}_i \, d\Omega_E} \right) \left(\int_{\partial\Omega_E} \alpha^p \rho_0 c^2 N_i \underline{n} \, d\partial\Omega_E \right) \cdot \underline{x}_{d(i)}}{\sum_{i=1}^{\mathcal{N}_N} \left(\frac{\int_{\Omega_E} \frac{\partial N_i}{\partial x_{d(i)}} \, d\Omega_E}{\int_{\Omega_E} \rho_0 \hat{N}_i \, d\Omega_E} \right) \left(\int_{\partial\Omega_E} \rho_0 c^2 N_i \underline{n} \, d\Omega_E \right) \cdot \underline{x}_{d(i)}} \tag{3.30}$$

This way, the resulting eigenvalues are the same ones as for a mono-model formulation:

$$\omega^2 = \frac{1}{|\Omega_E|} \sum_{i=1}^{\mathcal{N}_N} \left(\frac{\int_{\Omega_E} \frac{\partial N_i}{\partial x_{d(i)}} \, d\Omega_E}{\int_{\Omega_E} \rho_0 \hat{N}_i \, d\Omega_E} \right) \left(\int_{\partial\Omega_E} \rho_0 c^2 N_i \, \underline{n} \, d\Omega_E \right) \cdot \underline{x}_{d(i)} \tag{3.31}$$

Remark 3.3.4. *Note that in the case of the wave problem considered here, using $\widetilde{\alpha}^p$ to define $\hat{\alpha}^p$ ensures hyperbolicity as the eigenvalues ω are exactly the same as those of the mono-model problem. This was not the case for the transport equation studied in chapter 2.*

Remark 3.3.5. *Note that when the velocity is integrated at mid time step (see **Remark** 3.3.2 and section 3.1.2), the calculations lead to the same conclusion (see Appendix D).*

3.3.3 Analysis of $\widetilde{\alpha}^p$ for specific elements

As was done in the previous chapter, this section is dedicated to the comparison of the definition of $\widetilde{\alpha}^p$ proposed in (3.30) with $\bar{\alpha}^p$, the value resulting from the numerical integration of α^p on the entire element:

$$\bar{\alpha}^p = \frac{1}{|\Omega_E|} \int_{\Omega_E} \alpha^p \, d\Omega_E \tag{3.32}$$

The goal is to underline why using $\widetilde{\alpha}^p$ is, once again, preferable. We recall that the critical time step is proportional to $\hat{\alpha}_p$ so that the higher its value, the more stable the approach.

3.3.3.1 A 1D element

Let us consider the one dimensional element presented in section 2.3.4.2 and represented in Figure 2.3. Once again, the value of $\widetilde{\alpha}^p$ is the samefor all considered cases and equal to $\frac{1}{2}(\alpha_{1,1}+\alpha_{1,2})$. The value of $\bar{\alpha}^p$, on the other hand, differs.

$$\begin{cases} \text{Case A: } \bar{\alpha}^p_A = \dfrac{1}{2}(\alpha_{1,1}+\alpha_{1,2}) & \text{so that } \bar{\alpha}^p_A = \hat{\alpha}^p \\ \text{Case B: } \bar{\alpha}^p_B = \dfrac{1}{2}(\alpha_{1,1}(1+\delta)L + \alpha_{1,2}(1-\delta)L) & \text{so that } \bar{\alpha}^p_B > \hat{\alpha}^p \\ \text{Case C: } \bar{\alpha}^p_C = \dfrac{1}{2}(\alpha_{1,1}(1-\delta)L + \alpha_{1,2}(1+\delta)L) & \text{so that } \bar{\alpha}^p_B < \hat{\alpha}^p \end{cases} \tag{3.33}$$

The analysis completed in section 2.3.4.2 is thus still valid for 1D elements. We recall its conclusions:

- If the inner boundary of the coupling zone is aligned with the mesh of the substrate and the outer one is aligned with the mesh of the patch, then $\bar{\alpha}^p$ induces a critical time greater or equal to the one induced by $\widetilde{\alpha}^p$. Yet, that latter is computationally feasible.
- In any other cases, expression $\widetilde{\alpha}^p$ should be used as it leads to a computationally feasible critical time step, which $\bar{\alpha}^p$ is not ensured to do.

Again, a parallel can be drawn with structural elastodynamics (see remark 2.3.3).

3.3.3.2 2D and 3D elements

Let us consider a triangular element with vertices $(S_i)_{i\in[|1;3|]}$, crossed by the boundary of the coupling zone so that the element is in one of the three cases A, B or C aforementioned in section 2.3.4.2 and represented in Figure 2.5 for 2D triangular elements.

First, we assume that the weight function is planar on the element so that α^p is linear on its edges. Under such an assumption, we can show[16] that $\widetilde{\alpha}^p = \frac{1}{3}(\alpha^p(S_1) + \alpha^p(S_2) + \alpha^p(S_3)) = \bar{\alpha}^p$. We obtained the same result in the previous chapter for $\widetilde{\alpha}^q$. In fact, the reasoning done in section 2.3.4.2 still holds. Its conclusions are recalled here:

- There are no ways to ensure that $\bar{\alpha}^p > \widetilde{\alpha}^p$ for an arbitrary element so that $\hat{\alpha}^p$ should always be set to $\widetilde{\alpha}^p$.
- It is recommended to align the inner boundary of the coupling zone with the mesh of the substrate as a preventive measure. Note that for the wave problem, this is not necessary as imposing $\hat{\alpha}^p = \widetilde{\alpha}^p$ ensures optimal stability. Yet, when extending to the Euler equations, this practical measure should be enforced.

Interestingly enough, the value that needs to be assigned to $\hat{\alpha}^p$ is not quite the same as the one found for $\hat{\alpha}^q$ in the previous chapter. Yet, they both only take into account the value of the weight functions along the boundary of the elements. Note that in the current case, such a value ensures optimal stability, that is, it leaves the critical time step unaltered for the wave problem.

[16] For calculations, see Appendix E.

Remark 3.3.6. *Note that although we are assuming, throughout this study, that the coupling zone are the same for both equations, the results hold if different coupling zones are chosen.*

Remark 3.3.7. *The stability results suggests to impose $\hat{\alpha}^v$ to be constant on every element. It is interesting to note that it was one of the approaches proposed for the treatment of the equilibrium equations for elastodynamics (see chapter 1).*

3.3.4 Illustration of previous results on test cases

3.3.4.1 Comparison between $\widetilde{\alpha}^p$ and $\bar{\alpha}^p$

In the following, we illustrate the importance of the previous results on the set of test cases introduced hereafter. Let us consider a first regular mesh of size 20m by 20m and made up of 1.0m by 1.0m quadrangles, as represented in Figure 3.1. The mesh of the patch is of size 10m by 10m and also made up of 1.0m by 1.0m quadrangles. It is overlapped in the center of the substrate and rotated by an angle θ, as represented in Figure 3.1. As seen previously, the critical time step for the wave problem only depends on the geometry and on the weight functions. Thus, when studying the stability, there are no need to set initial conditions. We recall that the critical time step and the elementary critical time steps are computed using definition 3.22.

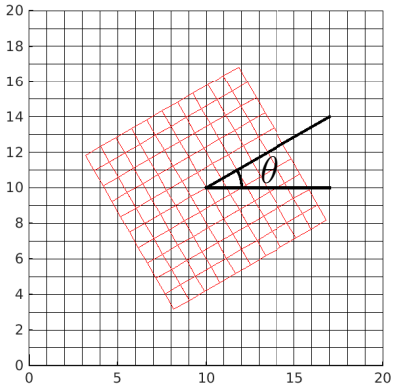

Figure 3.1: The substrate, in black, is 20m by 20m while the patch, in red, is 10m by 10m. Both are made up of unit quadrangles and the patch is rotated, with respect to the substrate, by an angle of θ.

In the previous sections, we made three recommendations to ensure stability for the Full Arlequin approach. First, we argued that aligning the boundaries of the coupling zone with the appropriate mesh ensures that the elementary critical time step does not tend to zero with α_0, the value of the weight parameter for the substrate in the free zone (see section 1.1.2). Secondly, we advised to impose a uniform weight on each element for the momentum equation and finally, we showed that using expression (3.36) to define $\hat{\alpha}^p$ ensured optimal stability. In order to show the relative efficiency of each parameter, we consider all eight combinations of these parameters which leads to the eight approaches numbered in Table 3.1.

Approach #	Γ_{in}	$\hat{\alpha}^p$	$\hat{\alpha}^v$
1	substrate	boundary	averaged
2	substrate	boundary	not averaged
3	substrate	volume	averaged
4	substrate	volume	not averaged
5	patch	boundary	averaged
6	patch	boundary	not averaged
7	patch	volume	averaged
8	patch	volume	not averaged

Table 3.1: Approaches numbering – The outer boundary of the coupling zone is always assumed to be aligned with the mesh of the patch while the inner boundary, denoted Γ_{in}, can be aligned with either one. The value of $\hat{\alpha}^p$ can either be defined on the 'volume' by expression (3.32) or on the 'boundary' using expression (3.36). Finally, $\hat{\alpha}^v$ is either averaged or not (we assume that $\hat{\alpha}^v = \bar{\alpha}^v$).

Two sets of test cases are considered. First, we consider the test case presented in Figure 3.1 for $\theta = 7.5°$. For each approach, we compute the ratio of the critical time step for the test case over the reference, optimal value of the test case[17] for different values of α_0. The meshes and the weight functions are represented in Figures 3.2 and 3.3 for an inner boundary of the coupling zone aligned with the mesh of the substrate and that of the patch respectively.

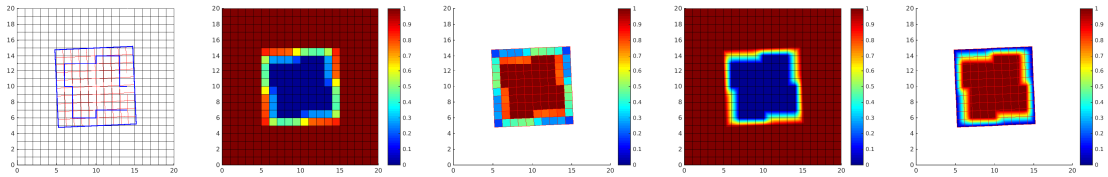

Figure 3.2: Multi-model mesh for the test case (left). The mesh of the substrate is represented in black while that of the patch is represented in red. The boundaries of the coupling zone are represented in blue. The weight functions are also represented, first α^v (center left) and then α^p (right). In this example, $\alpha_0 = 1.0 \times 10^{-3}$.

The computed ratios are represented in Figure 3.4. We can observe that only approaches 1 and 5, that is, the ones following our recommendations, yield an optimal time step. All the other ones do not reach optimal time step and although approaches 2, 3 and 4 still maintain a reasonably high time step, there are no way predicting what that values is or if it remains high for other problems. Note that approaches 6 to 8, for which the coupling zone is aligned with the mesh of the patch, are the ones for which the time step drops the most.

A second set of test case is now considered. The value of α_0 is now set to 1.0×10^{-6} and the angle θ varies from 0° to 45° (for symmetry reasons). A few of those configurations

[17] obtained with all weights functions set to 1.

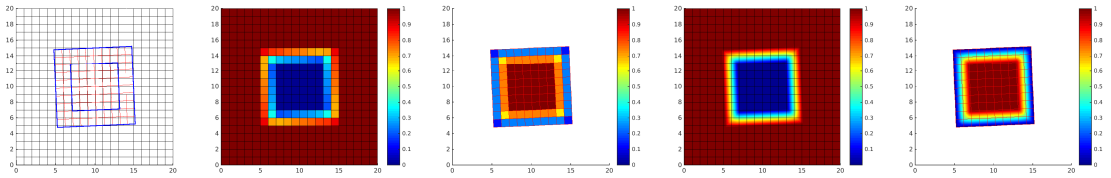

Figure 3.3: Multi-model mesh for the test case with boundaries of the coupling zone aligned with the mesh of the patch (left). The mesh of the substrate is represented in black while that of the patch is represented in red. The boundaries of the coupling zone are represented in blue. The weight functions are also represented, first α^v (center left) and then α^p (right). In this example, $\alpha_0 = 1.0 \times 10^{-3}$.

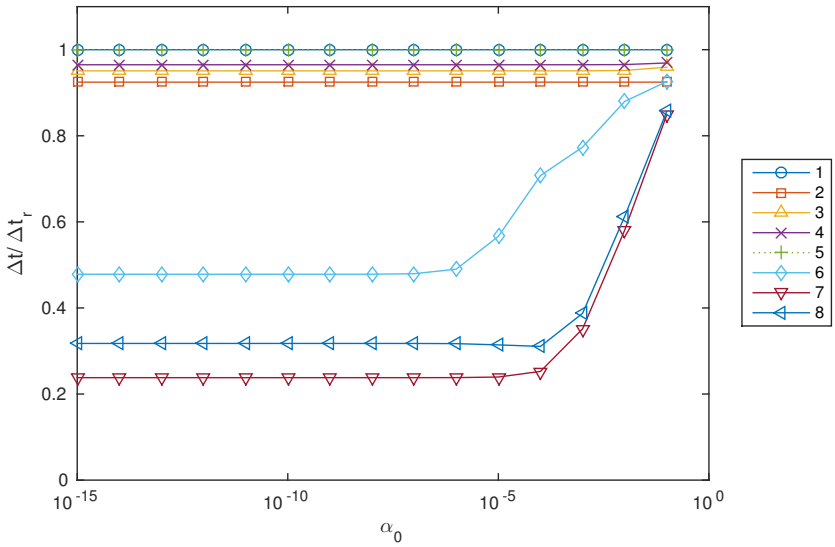

Figure 3.4: Evolution of the normalised elementary critical time step for different values of α_0 for all 8 approaches defined in Table 3.1.

are represented in Figures 3.5 and 3.6.

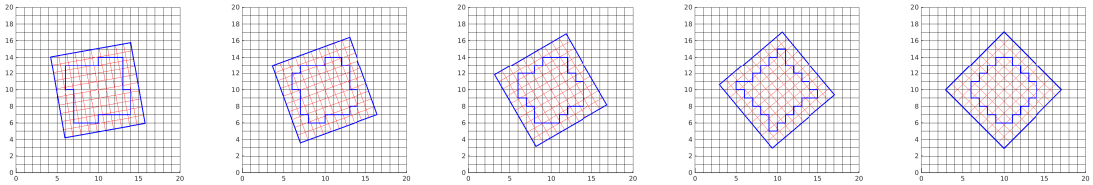

Figure 3.5: Multi-model meshes with boundaries of the coupling zone aligned with the mesh of the patch for angles (from left to right) 10°, 20°, 30°, 40° and 45°. The mesh of the substrate is represented in black while that of the patch is represented in red. The boundaries of the coupling zone are represented in blue. The inner boundary of the coupling zone is aligned with the mesh of the substrate.

For each approach and each configuration, we compute the ratio of the critical time step for the test case over the reference, optimal value[18]. The results are represented

[18] obtained with all weights functions set to 1.

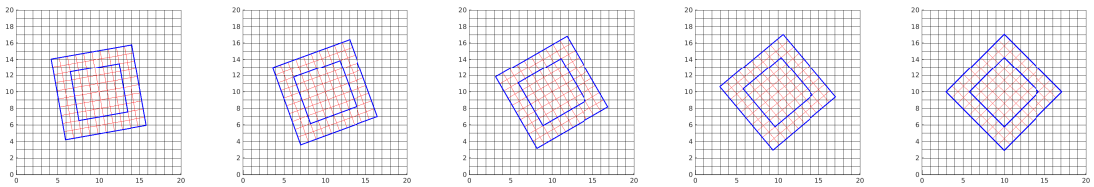

Figure 3.6: Multi-model meshes with boundaries (in blue) of the coupling zone aligned with the mesh of the patch for angles (from left to right) 10°, 20°, 30°, 40° and 45°. The mesh of the substrate is represented in black while that of the patch is represented in red.

in Figure 3.7.

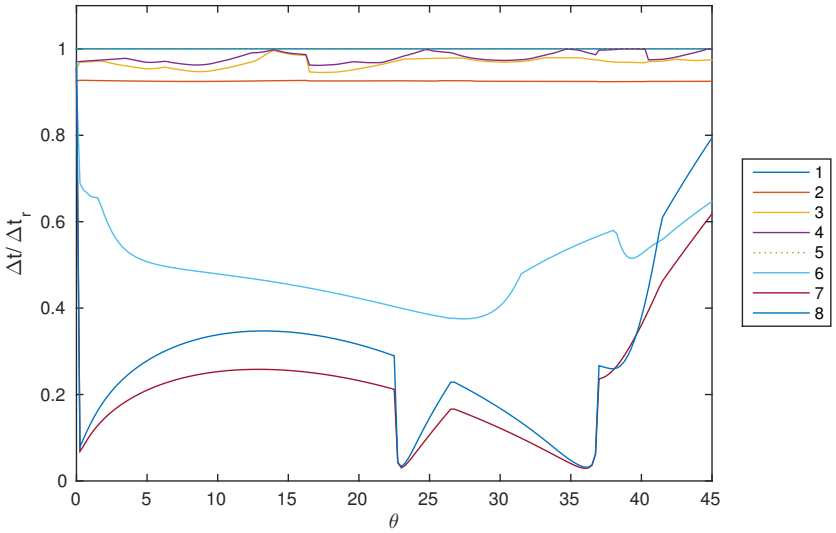

Figure 3.7: Evolution of the normalised elementary critical time step for different values of θ for all 8 approaches defined in Table 3.1.

We can observe that the only approaches that yield an optimal value and are independent of the geometry are approaches 1 and 5 which have in common that they follow our recommendations. Interestingly enough, even when $\theta = 0$, only the approaches 1 and 5 yield an optimal time step, as can be seen in Table 3.2. Note that as the mesh of the patch and the substrate are conforming for $\theta = 0$, approaches 1 and 5, 2 and 6, 3 and 7 and approaches 4 and 8 are the same.

Approach #	1-5	2-6	3-7	4-8
$\Delta t/\Delta t_r$	1.000	0.926	0.955	0.970

Table 3.2: Normed value of the critical time step for each approach ($\theta = 0$).

We can see that even when the meshes are conforming, the recommendations given should be followed in order to ensure that the Arlequin framework does not alter the time step.

Remark 3.3.8. *Note that it was verified that only approaches 1 and 5 guarantee an optimal critical time step for triangular elements.*

Remark 3.3.9. *Note that all these computations were done for a proper integration of the flow. Yet, if α^p is averaged on each edge, similar results and behaviours are obtained.*

3.3.4.2 Comparison between $\tilde{\alpha}^p$ and $\tilde{\alpha}^q$

We also compared the modified definition $\tilde{\alpha}^p$ from expression 3.30 with $\tilde{\alpha}^q$ from expression 3.32, the one obtained in the previous chapter (see section 2.3.4) for the convective transport equation alone. We consider the previous two tests introduced in the previous section and compare $\tilde{\alpha}^p$ and $\tilde{\alpha}^q$ when α_0 and θ vary. The different approaches and their specificities are given in Table 3.3.

Approach #	Γ_{in}	$\hat{\alpha}^p$	$\hat{\alpha}^v$
1	substrate	$\tilde{\alpha}^p$	averaged
A	substrate	$\tilde{\alpha}^q$	averaged
B	substrate	$\tilde{\alpha}^q$	not averaged
C	patch	$\tilde{\alpha}^q$	averaged
D	patch	$\tilde{\alpha}^q$	not averaged

Table 3.3: Approach numbering – The outer boundary of the coupling zone is always assumed to be aligned with the mesh of the patch while the inner boundary, denoted Γ_{in}, can be aligned with either one. The value of $\hat{\alpha}^p$ can either be set to $\tilde{\alpha}^p$ or $\tilde{\alpha}^q$. Finally, $\hat{\alpha}^v$ is either averaged or not (we assume that $\hat{\alpha}^v = \bar{\alpha}^v$).

The results of the first study, for which α_0 varies at a set $\theta = 7.5°$, are represented in FIGURE 3.8. We observe similar results as in the previous section. Indeed, we can see that (1) if $\hat{\alpha}^p$ is not set to $\hat{\alpha}^p$ then the optimal time step is not reached (for any value of α_0) and (2) aligning Γ_{in} with the substrate yields higher values of the time step than with the patch. An interesting difference is that the time step is not monotonously decreasing[19] for approach D which has not been observed for any other approaches. Finally, note that using $\tilde{\alpha}^q$ yields higher time step than $\bar{\alpha}^p$.

The results of the second study, for which θ varies at a set $\alpha_0 = 1.0 \times 10^{-6}$, are represented in FIGURE 3.9. The observations made for the first study hold. We can see that although all the approaches imposing $\hat{\alpha}^p = \tilde{\alpha}^q$ only reach the optimal time step occasionally. Moreover, we once again observe that when Γ_{in} is aligned the substrate the critical time step drops, especially around $\theta = 23°$ and $\theta = 36°$. Finally, let us mention that using $\tilde{\alpha}^q$ seems preferable to $\bar{\alpha}^p$.

[19] when α_0 decreases.

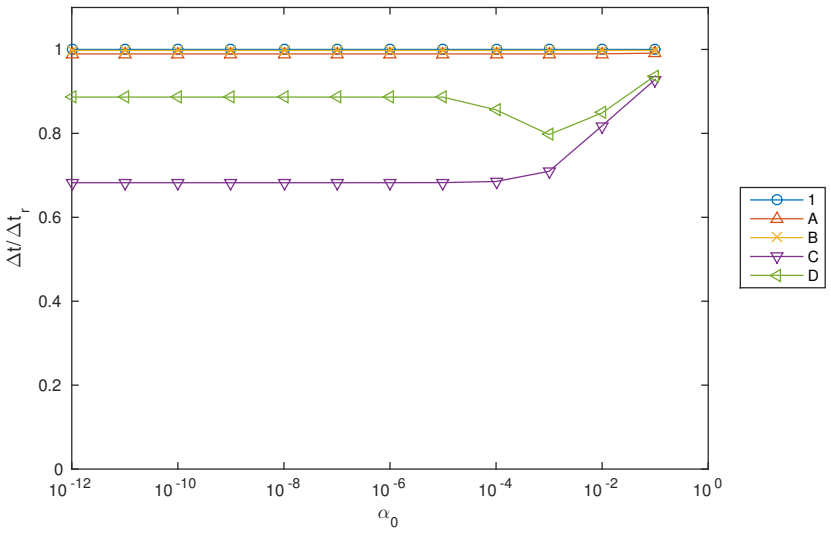

Figure 3.8: Evolution of the normalised elementary critical time step for different values of α_0 for all 5 approaches defined in Table 3.3.

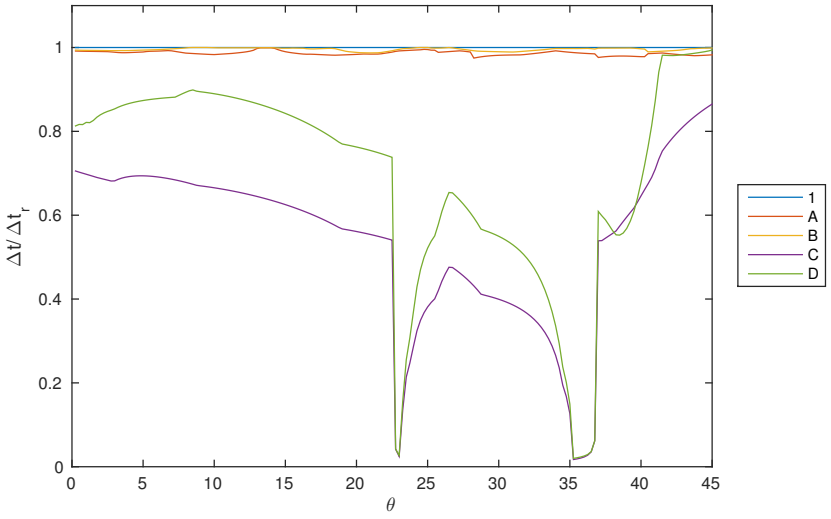

Figure 3.9: Evolution of the normalised elementary critical time step for different values of θ for all 5 approaches defined in Table 3.3.

3.3.5 Extension to the Euler equations

The aim of this last section is to propose an extension of formula (3.30) to both conservations equations of the Euler equations. In order to do so, we note that formula (3.30) can be written:

$$\widetilde{\alpha}^p = \frac{\displaystyle\sum_{i=1}^{\mathcal{N}_N} \left(\frac{\displaystyle\int_{\Omega_E} \frac{\partial N_i}{\partial x_{d(i)}}\, d\Omega_E}{\displaystyle\int_{\Omega_E} \rho_0 \hat{N}_i\, d\Omega_E} \right) \left(\int_{\partial\Omega_E} \alpha^p \phi_p N_i \underline{n}\, d\partial\Omega_E \right) \cdot \underline{x}_{d(i)}}{\displaystyle\sum_{i=1}^{\mathcal{N}_N} \left(\frac{\displaystyle\int_{\Omega_E} \frac{\partial N_i}{\partial x_{d(i)}}\, d\Omega_E}{\displaystyle\int_{\Omega_E} \rho_0 \hat{N}_i\, d\Omega_E} \right) \left(\int_{\partial\Omega_E} \phi_p N_i \underline{n}\, d\Omega_E \right) \cdot \underline{x}_{d(i)}} \tag{3.34}$$

with $\phi_p = \rho_0 c^2$ an 'convected-like' term. We thus propose to use the same formula for both transport equations of the Euler equations by substituting ϕ_q^n to ϕ_p in the above formula. We then obtain:

$$\hat{\alpha}^q(t^n) = \frac{\displaystyle\sum_{i=1}^{\mathcal{N}_N} \left(\frac{\displaystyle\int_{\Omega_E} \frac{\partial N_i}{\partial x_{d(i)}}\, d\Omega_E}{\displaystyle\int_{\Omega_E} \rho^n \hat{N}_i\, d\Omega_E} \right) \left(\int_{\partial\Omega_E} \alpha^q \phi_q^n N_i \underline{n}\, d\partial\Omega_E \right) \cdot \underline{x}_{d(i)}}{\displaystyle\sum_{i=1}^{\mathcal{N}_N} \left(\frac{\displaystyle\int_{\Omega_E} \frac{\partial N_i}{\partial x_{d(i)}}\, d\Omega_E}{\displaystyle\int_{\Omega_E} \rho^n \hat{N}_i\, d\Omega_E} \right) \left(\int_{\partial\Omega_E} \phi_q^n N_i \underline{n}\, d\partial\Omega_E \right) \cdot \underline{x}_{d(i)}} \tag{3.35}$$

with $q = \rho$ or ρE.

However, with such a definition, the value of the weight function for the mass matrices needs to be recalculated at every time step as it depends on both the flow ϕ_q^n. In order to circumvent this issue, we note that in formula (3.30), ρ_0 and c are uniform and constant over time so that we can rewrite the formula as

$$\hat{\alpha}^p_{modified} = \frac{\displaystyle\sum_{i=1}^{\mathcal{N}_N} \left(\frac{\displaystyle\int_{\Omega_E} \frac{\partial N_i}{\partial x_{d(i)}}\, d\Omega_E}{\displaystyle\int_{\Omega_E} \hat{N}_i\, d\Omega_E} \right) \left(\int_{\partial\Omega_E} \alpha^p N_i \underline{n}\, d\Omega_E \right) \cdot \underline{x}_{d(i)}}{\displaystyle\sum_{i=1}^{\mathcal{N}_N} \left(\frac{\displaystyle\int_{\Omega_E} \frac{\partial N_i}{\partial x_{d(i)}}\, d\Omega_E}{\displaystyle\int_{\Omega_E} \hat{N}_i\, d\Omega_E} \right) \left(\int_{\partial\Omega_E} N_i \underline{n}\, d\Omega_E \right) \cdot \underline{x}_{d(i)}} \tag{3.36}$$

This formula no longer introduces the flow nor the density and is thus independent of time. This is why, in this work, we chose to impose $\hat{\alpha}^q = \hat{\alpha}^p_{modified}$ for $q = \rho$ or ρE. Let us note that this expression is none other than the one that guarantees an optimal time step for the wave equation problem.

As seen previously, the inner boundary of the coupling zone should be aligned with the mesh of the substrate as a preventive measure (see section 3.3.3.2). Finally, we recall that, in practice, the time step for the Euler equations is computed as follows:

$$\Delta t = \text{csta} \times \min_{E \in \mathcal{S}_E} \frac{L_E}{|v_E| + |c_E|} \tag{3.37}$$

where L_E is a characteristic length of the element E, $|v_E|$ a norm of the velocity in that element, $|c_E|$ the norm of the speed velocity in the element and csta the security coefficient.

Note that in all the simulations presented in the next chapter, the recommendations detailed here were all followed and no stability issues were observed.

3.4 Conclusion

In this chapter, we formulated two multi-model approaches for the treatment of the fluid component in view of FSI applications. In particular, this chapter put emphasis on the stability of such multi-model approaches.

As the influence of the multi-model frameworks on the stability can not be studied for the non linear Euler equations, we introduced the equivalent acoustic problem. A recurring reasoning was led as we first recalled that it is sufficient to study the stability of the problem on a single element. Then, we introduced the relevant generalized eigenvalue problem whose eigenvalues define the critical time step. Next, we studied the influence of the multi-model frameworks on those eigenvalues and, thus, on the critical time step. Finally, we illustrated how the approaches proposed ensure a computationally feasible time step, which is not, a priori, guaranteed.

Now that we have defined two multi-model approaches for the treatment of the Euler equations – and showed that they were stable when explicit time integrators are used – we study the relative accuracy of each approach. This is done in the next chapter.

Chapter 4

Accuracy study of multi-model approaches for the explicit integration of the Euler equations

Contents

The objective of this thesis is to develop a multi-model approach able to account for local effects in transient FSI[1] simulations. In the last chapter, we formulated two multi-model approaches for the treatment of fluid dynamics. In order to ensure that they are computationally stable, we led a stability study and gave practical recommendations. In this chapter, we study the accuracy of the two multi-model approaches in order to determine if one is more precise than the other and should therefore be preferred for FSI applications.

In order to study the accuracy, we first consider a test case at equilibrium (section 4.1) and ensure that the fluid remains still (section 4.2)). Then, we introduce the strategy for the study of accuracy and briefly introduce two test cases (section 4.3). A convergence study is led on a test case for an ideal gas law as a first study of accuracy 4.4. Next, a precision study of these approaches is led on another test case for two gas laws 4.5. Finally, we conclude by discussing the advantages of using either approaches (section 4.6).

[1]Fluid Structure Interaction.

4.1 Steady state case

An easy test case for testing an approach is to observe if it maintains a stable equilibrium. Indeed, when at a stable equilibrium, the solution is supposed to remain constant over time and it is thus easy to evaluate if the solution yielded by the multi-model approaches is accurate.

We thus consider the test case presented in Figure 4.4 whose mesh is introduced in section 4.4. We assume that both models are filled with a still fluid (no initial velocity) at uniform pressure and density equal to $p_0 = 1.0 \times 10^5$ Pa and $\rho_0 = 1.30$ kg.m^{-3} respectively. The heat capacity ratio is equal to $\gamma = 1.402$, which is representative of typical atmospheric conditions.

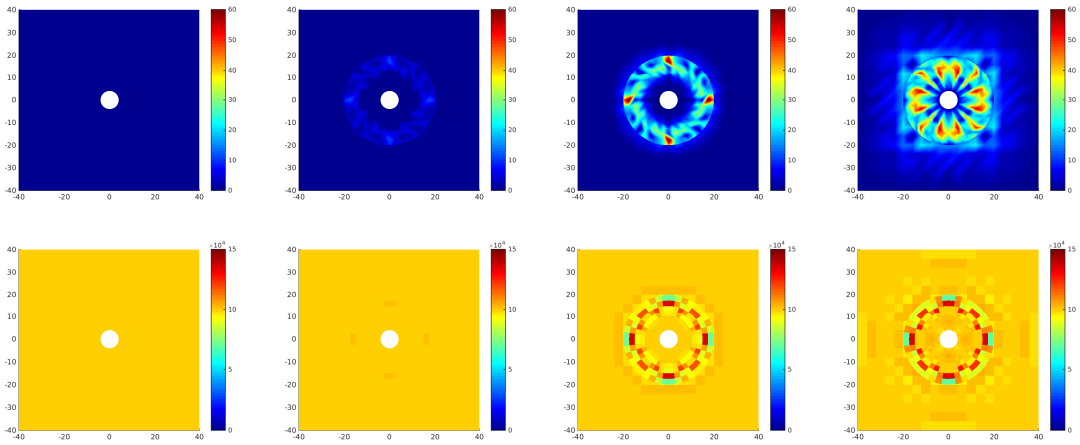

Figure 4.1: Evolution of the velocity (top) and pressure (bottom) at times $t_0 = 0$ms, $t_1 = 1$ms, $t_2 = 10$ms and $t_3 = 100$ms (from left to right).

We can observe in Figure 4.1 that the fluid does not remain still. In fact, velocities of the order of magnitude of the speed of sound[2] arise and variations of up to 50% of p_0 appear after[3] 10ms. The quantities $\|v\|_{L^2(\Omega)}(t)$ and $\|p - p_0\|_{L^1(\Omega)}(t)$ are computed for both multi-model approaches and represented in Figure 4.2.

4.2 Analysis of divergence-free force terms

Due to the introduction of the weight functions[4] in the considered formulations, the discrete Full Arlequin and Archimera problems are not able to cope with divergence-free force terms such as a uniform pressure so that a specific treatment is then needed. In order to illustrate this numerical phenomenon, let us consider, for instance, the case of a cylinder with non-deformable boundaries introduced in the previous section.

It is clear that the addition of any uniform pressure field to the entire domain should not alter the solution for the kinematic quantities. In the next sections, we show how

[2] An ideal gas law is used so that $c_s \approx 328$m.$^{-1}$, see section 4.3.

[3] A shock wave would have had the time to travel 30m during that time.

[4] See section 3.2.

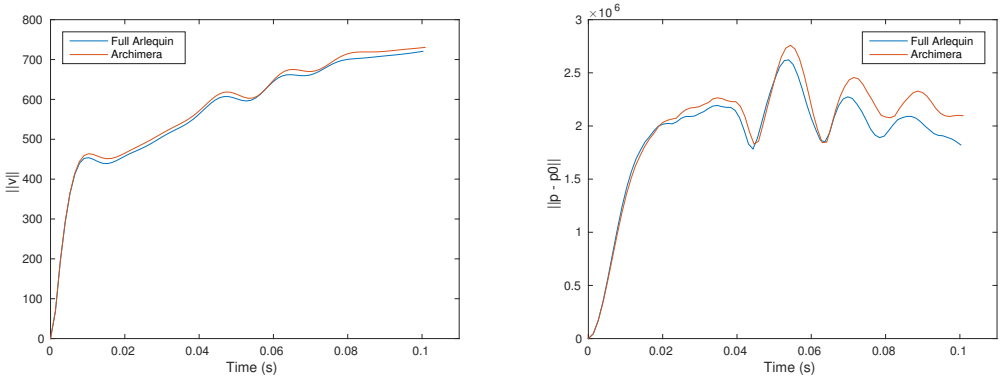

Figure 4.2: Evolution of $\|\underline{v}\|$ and $\|p - p_0\|$ over time.

this is the case for the continuous formulation but not for the discrete one. Note that as we only consider the momentum equation, the following is both valid for the Full Arlequin and Archimera approaches.

4.2.1 Continuous formulation

We thus consider the following problem, for which the time is discretized[5] but the variables are continuous on the domain. For the sake of conciseness, we neglect the convective terms.

Given $\{\rho_i^n, p_i^n\}$, $i \in \{1,2\}$, *the accelerations on each model* $\underline{\dot{v}}_1^n \in H_0^1(\Omega_1)$, $\underline{\dot{v}}_2^n \in H^1(\Omega_2)$ *and the Lagrange multiplier* $\underline{\lambda}_v \in H^1(\Omega_c)$ *are solutions of*:

$$\forall \underline{w}_1 \in H_0^1(\Omega_1),\ \forall \underline{w}_2 \in H^1(\Omega_2),\ \forall \underline{\mu} \in H^1(\Omega_c),$$

$$\begin{cases} \displaystyle\int_{\Omega_1} \hat{\alpha}_1^v \underline{\dot{v}}_1^n \cdot \underline{w}_1 \, dx + c_m(\underline{w}_1, \underline{\lambda}_v) = \int_{\Omega_1} \bar{\alpha}_1^v p_1^n \underline{\underline{I}} : \underline{\underline{\nabla w_1}} \, dx & \text{(4.1a)} \\ \displaystyle\int_{\Omega_2} \hat{\alpha}_2^v \underline{\dot{v}}_2^n \cdot \underline{w}_2 \, dx - c_m(\underline{w}_2, \underline{\lambda}_v) = \int_{\Omega_2} \bar{\alpha}_2^v p_2^n \underline{\underline{I}} : \underline{\underline{\nabla w_2}} \, dx & \text{(4.1b)} \\ c_m(\underline{\dot{v}}_1^n - \underline{\dot{v}}_2^n, \underline{\mu}) = 0 & \text{(4.1c)} \end{cases}$$

Then, if a uniform pressure field p_0 is added to both p_1 and p_2, the accelerations are unchanged and a new Lagrange multiplier $\underline{\lambda}_v + \underline{\lambda}_0$ needs to be found such that:

$$\forall \underline{w}_1 \in H_0^1(\Omega_1),\ \forall \underline{w}_2 \in H^1(\Omega_2),$$

$$\begin{cases} c_m(\underline{w}_1, \underline{\lambda}_0) = \displaystyle\int_{\Omega_1} \bar{\alpha}_1^v p_0 \underline{\nabla} \cdot \underline{w}_1 \, dx & \text{(4.2a)} \\ c_m(\underline{w}_2, \underline{\lambda}_0) = -\displaystyle\int_{\Omega_2} \bar{\alpha}_2^v p_0 \underline{\nabla} \cdot \underline{w}_2 \, dx & \text{(4.2b)} \end{cases}$$

As $\bar{\alpha}_1^v + \bar{\alpha}_2^v = 1$ and because $\bar{\alpha}_1^v$ is uniformly equal to $\bar{\alpha}_{1_f}^v$ on Ω_f, equation (4.2b) gives:

$$\forall \underline{w}_2 \in H^1(\Omega_2),$$

[5] See section 3.1.2.

$$c_m(\underline{w}_2, \underline{\lambda}_0) = -\int_{\Omega_2} p_0 \underline{\nabla} \cdot \underline{w}_2 \, dx + \int_{\Omega_2} \bar{\alpha}_1^v p_0 \underline{\nabla} \cdot \underline{w}_2 \, dx \tag{4.3a}$$

$$= -\int_{\partial\Omega_2} p_0 \underline{w}_2 \cdot \underline{n} \, dx + \int_{\Omega_c} \bar{\alpha}_1^v p_0 \underline{\nabla} \cdot \underline{w}_2 \, dx + \int_{\partial\Omega_f} \bar{\alpha}_{1f}^v p_0 \underline{w}_2 \cdot \underline{n} \, dx \tag{4.3b}$$

Furthermore, $\bar{\alpha}_1^v$ being uniformly equal to 1 on $\Omega_1 \backslash \Omega_2$ and uniform on Ω_f, the equation (4.2a) gives:

$\forall \underline{w}_1 \in H_0^1(\Omega_1)$,

$$c_m(\underline{w}_1, \underline{\lambda}_0) = -\int_{\partial\Omega_2} p_0 \underline{w}_1 \cdot \underline{n} \, dx + \int_{\Omega_C} \bar{\alpha}_1^v p_0 \underline{\nabla} \cdot \underline{w}_1 \, dx + \int_{\partial\Omega_f} \bar{\alpha}_{1f}^v p_0 \underline{w}_1 \cdot \underline{n} \, dx \tag{4.4}$$

Assuming a sufficent regularity of the domain Ω_c, there exist continuous extension operators from $H^1(\Omega_c)$ to $H_0^1(\Omega_1)$ and to $H^1(\Omega_2)$ (see, *e.g.*, [178]). Besides, the restriction of an element of $H_0^1(\Omega_1)$ or $H^1(\Omega_2)$ to Ω_1 belongs to $H^1(\Omega_c)$. Then, the two equations (4.2a) and (4.2b) are equivalent to:

$\forall \underline{w}_c \in H^1(\Omega_c)$,

$$c_m(\underline{w}_c, \underline{\lambda}_0) = -\int_{\partial\Omega_2} p_0 \underline{w}_c \cdot \underline{n} \, dx + \int_{\Omega_C} \bar{\alpha}_1^v p_0 \underline{\nabla} \cdot \underline{w}_c \, dx + \int_{\partial\Omega_f} \bar{\alpha}_{1f}^v p_0 \underline{w}_c \cdot \underline{n} \, dx \tag{4.5}$$

Then, c_m being an inner product of $H^1(\Omega_c)$, and assuming that the right hand side is a continuous linear functional of $H^1(\Omega_c)$ with respect to w_c, then the Riesz representation theorem gives that there exists a unique $\underline{\lambda}_0 \in H^1(\Omega_c)$ solution of this equation. So, as expected, the solution of the continuous arlequin problem for the kinematic fields are not affected by the addition of a uniform component in the pressure field.

Remark 4.2.1. *If the weight functions are chosen uniform in the coupling zone, then expression* (4.5) *becomes:*

$\forall \underline{w}_c \in H^1(\Omega_c)$,

$$c_m(\underline{w}_c, \underline{\lambda}_0) = (\bar{\alpha}_{1c}^v - 1) \int_{\partial\Omega_2} p_0 \underline{w}_c \cdot \underline{n} \, dx + \left(\bar{\alpha}_{1f}^v - \bar{\alpha}_{1c}^v\right) \int_{\partial\Omega_f} p_0 \underline{w}_c \cdot \underline{n} \, dx \tag{4.6}$$

4.2.2 Discrete formulation

However, as observed in the representative example in section 4.1, the previous result does not hold for the discrete problem. Let $\mathcal{T}_1$ and $\mathcal{T}_2$ be the meshes of each model respectively. We now have $\underline{w}_1 \in \mathcal{V}_1 \subset H_0^1(\Omega_1)$, $\underline{w}_2 \in \mathcal{V}_2 \subset H^1(\Omega_2)$ and $\underline{\lambda}_0 \in \mathcal{M} \subset \mathcal{V}_1$ and equations (4.2a) and (4.2b) are no longer equivalent to equation (4.5). Then, there is no guarantee that there a Lagrange multiplier exists such that (4.2a) and (4.2b) are both verified. Hence, the accelerations can no longer be assumed to be null so that it is as if ghost forces arise. In the following, we propose a way to handle these ghost forces.

Let us now consider the discrete system resulting from the discretization of (4.1) (see Chapter 3 for notations):

$$\begin{pmatrix} \underline{\underline{M}}^n_{v,1} & \underline{\underline{0}} & \underline{\underline{C}}_1^T \\ \underline{\underline{0}} & \underline{\underline{M}}^n_{v,2} & \underline{\underline{C}}_2^T \\ \underline{\underline{C}}_1 & \underline{\underline{C}}_2 & \underline{\underline{0}} \end{pmatrix} \begin{pmatrix} \underline{\dot{v}}_1^n \\ \underline{\dot{v}}_2^n \\ \underline{\lambda} \end{pmatrix} = \begin{pmatrix} \underline{F}_1 + p_0 \underline{F}_1^0 \\ \underline{F}_2 + p_0 \underline{F}_2^0 \\ \underline{0} \end{pmatrix} \tag{4.7}$$

$p_0\underline{F}_1^0$ and $p_0\underline{F}_2^0$ represent the uniform component of the pressure field. Assuming that the discretized equations (4.2a) and (4.2b) both have solutions denoted $\underline{\lambda}_1$ and $\underline{\lambda}_2$, that is, $\underline{\underline{C}}_1^T\underline{\lambda}_1 = p_0\underline{F}_1^0$ and $\underline{\underline{C}}_2^T\underline{\lambda}_2 = p_0\underline{F}_2^0$, then the system can be written:

$$\begin{pmatrix} \underline{\underline{M}}_1 & \underline{\underline{0}} & \underline{\underline{C}}_1^T \\ \underline{\underline{0}} & \underline{\underline{M}}_2 & -\underline{\underline{C}}_2^T \\ \underline{\underline{C}}_1 & -\underline{\underline{C}}_2 & \underline{\underline{0}} \end{pmatrix} \begin{pmatrix} \underline{\dot{v}}_1^n \\ \underline{\dot{v}}_2^n \\ \underline{\lambda}' \end{pmatrix} = \begin{pmatrix} \underline{F}_1 + \underline{\underline{C}}_1^T \left(\frac{\underline{\lambda}_1 - \underline{\lambda}_2}{2}\right) \\ \underline{F}_2 + \underline{\underline{C}}_2^T \left(\frac{\underline{\lambda}_1 - \underline{\lambda}_2}{2}\right) \\ \underline{0} \end{pmatrix} \tag{4.8}$$

where $\underline{\lambda}' = \underline{\lambda} - \frac{1}{2}(\underline{\lambda}_1 + \underline{\lambda}_2)$. We can observe that the perturbation at the right hand side of the system due to the uniform component of the pressure field is proportional to the difference between the solution of the discretized equations (4.2a) and (4.2b). A simple way to filter out the uniform component of the pressure is to enrich the coupling matrices as follows:

$$\begin{pmatrix} \underline{\underline{M}}_1 & \underline{\underline{0}} & \underline{\underline{C}}_1^T & \underline{F}_1^0 \\ \underline{\underline{0}} & \underline{\underline{M}}_2 & -\underline{\underline{C}}_2^T & \underline{F}_2^0 \\ \underline{\underline{C}}_1 & -\underline{\underline{C}}_2 & \underline{\underline{0}} & 0 \\ \underline{F}_1^{0T} & \underline{F}_2^{0T} & 0 & 0 \end{pmatrix} \begin{pmatrix} \underline{\dot{v}}_1^n \\ \underline{\dot{v}}_2^n \\ \underline{\lambda} \\ \eta \end{pmatrix} = \begin{pmatrix} \underline{F}_1 + p_0 \underline{F}_1^0 \\ \underline{F}_2 + p_0 \underline{F}_2^0 \\ \underline{0} \\ 0 \end{pmatrix} \tag{4.9}$$

which is equivalent to:

$$\eta = p_0 \tag{4.10a}$$

$$\begin{pmatrix} \underline{\underline{M}}_1 & \underline{\underline{0}} & \underline{\underline{C}}_1^T \\ \underline{\underline{0}} & \underline{\underline{M}}_2 & -\underline{\underline{C}}_2^T \\ \underline{\underline{C}}_1 & -\underline{\underline{C}}_2 & \underline{\underline{0}} \end{pmatrix} \begin{pmatrix} \underline{\dot{v}}_1^n \\ \underline{\dot{v}}_2^n \\ \underline{\lambda}' \end{pmatrix} = \begin{pmatrix} \underline{F}_1 \\ \underline{F}_2 \\ \underline{0} \end{pmatrix} \tag{4.10b}$$

The computation of $\underline{F}_1^0$ and $\underline{F}_2^0$ is completed before the time integration is initiated by creating a fictive motionless problem for a fluid at a uniform pressure. The η unknown will then match the actual pressure uniform component in the coupling zone at each time step. In the case of a problem with non fixed-wall boundaries, only the degrees of freedom related to shape functions intersecting the coupling zone should be kept in the computed $\underline{F}_1^0$ and $\underline{F}_2^0$. The values of the degrees of freedom located at the non-fixed wall boundaries must then be set to zero.

Remark 4.2.2. *This phenomenon is not restricted to the pressure field for fluid dynamics but, more generally, to any divergence-free component in a force/flux-like term. Indeed, in the general case of a conservation equation, every divergence-free component in the flux (which then should have no influence on the solution) will show the same pathology for some given discretization due to the weight functions which make such a component not divergence-free any more. For example, for explicit structural dynamics problems considered in 1, the stress field will behave the same. Indeed, if at a stable equilibrium, the solution is a uniform stress field on the domain, ghost forces will arise.*

Yet, it usually does not occur for structural problems as the stress field at equilibrium is usually null[6]. Yet, special care should be taken when considering a residual stress field or pre-stressed material. Note that this phenomenon is not limited to dynamics and can occur for static structural computation within the Arlequin framework.

The stability study and the extension of the Arlequin framework to divergence-free force terms are now complete. In the next section, we compare the accuracy of the different multi-model approaches on two test cases.

4.3 Applications and examples

In the following test cases, the equation of state is assumed to be that of the ideal gas law, that is, $p = (\gamma - 1)\rho e$, where γ is the heat capacities ratio. It is representative of how air behaves in normal conditions.

In the following two sections, we consider two test cases and for each one, we introduce a quantity of interest to evaluate which of the two multi-model approaches developed in this work is more accurate. A "Full Chimera" approach is also considered for which all three Euler equations are treated by a Chimera-like treatment. The purpose of introducing such a method is to compare the accuracy of the multi-model approaches developed in this work with the one yielded by a reference approach in the literature. Finally, one last multi-model approach is considered which uses a Chimera-like approach for the treatment of the momentum equation and the Arlequin framework for the treatment of the convective transport equations. The aim of considering such an approach, hereafter referred to as the Chimequin approach[7], is to observe if trends arise due to the framework used. The four multi-model approaches are recalled in Table 4.1.

		Momentum	
		Arlequin	Chimera
Transport	Arlequin	Full Arlequin	Archimera
	Chimera	Chimequin	Full Chimera

Table 4.1: Multi-model approaches designation depending on the framework chosen for the momentum equation and the one for the transport equations (conservation of mass and energy equations).

4.4 Local introduction of a fixed cylinder

4.4.1 Presentation

We consider a closed square domain filled with a fluid. In its center lies a rigid, fixed, cylinder as shown in Figure 4.3. The domain is 100m long while the cylinder has a 4m

[6]This is the case for the applications considered in 1 which is why ghost forces were not observed.
[7]for hybrid CHIMEra/ArlEQUIN approach.

wide diameter. The fluid is assumed to slip on every wall of the domain, including the cylinder. There are no initial motion in the domain[8] and the fluid is assumed to be in two different states. In one region (in blue in Figure 4.3), the initial density of the fluid is $\rho_L = 1.3$ kg.m^{-3} and its initial pressure is $p_L = 1.0 \times 10^5$ Pa. In the second region right of the cylinder (in brown in Figure 4.3), the density is of the fluid is $\rho_R = 13$ kg.m^{-3} and its initial pressure is $p_R = 1.0 \times 10^6$ Pa.

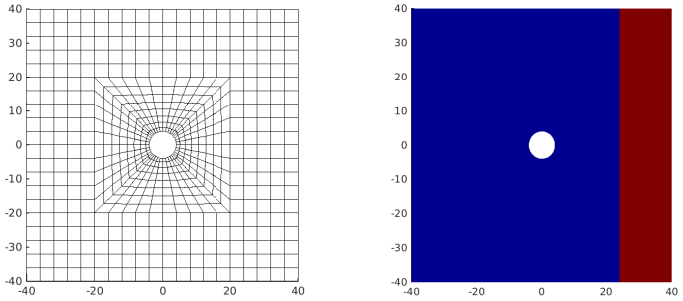

Figure 4.3: The mesh of the mono-model problem formulation is represented (left) as well as the initial conditions (right).

A shock wave is initiated at the boundary of the two zones ($x = 24$m). It spreads leftward and hits the cylinder. As the wave advances past the cylinder, the wave bounces off its right side and the pressure on its left side decreases. The wave continues to propagate until it reaches the left wall which is when the simulation ends.

An example of a mono-model mesh is represented in Figure 4.3. Away from the cylinder, the mesh is made of 2m $\times$ 2m square quadrangles. The quadrangles progressively diminish in size towards the cylinder so that the cylinder is discretized by 40 edges. the reference solution is obtained on a mesh four times smaller than the one in Figure 4.3, that is, with 0.5m $\times$ 0.5m quadrangles away from the cylinder and a cylinder discretized with 169 edges.

The multi-model meshes are represented in Figure 4.4. The main domain, referred to as the substrate and in black in the figure, is uniformly composed of the same 2m $\times$ 2m square quadrangles. The patch, in red in the figure, models the cylinder. Its mesh is in the shape of a web, which is adapted to circles, and is designed so that the cylinder has a similar discretization as in the mono-model mesh (see Figure 4.4). On the farthest ring of the mesh, the elements are about the same size as those of the substrate. Finally, in Figure 4.4, we show the zones as well as the weight functions.

In all the simulations presented hereafter, we used a quadratic and linear artificial viscosity[9] set to 2.56 and 0.1 respectively while the security coefficient is set[10] to csta = 0.45. When relevant, we imposed $\hat{\alpha}^{\rho} = \hat{\alpha}^{\rho E} = \hat{\alpha}^{p}$ and $\alpha_0 = 1.0 \times 10^{-6}$. As usual, the outer boundary of the coupling zone Γ_{out} is aligned with the mesh of the patch while the inner one is aligned with the one of the substrate. The size of the coupling zone is such that two at least one entire element of the patch is included in the radial direction for every angle. For all three equations, the mediator space is discretized as the substrate.

[8] the velocity is uniformly equal to 0.

[9] See for instance [179]. Note that the artificial is necessary in order to handle the dissipated energy by shocks.

[10] The use of artificial viscosity imposes the security coefficient to be inferior to 0.5.

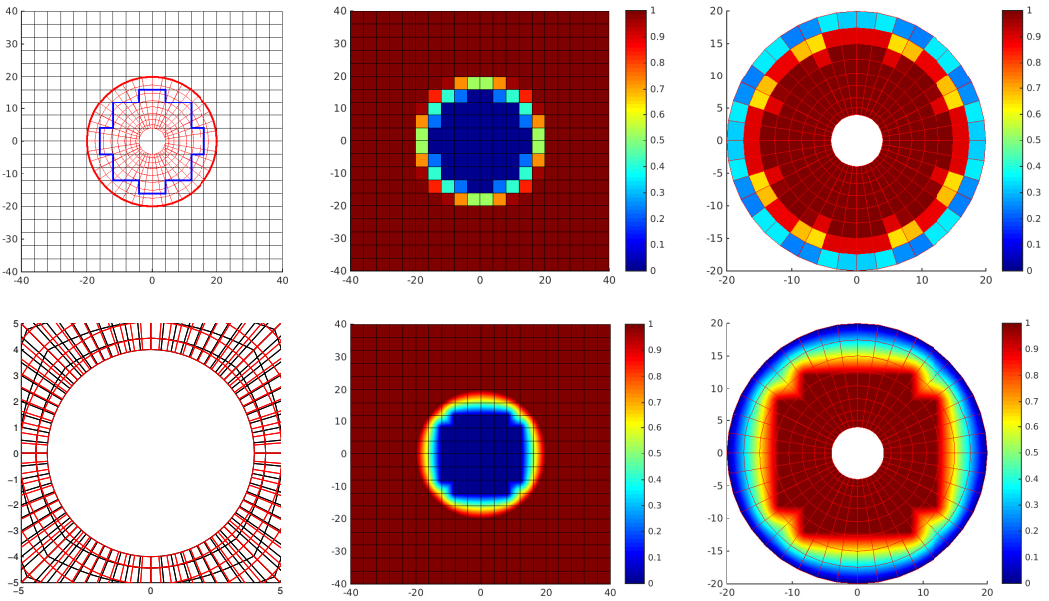

Figure 4.4: TOP LEFT – The multi-model meshes are represented as well as the boundaries $\Gamma_{1\to 2}$ (red) and $\Gamma_{2\to 1}$ (blue). BOTTOM LEFT – Comparison of the discretization of the cylinder for the multi-model mesh (red) and the mono-model one (black). As can be observed, they are fairly similar. CENTER – Representation of the weight function α_1^v (top) and α_1^q (bottom) for the substrate. RIGHT – Representation of the weight function α_2^v (top) and α_2^q (bottom) for the patch.

4.4.2 Solution

The solution for the norm of the velocity as well as the pressure are represented in the following figures. The reference solution is presented in Figure 4.5 and the multi-model ones in Figures 4.6 - 4.9.

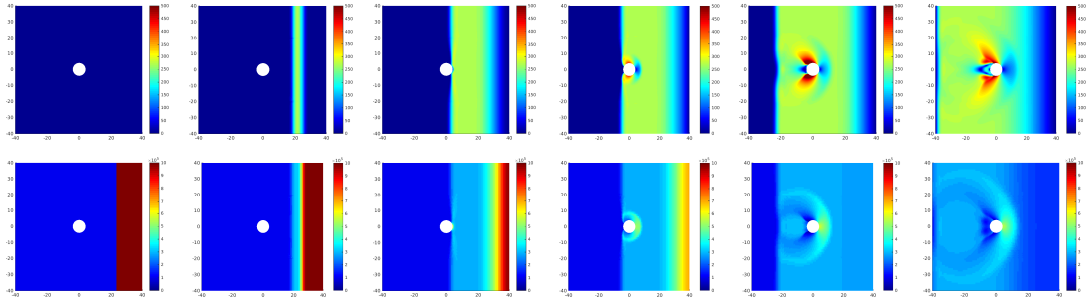

Figure 4.5: Reference solution for the velocity v (top row) and the pressure p at instants (from left to right) $t_0 = 0.0$ms, $t_1 = 10.0$ms, $t_2 = 40.0$ms, $t_3 = 55.0$ms, $t_4 = 90.0$ms and $t_0 = 120.0$ms.

We can observe that, visually, the solutions yielded by the multi-model approaches are very similar to the reference one.

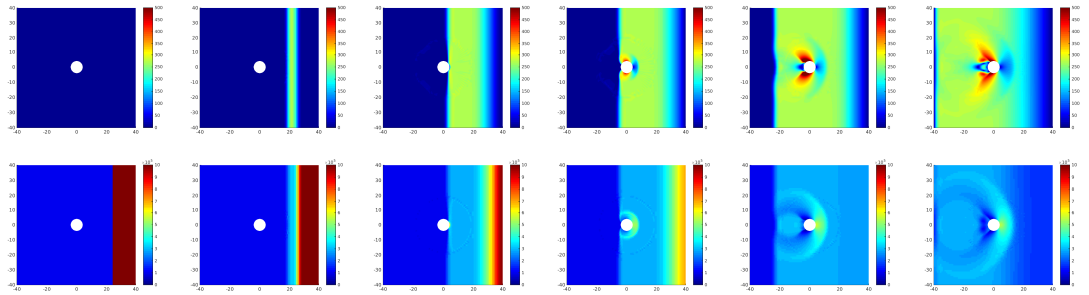

Figure 4.6: Full Arlequin solution for the velocity v (top row) and the pressure p at instants (from left to right) $t_0 = 0.0$ms, $t_1 = 10.0$ms, $t_2 = 40.0$ms, $t_3 = 55.0$ms, $t_4 = 90.0$ms and $t_0 = 120.0$ms.

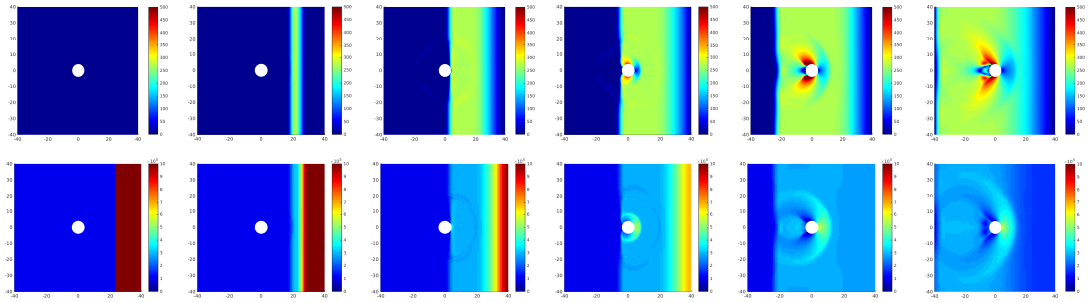

Figure 4.7: Archimera solution for the velocity v (top row) and the pressure p at instants (from left to right) $t_0 = 0.0$ms, $t_1 = 10.0$ms, $t_2 = 40.0$ms, $t_3 = 55.0$ms, $t_4 = 90.0$ms and $t_0 = 120.0$ms.

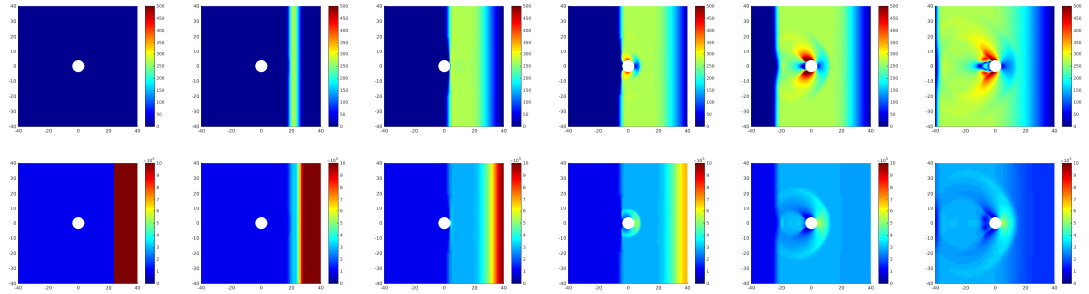

Figure 4.8: Full Chimera solution for the velocity v (top row) and the pressure p at instants (from left to right) $t_0 = 0.0$ms, $t_1 = 10.0$ms, $t_2 = 40.0$ms, $t_3 = 55.0$ms, $t_4 = 90.0$ms and $t_0 = 120.0$ms.

4.4.3 Study of the accuracy of the multi-model approaches

In order to evaluate the accuracy of the multi-model approaches, we introduce the following quantity of interest:

$$F_p(t) = \int_{\text{cylinder}} p(t)\ \underline{n} \cdot \underline{x}\ d\Omega \tag{4.11}$$

where p denotes the pressure, $\underline{n}$ the normal to the cylinder and $\underline{x}$ the unit vector in the horizontal direction. F_p, the resulting force along the x axis, is represented in Figure

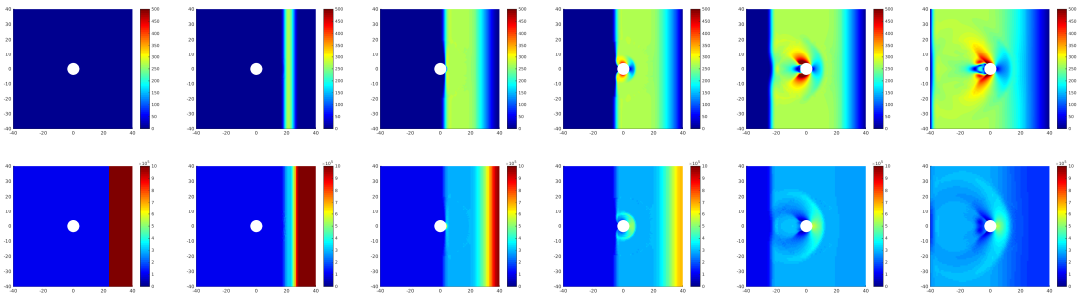

Figure 4.9: Chimequin solution for the velocity v (top row) and the pressure p at instants (from left to right) $t_0 = 0.0$ms, $t_1 = 10.0$ms, $t_2 = 40.0$ms, $t_3 = 55.0$ms, $t_4 = 90.0$ms and $t_0 = 120.0$ms.

4.10 for all multi-model approaches and compared with the reference solution.

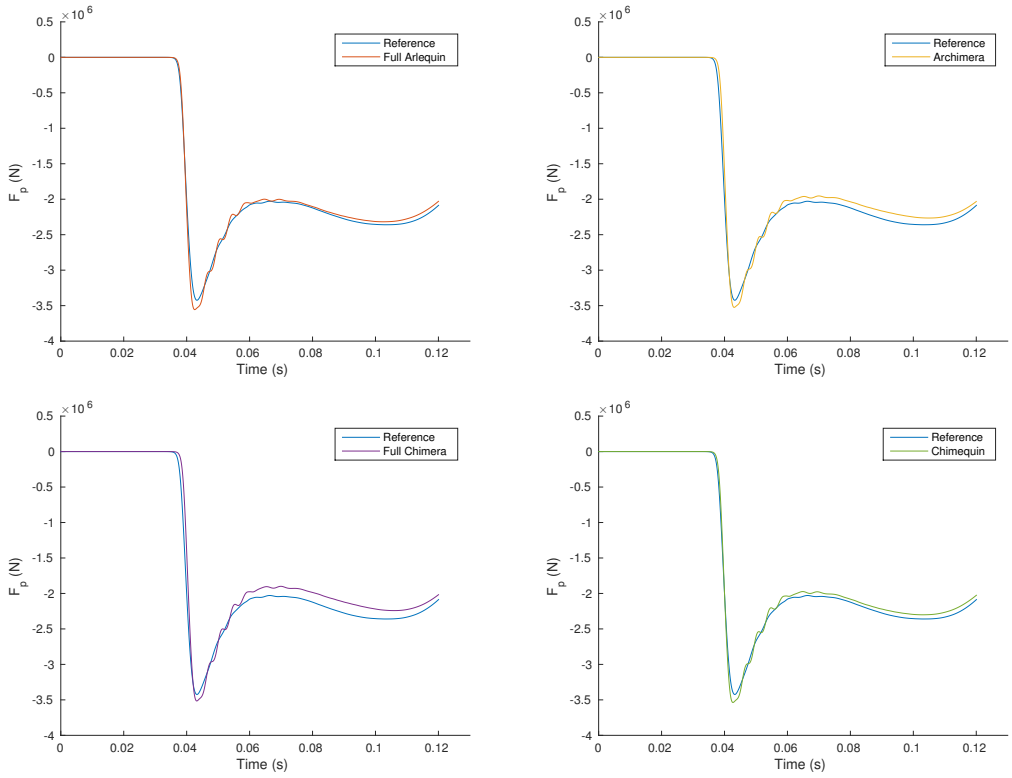

Figure 4.10: F_p is represented for all four approaches. On all figures, the reference value of F_p, computed for the mono-model problem, is represented in blue.

A few observations can be made. First, we observe that, despite the use of artificial viscosity, both multi-model approaches slightly oscillate after the front of the shock has reached the cylinder. Also, both approaches present a small overshoot of F_p at its peak (3.9% for the Full Arlequin approach and 2.9% for the Archimera one). The Full Arlequin approach yields a more accurate solution than the Archimera when the force stabilizes (after $t = 60$ms). Moreover, for the Archimera approach, the front of the shock hits the cylinder slightly late.

In order to quantify these observations, we introduce the following error measure:

$$E_{F_p} = \frac{\int_t |F_p^m(\tau) - F_p^r(\tau)| \, d\tau}{\int_t |F_p^r(\tau)| \, d\tau} \tag{4.12}$$

where r refers to the reference solution and m to the multi-model approach being compared. A convergence study was led for both multi-model approaches. Three meshes of respectively 620, 2160 and 8000 degrees of freedom were considered. The value of the error measure defined by expression (4.12) is represented for all three meshes and all multi-model approaches in Figure 4.11.

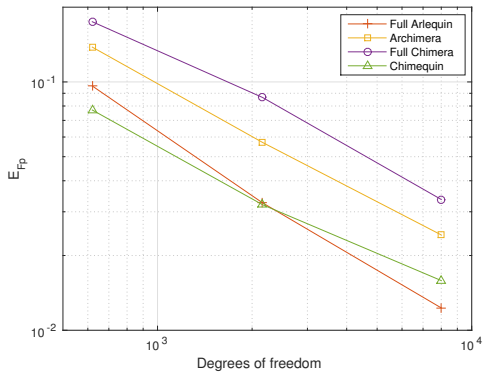

Figure 4.11: Convergence study for the error measure E_{F_p} for all four multi-model approaches.

We can observe on that convergence study that the Full Arlequin presents better convergence properties than the Archimera one. Indeed, not only does it have a faster convergence rate but it yields solution with a lower error measure E_{F_p}. Yet, more cases should be tested in order to claim that the Full Arlequin approach is more accurate than the Archimera. However, for memory reasons we were not able to accomplish it.

Still, it is interesting to notice that both are more accurate than the Chimera-like approach which implies (1) that the ghost forces due to the divergence free pressure term was efficiently handled and (2) that both the Full Arlequin and the Archimera approaches are worth being considered as an alternative to Chimera approaches.

Finally, we can note that the two most accurate multi-model approaches are the ones that use an Arlequin coupling for the transport equations while the two least accurate ones use a Chimera-like approach for them.

4.5 Local insertion of a channel between chambers

4.5.1 Presentation

We consider two different chambers of equal size but in different states, as shown in Figure 4.12. The chambers are 4m apart and have equal size 20m $\times$ 10m. The fluid in both chambers is assumed to be initially motionless. The fluid in the left chamber is at

density $\rho_L = 1.3$ kg.m^{-3} and pressure $p_L = 1.0 \times 10^5$ Pa while the fluid in the right one is at density $\rho_R = 6.8$ kg.m^{-3} and pressure $p_R = 5.0 \times 10^6$ Pa. A 4m $\times$ 2m connecting channel joins the two chambers. The discontinuity in fluid properties occurs in the middle of the channel, as can be seen in Figure 4.12. The fluid is assumed to slip on each wall of the domain. Finally, we used a quadratic and linear artificial viscosity (see [179]) set to 2.56 and 0.1 respectively and a security coefficient[11] set to csta = 0.45.

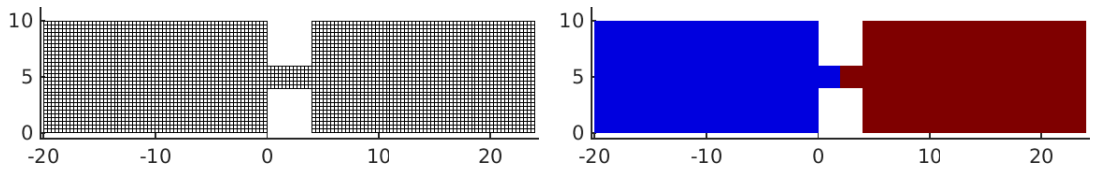

Figure 4.12: The mono-model mesh is represented discretized with quadrangle of same size and such that six elements fit vertically in the channel (left). Initial conditions for the channel test case is also represented (right). The domain in blue is at initial conditions (p_L, ρ_L) and the one in brown at initial conditions (p_R, ρ_R). The initial conditions are such that the temperature is uniform at $t = 0$s.

We only consider the first 120ms of the simulation, the time it takes for the shock wave spreading left to bounce off the far left wall and reach the channel. During that time the fluid in the right chamber pours into the left one and waves are initiated at the discontinuity and spread through the chambers, as can be seen in Figure 4.13. In the latter, the solution for the horizontal velocity $\underline{v} \cdot \underline{x}$ (top), the vertical velocity $\underline{v} \cdot \underline{y}$ (bottom) and pressure are represented at instants $t_0 = 10$ms, $t_0 = 18$ms, $t_0 = 35$ms, $t_0 = 60$ms, $t_0 = 90$ms and $t_0 = 120$ms. We can observe that a strong current is created in the horizontal axis and goes from the channel to the far left wall. In the left chamber, the fluid circles back along the top and bottom walls. In comparison, the right chamber is rather motionless, except at the right end of the channel where the fluid accelerates as it enters the channel. Yet, we can see a rarefaction wave propagating rightward as the pressure in that chamber slowly decreases.

Remark 4.5.1. *Note that as we are using a FEM discretization for the momentum equation, it is difficult to ensure the slip condition for the different corners of the channel. In this work, we chose to impose $\underline{v} \equiv \underline{0}$ at every such corner. This implies that there is a 'boundary layer' effect around these corners and it is as if the fluid was artificially viscous. The smaller the elements in these regions, the less intense this effect is.*

4.5.2 Multi-model solutions

The multi-model mesh is represented in Figure 4.14. The chambers (in black in the figure) are made of square elements of length 2.3m while the channel is inserted through the patch (in red in the figure). In Figure 4.14 the weight functions α^v and α^p are also represented.

[11] The use of artificial viscosity imposes the security coefficient to be inferior to 0.5.

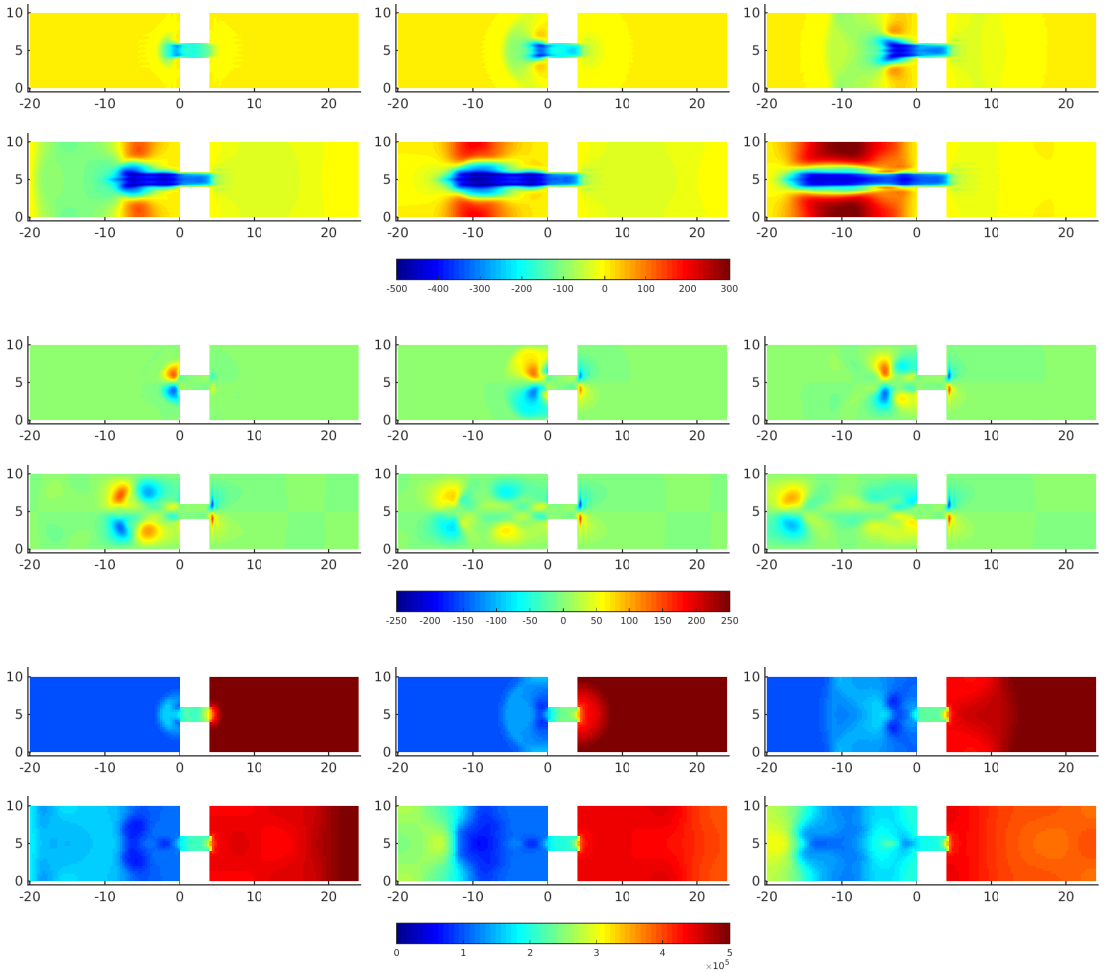

Figure 4.13: Mono-model solution for the channel test case for the horizontal (top) and vertical (middle) velocity as well as the pressure (bottom) at different instants (from left to right, from top to bottom). The solution is represented for the mesh represented in Figure 4.12.

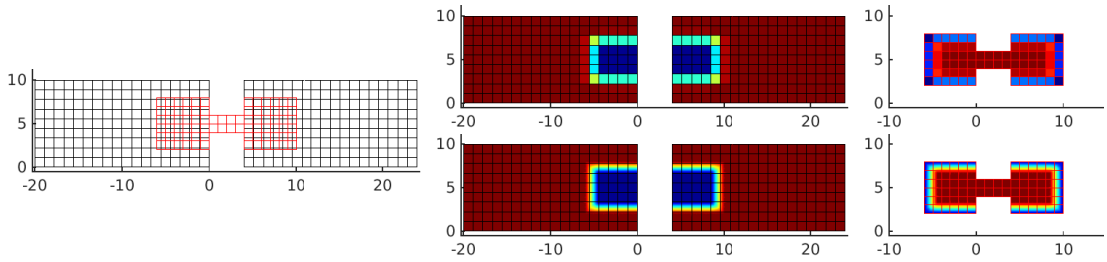

Figure 4.14: The meshes of the substrate (black) and the patch (red) are represented on the left. The weight functions α^v (top) and α^p (bottom) are represented in the center (substrate) and the left (patch) figures. Here, only two elements fit vertically in the channel so as to better assess the spatial evolution of the weight functions.

The solution obtained for the different multi-model approaches are represented hereafter. For those simulations, the patch is made up of the same elements as the mono-

model mesh while the substrate is slightly coarser[12] (so that the models are not compatible in Ω_c). For all these computations, we used a quadratic artificial viscosity set to 2.56 and a csta parameter set to 0.45. When relevant, we imposed $\hat{\alpha}^{\rho} = \hat{\alpha}^{\rho E} = \tilde{\alpha}^{p}$ and $\alpha_0 = 1.0 \times 10^{-6}$. As always, the outer boundary of the coupling zone Γ_{out} is aligned with the mesh of the patch and the inner one Γ_{in} is aligned with the mesh of the substrate. The size of the coupling zone is such that two entire elements of both models are inside the coupling zone in both directions. The mediator space is discretized as the substrate for the momentum equation and as the patch for the transport equations.

Remark 4.5.2. *There are actually two coupling zones, on the left and one on the right. For the Full Arlequin and the Archimera approaches, we thus used two distinct Lagrange multipliers to handle the ghost forces (see section 4.2).*

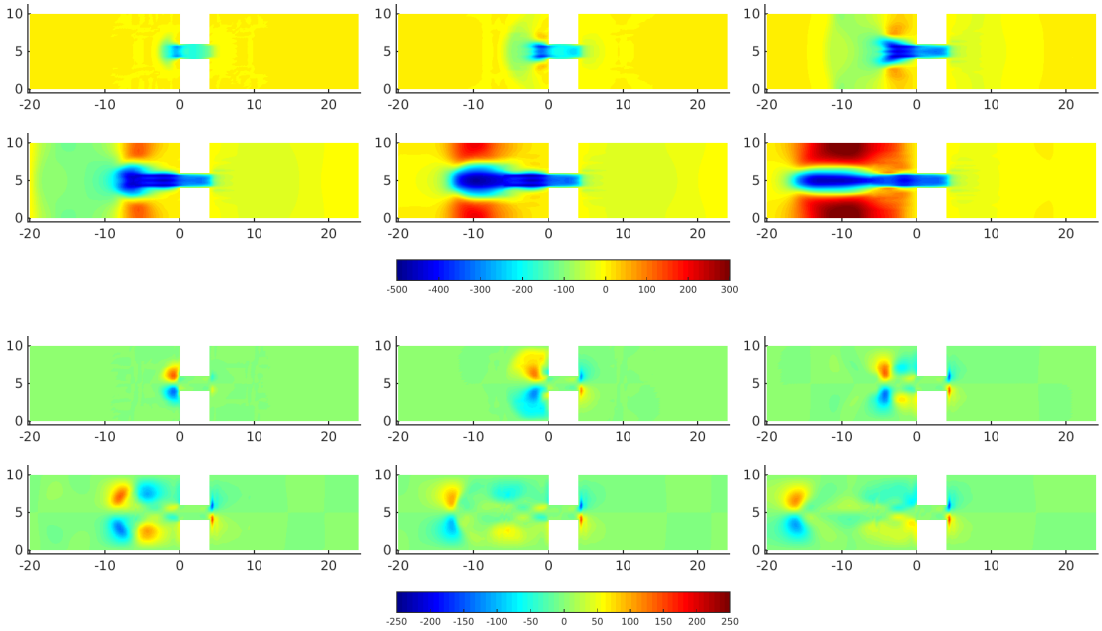

Figure 4.15: Full Arlequin solution for the channel test case for the horizontal (top) and vertical (bottom) velocities at different instants (from left to right, from top to bottom).

We can see that, qualitatively, all the multi-model approaches yield a solution very close to the mono-model solution obtained in section 4.5.1.

Remark 4.5.3. *Note that in all the figures showing the solution of the multi-model solutions, the exact solution in the coupling zone is not computed. Instead, the solution of the patch was arbitrarily shown.*

[12] To be exact, the length of the square elements is equal to $\frac{10}{29}$m ≈ 0.345m.

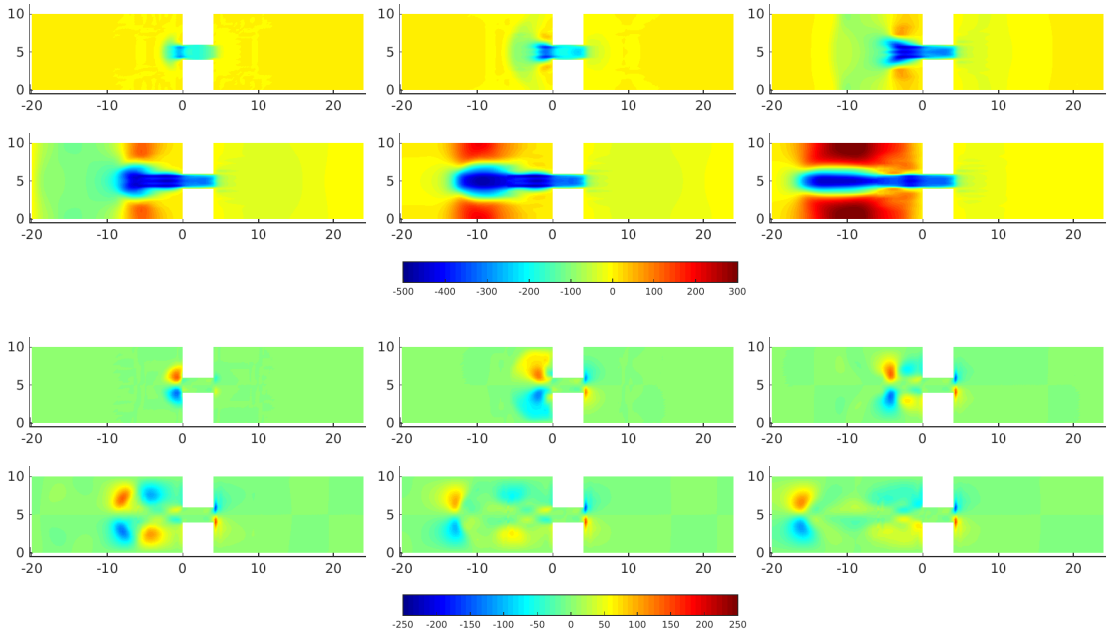

Figure 4.16: Archimera solution for the channel test case for the horizontal (top) and vertical (bottom) velocities at different instants (from left to right, from top to bottom).

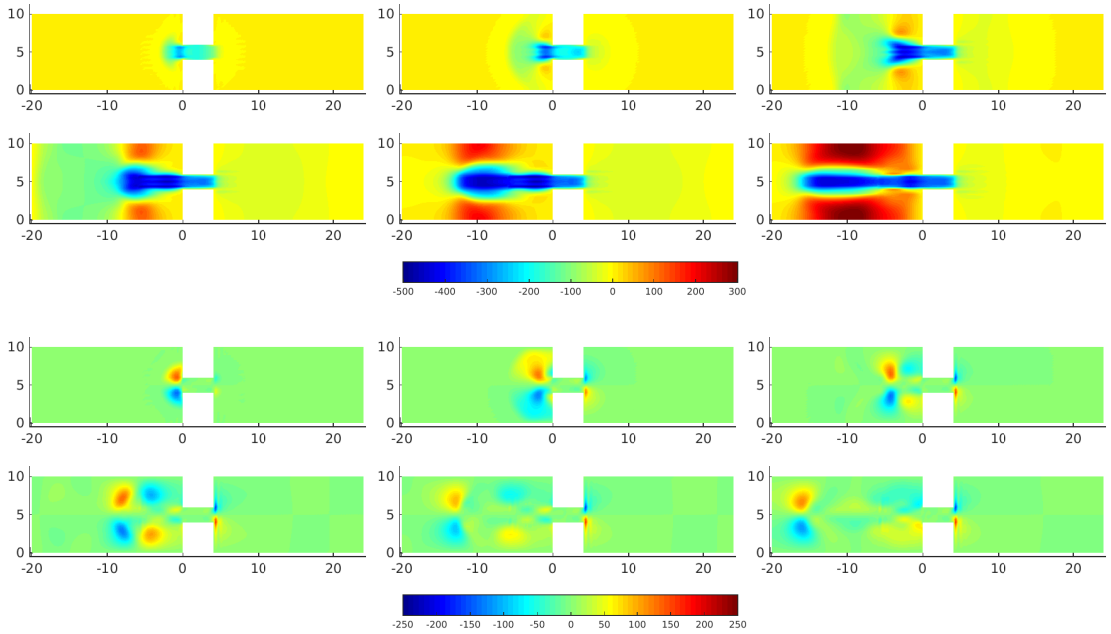

Figure 4.17: Full Chimera solution for the channel test case for the horizontal (top) and vertical (bottom) velocities at different instants (from left to right, from top to bottom).

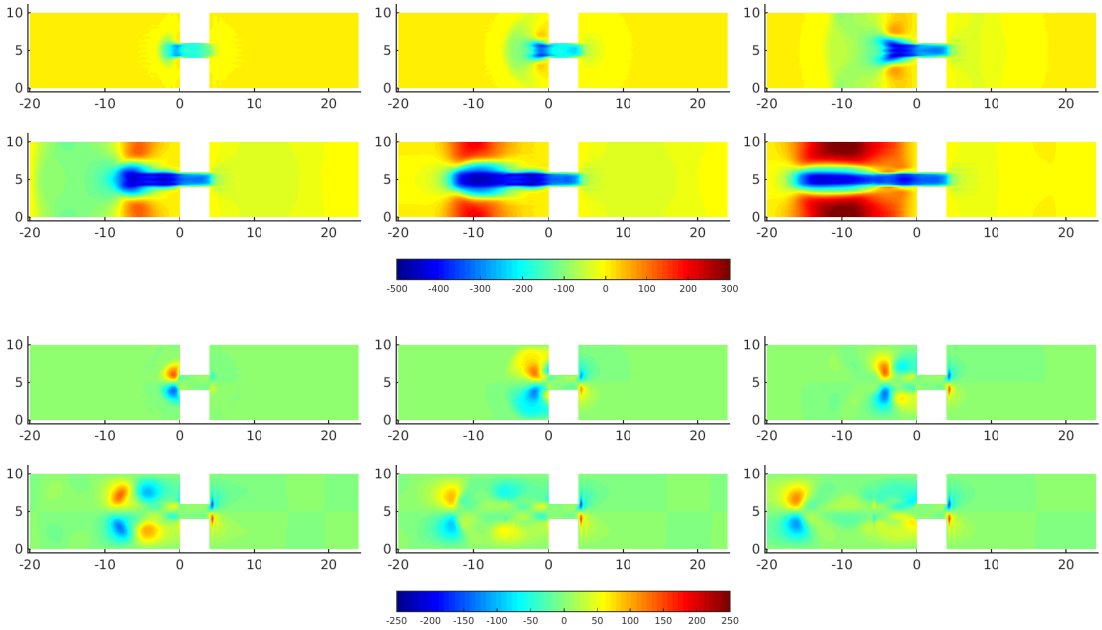

Figure 4.18: Chimequin solution for the channel test case for the horizontal (top) and vertical (bottom) velocities at different instants (from left to right, from top to bottom).

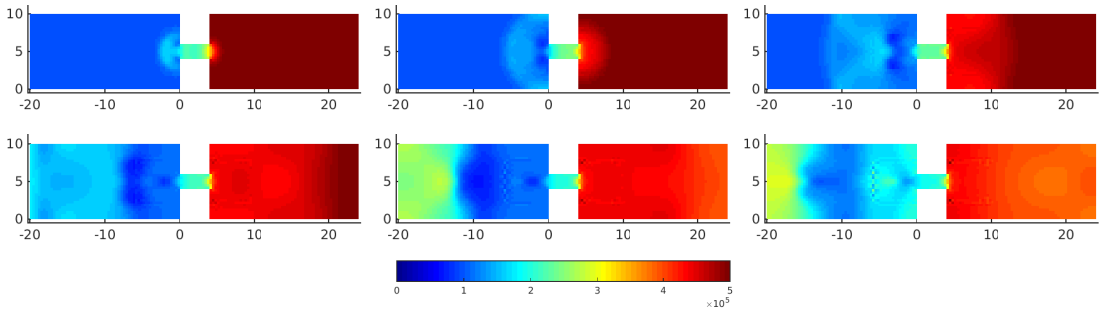

Figure 4.19: Full Arlequin solution for the channel test case for the pressure at different instants (from left to right, from top to bottom).

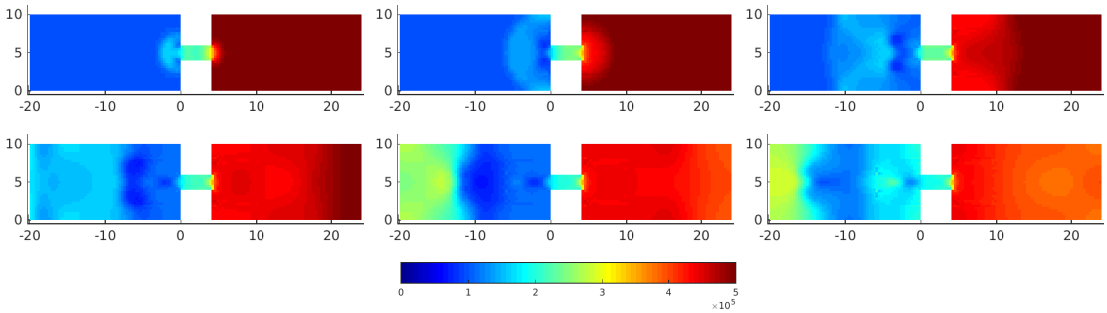

Figure 4.20: Archimera solution for the channel test case for the pressure at different instants (from left to right, from top to bottom).

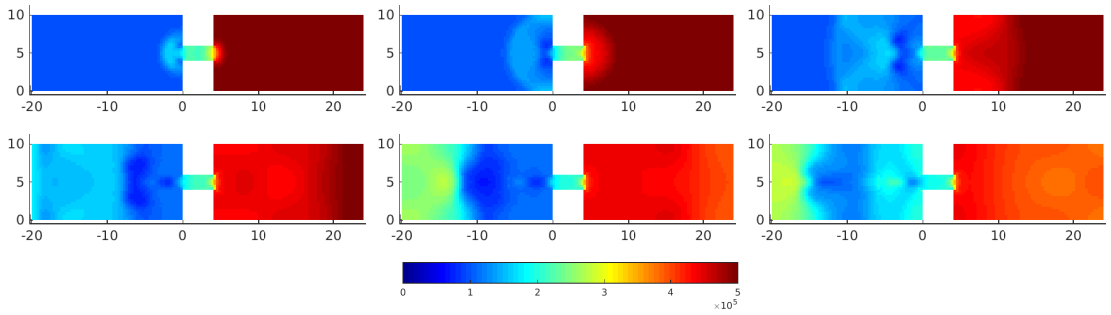

Figure 4.21: Full Chimera solution for the channel test case for the pressure at different instants (from left to right, from top to bottom).

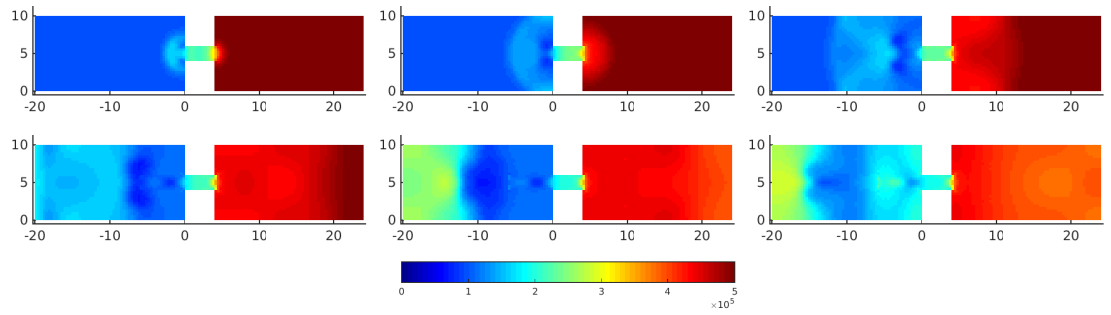

Figure 4.22: Chimequin solution for the channel test case for the pressure at different instants (from left to right, from top to bottom).

4.5.3 Convergence study

In order to compare the accuracy of the multi-model approaches, a convergence study was led. The meshes of both models are gradually refined. The number of elements in the vertical direction of channel increases from 2 to 10 so that the patch is made up of square elements of length of $\frac{2}{N_e}$m where N_e is the number of elements in the vertical direction. The mesh of the substrate is made up of slightly coarser square elements[13].

For all these computations, we used a quadratic artificial viscosity set to 2.56 and a csta parameter set to 0.45. When relevant, we imposed $\hat{\alpha}^{\rho} = \hat{\alpha}^{\rho E} = \tilde{\alpha}^{p}$ and $\alpha_0 = 1.0 \times 10^{-6}$. As always, the outer boundary of the coupling zone Γ_{out} is aligned with the mesh of the patch and the inner one Γ_{in} is aligned with the mesh of the substrate. The mediator space is discretized as the substrate for all three equations.

The reference solution is computed on a mono-model mesh made up of $13,312$ square elements of length 0.125m corresponding to 16 elements in the vertical direction of the channel. For the reference solution, we also used a quadratic artificial viscosity set to 2.56 and a csta parameter set to 0.45.

In order to evaluate the accuracy of the multi-model approaches, we consider two quantities of interest: the flow at the right end of the channel, denoted $f(t) = \rho(t)\underline{v}(t)L$, and the pressure forces on the left wall of the domain. We thus consider the following two error measures:

$$E_f = \frac{1}{\mathcal{N}_T} \sum_{n=1}^{\mathcal{N}_T} \frac{|f^m(t^n) - f^r(t^n)|}{|f^r(t^n)|} \tag{4.13a}$$

$$E_{LW} = \frac{1}{\mathcal{N}_T} \sum_{n=1}^{\mathcal{N}_T} \frac{\int_{x=-20m} |(p^m(t^n) - p^r(t^n))\underline{n} \cdot \underline{x}| \, dx}{\int_{x=-20m} |p^r(t^n)\underline{n} \cdot \underline{x}| \, dx} \tag{4.13b}$$

where r refers to the reference solution and m to the multi-model approach being compared. The convergence study was led for both error measures. The results obtained are represented in Figure 4.23.

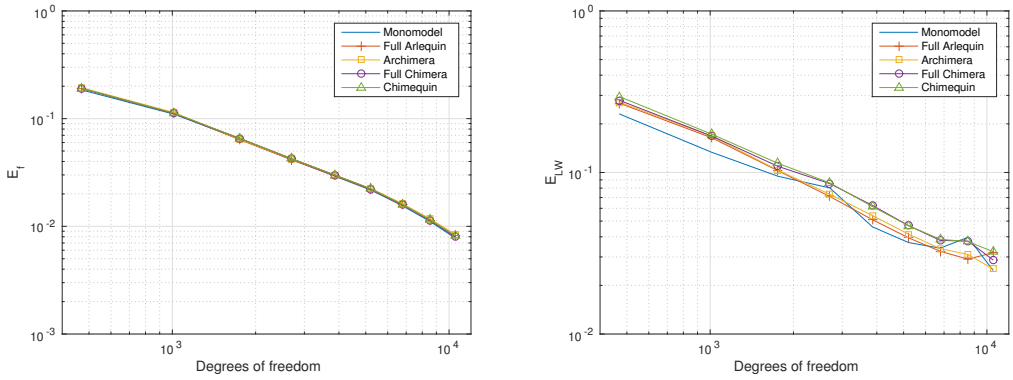

Figure 4.23: Convergence study of error measure E_f(left) and E_{LW} (right) for all four multi-model approaches as well as for the mono-model one.

[13]To be exact, the length of the square elements of the substrate is equal to $\frac{10}{5N_e-1}$.

We can observe that all four multi-model properties seem to have similar convergence properties and no multi-model approach should be preferred based on that criteria. In the following sections, we consider other parameters that might influence the accuracy of the multi-model approaches.

4.5.4 Influence of the size of the coupling zone on the accuracy

Hereafter, we study the influence of the size of the coupling zone on the solution. We consider the multi-model discretization corresponding to 7 elements in the vertical direction of the channel. While Γ_{out} is always aligned with the outer mesh of the patch, we consider 5 positions of Γ_{in}, all represented in Figure 4.24. All positions of Γ_{in} are

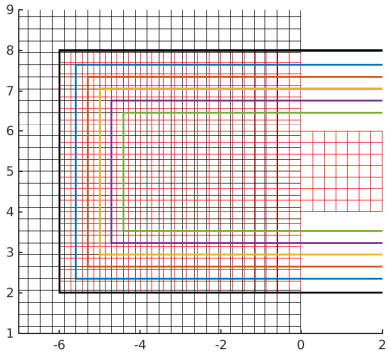

Figure 4.24: Different Γ_{in} positions.

aligned with the mesh of the substrate with exactly 1, 2, 3, 4 and 5 entire elements of the patch inside the coupling zone in every direction. They are represented in Figure 4.24 in blue, red, yellow, purple and green respectively. The relative error measures e_f and e_{LW}, defined hereafter by expression 4.14, were computed for each position of Γ_{in}. The results are represented in Figure 4.25 with

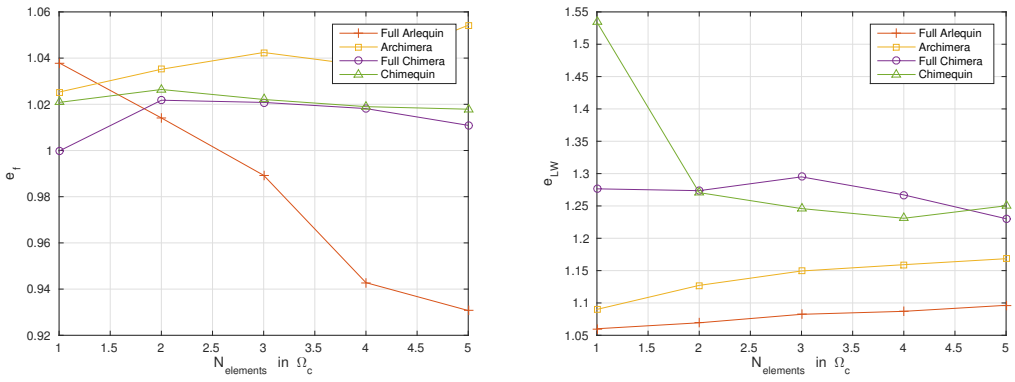

Figure 4.25: Influence of the size of the coupling zone on the relative error measures e_f and e_{LW}.

$$e_f = \frac{E_f^m}{E_f^{r7}} \text{ and } e_{LW} = \frac{E_{LW}^m}{E_{LW}^{r7}} \tag{4.14}$$

where m refers to the multi-model approach and r_7 to the mono-model solution obtained with square elements of size $\frac{2}{7}$m ≈ 0.286m, corresponding to the discretization of the elements of the patch in the multi-model discretization.

We can observe that the Full Chimera and Chimequin approaches are not affected by the size of the coupling zone, except when exactly one entire element of the patch is in the coupling zone. For both the Archimera and Full Arlequin approaches, the value of e_{LW} slowly increases with the size of the coupling zone. For e_f on the other hand, the error measure decreases with the coupling zone for the Full Arlequin Approach and increases for the Archimera one. Yet, for all multi-model approaches, we can say that the size of the coupling zone has little influence on the quantities of interest considered.

4.6 Conclusion

In this chapter, we studied the accuracy of the Archimera and Full Arlequin approaches. We first observed that ghost forces arise in both approaches so that stable equilibriums can not be accurately simulated. We showed that it was due to the use of weight functions in the momentum equations but also to the discretization of divergence-free force terms. We proposed to filter the component of these ghost forces related to the uniform component of the stress field at each time step by enriching the coupling matrices.

Then, we compared the accuracy of both multi-model approaches on two test cases representative of the applications presented in the Introduction. In each test case, we compared their accuracy with a reference multi-model approach of the literature called the Chimera approach. We observed that the multi-model approaches proposed in this work yielded solutions whose accuracy is the same order of magnitude as the reference solution. Although it proved to show similar, if not better, convergence properties as the Chimera approach, more test cases and less naive implementations of the Chimera approach should be considered. Yet, it shows that the two multi-model approaches proposed in this work should be considered as an alternative to the Chimera approach when implementing multi-model approaches for fluid dynamics applications. Moreover, both the Full Arlequin and the Archimera approaches are all the more relevant alternatives as they are better adapted to the algorithm implemented in EUROPLEXUS[14]*. Finally, we observed that the size of the coupling zone had little influence on the solution for both multi-model approaches.*

The next step is to extend the previous results to formulate multi-model approaches in FSI simulations which is a perspective of this work.

[14]See Appendix A.

Conclusion

The objective of this thesis was to design a numerical tool able to superimpose domains with different properties in transient fluid-structure interaction (FSI) phenomenons. This numerical tool also had to be compatible with explicit time integration and allow for the different domains to be discretized with non conforming mesh. Such a numerical tool was then to be used to improve the modelling in simulations of Design Basis Accidents (DBAs) in Europlexus.

In order to accomplish this objective, we proposed to design such a tool for superimposed elastic structures and superimposed fluid domains separately with the perspective of further combining them in order to deal with fluid structure interaction. After a thorough study of the state of the art of multi-modelling methods, we chose to use the Arlequin and Chimera methods as they had proven to yield accurate solutions when simulating structural and fluid mechanics and presented the advantage of allowing for meshes of different models to be independently meshed.

The first step was to tackle the issue of the superimposition of elastic structures in transient dynamics, taking into account the final orientation of the proposed works towards fluid structure interaction. We applied the Arlequin framework to superimposition of elastic structure in explicit dynamics. Then, we analysed the influence of the different Arlequin components on the critical time step in order to ensure that it would not be adversely affected. We showed that special care was needed in order to ensure a computationally feasible time step and proposed two approaches to this end. As one of these approaches was inferred from a one dimensional example, we observed that they still ensured a feasible time step for 2D cases. Finally, we showed that the approaches proposed led to accurate solutions for representative transient test cases.

The second step was to design suitable superimposing techniques for transient fluid dynamics. In view of FSI applications in Europlexus, the momentum equation was treated in a non conservative form using the Finite Element Method (FEM) while a Finite Volume scheme was used for the other two equations. The Arlequin method was chosen for the treatment of the momentum equation as it allows to deal with structure and fluid degrees of freedom in a unified way, which would be convenient in a FSI context. For the other two equations, we proposed three different approaches which we applied to the convective transport equation. We compared them on both their stability and accuracy properties. Although one was shown not to yield accurate solutions, the other two approaches proved to show good stability properties and yield accurate solution on representative test cases. As none presented better converging properties, both were considered so that two multi-model approaches were proposed for the treatment of the Euler equations. The first one, called the Full Arlequin approach uses the Arlequin framework for all three equations. The second one also uses the

Arlequin framework for the momentum equation but uses a Chimera-like treatment for the other two equations. Yet, both presented spurious effects when applied to the Euler equations. We proposed a method to mitigate these effects. After analysing the stability of the different approaches and showing how to ensure a feasible time step, convergence studies were led on different test cases. Both approaches presented similar convergence properties so that both should be considered for FSI applications.

The last step would is to design multi-modelling FSI approaches and will be handled in future works.

There are three main ways in which this work could be continued. The first and most obvious way is to apply the reasoning and results obtained in this work to fluid structure interaction multi-modelling. A first step would be to treat such problem would be to use a Lagrangian description for the fluid and compatible structure/fluid interfaces in both models. This, way, only the FSI link conditions would have to be dealt with. Then, the extension of the approaches implemented in this work to other techniques, such as an Arbitrary Lagrangian Eulerian (ALE) description or Immersed Boundaries Conditions (IBC) would be useful as they are used in Europlexus for the simulation of DBAs.

A second prospect is to improve the numerical properties of the multi-modelling approaches proposed for the structural and fluid components. For instance, using higher order schemes may lead to more accurate solutions. Indeed, second order space and time schemes in Europlexus have shown to yield more accurate solutions when dealing with shock propagation [180]. Moreover, these solutions do not depend on the value of the time step and in particular of the csta parameter. However, these results rely on a fully conservative Finite Volume approach so that they do not hold for an Arlequin formulation similar for both structure and non-conservative fluid transport. A new formulation accounting for specific fluid links built between Finite Elements and Finite Volumes will have to be entirely designed. Another example of a numerical improvement is a higher order treatment of the ghost forces to mitigate even more their consequences on the solution.

Finally, a last prospect is to extend the different multi-model approaches developed to cases for which the two models are integrated in time using different time steps. This would be particularly useful in cases for which the meshes have elements of different sizes.

Appendix A

Presentation of Fluid Structure Interaction modelling in Europlexus

In this appendix, we aim to briefly present the modelling of Fluid Structure Interaction (FSI) in Europlexus, which is the basis of the work developed in this thesis.

A.1 Time integration scheme

The time is discretized at different instants t^n such that $t^n = \sum_{i=0}^{n} \Delta t^n$ where $\Delta t^n = t^n - t^{n-1}$ is called the time step. The time integration of the kinematic quantities is carried out through the central difference explicit scheme for both the structure and the fluid. From time step n to time step $n+1$, we have (we assume for clarity a constant time step):

$$\left\{\begin{array}{lcll} \underline{\dot{u}}^{n+\frac{1}{2}} & = & \underline{\dot{u}}^{n} & + \frac{1}{2}\Delta t\ \underline{\ddot{u}}^{n} \\ \underline{u}^{n+1} & = & \underline{u}^{n} & + \Delta t\ \underline{\dot{u}}^{n+\frac{1}{2}} \\ \underline{\dot{u}}^{n+1} & = & \underline{\dot{u}}^{n+\frac{1}{2}} & + \frac{1}{2}\Delta t\ \underline{\ddot{u}}^{n+1} \\ \underline{v}^{n+\frac{1}{2}} & = & \underline{v}^{n} & + \frac{1}{2}\Delta t\ \underline{\dot{v}}^{n} \\ \underline{v}^{n+1} & = & \underline{v}^{n+\frac{1}{2}} & + \frac{1}{2}\Delta t\ \underline{\dot{v}}^{n+1} \end{array}\right. \tag{A.1}$$

where $\underline{u}$ is the displacement of the structure, $\underline{v}$ the velocity of the fluid and $\cdot$ denotes the time derivative. Note that, hereafter, the superscript n on a variable denotes its value at instant t^n.

A.2 Structural component

The equation of motion describing the behaviour of the structural component is as follows (in strong form):

$$\rho \frac{\partial^2 \underline{u}}{\partial t^2} - \mathrm{div}[\underline{\underline{\sigma}}(\varepsilon)] + \underline{f}_{F\to S} = \underline{f}^{S}_{vol} \tag{A.2}$$

where ρ is the density, $\underline{u}$ the displacement of the structure, $\underline{\underline{\sigma}}$ the Cauchy stress tensor, ε the strain tensor, $\underline{f}_{F\to S}$ the force exerted on the structure by the fluid and $\underline{f}^{S}_{vol}$ represents volume forces. The structure can be modelled by a variety of constitutive laws, from elasticity to plasticity and damage. In this work however, we limit ourselves to elasticity with no volume forces.

The structural domain is discretized using the Finite Element Method (FEM). The discretized equation of motion is then:

$$\underline{\underline{M}}_S \; \underline{\ddot{u}}^{n+1} = \underline{F}_S^{n+1} \tag{A.3}$$

where $\underline{\underline{M}}_S$ is the mass matrix, made diagonal by mass lumping techniques[1] while $\underline{F}_S^{n+1}$ represents internal forces.

A.3 Fluid component

The fluid is modelled by the Euler equations (strong form):

$$\begin{cases} \dfrac{\partial \rho}{\partial t} + \mathrm{div}(\rho \underline{v}) = 0 & \text{(conservation of mass equation)} \\ \dfrac{\partial \rho \underline{v}}{\partial t} + \rho \underline{\underline{(v \cdot \nabla)}} \underline{v} + \underline{\nabla p} + \underline{f}_{S \to F} = \underline{f}_{vol}^{F} & \text{(conservation of momentum equation)} \\ \dfrac{\partial \rho E}{\partial t} + \mathrm{div}[(\rho E + p)\underline{v}] = 0 & \text{(conservation of energy equation)} \end{cases} \tag{A.4}$$

where u is the velocity of the fluid, p the pressure, E the total energy, $\underline{f}_{S \to F}$ the force exerted on the fluid by the structure and $\underline{f}_{vol}^{F}$ volume forces. Note that in the present work we do not consider the latter.

The mass and energy conservation equations are treated with a Finite Element procedure. The momentum equation is treated in a non conservation form using the Finite Element Method (FEM). Thus, the fluid velocity variables are located at the nodes of the fluid grid so that link conditions with the structure, whose kinematic variables are also located at the nodes, are easily imposed (see hereafter). The discretized momentum equation can be written:

$$\underline{\underline{M}}_F^{n+1} \; \underline{\dot{v}}^{n+1} = \underline{F}_F^{n+1} \tag{A.5}$$

where $\underline{\underline{M}}_F^{n+1}$ is the mass matrix for the fluid while $\underline{F}_F^{n+1} = \underline{F}_p^{n+1} + \underline{F}_t^{n+1}$ with $\underline{F}_p^{n+1}$ the forces resulting from the pressure and $\underline{F}_t^{n+1}$ the force resulting from the convective term in a finite element framework (see [177]).

A.4 FSI link conditions

The boundary between the fluid and the structure is treated through link conditions on the accelerations of both component. It yields the following linear system to solve at each time step:

$$\begin{cases} \begin{pmatrix} \underline{\underline{M}}_S \\ \underline{\underline{M}}_F^{n+1} \end{pmatrix} \begin{pmatrix} \underline{\ddot{u}}^{n+1} \\ \underline{\dot{v}}^{n+1} \end{pmatrix} + \begin{pmatrix} \underline{\underline{C}}_S^{n+1} \\ \underline{\underline{C}}_F^{n+1} \end{pmatrix}^T \underline{\lambda}^{n+1} = \begin{pmatrix} \underline{F}_S^{n+1} \\ \underline{F}_F^{n+1} \end{pmatrix} \\ \underline{\underline{C}}_S^{n+1} \underline{\ddot{u}}^{n+1} + \underline{\underline{C}}_F^{n+1} \underline{\dot{v}}^{n+1} = \underline{B}^{n+1} \end{cases} \tag{A.6}$$

[1] See for instance [REF].

where the matrices $\underline{\underline{C}}_S^{n+1}$ and $\underline{\underline{C}}_F^{n+1}$ account for kinematic constraints expressing boundary conditions, fluid-structure interaction links and purely structural links, such as unilateral contact. The variable $\underline{\lambda}^{n+1}$ is called the Lagrange multiplier (see for example [175]).

Appendix B

Presentation of the Arlequin method

The Arlequin method is a general framework that allows for the superimposition of models in computational mechanics. The aim of this appendix is to present the Arlequin framework and show, on simple examples, how to build an Arlequin problem formulation. First, we recall the objectives and principles of the method and illustrate it on a basic example (section B.1). Then we present the three components of the method for static structural problems. We focus on the latter because it is the type of problems for which there are theoretical results for convergence (section B.2). Finally, we show how this framework can be extended to structural dynamic applications (section B.3).

Note that the following is largely inspired from the thesis of Guillaume Rateau [100] and is mostly a translation of his presentation of the Arlequin method.

B.1 Presentation of the objectives and principles of the Arlequin method

The Arlequin Method was designed in order to locally change a global mechanical model while saving human and machine resources. Indeed, in many structural mechanics applications, it is of primary importance to be able to introduce local defects in a global, usually coarse, model; to be able to change the local behaviour or to relax sound hypotheses like the classical continuum mechanics in the neighbourhood of singularities or other critical points.

In those cases, different modelling in separate parts of the domain is required. Thus, the objective of the method was to develop a general framework for the resolution of structural mechanics problems in static for every part of the domain simultaneously. To do so, each different part of the global domain is assigned a specific model.

The Arlequin method is based on three principles. The first one is that both models are superimposed. The second principle is that the coupling of the different domains is not done on interfaces but on a volume. Moreover, for both generality and flexibility, a model's boundaries do not have to be conforming with another model's modelling (for example, meshes are allowed to be non-conforming). Thus, in areas where two

models coexists, that is, are superimposed, the global solution is obtained through the mix of both modelling. In these areas where two models coexists, the total energy is split between each model. This energy splitting is the third principle of the Arlequin method. To split the energy across models, weight parameters are introduced for each model. These weight parameters form a partition of unity so as to account for the total energy adequately.

The Arlequin method and its three principles are illustrated in the following basic example ([100], [93]). Let us consider an elastic cantilever beam with a uniform force applied at its free end (static case), as represented in Figure B.1. For this specific problem, we consider three different modellings which, in this case, correspond to three different scales:

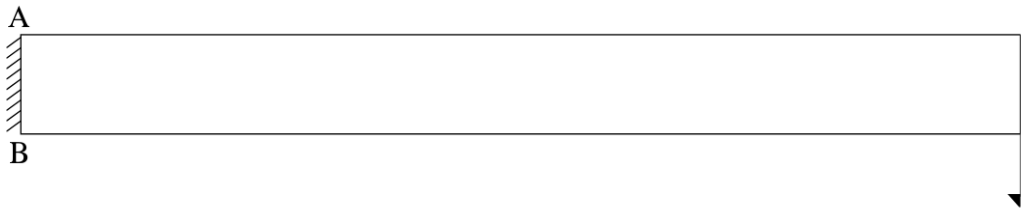

Figure B.1: We consider an elastic cantilever beam anchored on its left end and undergoing a uniform vertical force at its free end (Image taken from [100]). We can see that two types of overlapping are considered. When only parts of the two models overlap, we call such problems about junction problems (Ω_{beam} and Ω_{bc} for instance). When one model is strictly embedded in the other, it is referred to as a zoom problem ($\Omega_{singularity}$ in Ω_{bc} for instance).

1. Away from the embedded side of the beam, the strain profile is linear across the beam's thickness. Thus, a one dimensional modelling is sufficient to describe the beam's behaviour in that region. This region is represented by domain Ω_{beam} in FIGURE B.2.

2. Close to the embedded part of the cantilever, boundary layer effects appear. they can be best modelled by a two dimensional model using the finite element method. This region is represented by domain Ω_{bc} in FIGURE B.2.

3. Finally, the sudden change of boundary conditions creates a singularity in the solution at points A and B of the beam in FIGURE B.2. This last region needs a discrete, fine modelling. This region is represented by domain $\Omega_{singularity}$ in FIGURE B.2.

In the Arlequin framework, this problem is simultaneously solved for all models. Thus, we solve for the solution field $[\underline{u}_{beam}, \underline{u}_{bc}, \underline{u}_{singularity}]^T$ under the following condition:

$$\begin{cases} < \underline{u}_{beam} - \underline{u}_{bc} > = 0 \quad \text{on} \quad \Omega_{beam} \cap \Omega_{bc} \\ < \underline{u}_{bc} - \underline{u}_{singularity} > = 0 \quad \text{on} \quad \Omega_{singularity} \end{cases} \tag{B.1}$$

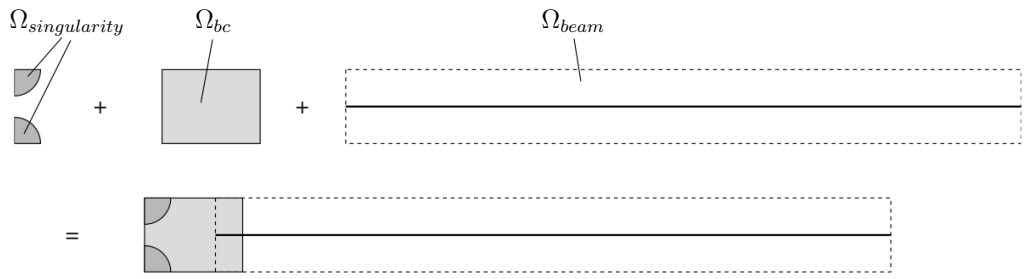

Figure B.2: The cantilever is now modelled by three distinct models corresponding to different scales (Image taken from [100]).

where the mathematical operator $< \cdot >$ will be defined in the next section. Once the solution field on each model is obtained, the global solution is then built thanks to the energy splitting weight parameters (α where Ω_{beam} and Ω_{bc} coexist and β where Ω_{bc} and $\Omega_{singularity}$ coexist). It is done in the following way.

$$\begin{cases} \underline{u}_{beam} & & & \text{on} & \Omega_{beam} \setminus \Omega_{bc} \\ \alpha \underline{u}_{beam} & + & (1-\alpha)\underline{u}_{bc} & \text{on} & \Omega_{beam} \cap \Omega_{bc} \\ \underline{u}_{bc} & & & \text{on} & \Omega_{bc} \setminus (\Omega_{beam} \cup \Omega_{singularity}) \\ \beta \underline{u}_{bc} & + & (1-\beta)\underline{u}_{singularity} & \text{on} & \Omega_{bc} \cap \Omega_{singularity} \end{cases} \tag{B.2}$$

where $\alpha, \beta \in [0,1]$.

In this section, we presented the objective and the principles of the Arlequin method. In the next one, we detail the mathematical tools used to implement the method.

B.2 Making of an Arlequin formulation

In this section, we show how to obtain an Arlequin formulation of the equations describing a structural problem in static. For simplicity, but without loss of generality, we will consider an elastic body. First, we present the formulation of a mono-model (one model) for static structural applications (subsection B.2.1). Then, we show how to formulate the corresponding multi-model problem in the Arlequin framework (subsection B.2.2).

B.2.1 Formulation of a mono-model formulation for static structural mechanics applications

We consider an isotropic elastic body occupying a bounded, regular domain $\Omega \in \mathbb{R}^d$. The boundary $\partial\Omega$ of Ω is partitioned into two parts, Γ_u and Γ_h, such that $\Gamma_u \cap \Gamma_h = \emptyset$. The body is submitted to volume forces $g \in L^2(\Omega)$, prescribed displacements u_p on $\Gamma_u \neq \emptyset$ and prescribed boundary forces $h \in L^2(\Gamma_h)$ on Γ_h. Let $\underline{\underline{\sigma}}$ be the Cauchy stress tensor and $\underline{\underline{\varepsilon}}$ the infinitesimal strain tensor. The strain tensor is given by $\underline{\underline{\varepsilon}} = \underline{\underline{\nabla^S u}} = \frac{1}{2}(\underline{\underline{\nabla u}} + \underline{\underline{\nabla^T u}})$ while the stress tensor is given by Hooke's law : $\underline{\underline{\sigma}} = \underline{\underline{\underline{\underline{D}}}} : \underline{\underline{\varepsilon}}$ where $\underline{\underline{\underline{\underline{D}}}}$ is the elastic tensor.

Let $\underline{u}$ be the displacement field such that the problem reads:

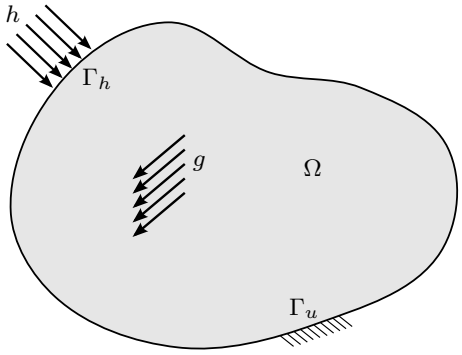

Figure B.3: A general structural mechanics problem.

Find $\underline{u} \in \mathcal{H}^1$ *so that*

$$\forall \underline{v} \in \mathcal{H}^1,\ k(\underline{u}, \underline{v}) = f(\underline{v}) \tag{B.3}$$

where k are the internal virtual forces and f the external virtual ones.

$$\begin{aligned} \forall \underline{u}, \underline{v} \in \mathcal{H}^1, \quad k(\underline{u}, \underline{v}) &= \int_\Omega \underline{\underline{\sigma}}(\underline{u}) : \underline{\underline{\varepsilon}}(\underline{v})\ d\Omega \\ \forall \underline{v} \in \mathcal{H}^1_0, \qquad f(\underline{v}) &= \int_\Omega \underline{g} \cdot \underline{v}\ d\Omega + \int_{\Gamma_h} \underline{h} \cdot \underline{v}\ d\Gamma_h \end{aligned} \tag{B.4}$$

The total energy then equals

$$\forall \underline{v} \in \mathcal{H}^1_0,\ E(\underline{v}) = \frac{1}{2}\int_\Omega \underline{\underline{\sigma}}(\underline{v}) : \underline{\underline{\varepsilon}}(\underline{v})\ d\Omega - \int_\Omega \underline{g} \cdot \underline{v}\ d\Omega - \int_{\Gamma_h} \underline{h} \cdot \underline{v}\ d\Gamma_h \tag{B.5}$$

Remark B.2.1. *Note that problem B.3 is equivalent to the optimization problem [95]:*

$$\min_{\underline{v} \in \mathcal{H}^1_0} E(\underline{u}) \tag{B.6}$$

In the next section, we show how to obtain the multi-model formulation in the Arlequin framework.

B.2.2 Formulation of a multi-model static structural problem in the Arlequin framework

In this section, we restrain ourselves to two models without loss of generality and the hypotheses and notations from the previous section hold. We formulate the two-model problem in the Arlequin framework by focusing on the different principles of the method.

Superimposition of models Let us consider two models defined on two open sets Ω_1 and Ω_2. They form a partition of the global domain $\Omega = \Omega_1 \cup \Omega_2$ such that $S = \Omega_1 \cap \Omega_2 \neq \emptyset$. For clarity, we assume that Γ_g and Γ_u are exclusively included in the first and second model respectively (see Figure B.4). As $S \neq \emptyset$, the two models coexist in this region. Moreover, if the modelling of both models is identical then so should the mechanical states.

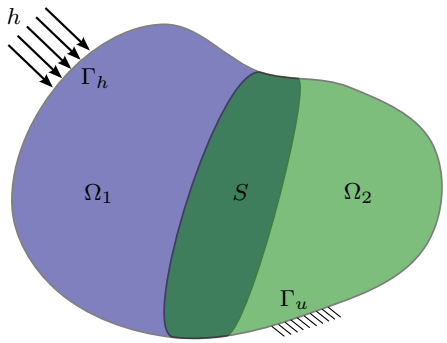

Figure B.4: An example of a 2-model Arlequin problem representative of the problem in Figure B.3.

Volume coupling The two models now need to be coupled to each other.

On the region S, we define a gluing zone S_g such that $S_g \subset S$ and $S_g \neq \emptyset$ on which we activate ghost forces[1] to enforce the mechanical states of both models to be equal. The space of quantities (for example displacements, stress or strain) enforced to be equal is called the mediator space $\mathcal{M}$.

The mechanical state quantities of both models must then be projected unto the mediator space. In order to do so, a mathematical operator, called the coupling operator must be defined. This operator can be built thanks to various scalar products.

Finally, as the Arlequin method uses a variational formulation, the mechanical states are weakly enforced. To enforce them, ghost forces are introduced thanks to Lagrange multipliers, the penalty method or a combination of both [181].

Splitting of the energy to each model In the gluing zone, both models coexist. Thus each model contributes its energy to the global model so that the energy in accounted for twice. This is why weight parameters, also called weight functions, that form a partition of unity, are introduced. These weight functions can be different for each energy contribution. For instance, a set of weight functions (α_1, α_2) can be used for the work of internal forces while another one, say (β_1, β_2) can be used for the work of external forces.

A set of weight functions are then defined by

$$\forall(\alpha_1,\alpha_2),\ \alpha_1 : \Omega_1 \to [0,1]; \alpha_2 : \Omega_2 \to [0,1];\ \begin{cases} \alpha_1 & = & 1 & \text{on} & \Omega_1 \setminus \Omega_2 \\ \alpha_2 & = & 1 & \text{on} & \Omega_2 \setminus \Omega_1 \\ \alpha_1 + \alpha_2 & = & 1 & \text{on} & \Omega_1 \cap \Omega_2 \end{cases} \tag{B.7}$$

Example of weight functions are presented in Figure B.5.

[1]Note that force is meant in a broad sense and depends on the mediator space $\mathcal{M}$.

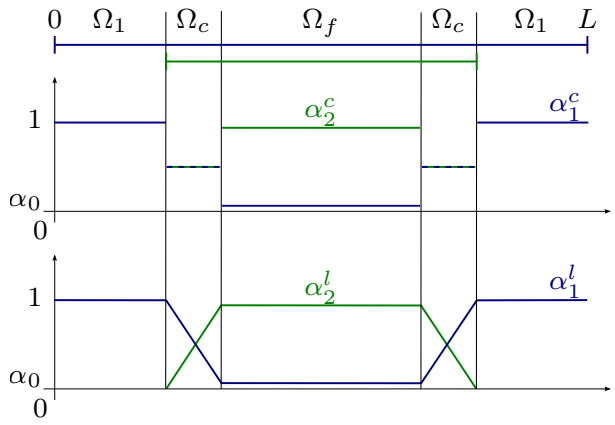

Figure B.5: Example of piecewise constant (α_1^c, α_2^c) and linear (α_1^l, α_2^l) weight functions for two 1D overlapped domains (in blue and green).

Let $\mathcal{V}_1$ and $\mathcal{V}_2$ be the eligible cinematic fields for each model. The weighted virtual works are then equal to :

$$\begin{array}{llll} \forall \underline{u}_1, \underline{v}_1 & \in \mathcal{H}^1 \times \mathcal{H}^1_0, & k_1(\underline{u}_1, \underline{v}_1) & = \displaystyle\int_{\Omega_1} \alpha_1 \underline{\underline{\sigma}}(\underline{u}_1) : \underline{\underline{\varepsilon}}(\underline{v}_1)\ d\Omega_1 \\ \forall \underline{v}_1 & \in \mathcal{H}^1_0, & f_1(\underline{v}_1) & = \displaystyle\int_{\Omega_1} \beta_1 \underline{g} \cdot \underline{v}_1\ d\Omega_1 \\ \forall \underline{u}_2, \underline{v}_2 & \in \mathcal{H}^1 \times \mathcal{H}^1_0, & k_2(\underline{u}_2, \underline{v}_2) & = \displaystyle\int_{\Omega_2} \alpha_2 \underline{\underline{\sigma}}(\underline{u}_2) : \underline{\underline{\varepsilon}}(\underline{v}_2)\ d\Omega_2 \\ \forall \underline{v}_2 & \in \mathcal{H}^1, & f_2(\underline{v}_2) & = \displaystyle\int_{\Omega_2} \beta_2 \underline{g} \cdot \underline{v}_2\ d\Omega_2 + \int_{\Gamma_h} \underline{h} \cdot \underline{v}_2\ d\Gamma_h \end{array} \tag{B.8}$$

The energy contribution of each model is then:

$$\forall i = 1,2\ \forall \underline{v}_i \in \mathcal{H}^1_0,\ E_i(\underline{v}_i) = \frac{1}{2}\int_{\Omega_i} \alpha_i \underline{\underline{\sigma}}(\underline{v}_i) : \underline{\underline{\varepsilon}}(\underline{v}_i)\ d\Omega_i - \int_{\Omega_i} \beta_i \underline{g} \cdot \underline{v}_i\ d\Omega_i - \int_{\partial\Omega_i} \underline{h} \cdot \underline{v}_i\ d\partial\Omega_i \tag{B.9}$$

Arlequin formulation In the following, we consider the mediator space $\mathcal{M}$ to be the space of all eligible displacements fields, use Lagrange multipliers for the coupling and denote by c the coupling operator (denoted $< \cdot >$ in equation B.1). The Arlequin formulation then reads:

Find $(\underline{u}_1, \underline{u}_2, \underline{\lambda}) \in \mathcal{H}^1 \times \mathcal{H}^1 \times \mathcal{M}$ *so that*

$$\forall (\underline{v}_1, \underline{v}_2, \underline{\mu}) \in \mathcal{H}^1_0 \times \mathcal{H}^1_0 \times \mathcal{M},\ \left\{ \begin{array}{l} k_1(\underline{u}_1, \underline{v}_1) + c(\underline{v}_1, \lambda) = f_1(\underline{v}_1) \\ k_1(\underline{v}_2, \underline{v}_2) - c(\underline{v}_2, \lambda) = f_2(\underline{v}_2) \\ c(\underline{u}_1 - \underline{u}_2, \underline{\mu}) = 0 \end{array} \right. \tag{B.10}$$

Remark B.2.2. *As en example, the coupling operator c can be defined as*

$$c(\underline{v}, \underline{\lambda}) = \int_{S_g} \underline{v} \cdot \underline{\lambda} + \mathcal{L}^2 \underline{\underline{\varepsilon}}(\underline{v}) : \underline{\underline{\varepsilon}}(\underline{\lambda})\ dS_g \tag{B.11}$$

where $\mathcal{L}$ is homogeneous to a distance and is representative of the size of the gluing zone S_g. Note that in this work and in most works found in the literature, the term *coupling* zone is preferred to *gluing zone*.

Remark B.2.3. *As for the mono-model formulation (see remark B.2.1), the Arlequin formulation B.10 is equivalent to a optimization problem [95] :*

$$\min_{(\underline{v}_1,\underline{v}_2)\in\mathcal{H}_0^1\times\mathcal{H}_0^1}\ \max_{\underline{\mu}\in\mathcal{M}}\{E_1(\underline{v}_1)+E_2(\underline{v}_2)+c(\underline{v}_1-\underline{v}_2,\underline{\mu})\} \tag{B.12}$$

The methodology to obtain an Arlequin formulation was presented here for static applications. It was done so because they are the type of problems for which there are theoretical proof that the Arlequin formulation converges towards the solution of the problem [93] [94] [95] [96] [100]. Nevertheless, the Arlequin method was extended to structural dynamics [115] [116]. In the next section, we present the methodology for the extension of the Arlequin method to structural dynamics.

B.3 Extension of the Arlequin method to structural dynamics applications

In this section, for clarity and without loss of generality, we restrict ourselves to the study of elastodynamics applications. As in the previous section, we first present the mono-model formulation for structural dynamics (section B.3.1). Then, we extend the Arlequin framework to structural dynamics applications. In order to do so, we emphasize the changes induced by dynamics (section B.3.2).

B.3.1 Mono-model formulation for structural dynamics applications

We consider an isotropic elastic body occupying a bounded, regular domain $\Omega \in \mathbb{R}^d$. Let $\underline{u}$, $\underline{\dot{u}}$ and $\underline{\ddot{u}}$ denote the displacement, velocity, and acceleration fields while $\underline{u}^0$ and $\underline{\dot{u}}^0$ are the initial displacement and velocity. The boundary $\partial\Omega$ of Ω is partitioned into two parts, Γ_u and Γ_h, such that $\Gamma_u \cap \Gamma_h = \emptyset$. The body is submitted to volume forces $\underline{g} \in L^2(\Omega)$, prescribed displacements $\underline{u}_p$ on $\Gamma_u \neq \emptyset$ and prescribed boundary forces $\underline{h}$ on Γ_h. Let ρ be the material density, $\underline{\underline{\sigma}}$ the Cauchy stress tensor, and $\underline{\underline{\varepsilon}}$ the infinitesimal strain tensor. The strain tensor is given by $\underline{\underline{\varepsilon}} = \underline{\underline{\nabla^S u}} = \frac{1}{2}(\underline{\underline{\nabla u}} + \underline{\underline{\nabla^T u}})$ while the stress tensor is given by Hooke's law : $\underline{\underline{\sigma}} = \underline{\underline{\underline{\underline{D}}}} : \underline{\underline{\varepsilon}}$ where $\underline{\underline{\underline{\underline{D}}}}$ is the elastic tensor.

The weak mono-model formulation of this problem reads as follows:

Given $\underline{g}$, $\underline{h}$, $\underline{u}_p$, $\underline{u}^0$ and $\underline{\dot{u}}^0$, find $\underline{u}(t) \in \mathcal{H}^1, t \in [0,T]$ such that

$$\forall \underline{v} \in \mathcal{H}_0^1,\ m(\underline{u}(t),\underline{v}) + k(\underline{u}(t),\underline{v}) = f(\underline{v}) \tag{B.13}$$

with

$$\begin{aligned} m(\underline{u}(t),\underline{v}) &= \int_{\Omega_1} \rho \frac{d^2\underline{u}}{dt^2}(t)\cdot\underline{v}\ d\Omega_1 \\ k(\underline{u}(t),\underline{v}) &= \int_{\Omega_1} \underline{\underline{\sigma}}(\underline{u}(t)) : \underline{\underline{\varepsilon}}(\underline{v})\ d\Omega_1 \\ f(\underline{v}) &= \int_{\Omega_1} \underline{g}(t)\cdot\underline{v}\ d\Omega_1 + \int_{\Gamma_h} \underline{h}(t)\cdot\underline{v}\ d\Gamma_h \end{aligned} \tag{B.14}$$

where $\mathcal{H}^1$ is the trial function space and $\mathcal{H}_0^1$ the test function space.

The total energy then equals:

$$\forall \underline{v} \in \mathcal{H}_0^1,\ E(\underline{v}) = \frac{1}{2}\int_\Omega \rho \underline{\dot{v}}^2\ d\Omega + \frac{1}{2}\int_\Omega \underline{\underline{\sigma}}(\underline{v}) : \underline{\underline{\varepsilon}}(\underline{v})\ d\Omega - \int_\Omega \underline{g}\cdot\underline{v}\ d\Omega - \int_{\Gamma_h} \underline{h}\cdot\underline{v}\ d\Gamma_h \quad \text{(B.15)}$$

B.3.2 Multi-model Arlequin formulation for structural dynamics applications

In this section, we restrain ourselves to two models without loss of generality and the hypotheses and notations from the previous section hold. The superimposition of the two models in elastodynamics in is no different than in static cases. Thus, the two features of the Arlequin framework that change are the volume coupling and the splitting of the energy.

Volume coupling The only thing that changes is the mediator space. Indeed, the ghost forces are still weakly enforced on the gluing zone S_g thanks to a coupling operator. However, the mechanical states enforced to be equal does not have to be the displacement field but can be, depending on the time integrator and resolution algorithm, the displacement, velocity or acceleration fields. The most natural choice is the acceleration field.

Splitting of the energy to each model A new term, the kinetic energy $\int_\Omega \rho\|\underline{\dot{v}}\|^2\ d\Omega$, contributes to the total energy. This new term also needs to be split between the two models so that a new (γ_1, γ_2) set of weight parameters needs to be introduced.

Arlequin formulation We thus have the following multi-model formulation for structural elastodynamics.

Given $\underline{g}$, $\underline{h}$, $\underline{u}_p$, $\underline{u}_0$ *and* $\underline{\dot{u}}_0$, *find* $(\underline{u}_1(t), \underline{u}_2(t), \underline{\lambda}(t)) \in \mathcal{H}^1 \times \mathcal{H}^1 \times \mathcal{M}, t \in [0,T]$ *such that*

$$\left\{\begin{array}{ll} \forall\ \underline{v}_1 \in \mathcal{H}_0^1, & m_1(\underline{u}_1(t), \underline{v}_1) + k_1(\underline{u}_1(t), \underline{v}_1) + c(\underline{u}_1(t), \underline{\lambda}(t)) = f_1(\underline{v}_1) \\ \forall\ \underline{v}_2 \in \mathcal{H}_0^1, & m_2(\underline{u}_2(t), \underline{v}_2) + k_2(\underline{u}_2(t), \underline{v}_2) - c(\underline{u}_2(t), \underline{\lambda}(t)) = f_2(\underline{v}_2) \\ \forall\ \underline{\mu} \in \mathcal{M}, & c(\underline{\mu}, \underline{\ddot{u}}_1(t) - \underline{\ddot{u}}_2(t)) = 0 \end{array}\right. \quad \text{(B.16)}$$

with (i=1,2)

$$\begin{array}{rcl} m_i(\underline{u}(t), \underline{v}) & = & \displaystyle\int_{\Omega_i} \gamma_i \rho\ \frac{d^2\underline{u}}{dt^2}(t)\cdot\underline{v}\ d\Omega_i \\ k_i(\underline{u}(t), \underline{v}) & = & \displaystyle\int_{\Omega_i} \alpha_i\ \underline{\underline{\sigma}}(\underline{u}(t)) : \underline{\underline{\varepsilon}}(\underline{v})\ d\Omega_i \\ f_i(\underline{v}) & = & \displaystyle\int_{\Omega_i} \beta_i\ \underline{g}(t)\cdot\underline{v}\ d\Omega_i + \int_{\partial\Omega_i} \beta_i\ \underline{h}(t)\cdot\underline{v}\ d\partial\Omega_i \\ c(\underline{w}(t), \underline{\mu}) & = & \displaystyle\int_{\Omega_c} \underline{w}(t)\cdot\underline{\mu} + \mathcal{L}^2\ \underline{\underline{\varepsilon}}(\underline{w}(t)) : \underline{\underline{\varepsilon}}(\underline{\mu})\ d\Omega_c \end{array} \quad \text{(B.17)}$$

$\mathcal{M}$ is the mediator space, $\mathcal{L}$ is a strictly positive parameter homogeneous to a length (typically the thickness of the coupling zone), and $\underline{w} \in \mathcal{H}^1$ is an acceleration gap field.

The energy contribution of each model is thus:

$$\forall \underline{v} \in \mathcal{H}_0^1,\ E_i(\underline{v}) = \frac{1}{2}\int_{\Omega_i} \gamma_i \rho \|\underline{\dot{v}}\|^2\, d\Omega_i + \frac{1}{2}\int_{\Omega_i} \alpha_i \underline{\underline{\sigma}}(\underline{v}) : \underline{\underline{\varepsilon}}(\underline{v})\, d\Omega_i - \int_{\Omega_i} \beta_i \underline{g}\cdot\underline{v}\, d\Omega_i - \int_{\partial\Omega_i} \beta_i \underline{h}\cdot\underline{v}\, d\partial\Omega_i \tag{B.18}$$

so that the total energy equals [115]:

$$\forall \underline{v} \in \mathcal{H}_0^1,\ E_{tot} = E_1(\underline{v}) + E_2(\underline{v}) + E_c(\underline{\lambda}) \tag{B.19}$$

where E_c is the coupling energy. In our case, it is the energy associated to the Lagrange multipliers.

Appendix C

Example of the influence of initial conditions on Differential Algebraic System

The objective of this appendix is to underline the importance of condition (1.30) for constrained problem. In order to do so, we consider the following constrained example and show that if condition (1.30) is not met, a weak instability appears so that the solution diverges, as expected.

C.1 Presentation

We consider two identical masses m on a frictionless floor. They are connected by a spring k and one of the masses is also connected to a wall through another spring k. We denote by x_1 and x_2 the displacement of each mass. This system is represented in Figure C.1.

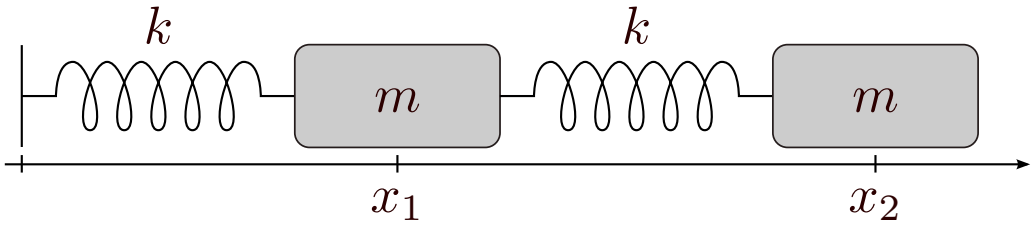

Figure C.1: A mass m at displacement x_1 is connected to a wall and to another mass through springs with a stiffness equal to k. The displacement of second mass is denoted by x_2 and the problem is assumed to stay in one dimension.

The mass matrix $\underline{\underline{M}}$ and the stiffness matrix $\underline{\underline{K}}$ of the system are given by

$$\underline{\underline{M}} = m \begin{pmatrix} 1 & 0 \\ 0 & 1 \end{pmatrix} \text{ and } \underline{\underline{K}} = k \begin{pmatrix} 2 & -1 \\ -1 & 1 \end{pmatrix} \tag{C.1}$$

We consider the constraint $k(\ddot{x_1} + \ddot{x_2}) = 0$, that is, $\underline{C}\ddot{\underline{X}} = 0$ with $\underline{X} = (x_1, x_2)$ and $\underline{C} = k[1\ 1]$. The overall constrained system can thus be written as the following

differential algebraic system.

$$\begin{pmatrix} \underline{\underline{M}} & \underline{\underline{C}}^T \\ \underline{\underline{C}} & 0 \end{pmatrix} \begin{bmatrix} \ddot{\underline{X}}^n \\ \ddot{\nu}^n \end{bmatrix} + \begin{pmatrix} \underline{\underline{K}} & \underline{0} \\ \underline{0} & 0 \end{pmatrix} \begin{bmatrix} \underline{X}^n \\ \nu^n \end{bmatrix} = \begin{pmatrix} 0 \\ 0 \end{pmatrix} \tag{C.2}$$

This system corresponds to the type of problems studied in section 1.2. In the following, we first consider initial conditions that meet (1.30) and obtain a bounded solution. Then, we impose initial conditions that do not meet (1.30) and show that the solution diverges.

C.2 Solution for constrained initial conditions

We impose $(x_1(0), x_2(0)) = (1, -1)$ and $(\dot{x}_1(0), \dot{x}_2(0)) = (-2, 2)$ so that conditions (1.30) are met. The solution obtained is represented in Figure C.2.

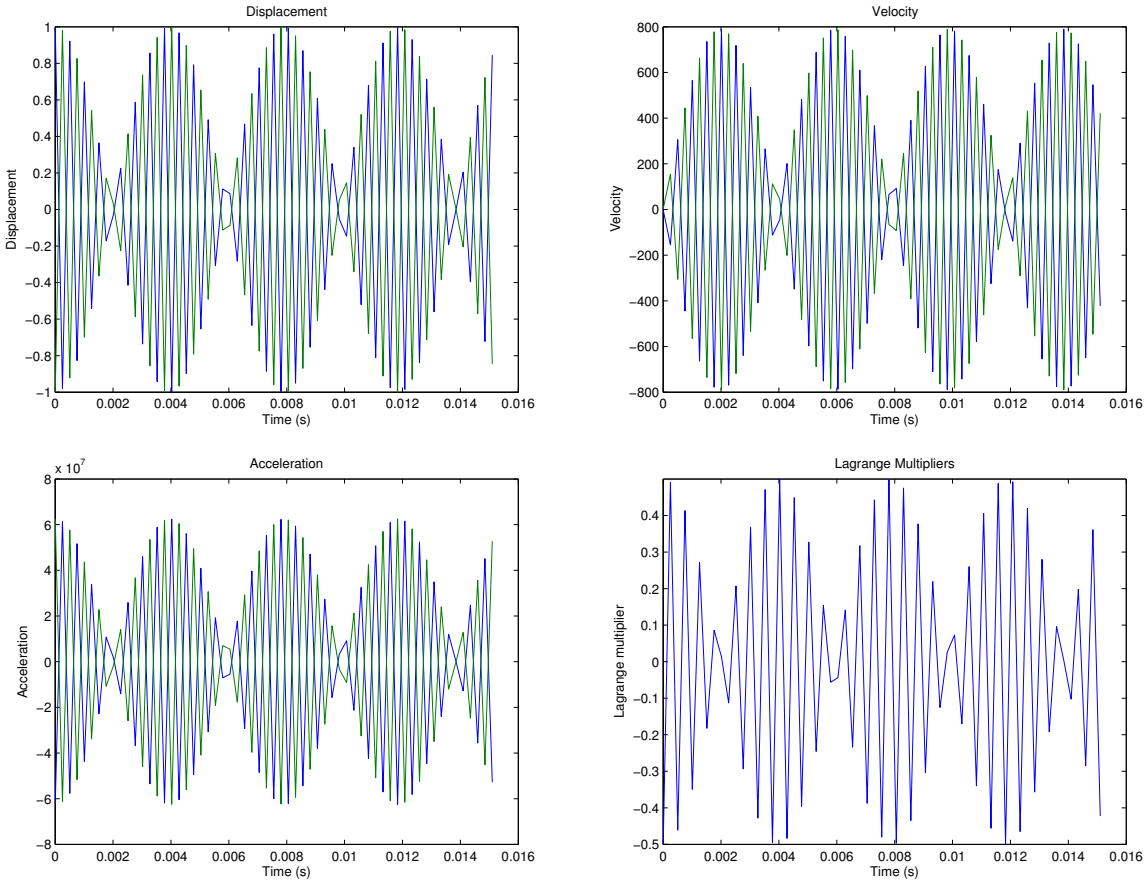

Figure C.2: Time evolution of the displacement (top left), the velocity (top right), the acceleration (bottom left) and the Lagrange multipliers for initial conditions $(x_1(0), x_2(0)) = (1, -1)$ et $(\dot{x}_1(0), \dot{x}_2(0)) = (-2, 2)$. When relevant, quantities relative to the first mass are in blue and those for the second mass are in green.

We can see that, consistent with what was shown in section 1.2, the kinematic quantities are bounded over time. Moreover, the total energy remains constant, as can be seen in Figure C.3.

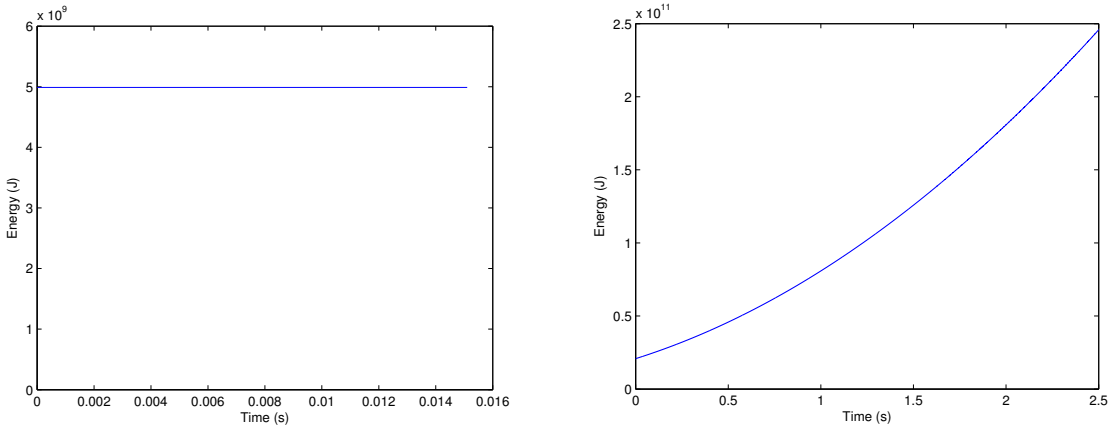

Figure C.3: Total energy of the system over time for constrained initial conditions (left) and unconstrained initial conditions (right).

C.3 Solution for unconstrained initial conditions

Now, we assume that the initial conditions do not meet conditions (1.30) so that we obtain the solution represented in Figure C.4.

In line with what was shown in section 1.2, the acceleration and the velocity are bounded over time. Also, as expected, the displacement is diverging linearly. Thus, we can see in Figure C.3 that the total energy diverges exponentially. It is also interesting to note that the Lagrange multiplier also diverge linearly. In fact, we can show that for this particular problem, we have $\forall n,\ \lambda^n = -\frac{1}{2}x_1^n$ which is exactly what we observe.

In the last two sections, we observed how initial conditions can influence the stability. In particular, we saw that unconstrained initial conditions lead to a diverging total energy. These results can also be obtained through a spectral analysis, as was done in section 1.2.

C.4 Spectral Analysis

In this section, a spectral analysis is completed to show that certain initial conditions can lead to a divergent solution. In order to do so, we consider the amplification matrix $\underline{\underline{\mathcal{A}}}$ of the system for all kinematic quantities, that is, for $\underline{V}_{ddl}^n = [x_1^n, \dot{x_1}^n, \ddot{x_1}^n, x_2^n, \dot{x_2}^n, \ddot{x_2}^n]^T$. $\underline{\underline{\mathcal{A}}}$ is thus defined such that $\underline{V}_{ddl}^{n+1} = \underline{\underline{\mathcal{A}}}\underline{V}_{ddl}^n$. Hence, $\underline{\underline{\mathcal{A}}}$ equals

$$\underline{\underline{\mathcal{A}}} = \frac{1}{8}\begin{pmatrix} 8 & 8 & 4 & 0 & 0 & 0 \\ -6\Omega^2 & 8-6\Omega^2 & 4-3\Omega^2 & 4\Omega^2 & 4\Omega^2 & 2\Omega^2 \\ -12\Omega^2 & -12\Omega^2 & -6\Omega^2 & 4\Omega^2 & 4\Omega^2 & 2\Omega^2 \\ 0 & 0 & 0 & 8 & 8 & 4 \\ 6\Omega^2 & 6\Omega^2 & 3\Omega^2 & -4\Omega^2 & 8-4\Omega^2 & 4-2\Omega^2 \\ 12\Omega^2 & 12\Omega^2 & 6\Omega^2 & -8\Omega^2 & -8\Omega^2 & -4\Omega^2 \end{pmatrix} \tag{C.3}$$

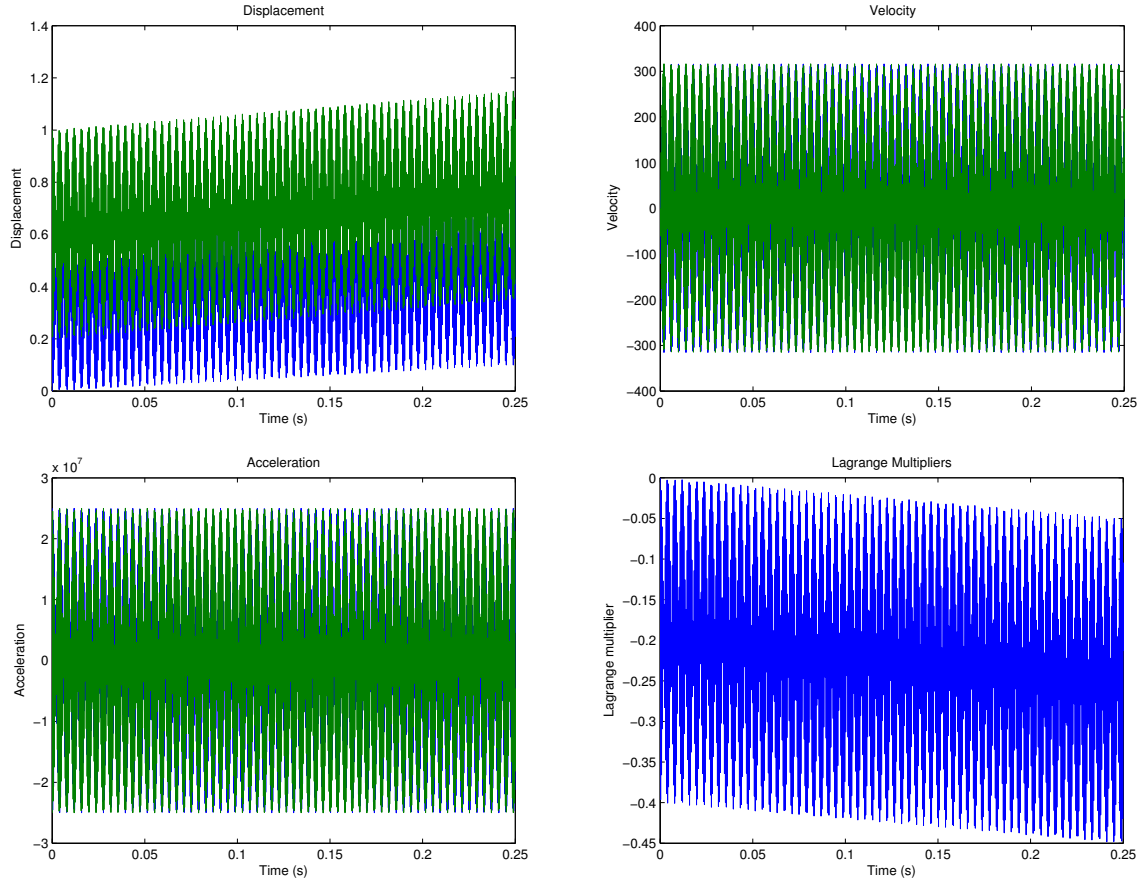

Figure C.4: Time evolution of the displacement (top left), the velocity (top right), the acceleration (bottom left) and the Lagrange multipliers for initial conditions $(x_1(0), x_2(0)) = (0, 1)$ et $(\dot{x}_1(0), \dot{x}_2(0)) = (2, -1)$. When relevant, quantities relative to the first mass are in blue and those for the second mass are in green.

Thanks to the software ©MAPLE, we obtain the six eigenvalues of the $\underline{\underline{\mathcal{A}}}$:

$$\lambda_1 = \lambda_2 = 0;\ \lambda_3 = f_3(\Omega^2);\ \lambda_4 = f_4(\Omega^2);\ \lambda_5 = \lambda_6 = 1. \tag{C.4}$$

The first two eigenvalues do not affect the stability. The absolute value of the third and the fourth ones need to be lower than one, that is, $|f_3(\Omega^2)| < 1$ and $|f_4(\Omega^2)| < 1$, which leads to stability conditions of type (1.22). Finally, as expected, 1 is an eigenvalue with a geometrical multiplicity of only 1. The software ©MAPLE can also yield the eigenvector V_d that spans the eigenset for eigenvalue 1.

$$\underline{V}_d = \left[-1, \frac{1}{2}, 0, -1, \frac{1}{2}, 0\right]^T \tag{C.5}$$

We can see that the components of the vector that are not equal to 0 are the ones corresponding to the displacement and velocity of the masses, which is consistent with the study of constraints completed in section (1.2).

Appendix D

Influence of the weight function on the elementary critical time step for the wave problem with velocity integrated at mid time step

In this Appendix, we show that imposing $\hat{\alpha}^p = \tilde{\alpha}^p$ ensures optimal stability for the wave problem, even if the discrete velocity is integrated at mid step.

D.1 Problem formulations

In the case the velocity $\underline{v}$ is integrated at every time step n, then the elementary problem[1] can be written[2]:

Problem D.1. $\forall \underline{w} \in \mathcal{H}_0^1$,

$$\left\{ \begin{array}{rcl} \displaystyle\int_{\Omega_E} \rho_0 \hat{\alpha}^v \dot{\underline{v}}^n \cdot \underline{w} \; d\Omega_E & = & \displaystyle\int_{\Omega_E} \bar{\alpha}^v p^n \underline{\underline{I}} : \underline{\underline{(\nabla w)}} \; d\Omega_E \\ \displaystyle\int_{\Omega_E} \hat{\alpha}^p \dot{p}^n \; d\Omega_E & = & \displaystyle\sum_{i=1}^{\mathcal{N}_N} \left(\int_{\partial\Omega_E} \alpha^p \rho_0 c^2 \underline{v}^n \cdot \underline{n} \; d\partial\Omega_E \right) \end{array} \right. \tag{D.1}$$

using notations of Chapter 3. The time integrator used is

$$\underline{U}^{n+1} = \underline{U}^n + \Delta t \dot{\underline{U}}^n \tag{D.2}$$

with $\underline{U}^n = [\underline{v}^n, p^n]^T$ *and* Δt *the critical time step.*

In the case the velocity $\underline{\tilde{v}}$ is integrated at mid time step $n + \frac{1}{2}$, then the elementary problem can be written:

Problem D.2. $\forall \underline{w} \in \mathcal{H}_0^1$,

$$\left\{ \begin{array}{rcl} \displaystyle\int_{\Omega_E} \rho_0 \hat{\alpha}^v \dot{\underline{\tilde{v}}}^{n+\frac{1}{2}} \cdot \underline{w} \; d\Omega_E & = & \displaystyle\int_{\Omega_E} \bar{\alpha}^v p^n \underline{\underline{I}} : \underline{\underline{(\nabla w)}} \; d\Omega_E \\ \displaystyle\int_{\Omega_E} \hat{\alpha}^p \dot{p}^{n+1} \; d\Omega_E & = & \displaystyle\sum_{i=1}^{\mathcal{N}_N} \left(\int_{\partial\Omega_E} \alpha^p \rho_0 c^2 \underline{\tilde{v}}^{n+\frac{1}{2}} \cdot \underline{n} \; d\partial\Omega_E \right) \end{array} \right. \tag{D.3}$$

[1] We consider the Full Arlequin formulations as it is the most general case when analysing the influence of the weight function.

[2] By hypothesis we do not consider the coupling matrices.

using notations of Chapter 3. The time integrator used is

$$\underline{\tilde{U}}^{n+1} = \underline{\tilde{U}}^{n} + \Delta t \underline{\dot{\tilde{U}}}^{n} \tag{D.4}$$

with $\underline{\tilde{U}}^{n} = [\underline{\tilde{v}}^{n+\frac{1}{2}}, p^{n+1}]^T$ *and* Δt *the critical time step.*

Remark D.1.1. *Note that in* **Problem** D.1*, both equations can be solved simultaneously while for* **Problem** D.2*, the equations need to be solved alternatively (the acceleration one at mid time step and the pressure one at time steps* n*).*

D.2 Amplification matrix for each formulation

In order to show the main difference in the study of the stability of the two problem formulations, we propose to introduce their respective amplification matrix[3].

D.2.1 Amplification matrix and stability of Problem D.1

Equation (D.1) of **Problem** D.1 can be written, in matrix form as follows

$$\underline{\underline{M}}\underline{\dot{U}}^{n} + \underline{\underline{K}}\underline{U}^{n} = 0 \tag{D.5}$$

where $\underline{\underline{M}} = \text{diag}(\underline{\underline{M}}_v, \mathcal{D}_p)$ with $\underline{\underline{M}}_v$ the lumped mass matrix, $\underline{U}^n = [v_1^n, ..., v_{\mathcal{N}_N}^n, p^n]^T$ and $\underline{\underline{K}}$ is defined as follows:

$$\underline{\underline{K}} = \begin{pmatrix} \underline{\underline{0}}_{\mathcal{N}_N,\mathcal{N}_N} & \underline{K}_v \\ \underline{K}_p^T & 0 \end{pmatrix} \tag{D.6}$$

where $\underline{K}_v$ is the assembled pressure vector such that $\underline{K}_v \underline{p}^n$ yields the pressure forces at time t^n, $\underline{K}_p$ the assembled transport matrix such that $\underline{K}_p^T \underline{v}^n$ yields the flow at time t^n and $\underline{\underline{0}}_{n_1,n_2}$ is the matrix of size $n_1 \times n_2$ with zeros everywhere. We recall that $\mathcal{N}_E$ is the number of elements of the mesh and $\mathcal{N}_N$ the number of degrees of freedom associated to the velocity. We have:

$$\begin{cases} (\underline{\underline{M}}_v)_{jk} &= \left(\rho_0 \int_\Omega \hat{\alpha}^v \hat{N}_j \, d\Omega\right) \delta_{jk} & \forall\ j,k \in \mathcal{S}_N \\ D_p &= \int_{\Omega_E} \hat{\alpha}^p \, d\Omega_E & \\ (\underline{K}_v)_j &= \int_{\Omega_E} \bar{\alpha}^v \frac{\partial N_j}{\partial x_{d(j)}} \, d\Omega_E & \forall\ j \in \mathcal{S}_N \\ (\underline{K}_p)_j &= \int_{\partial\Omega_E} \rho_0 c^2 N_j \underline{n} \cdot \underline{x}_{d(j)} \, d\partial\Omega_E & \forall\ j \in \mathcal{S}_N \end{cases} \tag{D.7}$$

using notations from Chapter 3.

The amplification matrix of **Problem** D.1, $\underline{\underline{\mathcal{A}}}$, is such that $\underline{U}^{n+1} = \underline{\underline{\mathcal{A}}}\underline{U}^n$. By multiplying by $\underline{\underline{M}}^{-1}$ equation (D.5) and substituting the obtain formula for $\underline{\dot{U}}^n$ in the time integrator (D.2), we obtain the following.

$$\underline{U}^{n+1} = (\underline{\underline{I}} - \Delta t \underline{\underline{M}}^{-1} \underline{\underline{K}}) \underline{U}^n \tag{D.8}$$

[3]See section 1.2.

so that we have $\underline{\underline{\mathcal{A}}} = \underline{\underline{I}} - \Delta t \underline{\underline{M}}^{-1} \underline{\underline{K}}$. The stability is then obtained by studying under which condition, called CFL condition, the spectral radius of $\underline{\underline{\mathcal{A}}}$ is strictly lower than 1. We obtain[4] the following condition.

$$\Delta t < \frac{2}{\max \tilde{\omega}} \tag{D.9}$$

where the $\tilde{\omega}$ are the eigenvalues of the generalized eigenvalue problem of $\underline{\underline{M}}$ and $\Delta t \underline{\underline{K}}$.

D.2.2 Amplification matrix and spectral stability of Problem D.2

Equation (D.3) **Problem** D.2 can be written in matrix form as follows

$$\underline{\underline{M}} \dot{\underline{U}}^n + \begin{pmatrix} \underline{\underline{0}}_{\mathcal{N}_N,\mathcal{N}_N} & \underline{K}_v \\ \underline{K}_p^T & 0 \end{pmatrix} \begin{pmatrix} \underline{\tilde{v}}^{n+\frac{1}{2}} \\ p^n \end{pmatrix} = 0 \tag{D.10}$$

using previous notations.

Contrary to the previous section, some work needs to be done to obtain the amplification matrix of **Problem** D.2 $\underline{\underline{\tilde{\mathcal{A}}}}$. We use the time integrator for the velocity and substitute it in the second term of the left hand side of (D.10). We then use the last equation of (D.3) at time step n for the pressure and $n - \frac{1}{2}$ for the velocity. Finally, we obtain, after multiplying by $\underline{\underline{M}}^{-1}$:

$$\underline{U}^n = (\underline{\underline{I}} - \underline{\underline{M}}^{-1} \underline{\underline{\tilde{K}}}) \underline{U}^{n-1} \tag{D.11}$$

with

$$\underline{\underline{\tilde{K}}} = \begin{pmatrix} \underline{\underline{0}}_{\mathcal{N}_N,\mathcal{N}_N} & \underline{K}_v \\ \underline{K}_p^T & -\Delta t \underline{K}_p^T \underline{\underline{M}}_v^{-1} \underline{K}_v \end{pmatrix} \tag{D.12}$$

so that we have $\underline{\underline{\mathcal{A}}} = \underline{\underline{I}} - \Delta t \underline{\underline{M}}^{-1} \underline{\underline{\tilde{K}}}$. The stability is then obtained by studying under which condition, called CFL condition, the spectral radius of $\tilde{\mathcal{A}}$ is strictly lower than 1. We obtain[5] the following condition.

$$\Delta t < \frac{2}{\max \omega} \tag{D.13}$$

where the ω are the eigenvalues of $\underline{\underline{M}}$ and $\underline{\underline{\tilde{K}}}$.

D.2.3 Determination of the eigenvalues of the generalized eigenvalue problems

D.2.3.1 Eigenvalues for Problem D.1

The calculations were already made in section 3.3.2.1 and we found:

$$\omega^2 = \frac{1}{\left(\int_{\Omega_E} \hat{\alpha}^p \, d\Omega_E \right)} \sum_{i=1}^{\mathcal{N}} \left(\frac{\int_{\Omega_E} \bar{\alpha}^v \dfrac{\partial N_i}{\partial x_{d(i)}} \, d\Omega_E}{\int_{\Omega_E} \rho_0 \hat{\alpha}^v \hat{N}_i \, d\Omega_E} \right) \left(\int_{\partial \Omega_E} \alpha^p \rho_0 c^2 N_i \, \underline{n} \, d\partial\Omega_E \right) \cdot \underline{x}_{d(i)} \tag{D.14}$$

[4] See [154] or [174]
[5] See [154] or [174]

D.2.3.2 Eigenvalues for Problem D.2

Let $\underline{\tilde{U}}_E = [v_1, ..., v_{\mathcal{N}_N}, p_E]$ be an eigenvector of $\underline{\underline{M}}$ and $\underline{\underline{\tilde{K}}}$. The components of $\underline{\tilde{U}}_E$ thus verify:

$$\left\{ \begin{array}{rcll} \tilde{\omega} a_i v_i & = & b_i p_E, & \forall i \in [|1, \mathcal{N}_N|] \\ \tilde{\omega} d p_E & = & \displaystyle\sum_{i=1}^{\mathcal{N}_N} s_i v_i + \left(\sum_{i=1}^{\mathcal{N}_N} \frac{b_i}{a_i} s_i \right) p_E & \end{array} \right. \tag{D.15}$$

with

$$\left\{ \begin{array}{rcl} a_i & = & \rho_0 \displaystyle\int_{\Omega_E} \hat{\alpha}^v \hat{N}_i \, d\Omega_E \\ b_i & = & \displaystyle\int_{\Omega_E} \bar{\alpha}^v \frac{\partial N_i}{\partial x_{d(i)}} \, d\Omega_E \\ d & = & \displaystyle\int_{\Omega_E} \hat{\alpha}^p \, d\Omega_E \\ s_i & = & \displaystyle\int_{\partial\Omega_E} \alpha^p \rho_0 c^2 N_i \, \underline{n} \cdot \underline{x}_{d(i)} \, d\partial\Omega_E \end{array} \right. \tag{D.16}$$

The same calculations as in section 3.3.2.1 can be done. From the top equations of (D.15), we have each v_i as a function of p_E so that after substitution in the last equation, we obtain

$$\tilde{\omega}^2 = \frac{(1+\tilde{\omega})}{\left(\displaystyle\int_{\Omega_E} \hat{\alpha}^p \, d\Omega_E \right)} \sum_{i=1}^{\mathcal{N}} \left(\frac{\displaystyle\int_{\Omega_E} \bar{\alpha}^v \frac{\partial N_i}{\partial x_{d(i)}} \, d\Omega_E}{\displaystyle\int_{\Omega_E} \rho_0 \hat{\alpha}^v \hat{N}_i \, d\Omega_E} \right) \left(\int_{\partial\Omega_E} \alpha^p \rho_0 c^2 N_i \, \underline{n} \, d\partial\Omega_E \right) \cdot \underline{x}_{d(i)} \tag{D.17}$$

Although the solutions of (D.17) for $\tilde{\omega}$ are clearly different than those of (D.14) for ω, we can see that we can annul the influence of weight functions in exactly the same manner.

Appendix E

Computation of $\hat{\alpha}^p$ for triangular elements with constant weights on the edges.

In this appendix, we aim to show that if weight function is planar on a triangular element, then we have $\hat{\alpha^p} = \bar{\alpha}^p$, where $\hat{\alpha^p}$ and $\bar{\alpha}^p$ are defined in section 3.3 and whose expressions are hereby recalled:

$$\hat{\alpha}^p = \frac{\displaystyle\sum_{i=1}^{\mathcal{N}} \left(\frac{\displaystyle\int_{\Omega_E} \frac{\partial N_i}{\partial x_{d(i)}}\, dx}{\displaystyle\int_{\Omega_E} \rho_0 \hat{N}_i\, dx} \right) \left(\int_{\partial\Omega_E} \alpha^p \rho_0 c^2 N_i\ \underline{n}\ dx \right) \cdot \underline{x}_{d(i)}}{\displaystyle\sum_{i=1}^{\mathcal{N}} \left(\frac{\displaystyle\int_{\Omega_E} \frac{\partial N_i}{\partial x_{d(i)}}\, dx}{\displaystyle\int_{\Omega_E} \rho_0 \hat{N}_i\, dx} \right) \left(\int_{\partial\Omega_E} \rho_0 c^2 N_i\ \underline{n}\ dx \right) \cdot \underline{x}_{d(i)}} \tag{E.1}$$

$$\bar{\alpha}^p = \tfrac{1}{|\Omega_E|} \int_{\Omega_E} \alpha^p\, dx$$

E.1 Shape functions for a triangle

Let us consider a triangle with summits $A(x_A, y_A)$, $B(x_B, y_B)$ and $C(x_C, y_C)$. The shape functions are as follows

$$\begin{cases} N_A(x,y) &= 1 - \dfrac{(y_C - y_B)(x - x_A) + (x_B - x_C)(y - y_A)}{x_A(y_B - y_C) + x_B(y_C - y_A) + x_C(y_A - y_B)} \\ N_B(x,y) &= 1 - \dfrac{(y_A - y_C)(x - x_B) + (x_C - x_A)(y - y_B)}{x_A(y_B - y_C) + x_B(y_C - y_A) + x_C(y_A - y_B)} \\ N_C(x,y) &= 1 - \dfrac{(y_B - y_A)(x - x_C) + (x_A - x_B)(y - y_C)}{x_A(y_B - y_C) + x_B(y_C - y_A) + x_C(y_A - y_B)} \end{cases}$$

where N_I, x_I, y_I are, respectively, the shape function such that $N_I(I) = 1$, the x and y coordinates of summit I.

Note that the denominator of each shape function is none other than the volume of the element $|\Omega_E|$. In fact, we have

$$\int_{\Omega_E} N_1(x,y)\ d\Omega_E = \int_{\Omega_E} N_2(x,y)\ d\Omega_E = \int_{\Omega_E} N_3(x,y)\ d\Omega_E = \frac{1}{3}|\Omega_E|$$

We thus have:

$$\begin{array}{lllllllll}
\dfrac{\partial N_A}{\partial x}(x,y) & = & \dfrac{y_B - y_C}{2|\Omega_E|} & \dfrac{\partial N_B}{\partial x}(x,y) & = & \dfrac{y_C - y_A}{2|\Omega_E|} & \dfrac{\partial N_C}{\partial x}(x,y) & = & \dfrac{y_A - y_B}{2|\Omega_E|} \\
\dfrac{\partial N_A}{\partial y}(x,y) & = & \dfrac{x_C - x_B}{2|\Omega_E|} & \dfrac{\partial N_B}{\partial y}(x,y) & = & \dfrac{x_A - x_C}{2|\Omega_E|} & \dfrac{\partial N_C}{\partial y}(x,y) & = & \dfrac{x_B - x_A}{2|\Omega_E|}
\end{array}$$

E.2 Value of $\hat{\alpha}^p$

E.2.1 Value of the denominator

The only term left to be determined in the expression of $\hat{\alpha}^p$ in E.1 is the term $\sum_{e_i} = \int_{e_i} \alpha_{e_i} \underline{n}\ dx$. First, the outer normed normal to the element needs to be defined. We have:

$$\left\{ \begin{array}{l} \underline{n}_{AB} = (y_B - y_A, x_A - x_B) \\ \underline{n}_{AC} = (y_A - y_C, x_C - x_A) \\ \underline{n}_{BC} = (y_C - y_B, x_B - x_C) \end{array} \right.$$

We then have:

$$\begin{array}{rcl}
\displaystyle\sum_{e_i} \int_{e_i} N_A \underline{n}\ dx & = & \dfrac{1}{2}(\underline{n}_{AB} + \underline{n}_{AC}) \\
& = & \dfrac{1}{2}(y_B - y_C, x_C - x_B) \\
\displaystyle\sum_{e_i} \int_{e_i} N_B \underline{n}\ dx & = & \dfrac{1}{2}(\underline{n}_{AB} + \underline{n}_{BC}) \\
& = & \dfrac{1}{2}(y_C - y_A, x_A - x_C) \\
\displaystyle\sum_{e_i} \int_{e_i} N_C \underline{n}\ dx & = & \dfrac{1}{2}(\underline{n}_{BC} + \underline{n}_{AC}) \\
& = & \dfrac{1}{2}(y_A - y_B, x_B - x_A)
\end{array}$$

Finally, we have:

$$\begin{aligned}
\left(\frac{\int_{\Omega_E}\frac{\partial N_1}{\partial x}\,d\Omega_E}{\int_{\Omega_E}N_1\,d\Omega_E}\right)\sum_{e_i}\int_{e_i}N_1\underline{n}\,dx\cdot\underline{x} &= \frac{3}{4|\Omega_E|}(y_B-y_C)^2\\
\left(\frac{\int_{\Omega_E}\frac{\partial N_1}{\partial y}\,d\Omega_E}{\int_{\Omega_E}N_1\,d\Omega_E}\right)\sum_{e_i}\int_{e_i}N_1\underline{n}\,dx\cdot\underline{y} &= \frac{3}{4|\Omega_E|}(x_C-x_B)^2\\
\left(\frac{\int_{\Omega_E}\frac{\partial N_2}{\partial x}\,d\Omega_E}{\int_{\Omega_E}N_2\,d\Omega_E}\right)\sum_{e_i}\int_{e_i}N_2\underline{n}\,dx\cdot\underline{x} &= \frac{3}{4|\Omega_E|}(y_C-y_A)^2\\
\left(\frac{\int_{\Omega_E}\frac{\partial N_2}{\partial y}\,d\Omega_E}{\int_{\Omega_E}N_2\,d\Omega_E}\right)\sum_{e_i}\int_{e_i}N_2\underline{n}\,dx\cdot\underline{y} &= \frac{3}{4|\Omega_E|}(x_A-x_C)^2\\
\left(\frac{\int_{\Omega_E}\frac{\partial N_3}{\partial x}\,d\Omega_E}{\int_{\Omega_E}N_3\,d\Omega_E}\right)\sum_{e_i}\int_{e_i}N_3\underline{n}\,dx\cdot\underline{x} &= \frac{3}{4|\Omega_E|}(y_A-y_B)^2\\
\left(\frac{\int_{\Omega_E}\frac{\partial N_3}{\partial y}\,d\Omega_E}{\int_{\Omega_E}N_3\,d\Omega_E}\right)\sum_{e_i}\int_{e_i}N_3\underline{n}\,dx\cdot\underline{y} &= \frac{3}{4|\Omega_E|}(x_B-x_A)^2
\end{aligned}$$

whose sum is equal to:

$$\frac{3}{4|\Omega_E|}(AB^2+BC^2+AC^2) \tag{E.2}$$

where AB is the length of the edge connecting summits A and B.

E.2.2 Value of the numerator

We thus consider that the weight functions are linear on each edge. We have:

$$\begin{aligned}
\sum_{e_i}\int_{e_i}\alpha N_1\underline{n}\,dx &= \frac{1}{6}\;[(2\alpha_A+\alpha_B)y_B-(2\alpha_A+\alpha_C)y_C+(\alpha_C-\alpha_B)y_A;\\
&\qquad (2\alpha_A+\alpha_C)x_C-(2\alpha_A+\alpha_B)x_B+(\alpha_B-\alpha_C)x_A]\\
\sum_{e_i}\int_{e_i}\alpha N_2\underline{n}\,dx &= \frac{1}{6}\;[(2\alpha_B+\alpha_C)y_C-(2\alpha_B+\alpha_A)y_A+(\alpha_A-\alpha_C)y_B;\\
&\qquad (2\alpha_B+\alpha_A)x_A-(2\alpha_B+\alpha_C)x_C+(\alpha_C-\alpha_A)x_B]\\
\sum_{e_i}\int_{e_i}\alpha N_3\underline{n}\,dx &= \frac{1}{6}\;[(2\alpha_C+\alpha_A)y_A-(2\alpha_C+\alpha_B)y_B+(\alpha_B-\alpha_A)y_C;\\
&\qquad (2\alpha_C+\alpha_B)x_B-(2\alpha_C+\alpha_A)x_A+(\alpha_A-\alpha_B)x_C]
\end{aligned}$$

From which we deduce:

$$\begin{aligned}
\left(\frac{\int_{\Omega_E}\frac{\partial N_1}{\partial x}\,d\Omega_E}{\int_{\Omega_E}N_1\,d\Omega_E}\right)\sum_{e_i}\int_{e_i}\alpha N_1\underline{n}\,dx\cdot\underline{x} &= \frac{1}{4|\Omega_E|}(y_B-y_C)((2\alpha_A+\alpha_B)y_B-(2\alpha_A+\alpha_C)y_C+(\alpha_C-\alpha_B)y_A))\\
\left(\frac{\int_{\Omega_E}\frac{\partial N_1}{\partial y}\,d\Omega_E}{\int_{\Omega_E}N_1\,d\Omega_E}\right)\sum_{e_i}\int_{e_i}\alpha N_1\underline{n}\,dx\cdot\underline{y} &= \frac{1}{4|\Omega_E|}(x_C-x_B)((2\alpha_A+\alpha_C)x_C-(2\alpha_A+\alpha_B)x_B+(\alpha_B-\alpha_C)x_A)\\
\left(\frac{\int_{\Omega_E}\frac{\partial N_2}{\partial x}\,d\Omega_E}{\int_{\Omega_E}N_2\,d\Omega_E}\right)\sum_{e_i}\int_{e_i}\alpha N_2\underline{n}\,dx\cdot\underline{x} &= \frac{1}{4|\Omega_E|}(y_C-y_A)((2\alpha_B+\alpha_C)y_C-(2\alpha_B+\alpha_A)y_A+(\alpha_A-\alpha_C)y_B)\\
\left(\frac{\int_{\Omega_E}\frac{\partial N_2}{\partial y}\,d\Omega_E}{\int_{\Omega_E}N_2\,d\Omega_E}\right)\sum_{e_i}\int_{e_i}\alpha N_2\underline{n}\,dx\cdot\underline{y} &= \frac{1}{4|\Omega_E|}(x_A-x_C)((2\alpha_B+\alpha_A)x_A-(2\alpha_B+\alpha_C)x_C+(\alpha_C-\alpha_A)x_B)\\
\left(\frac{\int_{\Omega_E}\frac{\partial N_3}{\partial x}\,d\Omega_E}{\int_{\Omega_E}N_3\,d\Omega_E}\right)\sum_{e_i}\int_{e_i}\alpha N_3\underline{n}\,dx\cdot\underline{x} &= \frac{1}{4|\Omega_E|}(y_A-y_B)(2\alpha_C+\alpha_A)y_A-(2\alpha_C+\alpha_B)y_B+(\alpha_B-\alpha_A)y_C)\\
\left(\frac{\int_{\Omega_E}\frac{\partial N_3}{\partial y}\,d\Omega_E}{\int_{\Omega_E}N_3\,d\Omega_E}\right)\sum_{e_i}\int_{e_i}\alpha N_3\underline{n}\,dx\cdot\underline{y} &= \frac{1}{4|\Omega_E|}(x_B-x_A)((2\alpha_C+\alpha_B)x_B-(2\alpha_C+\alpha_A)x_A+(\alpha_A-\alpha_B)x_C)
\end{aligned}$$

whose sum equals:

$$\frac{3}{4|\Omega_E|}(AB^2+BC^2+AC^2)\left(\frac{\alpha_A+\alpha_B+\alpha_C}{3}\right) \tag{E.3}$$

Conclusion We thus obtain:

$$\bar{\alpha}=\frac{\alpha_A+\alpha_B+\alpha_C}{3} \tag{E.4}$$

E.3 Value of $\bar{\alpha}^p$

We assumed that the weight function α^p is planar on the element so that it can be written $\alpha^p(x,y)=\alpha_A N_A(x,y)+\alpha_B N_B(x,y)+\alpha_C N_C(x,y)$. We recall that $\bar{\alpha}=\frac{\int_{\Omega_E}\alpha\ dx}{|\Omega_E|}$ so that we have

$$\int_{\Omega_E}\alpha\ dx=\frac{1}{3}|\Omega_E|(\alpha_A+\alpha_B+\alpha_C)$$

We thus also find:

$$\bar{\alpha}=\frac{\alpha_A+\alpha_B+\alpha_C}{3} \tag{E.5}$$

Appendix F

Complete discrete fluid dynamics formulation for the Full Arlequin approach

The weak discrete formulation for the Full Arlequin approach reads:

Given $\rho_1^0, \rho_1^0, p_1^0, p_2^0, \underline{v}_1^0$ *and* $\underline{v}_2^0$, *find* $\underline{u}(t) = (\underline{v}_1(t), \underline{v}_2(t), \underline{\lambda}_v, \rho_1(t), \rho_2(t), \lambda_\rho, E_1(t), E_2(t), \lambda_{\rho E}) \in \mathcal{H}^1 \times \mathcal{H}^1 \times \mathcal{H}^1 \times \mathcal{V} \times \mathcal{V} \times \mathcal{V} \times \mathcal{V} \times \mathcal{V} \times \mathcal{V}$, $t \in [0, T]$ *such that,*

$\forall (\underline{w}_1, \underline{w}_2, \underline{\mu}_v, \bar{w}_1, \bar{w}_2, \mu_\rho, \tilde{w}_1, \tilde{w}_2, \mu_{\rho E}) \in \mathcal{H}_0^1 \times \mathcal{H}_0^1 \times \mathcal{H}_0^1 \times \mathcal{V} \times \mathcal{V} \times \mathcal{V} \times \mathcal{V} \times \mathcal{V} \times \mathcal{V}$,

$$
\left\{
\begin{array}{l}
\displaystyle\int_{\Omega_1} \widehat{\alpha}_1^v \rho_1^n \dot{\underline{v}}_1^n \cdot \underline{w}_1 \, d\Omega_1 + \int_{\Omega_1} \widetilde{\alpha}_1^v \rho_1^n \underline{\underline{(v_1^{n-\frac{1}{2}} \cdot \nabla) v_1}}^{n\frac{1}{2}} \cdot \underline{w}_1 \, d\Omega_1 - \int_{\Omega_1} \overline{\alpha}_1^v p_1^n \underline{\underline{I}} : \underline{\underline{\nabla w_1}} \, d\Omega_1 + c_m(\underline{w}_1, \underline{\lambda}_v^n) = 0 \\
\displaystyle\int_{\Omega_2} \widehat{\alpha}_2^v \rho_2^n \dot{\underline{v}}_2^n \cdot \underline{w}_2 \, d\Omega_2 + \int_{\Omega_2} \widetilde{\alpha}_2^v \rho_2^n \underline{\underline{(v_2^{n-\frac{1}{2}} \cdot \nabla) v_2}}^{n-\frac{1}{2}} \cdot \underline{w}_2 \, d\Omega_2 - \int_{\Omega_2} \overline{\alpha}_2^v p_2^n \underline{\underline{I}} : \underline{\underline{\nabla w_2}} \, d\Omega_2 - c_m(\underline{w}_2, \underline{\lambda}_v^n) = 0 \\
c_m(\dot{\underline{v}}_1^n - \dot{\underline{v}}_2^n, \underline{\mu}_v) = 0 \\
\displaystyle\int_{\Omega_1} \widehat{\alpha}_1^\rho \dot{\rho}_1^n \; \bar{w}_1 \, d\Omega_1 + \int_{\Omega_1} \mathrm{div}(\alpha_1^\rho \rho_1^n \underline{v}_1^{n+\frac{1}{2}}) \bar{w}_1 \, d\Omega_1 + c_t(\bar{w}_1, \lambda_\rho^n) = 0 \\
\displaystyle\int_{\Omega_2} \widehat{\alpha}_2^\rho \dot{\rho}_2^n \; \bar{w}_2 \, d\Omega_2 + \int_{\Omega_2} \mathrm{div}(\alpha_2^\rho \rho_2^n \underline{v}_2^{n+\frac{1}{2}}) \bar{w}_2 \, d\Omega_2 - c_t(\bar{w}_2, \lambda_\rho^n) = 0 \\
c_t(\dot{\rho}_1^n - \dot{\rho}_2^n, \mu_\rho) = 0 \\
\displaystyle\int_{\Omega_1} \widehat{\alpha}_1^{\rho E} (\dot{\rho E})_1^n \; \tilde{w}_1 \, d\Omega_1 + \int_{\Omega_1} \mathrm{div}(\alpha_1^{\rho E} (\rho_1^n E_1^n + p_1^n) \underline{v}_1^{n+\frac{1}{2}}) \tilde{w}_1 \, d\Omega_1 + c_t(\tilde{w}_1, \lambda_{\rho E}^n) = 0 \\
\displaystyle\int_{\Omega_2} \widehat{\alpha}_2^{\rho E} (\dot{\rho E})_2^n \; \tilde{w}_2 \, d\Omega_2 + \int_{\Omega_2} \mathrm{div}(\alpha_2^{\rho E} (\rho_2^n E_2^n + p_2^n) \underline{v}_2^{n+\frac{1}{2}}) \tilde{w}_2 \, d\Omega_2 - c_t(\tilde{w}_2, \lambda_{\rho E}^n) = 0 \\
c_t((\dot{\rho E})_1^n - (\dot{\rho E})_2^n, \mu_{\rho E}) = 0
\end{array}
\right.
$$

Appendix G

Résumé

L'objectif de cette thèse est de concevoir un outil numérique capable de superposer des domaines ayant des caractéristiques différentes dans le cadre de l'interaction fluide-dtructure (IFS). Cet outil numérique doit être compatible avec l'intégration en temps explicite et permettre aux maillages des différents domaines d'être non conformes. Utilisé dans le logiciel Europlexus, ce dernier doit permettre une meilleure prise en compte des effets locaux lors de la simulation d'accidents graves dans les réacteurs nucléaires.

Afin d'atteindre un tel objectif, on propose, dans un premier temps, de développer un tel outil pour la superposition de structures et de fluides séparemment puis de les combiner pour le traitement de phénomènes d'interaction fluide-structure. Après une étude approfondie de l'état de l'art des différentes méthodes multi-modèles, les méthodes Arlequin et Chimère ont été retenues car elles présentent l'avantage de permettre aux différents domaines d'être maillés de manière indépendantes et ont déjà été utilisé avec succès pour la simulation de phénomènes de mécanique.

La première étape a donc été de proposer une approche multi-modèle pour la superposition de structures élastiques en dynamique rapide. Pour ce, la méthode Arlequin a été retenue et étendue à l'intégration explicite. En particulier, on a analysé l'influence des composants de la méthode Arlequin sur la stabilité. Après avoir montré que le pas de temps critique tend vers 0 dans certaines configurations, rendant la méthode unitilisable, on a proposé deux approches qui permettent de contourner ce problème. Puisque l'une d'entre elles est inspiré de résultats mono-dimensionnel, on l'a validé sur des examples en deux dimensions. Enfin, les deux approches proposées ont été appliquées à des cas représentatifs des applications nucléaires considérées dans ce travail et observé que celles-ci donnent des solutions précises, validant ainsi les deux approches.

La deuxième étape a consisté à proposer une approche multi-modèle pour la dynamique explicite des fluides. En vue d'une implémentation dans Europlexus, l'équation de conservation du moment a été traté par le formalisme des éléments finis. Les deux autres équations, par ailleurs, sont traitées par un formalisme volumes finis. Le formalisme Arlequin a été utilisé pour le traitement de l'équation de conservation du moment puisqu'il permet, dans un contexte d'IFS, de traiter les degrésde libertés du fluide et de la structure de manière unifiée. Pour l'équation de conservation de la masse et de l'énergie totale, trois approches ont été proposées et appliqué au problème du transport

convectif. Des études de stabilité et de précision ont ainsi été menées. Alors qu'une des approches ne permet pas d'obtenir de solutions précises, les deux autres, inspirées du formalisme Arlequin et Chimère respectivement, présentent des propriétés de convergence similaires. Les deux approches ont donc été considérées pour les équations d'Euler. Deux approches multi-modèles ainsi proposées.

La première utilise un formalisme Arlequin pour le traitement des trois équations tandis que la seconde utilise le formalisme Arlequin pour le traitement de l'équation de conservation de la quantité de mouvement mais un formalisme Chimère pour le traitement des équations de conservation de la masse et de l'énergie totale. Pour les deux approches, des forces fantômes apparaissent et viennent perturber la solution. Une approche a été proposée et implémentée avec succès pour minimiser leurs effets. Une analyse de stabilité des différentes approches a permis de montrer comment choisir les différents paramètres Arlequin pour garantir un pas de temps critique élevé. Les deux approches proposées présentent des propriétes de convergence semblables de sortent que les deux sont considérées pour le traitement de phénomènes d'IFS.

La dernirère étape, consistant à étendre les résultats précédents à l'IFS, fait l'objet de travaux futurs.

Bibliography

[1] IAEA. Safety assessment and verification for nuclear power plants. *Safety Guide, IAEA*, 2001.

[2] K. Pettersson et al. Nuclear fuel behaviour in loss of coolant accident (loca) conditions. Technical report, Organisation for economic co-operation and development, 2009.

[3] New acceptance criteria for emergency core-cooling systems of light-water-cooled nuclear power reactors, 1974.

[4] US Nuclear Regulatory Commission et al. Acceptance criteria for emergency core cooling systems for light-water nuclear power reactors. *10 Cfr 50.46*, 1978.

[5] T. Nakajima. Ria criteria in japan. Technical report, OECD, 2003.

[6] C. Grandjean. A state-of-the-art review of past programs devoted to fuel behavior under loca conditions. part one. clad swelling and rupture assembly flow blockage. Technical report, Technical Report SEMCA 2005-313, IRSN, 2005.

[7] C. Grandjean. A state-of-the-art review of past programs devoted to fuel behavior under loca conditions. part two. impact of clad swelling upon assembly cooling. Technical report, Technical Report SEMCA 2006-183, IRSN, 2006.

[8] B. Tarride. *Physique, fonctionnement et sûreté des REP: Maîtrise des situations accidentelles du système réacteur*. EDP sciences, 2013.

[9] A. J. Gomez, P. J. Garcia, A. Ortego, et al. Analysis of a reactivity initiated accident (ria) in cofrentes npp, cold and hot conditions with retran-3d. In *Proceedings of the 2005 water reactor fuel performance meeting*, page 1236. Japan: Atomic Energy Society of Japan, 2005.

[10] L. O. Jernkvist and A. R. Massih. *Nuclear fuel behaviour under reactivity-initiated accident (RIA) condition: State-of-the-art report*. Nuclear Energy Agency, Organisation for Economic Co-operation and Development (OECD), 2010.

[11] A. L. Florence, G. R. Abrahamson, and D. J. Cagliostro. Hypothetical core disruptive accident experiments on simple fast test reactor models. *nuclear Engineering and Design*, 38:95–108, 1976.

[12] J. F. Marchaterre. Overview of core disruptive accidents. *Nuclear Engineering and Design*, 42:11–17, 1977.

[13] P. Chellapandi, K. Velusamy, S. C. Chetal, S. B. Bhoje, Lal Harbans, and Sethi V.S. Analysis for mechanical consequences of a core disruptive accident in protoype fast breeder reactor. In *Transactions of the 17th International Conference on Structural Mechanics in Reactor Technology (SMiRT 17)*, Prague, Czech Republic, 2003.

[14] V. Faucher. Méthodes numériques et algorithmes parallèles pour la dynamique des systèmes fluide-structure fortement couplés. Technical report, Commissariat à l'énergie atomique et aux énergies alternatives, CEA/Saclay 91191 Gif-sur-Yvette Cedex France, 2014.

[15] U.S. Nuclear Regulatory Commission. *Nuclear Power for Electrical Generation. (Reactor Concepts Manual) USNRC Technical Training Center.* U.S. Nuclear Regulatory Commission, United States, 2012.

[16] V. Faucher, F. Crouzet, and F. Debaud. Mechanical consequences of loca in pwr: Full scale coupled 1d/3d simulations with fluid-structure interaction. *Nuclear Engineering and Design*, 270:359–378, 2014.

[17] V. Faucher, F. Crouzet, P. Piteau, P. Galon, and P. Izquierdo. Numerical and experimental analysis of transient wave propagation through perforated plates for application to the simulation of loca in pwr. *Nuclear Engineering and Design*, 253:1–11, 2012.

[18] WENRA. Wenra statement on safety objectives for new nuclear power plants. Technical report, Western European Nuclear Regulators Association, 2010.

[19] T. Suzuki, Y. Tobita, K. Kawada, et al. A preliminary evaluation of unprotected loss-of-flow accident for a prototype fast-breeder reactor. *Nuclear Engineering and Technology*, 47(3):240–252, 2015.

[20] K. Aoto, P. Dufour, Y. Hongyi, et al. A summary of sodium-cooled fast reactor development. *Progress in Nuclear Energy*, 77:247–265, 2014.

[21] M. J. Berger and J. Oliger. Adaptive mesh refinement for hyperbolic partial differential equations. *Journal of Computational Physics*, 53(3):484–512, 1984.

[22] M. J. Berger and P. Colella. Local adaptive mesh refinement for shock hydrodynamics. *Journal of Computational Physics*, 82(1):64–84, 1989.

[23] P. MacNeice, K. M. Olson, C. Mobarry, et al. Paramesh: A parallel adaptive mesh refinement community toolkit. *Computer Physics Communications*, 126(3):330–354, 2000.

[24] F. Casedei, P. Diez, and F. Verdugo. Adaptive 3d refinement and un-refinement of 8-node solid and fluid hexahedra in europlexus. Technical report, JRC European Commission (Institute for the Protection and Security of the Citizen), 2011.

[25] E. A. Volkov. A finite difference method for finite and infinte regions with piecewise smooth boundaries. *Docklady*, 168(5):744–747, 1966.

[26] E. A. Volkov. The method of composite meshes for finite and infinte regions with piecewise smooth boundaries. *Proceedings of the Steklov Institute of Mathematics*, 96:145–185, 1968.

[27] E. Sánchez-Palencia. Non-homogeneous media and vibration theory. *Lecture notes in physics*, 127, 1980.

[28] Stephen Whitaker. *The method of volume averaging*, volume 13. Springer Science & Business Media, 2013.

[29] G. Artini and D. Broc. A homogenisation method for a fsi problem: Application to a tube bundle row. In *ASME 2017 Pressure Vessels and Piping Conference*, pages V005T11A026–V005T11A026. American Society of Mechanical Engineers, 2017.

[30] W Hackbusch. *Multi-Grid Methods and Applications*. Springer, 1985.

[31] W. L. Briggs, V. E. Henson, and S. F. McCormick. *A multigrid tutorial*. Society for Industrial and Applied Mathematics, 1999.

[32] S. R. Fulton, P. E. Ciesielski, and W. H. Schubert. Multigrid method for periodic heterogeneous media. part 2: Mutliscale modeling and quality controll in multidimensional case. *Computer Methods in Applied Mechanics and Engineering*, 126:17–38, 1995.

[33] P. Lascaux and R. Théodor. *Analyse numérique matriciellle appliquée à l'art de l'ingénieur. Tome 2*. Masson, 1987.

[34] J. Fish and V. Belsky. Multigrid method for periodic heterogeneous media. part 1: Convergence studies for one-dimensional case. *Computer Methods in Applied Mechanics and Engineering*, 126:1–16, 1995.

[35] J. Fish and V. Belsky. Multigrid method for periodic heterogeneous media. part 2: Mutliscale modeling and quality controll in multidimensional case. *Computer Methods in Applied Mechanics and Engineering*, 126:17–38, 1995.

[36] R. H. Ni. A multiple-grid scheme for solving the euler equations. In AIAA, editor, *Proceedings of the 5th Computational Fluid Dynamics Conference*, pages 257–264, Palo Alto, CA, 1981.

[37] E. Katzer. Multigrid methods for hyperbolic equations. In *Multigrid methods III*, pages 253–263, Basel, 1991. Birkhauser Verlag.

[38] S. Amarala and J. W. L. Wan. Multigrid methods for systems of hyperbolic conservation laws. *Multiscale Modeling and Simulation*, 11(2):586–614, 2013.

[39] A Jameson. Solution of the euler equations for two-dimensional transonic flow by a multigrid method. *Journal of Computational and Applied Mathematics*, 13:327–355, 1983.

[40] A Jameson and S. Yoon. Multigrid solution of the euler equations using implicit schemes. In *Proceedings of the AIAA 23rd Aerospace Sciences Meeting (Reno,NV)*, page 293, New York, 1985. American Institute of Aeronautics and Astronautics.

[41] W. A. Mulder. Multigrid relaxation for the euler equations. *Journal of Computational Physics*, 60:235–252, 1985.

[42] W. A. Mulder. A new multigrid approach to convection problems. *Journal of Computational Physics*, 83:303–323, 1989.

[43] J. T. Oden and T. I. Zohdi. Analysis and adaptive modeling of highly heterogeneous elastic structure. *Computer Methods in Applied Mechanics and Engineering*, 148:367–391, 1997.

[44] J. T. Oden, K. Vemaganti, and N. Moës. Hierarchical modeling of heterogeneous solids. *Computer Methods in Applied Mechanics and Engineering*, 172(1-4):3–25, 1999.

[45] J. T. Oden and K. Vemaganti. Adaptive modeling of composite structures: Modeling error estimation. In *Texas Institute for Computational and Applied Mathematics*. Citeseer, 1999.

[46] F. Feyel and J-L. Chaboche. Fe2 multiscale approach for modelling the elastoviscoplatic behaviour of long fiber sic/ti composite materials. *Computer Methods in Applied Mechanics and Engineering*, 183(3-4):309–330, 2000.

[47] F. Feyel and J-L. Chaboche. A multiple finite element method (fe2) to describe the response of highly non-linear structures using generalized continua. *Computer Methods in Applied Mechanics and Engineering*, 192(28-30):3233–3244, 2003.

[48] I. Ramiere, R. Masson, B. Michel, and S. Bernaud. Un schéma de calcul multiéchelles de type éléments finis au carré pour la simulation de combustibles nucléaires hétérogènes. In *13eme Colloque National en Calcul des Structures*, Giens, France, 2017.

[49] S. Loehnert and T. Belytschko. A multiscale projection method for macro/microcrack simulations. *International Journal for Numerical Methods in Engineering*, 71(12):1466–1482, 2007.

[50] T. Belytschko, S. Loehnert, and J.-H. Song. Multiscale aggregating discontinuities: a method for circumventing loss of material stability. *International Journal for Numerical Methods in Engineering*, 73(6):869–894, 2008.

[51] A. S. Almgren, J. B. Bell, P. Colella, and T. Marthaler. A cartesian grid projection method for the incompressible euler equations in complex geometries. *SIAM Journal on Scientific Computing*, 18(5):1289–1309, 1997.

[52] A. S. Almgren, J. Bell, P. Colella, and L. Howell. An adaptive projection method for the incompressible euler equations. In *11th Computational Fluid Dynamics Conference*, page 3345, 1993.

[53] D. P. Young, R. G. Melvin, M. B. Bieterman, et al. A locally refined rectangular grid finite element method: application to computational fluid dynamics and computational physics. *Journal of Computational Physics*, 92(1):1–66, 1991.

[54] M. Geers, V. Kouznetsova, and WAM Brekelmans. Multi-scale computational homogenization: Trends and challenges. *Journal of computational and applied mathematics*, 234(7):2175–2182, 2010.

[55] T. J. R. Hughes. Multiscale phenomena : Green's functions, the dirichlet-to-neumann for- mulation, subgrid scale models, bubbles and the origins of stabilized methods. *Computer Methods in Applied Mechanics and Engineering*, 127:387–401, 1995.

[56] T. J. R. Hughes, G.R. Feijo, L. Mazzei, and J.B Quincy. The variational multiscale method - a paradigm for computational mechanics. *Computer Methods in Applied Mechanics and Engineering*, 166:3–24, 1998.

[57] T. J. R. Hughes, G. Scovazzi, and L. P. Franca. Multiscale and stabilized methods. *Encyclopedia of Computational Mechanics Second Edition*, 2004.

[58] V. Gravemeier. *The variational multiscale method for laminar and turbulent incompressible flow*. Institut für Baustatik der Universität Stuttgart, Stuttgart, Deutschland, 2003.

[59] V. Gravemeier, S. Lenz, and W. A. Wall. Variational multiscale methods for incompressible flows. *International Journal of Computing Science and Mathematics*, 1(2-4):444–466, 2007.

[60] N. Ahmed, T. C. Rebollo, V. John, and S. Rubino. A review of variational multiscale methods for the simulation of turbulent incompressible flows. *Archives of Computational Methods in Engineering*, 24(1):115–164, 2017.

[61] T. J. R. Hughes, L. Mazzei, and K. E. Jansen. Large eddy simulation and the variational multiscale method. *Computing and Visualization in Science*, 3(1-2):47–59, 2000.

[62] U Rasthofer, W. A Wall, and V. Gravemeier. An extended algebraic variational multiscale-multigrid-multifractal method for large-eddy simulation of turbulent two-phase flow. In *10th International Workshop on Variational Multiscale and Stabilized Finite Elements (VMS2015)*, 2015.

[63] I. Babuska and J. M. Melenk. The partition of unity method. *International Journal for Numericals Methods in Engineering*, 40:727–758, 1997.

[64] J. M. Melenk and I. Babuska. The partition of unity finite element method: basic theory and applications. *Computer methods in applied mechanics and engineering*, 139(1-4):289–314, 1996.

[65] T. Belytschko, R. Gracie, and G. Ventura. A review of extended/generalized finite element methods for material modeling. *Modelling and Simulation in Materials Science and Engineering*, 17(4):043001, 2009.

[66] T. Strouboulis, I. Babuska, and K. Copps. The design and analysis of the generalized finite element method. *Computer Methods in Applied Mechanics and Engineering*, 181:43–69, 2000.

[67] N. Moës, J. Dolbow, and T. Belytschko. A finite element method for crack growth without remeshing. *International journal for numerical methods in engineering*, 46(1):131–150, 1999.

[68] J. Dolbow, N. Moës, and T. Belytschko. Discontinuous enrichment in finite elements with a partition of unity method. *Finite elements in analysis and design*, 36:235–260, 2000.

[69] C. A. Duarte and D.-J. Kim. Analysis and applications of a generalized finite element method with global–local enrichment functions. *Computer Methods in Applied Mechanics and Engineering*, 197(6-8):487–504, 2008.

[70] D.-J. Kim, J. P. Pereira, and C. A. Duarte. Analysis of three-dimensional fracture mechanics problems: A two-scale approach using coarse-generalized fem meshes. *International Journal for Numerical Methods in Engineering*, 81(3):335–365, 2010.

[71] J. A. Sethian. *Level set methods and fast marching methods: evolving interfaces in computational geometry, fluid mechanics, computer vision, and materials science*, volume 3. Cambridge university press, 1999.

[72] S. Osher and R. P. Fedkiw. Level set methods: an overview and some recent results. *Journal of Computational physics*, 169(2):463–502, 2001.

[73] N. Sukumar, N. Moës, B. Moran, and T. Belytschko. Extended finite element method for three-dimensional crack modelling. *International Journal for Numerical Methods in Engineering*, 48(11):1549–1570, 2000.

[74] H. Ben Dhia and O. Jamond. On the use of xfem within the arlequin framework fir the simulation of crack propagation. *Computer Methods in Applied Mechanics and Engineering*, 199(21-22):1403–1414, 2010.

[75] N. Sukumar, D. L. Chopp, N. Moës, and T. Belytschko. Modeling holes and inclusions by level sets in the extended finite-element method. *Computer methods in applied mechanics and engineering*, 190(46-47):6183–6200, 2001.

[76] T. Menouillard, J. Réthoré, A. Combescure, and H. Bung. Efficient explicit time stepping for the extended finite element method (x-fem). *International Journal for Numerical Methods in Engineering*, 68:911–939, 2006.

[77] T. Menouillard, J. Réthoré, N. Moës, A. Combescure, and H. Bung. Mass lumping strategies for x-fem explicit dynamics: Application to crack propagation. *International Journal for Numerical Methods in Engineering*, 74:447–474, 2008.

[78] T. Elguedj, A. Gravouil, and H. Maigre. An explicit dynamics extended finite element method. part 1: mass lumping for arbitrary enrichment functions. *Computer Methods in Applied Mechanics and Engineering*, 198(30-32):2297–2317, 2009.

[79] A. Gravouil, T. Elguedj, and H. Maigre. An explicit dynamics extended finite element method. part 2: Element-by-element stable-explicit/explicit dynamic scheme. *Computer Methods in Applied Mechanics and Engineering*, 198(30-32):2318–2328, 2009.

[80] C. Bernardi. A new nonconforming approach to domain decomposition: the mortar element method. *Nonlinear partial equations and their applications*, 1989.

[81] F. B. Belgacem, P. Hild, and P. Laborde. The mortar finite element method for contact problems. *Mathematical and Computer Modelling*, 28(4-8):263–271, 1998.

[82] C. Bernardi, Y. Maday, and A. T. Patera. Domain decomposition by the mortar element method. In *Asymptotic and numerical methods for partial differential equations with critical parameters*, pages 269–286. Springer, 1993.

[83] K. C. Park and C. A. Felippa. A variational principle for the formulation of partitioned structural systems. *International Journal for Numerical Methods in Engineering*, 47(1-3):395–418, 2000.

[84] V. B. Shenoy, R. Miller, E. B. Tadmor, D. Rodney, R. Phillips, and M. Ortiz. An adaptive finite element approach to atomic-scale mechanics – the quasicontinuum method. *Journal of the Mechanics and Physics of Solids*, 47(3):611–642, 1999.

[85] W. A. Curtin and R. E. Miller. Atomistic/continuum coupling in computational materials science. *Modelling and simulation in materials science and engineering*, 11(3):R33, 2003.

[86] F. F. Abraham, J. Q. Broughton, N. Bernstein, and E. Kaxiras. Spanning the length scales in dynamic simulation. *Computer in Physics*, 12(6):538–546, 1998.

[87] R. E. Rudd and J. Q. Broughton. Concurrent coupling of length scales in solid state systems. *Physica status solidi (b)*, 217(1):251–291, 2000.

[88] T. Belytschko and S. P. Xhiao. Coupling methods for continuum model with molecular model. *International Journal for Multiscale Computational Engineering*, 1(1), 2003.

[89] S. P. Xiao and T. Belytschko. A bridging domain method for coupling continua with molecular dynamics. *Computer Methods in Applied Mechanics and Engineering*, 193(17-20):1645–1669, 2004.

[90] M. Xu and T. Belytschko. Conservation properties of the bridging domain method for coupled molecular/continuum dynamics. *International Journal for Numerical Methods in Engineering*, 76(3):278–294, 2008.

[91] G. J. Wagner and Liu W. K. Coupling of atomistic and continuum simulations using a bridging scale decomposition. *Journal of Computational Physics*, 190(1):249–274, 2003.

[92] W. K. Liu, H. S. Park, D. Qian, et al. Bridging scale methods for nanomechanics and materials. *Computer Methods in Applied Mechanics and Engineering*, 195(13-16):1407–1421, 2006.

[93] H. Ben Dhia. Multiscale mechanical problems : the arlequin method. *Comptes Rendus de l'Académie des Sciences série IIb, Paris Série I*, 326:899–904, 1998.

[94] H. Ben Dhia. Numerical modelling of multiscale problems: the arlequin method. In ECCM, editor, *CD Proceedings of ECCM'99*, Munchen, Deutschland, 1999.

[95] H. Ben Dhia and G. Rateau. Contact problems in the arlequin framework. *Comptes Rendus de l'Académie des Sciences, Paris Série I*, 332:649–654, 2001.

[96] H. Ben Dhia and G. Rateau. Application of the arlequin method to some structures with defects. *Revue Européenne des éléments finis*, 11:291–304, 2002.

[97] H. Ben Dhia and G. Rateau. The arlequin method as a flexible engineering design tool. *Numerical Methods in Engineering*, 62(11):1442–1462, 2005.

[98] H. Ben Dhia. Further insights by theoretical investigations of the multiscale arlequin method. *International Journal for Multiscale Computational Engineering*, 6(3):215–232, 2008.

[99] H. Ben Dhia and M. Zarroug. Mathematical analysis of the mixed arlequin method. *3rd Contact Mechanics International Symposium*, 2001.

[100] G. Rateau. *Méthode Arlequin pour les problèmes mécaniques multi-échelles*. PhD thesis, École Centrale de Paris, 2003.

[101] S. Prudhomme, H. Ben Dhia, P. T. Bauman, et al. Computational analysis of modeling error for the coupling of particle and continuum models by the arlequin method. *Computer Methods in Applied Mechanics and Engineering*, pages 3399–3409, 2008.

[102] S. Prudhomme, L. Chamoin, H. Ben Dhia, et al. An adaptive strategy for the control of modeling error in two-dimensional atomic-to-continuum coupling simulations. *Computer Methods in Applied Mechanics and Engineering*, pages 1887–1901, 2009.

[103] P. T. Bauman, H. Ben Dhia, N. Elkhodja, et al. On the application of the arlequin method to the coupling of particles and continuum models. *Computational Mechanics*, 42:511–530, 2008.

[104] P.T. Bauman, J. T. Oden, and S. Prudhomme. Adaptive multiscale modeling of polymeric materials with arlequin coupling and goals algorithms. *Computer Methods in Applied Mechanics and Engineering*, 198:799–818, 2009.

[105] I. Babuska. The finite element method with lagrangian multipliers. *Numerische Mathematik*, 20(3):179–192, 1973.

[106] L. Chamoin, J. T. Oden, and S. Prudhomme. A stochastic coupling method for atomic-to-continuum monte-carlo simulations. *Computer Methods in Applied Mechanics and Engineering*, pages 3530–3546, 2008.

[107] L. Chamoin et al. Ghost forces and spurious effects in atomic-to-continuum coupling methods by the arlequin approach. *International Journal for Numerical Methods in Engineering*, 83:1081–1113, 2010.

[108] Y. Chuzel. *Caractérisation expérimentale et simulation numérique d'impacts de glace à haute vitesse*. PhD thesis, Institut National des Sciences Appliquées de Lyon, Lyon, 2009.

[109] Y. Chuzel-Marmot, R. Ortiz, and A. Combescure. Three dimensional sph-fem gluing for simulation of fast impacts on concrete slabs. *Computers and Structures*, 89:2484–2494, 2011.

[110] F. Caleyron. *Simulation numérique par la méthode SPH de fuites de fluide consécutives à la déchirure d'un réservoir sous impact*. PhD thesis, Institut National des Sciences Appliquées de Lyon, Lyon, 2011.

[111] F. Caleyron, Y. Chuzel-Marmot, and A. Combescure. Modeling of reinforced concrete through sph-fe coupling and its application to the simulation of a projectile's impact onto a slab. *International Journal for Numerical Methods in Biomedical Engineering*, 27:882–898, 2011.

[112] Y. Chuzel-Marmot, A. Combescure, and R. Ortiz. Explicit dynamics "sph-finite element" coupling using the arlequin method. *European Journal of Computational Mechanics/Revue Européenne de Mécanique Numérique*, 17:5–7, 2012.

[113] F. Caleyron, A. Combescure, V. Faucher, et al. Sph modeling of fluid/solid interaction for dynamic failure analysis of fluid-filled thin shells. *Journal of Fluids and Structures*, 39:126–153, 2013.

[114] P. A. Guidault and T. Belytschko. On the l2 and the h1 couplings for an overlapping domain decomposition method using lagrange multipliers. *International Journal for Numerical Methods in Engineering*, 70:322–350, 2007.

[115] A. Ghanem, M. Torkhani, N. Mahjoubi, et al. Arlequin framework for multimodel, multi-time scale and heterogeneous time integrators for structural transient dynamics. *Computer Methods in Applied Mechanics and Engineering*, 254:292–308, 2012.

[116] A. Ghanem. *Contributions à la modélisation avancée des machines tournantes en dynamique transitoire dans le cadre Arlequin*. PhD thesis, Institut National des Sciences Appliquées de Lyon, Lyon, 2013.

[117] J. L. Steger and D. S. Chaussee. Generation of body-fitted coordinates using hyperbolic partial differential equations. *SIAM Journal of Scientific and Statistical Computing*, 1(4):431–437, 1983.

[118] Joseph L. Steger, F.Carroll Dougherty, and John A. Benek. A chimera grid scheme. *American Society of Mechanical Engineers, Fluids Engineering Division (Publication) FED*, 5, 02 1983.

[119] J. L. Steger and J. A. Benek. On the use of composite grid schemes in computational aerodynamics. *Computer Methods in Applied Mechanics and Engineering*, 64:301–320, 1987.

[120] Y. Zheng and M.-S. Liou. A novel approach of three-dimensional hybrid grid methodology: Part 1. grid generation. *Computer methods in applied mechanics and engineering*, 192(37-38):4147–4171, 2003.

[121] K.-H. Kao and M.-S. Liou. Advance in overset grid schemes-from chimera to dragon grids. *AIAA journal*, 33(10):1809–1815, 1995.

[122] R. Meakin. An efficient means of adaptive refinement within systems of overset grids. In *12th Computational Fluid Dynamics Conference*, page 1722, 1995.

[123] P. Gamnitzer and W. A. Wall. An ale-chimera method for large deformation fluid structure interaction. In *European Conference on Computational Fluid Dynamics*, Delft, Netherlands, 2006.

[124] E. L. Blades and D. L. Marcum. A sliding interface method for unsteady unstructured flow simulations. *International Journal for Numerical Methods in Fluids*, 53(3):507–529, 2007.

[125] C. Wolf. *A chimera simulation method and detached eddy simulation for vortex-airfoil interactions*. PhD thesis, Georg-August-Universität, Göttingien, 2011.

[126] E. J. Nielsen and Diskin B. Discrete adjoint-based design for unsteady turbulent flows on dynamic overset unstructured grids. *AIAA journal*, 51(6):1355–1373, 2013.

[127] R. L. Meakin. Moving body overset grid methods for complete aircraft tiltrotor simulations. In *11th Computational Fluid Dynamics Conference*, page 3350, 1993.

[128] T. Renaud, M. Costes, and S. Péron. Computation of goahead configuration with chimera assembly. *Aerospace Science and Technology*, 19:50–57, 2012.

[129] T. Renaud, A. Le Pape, and S. Péron. Numerical analysis of hub and fuselage drag breakdown of a helicopter configuration. *CEAS Aeronautical Journal*, 4(4):409–419, 2013.

[130] P. Buning, I. Chiu, S. Obayashi, Y. Rizk, and J. Steger. Numerical simulation of the integrated space shuttle vehicle in ascent. In *15th Atmospheric Flight Mechanics Conference*, page 4359, 1988.

[131] R. Gomez and E. Ma. Validation of a large scale chimera grid system for the space shuttle launch vehicle. In *12th Applied Aerodynamics Conference*, page 1859, 1994.

[132] A. Jameson, W. Schmidt, and E. Turkel. Numerical solution of the euler equations by finite volume methods using runge kutta time stepping schemes. In *14th fluid and plasma dynamics conference*, page 1259, 1981.

[133] J. A. Benek, J. L. Steger, and F. C. Dougherty. A flexible grid embedding technique with application to the euler equations. *AIAA papers*, pages 373–382, 1983.

[134] G. Houzeaux, B. Eguzkitza, R. Aubry, et al. A chimera method for the incompressible navier-stokes equations. *International Journal for Numerical Methods in Fluids*, 75:155–183, 2014.

[135] M. J. Berger. On conservation at grid interfaces. *SIAM journal on numerical analysis*, 24(5):967–984, 1987.

[136] C. Benoît. *Méthode d'adaptation de maillages au moyen d'algorithmes génétiques pour le calcul d'écoulements compressibles*. PhD thesis, ENSAM, Paris, 1999.

[137] Z.-N. Wu. Uniqueness of steady-state solutions for difference equations on overlapping grids. *SIAM journal on numerical analysis*, 33(4):1336–1357, 1996.

[138] Z. Wang, H. Yang, and A. Przekwas. Implicit conservative interfacing for 3d overlapped chimera grids. In *12th Computational Fluid Dynamics Conference*, page 1683, 1995.

[139] Z. J. Wang. A fully conservative interface algorithm for overlapped grids. *Journal of Computational Physics*, 122(1):96–106, 1995.

[140] P. Brenner. Simulation du mouvement relatif de corps soumis à un écoulement instationnaire par une méthode de chevauchement de maillages. In *AGARD CONFERENCE PROCEEDINGS AGARD CP*, pages 32–32. AGARD, 1996.

[141] T. Berglind. A hybrid structured-unstructured grid method for aerodynamic flow simulations. In *33rd Aerospace Sciences Meeting and Exhibit*, page 51, 1995.

[142] G. Starius. Composite mesh difference methods for elliptic and boundary value problems. *Numerische Mathematik*, 28:243–258, 1977.

[143] G. Starius. On composite mesh difference methods for hyperbolic differential equations. *Numerische Mathematik*, 35(3):243–258, 1980.

[144] B. Gustafsson, H.-O. Kreiss, and A. Sundström. Stability theory of difference approximations for mixed initial boundary value problems. ii. *Mathematics of Computation*, pages 649–686, 1972.

[145] A. Lerat and Z. N. Wu. Stable conservative multidomain treatments for implicit euler solvers. *Journal of computational physics*, 123(1):45–64, 1996.

[146] Z.-N. Wu. Theoretical aspects of composite grid methods in computational fluid dynamics. In *Computational Fluid Dynamics 2000*, pages 749–754. Springer, 2001.

[147] E. Pärt-Enander and B. Sjögreen. Conservative and non-conservative interpolation between overlapping grids for finite volume solutions of hyperbolic problems. *Computers & fluids*, 23(3):551–574, 1994.

[148] F. Brezzi, J.-L. Lions, and O. Pironneau. Analysis of a chimera method. *Comptes Rendus de l'Académie des Sciences-Series I-Mathematics*, 332(7):655–660, 2001.

[149] F. Hecht, J.-L. Lions, and O. Pironneau. Domain decomposition algorithm for computer aided design. In *Applied nonlinear analysis*, pages 185–198. Springer, 2002.

[150] S. Péron. *Méthode d'assemblage de maillages recouvrants autour de géométries complexes pour des simulations en aérodynamique compressible.* PhD thesis, École Nationale Supérieure d'Arts et Métiers, 2014.

[151] O. Jamond. *Propagation numérique de zones critiques dans un pneumatique par approches multi-modèles.* PhD thesis, École Centrale Paris, 2011.

[152] A. Fernier, V. Faucher, and O. Jamond. Multi-model arlequin method for transient structural dynamics with explicit time integration. *International Journal for Numerical Methods in Engineering*, 112(9):1194–1215, 2017.

[153] D. Boffi, A. Buffa, and L. Gastaldi. Convergence analysis for hyperbolic evolution problems in mixed form. *Numerical Linear Algebra with Applications*, 20:541–556, 2013.

[154] R. J. LeVeque. *Finite volume methods for hyperbolic problems*, volume 31. Cambridge university press, 2002.

[155] A. Gravouil. *Méthode multi-échelles en temps et en espace avec décomposition de domaines pour la dynamique non-linéaire des structures.* PhD thesis, École Nationale Supérieure de Cachan, 2000.

[156] E. Hinton, T. Rock, and O. C. Zienkiewicz. A note on mass lumping in the related processes in the finite element method. *Earthquake Engineering and Strucutral Dynamics*, 4:245–249, 1976.

[157] A. Cardona and M. Geradin. Time integration of the equations of motion in mechanism analysis. *Computers and Strucutures*, 33(3):801–820, 1989.

[158] C. Farhat, L. Crivelli, and M. Geradin. Implicit time integration of a class of constrained hybrid formulations - part i: Spectral stability theory. *Computers Methods in Applied Mechanics and Engineering*, 125:71–107, 1995.

[159] T. J. R. Hughes and W. K. Liu. Implicit-explicit finite elements in transient analysis: Stability theory. *Journal of Applied Mechanics*, 45:371–374, 1978.

[160] T. Belytschko, N. Moës, S. Usui, and C. Parimi. Arbitrary discontinuities in finite elements. *International Journal for Numerical Methods in Engineering*, 50(4):993–1013, 2001.

[161] T. Belytschko and T. Black. Elastic crack growth in finite elements with minimal remeshing. *International journal for numerical methods in engineering*, 45(5):601–620, 1999.

[162] N. Moës, A. Gravouil, and T. Belytschko. Non-planar 3d crack growth by the extended finite element and level sets – part i: Mechanical model. *International Journal for Numerical Methods in Engineering*, 53(11):2549–2568, 2002.

[163] A. Gravouil, N. Moës, and T. Belytschko. Non-planar 3d crack growth by the extended finite element and level sets – part ii: Level set update. *International Journal for Numerical Methods in Engineering*, 53(11):2569–2586, 2002.

[164] C. Daux, N. Moës, J. Dolbow, N. Sukumar, and T. Belytschko. Arbitrary branched and intersecting cracks with the extended finite element method. *International journal for numerical methods in engineering*, 48(12):1741–1760, 2000.

[165] P. Rozycki, N. Moës, E. Bechet, and C. Dubois. X-fem explicit dynamics for constant strain elements to alleviate mesh constraints on internal or external boundaries. *Computer Methods in Applied Mechanics and Engineering*, 197(5):349–363, 2008.

[166] T. Belytschko, H. Chen, J. Xu, and G. Zi. Dynamic crack propagation based on loss of hyperbolicity and a new discontinuous enrichment. *International journal for numerical methods in engineering*, 58(12):1873–1905, 2003.

[167] B. Prabel, A. Combescure, A. Gravouil, and S. Marie. Level set x-fem non-matching meshes: application to dynamic crack propagation in elastic-plastic media. *International Journal for Numerical Methods in Engineering*, 69(8):1553–1569, 2007.

[168] J. Réthoré, A. Gravouil, and A. Combescure. An energy-conserving scheme for dynamic crack growth using the extended finite element method. *International Journal for Numerical Methods in Engineering*, 63(5):631–659, 2005.

[169] R. de Borst, J. J. C. Remmers, and A. Needleman. Mesh-independent discrete numerical representations of cohesive-zone models. *Engineering fracture mechanics*, 73(2):160–177, 2006.

[170] J. J. C. Remmers, R. de Borst, and A. Needleman. The simulation of dynamic crack propagation using the cohesive segments method. *Journal of the Mechanics and Physics of Solids*, 56(1):70–92, 2008.

[171] S.-Y. Chang. An explicit method with improved stability property. *International Journal for Numerical Methods in Engineering*, 77(8):1100–1120, 2009.

[172] V. Faucher, M. Bulik, and P. Galon. Updated vofire algorithm for fast fluid-structure transient dynamics with multi-component stiffened fas flows implementing anti-dissipation on unstructured grids. *Journal of Fluids and Structure*, 74:64–89, 2017.

[173] O. Jamond and V. Faucher. Regularized immersed boundary-type formulation for fast transient dynamics with fluid-structure interaction. *Advances in Engineering Software*, 108:1–23, 2017.

[174] G. Allaire. *Analyse numérique et optimisation: Une introduction à la modélisation mathématique et à la simulation numérique*. Editions Ecole Polytechnique, 2005.

[175] V. Faucher. Advanced parallel strategy for strongly coupled fast transient fluid-structure dynamics with dual management of kinematic constraints. *Advances in Engineering Software*, 67:70–89, 2014.

[176] F. Daude, J. Berland, T. Emmert, P. Lafon, F. Crouzet, and C. Bailly. A high-order finite-difference algorithm for direct computation of aerodynamic sound. *Computers & Fluids*, 61:46–63, 2012.

[177] J. Donea and A. Huerta. *Finite element methods for flow problems*. John Wiley & Sons, 2003.

[178] P. Grisvard. *Elliptic problems in nonsmooth domains*, volume 69. SIAM, 2011.

[179] J. Von Neumann and R. D. Richtmyer. A method for the numerical calculation of hydrodynamic shocks. *Journal of applied physics*, 21(3):232–237, 1950.

[180] J. Galon, P.and Nunziati. Méthode des volumes finis dans europlexus - extension du schéma à l'ordre deux en espace et en temps. Technical report, Commissariat à l'énergie atomique, 07 2007.

[181] B. R. Feiring, D. T. Phillips, and G. L Hogg. Penalty function techniques: a tutorial. *Computers & industrial engineering*, 9(4):307–326, 1985.

université PARIS-SACLAY
ÉCOLE DOCTORALE
Sciences mécaniques et énergétiques, matériaux et géosciences (SMEMAG)

Titre: Couplage multi-modèle en dynamique rapide avec interaction fluide-structure

Mots clés: Multi-modèle, Arlequin, Chimère, Intégration Explicite, IFS.

Résumé: Dans l'industrie nucléaire, la simulation de transitoires accidentels à l'échelle d'un réacteur devient une composante d'importance croissante de la démonstration de sûreté à destination des agences de surveillance nationales. Elle permet ainsi de limiter le recours à des expériences complexes et coûteuses tout en facilitant l'évaluation des stratégies de mitigation. Cependant, les modèles mis en jeu sont inévitablement volumineux et construits avec une finesse de modélisation rendant difficile la prise en compte de détails géométriques locaux pourtant susceptibles d'influencer significativement la solution globale. Dans ce travail de thèse, on propose ainsi des approches multi-modèles pour l'intégration de tels détails dans un modèle global sans modification du maillage initial (on parle aussi de zoom numérique). Des techniques sont proposées aussi bien pour les structures que pour les fluides, avec un souci de démontrer la précision et la stabilité de la solution multi-modèles couplée comparée à une solution de référence à une seule échelle. Ce travail intègre deux spécificités propres, à savoir son adéquation avec les contraintes de la dynamique rapide avec intégration temporelle explicite et l'objectif de traiter simultanément la superposition de modèles et l'interaction fluide-structure.

Title: Multi-model coupling for transient fluid structure interaction.

Keywords: Multi-model, Arlequin, Chimera, Explicit Integration, FSI.

Abstract: In nuclear industry, simulating accidental transient sequences at full reactor scale is becoming an increasingly important feature of the safety demonstration towards national agencies. It thus allows limiting the number of complex and costly experiments, while simplifying and accelerating the evaluation of mitigation strategies. However, the implemented numerical models are inevitably heavy to build and maintain, with a global modelling scale making it difficult to account for local geometric details yet able to significantly influence the physical solution. To provide an answer to this problematics, this PhD work is dedicated to multi-model approaches designed to integrate such details into bigger models with no modification at the global level (techniques often designated as numerical zoom techniques). Some methods are proposed for both structures and fluids, with special care given to the accuracy and stability of the coupled multi-scale solution compared to a single-scale reference solution. This work handles two very specific topics, namely its compatibility with numerical features imposed by fast transient dynamics with explicit time integration, and the general objective of simultaneously dealing with superimposed models and fluid-structure interaction.

Université Paris-Saclay
Espace Technologique / Immeuble Discovery
Route de l'Orme aux Merisiers RD 128 / 91190 Saint-Aubin, France